DISSERTATION

COMPARISON OF CONVECTIVE CLOUDS OBSERVED BY SPACEBORNE W-BAND RADAR AND SIMULATED BY CLOUD-RESOLVING ATMOSPHERIC MODELS

Submitted by

Jason B. Dodson

Department of Atmospheric Science

In partial fulfillment of the requirements

For the Degree of Doctor of Philosophy

Colorado State University

Fort Collins, Colorado

Spring 2014

Doctoral Committee:

Advisor: David Randall

Thomas Birner
Eric Maloney
V. Chandrasekar

ABSTRACT

COMPARISON OF CONVECTIVE CLOUDS OBSERVED BY SPACEBORNE W-BAND RADAR AND SIMULATED BY CLOUD-RESOLVING ATMOSPHERIC MODELS

Deep convective clouds (DCCs) play an important role in regulating global climate through vertical mass flux, vertical water transport, and radiation. For general circulation models (GCMs) to simulate the global climate realistically, they must simulate DCCs realistically. GCMs have traditionally used cumulus parameterizations (CPs). Much recent research has shown that multiple persistent unrealistic behaviors in GCMs are related to limitations of CPs. Two alternatives to CPs exist: the global cloud-resolving model (GCRM), and the multiscale modeling framework (MMF). Both can directly simulate the coarser features of DCCs because of their multi-kilometer horizontal resolutions, and can simulate large-scale meteorological processes more realistically than GCMs. However, the question of realistic behavior of simulated DCCs remains. How closely do simulated DCCs resemble observed DCCs?

In this study I examine the behavior of DCCs in the Nonhydrostatic Icosahedral Atmospheric Model (NICAM) and Superparameterized Community Atmospheric Model (SP-CAM), the latter with both single-moment and double-moment microphysics. I place particular emphasis on the relationship between cloud vertical structure and convective environment. I also emphasize the transition between shallow clouds and mature DCCs. The spatial domains used are the tropical oceans and the contiguous United States (CONUS), the latter of which produces frequent vigorous convection during the summer. CloudSat is used to observe DCCs, and A-Train and reanalysis data are used to represent the large-scale environment in which the clouds form.

The CloudSat cloud mask and radar reflectivity profiles for CONUS cumuliform clouds (defined as clouds with a base within the planetary boundary layer) during boreal summer are first averaged and compared. Both NICAM and SP-CAM greatly underestimate the vertical growth of cumuliform clouds. Then they are sorted by three large-scale environmental variables: total preciptable water (TPW), surface air temperature (SAT), and 500hPa vertical velocity (W500), representing the dynamical and thermodynamical environment in which the clouds form. The sorted CloudSat profiles are then compared with NICAM and SP-CAM profiles simulated with the Quickbeam CloudSat simulator. Both models have considerable difficulty representing the relationship of SAT and clouds over CONUS. For TPW and W500, shallow clouds transition to DCCs at higher values than observed. This may be an indication of the models' inability to represent the formation of DCCs in marginal convective environments. NICAM develops tall DCCs in highly favorable environments, but SP-CAM appears to be incapable of developing tall DCCs in almost any environment. The use of double moment microphysics in SP-CAM improves the frequency of deep clouds and their relationship with TPW, but not SAT. Both models underpredict radar reflectivity in the upper cloud of mature DCCs. SP-CAM with single moment microphysics has a particularly unrealistic DCC reflectivity profile, but with double moment microphysics it improves substantially. SP-CAM with double-moment microphysics unexpectedly appears to weaken DCC updraft strength as TPW increases, but otherwise both NICAM and SP-CAM represent the environment-versus-DCC relationships fairly realistically.

ACKNOWLEDGEMENTS

This work has been supported by the National Science Foundation Science and Technology Center for Multi-Scale Modeling of Atmospheric Processes, managed by Colorado State University under cooperative agreement. No. ATM-0425247. In addition, this work has been supported by the Jet Propulsion Laboratory (JPL) under a contract with the National Aeronautics and Space Administration (NASA), CloudSat award #NAS5-99237, and the Department of Atmospheric Science, Colorado State University.

TABLE OF CONTENTS

1. INTRODUCTION

Convective clouds are an important component of weather and climate, and thus remain a topic of active research in climate science. Shallow cumulus clouds enhance the mixing between the planetary boundary layer (PBL) and the free troposphere, and also increase the effective regional albedo where they occur. Cumulus congestus clouds moisten the middle troposphere, and often condition the regional environment for future deep convection [Benedict and Randall 2007, Waite and Khouider 2010]. Deep convective clouds (DCCs) play multiple roles in the atmosphere, resulting in them often having a far larger influence on weather and climate than is proportional to their size. DCCs often precipitate heavily, sometimes producing the only precipitation that some arid regions of Earth receive. They also transport large amounts of air, water, and heat vertically, and they create large regions of secondary clouds which can alter the regional and even global radiative balance. For these reasons representing convective clouds realistically in general circulation models (GCMs, also known as global circulation or global climate models) has been a long-standing effort.

The primary challenge is accounting for their disproportionally large meteorological effect given their small size. An individual DCC is roughly 10 km wide, much smaller than the horizontal grid box length for a conventional GCM. And yet groups of DCCs can have as much of an effect on weather and climate as much larger meteorological features, such as tropical and extratropical cyclones. GCMs can explicitly resolve the latter features to an extent, but not DCCs. Smaller convective clouds are also problematic for the same reason. So GCMs often rely on a cumulus parameterization scheme, a method of estimating the bulk effect of a group of convective clouds on each grid box. Developing a realistic scheme is not an easy task, and many

attempts have been made since the 1960s. Some have fared better than others, but all of them have significant limitations. Within the past decade, computing power has increased enough that other methods of representing convective clouds in climate models are just within feasibility. While full blown multi-centennial climate simulations with these new models are not yet possible, it is possible to create experiments to test what improvements (if any) these alternative methods will provide to conventional GCMs.

The purpose of this thesis is to examine the characteristics of convective clouds in two recently developed atmospheric models intended for climate research: the Nonhydrostatic Icosahedral Atmospheric Model (NICAM) and the Superparameterized Community Atmospheric Model (SP-CAM). Both models were developed in response to the problems with simulating convection that exist in conventional GCMs. Neither model can yet be considered a "true" climate model, in that they cannot be run for hundreds of simulated years to examine long-term climate variability and trends. But it is possible to use them for various experiments relevant for climate science.

Before discussing the details of these models and their simulated cloud characteristics, it is first necessary to address the scientific importance of this topic of investigation. The overview of the research topic neatly breaks down into three main questions. First, why investigate convective clouds? Why do they matter for weather and climate? Second, why investigate climate models? What can complex, often messy climate models tell us about the climate system that cannot be demonstrated with chalkboard calculations or much simpler mathematical models? And third, why investigate convective clouds in climate models? What are the limitations of simulating convective clouds in conventional GCMs, and what possible alternative approaches exist for these GCMs?

1.1 Why investigate convective clouds?

Convective clouds are commonly claimed to be highly important for meteorological and climatological processes. But it isn't always made clear what exactly clouds do in these processes, and by extension what exactly scientists hope to learn by further studying them. This section will identify and discuss the various roles that clouds play in these processes.

1.1.1 Latent heating

The troposphere does not exist in a radiative equilibrium. Air is mostly transparent to sunlight, so only about a third of the planetary insolation absorption comes from the atmosphere (Fig. 1.1) [Trenberth et al. 2009]. Some of this atmospheric absorption occurs in the stratosphere through ozone absorption of ultraviolet light, which further reduces troposphere direct heating from sunlight. Furthermore, the atmosphere emits more thermal infrared radiation to space and to the surface than it absorbs from the surface. These facts combined mean that the net radiative heating of the troposphere is negative. The troposphere cools at almost 1 K per day if radiation alone is considered.

The balance is made up through surface sensible and latent heat fluxes. Insolation absorbed by the surface both raises the surface temperature and evaporates/sublimates water. This heat crosses the lower atmospheric boundary at a rate of about 100 W m^{-2}. The latent heat flux dominates in most locations, but not in some locations over land (e.g deserts). However, this heating process, through conduction and molecular diffusion from the surface, by itself is not sufficient to warm the entire troposphere. This process only dominates within a few millimeters of the surface. Above that, wind is the primary transport. An atmospheric circulation of some kind is necessary to transport the surface heating throughout the depth of the troposphere.

Because this circulation is ultimately (but not always locally) convectively driven, the troposphere is said to be in radiative-convective equilibrium.

But how does the convective part of the balance work? Within the planetary boundary layer (PBL), there are often vigorous mixing processes like shear-driven turbulence and convective thermals which distribute the surface heating within 1-3 km of the surface. Above this, other processes are necessary. The originally proposed solution was planetary-scale convectively driven circulations, of which the Hadley cell is the most famous [Hadley 1735]. The basic idea is that the vertical component of the circulation would lift heated, moistened air from the PBL to the tropopause smoothly and evenly everywhere. This would be balanced by radiative cooling and subsidence in the subtropics. A similar vertical transport would be accomplished by the Ferrel and polar cells, though the Ferrel cell would be more complicated because it is not a thermally direct circulation.

This idea was brought to serious question in the mid- 20th century. Advances in meteorological measurements showed that mass ascent all across the tropics was incapable of transporting heating to the tropopause. Using moist static energy (MSE, the sum of sensible heat, latent heat, and geopotential) as a thermodynamic metric, there is an obvious climatological minimum in MSE in the middle troposphere (Fig. 1.2). A large-scale ascent region could transport heat upwards to this minimum, but it could not transport heat upward from there to the tropopause. Large-scale ascent would actually transport heat from the tropopause downward to the MSE minimum level. This quandary was mostly solved by Riehl and Malkus [1958], where they proposed what came to be known as the hot tower hypothesis (HTH). According to the HTH, there is no large-scale uniform ascent in the deep tropics. Instead, ascent occurs within undilute local convective updrafts ("hot towers", i.e. DCCs), where air rises rapidly from the

PBL to the tropopause as if it was in a chimney. While DCCs cover a tiny fraction of the tropical surface area, the updraft speeds are large enough to transport enough air and heat vertically to offset the large-scale cooling and subsidence from the descending branch of the Hadley circulation. The HTH solved the mid-tropospheric MSE minimum problem by allowing PBL air to "bypass" the minimum in these convective chimneys, just like a building's chimney allows heat and smoke generated on the ground floor to bypass the upper floors and emerge into the atmosphere above.

Recent field observations and model simulations show that the HTH is incomplete [Zipser 2003]. There are two main problems with it. First, the assumption of undilute updrafts does not hold up to careful scrutiny. The convective chimneys are very leaky. The convective entrainment rate from field observations of DCCs is often over 10% [Fierro et al 2009]. The ideal "hot tower" probably doesn't exist in the real atmosphere, or at least it's too rare to have a major climatological effect. Second, there has recently been more appreciation of the role that stratiform precipitation plays in the tropical hydrological cycle. Stratiform precipitation, usually generated from mesoscale convective systems, has a different signature vertical latent heating profile from DCCs. DCCs tend to warm the entire troposphere (above the PBL), while stratiform clouds warm the upper troposphere while cooling the lower troposphere. Recent observations, for example from TRMM, show that about half the precipitation in the tropics comes from stratiform clouds. The precipitation ratio is a rough proxy measurement for the latent heating ratio, so about half of the tropospheric heating comes from stratiform clouds, not DCCs. Nevertheless, it's probably unjust to say that the HTH has been discredited. It just needs major modification.

The role of DCCs in the extratropics is a little more complicated than in the tropics. While the Ferrel cell exists in a statistical sense, much of the actual vertical transport in the extratropics occurs within baroclinically-generated waves and cyclones [Schneider 2006]. This dominates the vertical transport in the northern extratropics during the winter. During the summer, baroclinity weakens, and DCCs/MCSs play a bigger role in vertical transport.

To summarize, convective clouds play a vital role in balancing the radiative heat loss in the troposphere with radiative heat gain from the surface. DCCs allow for a rapid connection between the PBL and upper troposphere, at least partially "bypassing" the middle troposphere and the MSE minimum through creating their own local environments. And if there is a rapid climatic change in the 21st century and beyond, DCCs will play a vital role in connecting thermodynamic changes on the surface and in the PBL with the upper troposphere. That is one major reason why there is continued interest in understanding the finer details of convective processes.

1.1.2 Vertical transport

Heat isn't the only thing transported vertically by DCCs, of course. Most gases ingested by the DCC are transported vertically by multiple kilometers in a short amount of time, within an hour or so. This is one of the vital processes that keep most atmospheric gases well mixed in the tropopause. Of particular importance are greenhouse gases (GHG, i.e. radiatively active), where the vertical profile of number concentration is an important influence in determining their radiative effect of the climatic energy budget.

Water vapor is an important special case to consider. Unlike most other atmospheric gases, water vapor is not a passive participant in deep convection. Water vapor is removed from the

atmosphere through precipitation within DCCs, and in fact this is a major mechanism that allows deep convection to occur as it is observed. Because water vapor tends to precipitate when it is lifted and cooled, it is difficult for large amounts of water vapor to survive the transport to the upper troposphere. This is why 95% of atmospheric water vapor exists below 500 hPa.

Water vapor has multiple functions in the upper troposphere. First, water vapor often condenses to form clouds. This is discussed in the next subsection. Second, water vapor contributes greatly to the greenhouse effect. Water vapor is the most abundant GHG by number and mass concentration, but its radiative effect on the top of the atmosphere (TOA) energy budget is limited by its low altitude. GHGs are more effective at lower temperature, i.e. higher in the troposphere. So lifting even a small amount of water vapor to the upper troposphere, through DCCs or other means, can have a disproportionately large effect on the TOA energy budget [Held and Soden 2000]. Finally, water vapor influences the chemistry of the upper troposphere and stratosphere (notably ozone) [Liu et al. 1976, Shindell 2001]. Water vapor in the upper troposphere can infiltrate the stratosphere through various troposphere/stratosphere interactions, but it can also be deposited directly into the stratosphere from the PBL via extremely tall DCCs [Sherwood and Dessler 2000]. These tropopause-penetrating DCCs are rare, estimated at about 0.5% of all DCCs in the tropics [Luo et al. 2008], but they can serve as a major source of stratospheric water vapor.

So how much water vapor ingested by a DCC survives to the upper troposphere? Unfortunately this is not an easy question to answer. DCCs are too complex and turbulent to use simple thermodynamical estimates. Perhaps the most well-known attempt to answer this question was made by Lindzen et al. [2001], who suggested that the vertical transport of water vapor by DCCs may not be constant. While their argument was aimed more at DCC-generated cirrus

clouds, it matters for water vapor as well. They used the metric of "precipitation efficiency", which is the ratio of water vapor mass ingested by the DCC to the water mass precipitated. Their basic argument was that precipitation efficiency is a function of sea surface temperature. Specifically, it increases as temperature increases. As sea surface temperature increases, less atmospheric water survives transport to the upper troposphere, and thus the vapor and cloud greenhouse effect is reduced. So an increase in sea surface temperature for whatever reason (e.g. anthropogenic climate change) would reduce the amount of upper tropospheric cloud and vapor, increasing the outgoing longwave radiation, and thus lowering sea surface temperature. This came to be known as the Iris hypothesis, the analogy being to an ocular iris which changes shape to moderate the light falling on the retina. Further investigation eventually showed the Iris hypothesis to be inconsistent with observations {Hartmann and Michelsen 2002, Lin et al. 2004]. But the hypothesis and the resulting discussion were still important for raising awareness of the role that DCCs might play in regulating upper tropospheric humidity in a changing climate.

Gases and heat are not the only quantities transported by convective clouds. Momentum is transported as well [Houze 1973]. Vertical shear can arise from various mechanisms from baroclinity to surface-induced friction. Convection acts to reduce vertical shear by transporting lower tropospheric momentum upward, and vice versa. The specific case where convective clouds transport fractionally-reduced momentum upward is called "cumulus friction" – the clouds effectively transmit surface friction to the free troposphere. The momentum transport in baroclinic situations, where vertical shear occurs through a deep tropospheric layer, can be more complicated, as DCCs are also affected by vertical shear [Weisman and Klemp 1981]. In high shear environments, DCCs tend to organize into squall lines and, if thermodynamic instability is great enough and the shear has a directional turn with height, supercells. This can make the

magnitude of momentum transport difficult to estimate, and also to simulate realistically in an atmospheric model.

1.1.3 Radiative effects

Clouds also influence the TOA energy budget, and can be significantly more complicated in their radiative effects than GHGs [Hartmann et al. 1992, Stephens 2005]. First and foremost, clouds interact with shortwave radiation as well as longwave. This interaction mostly results in insolation being scattered back to space, but in certain circumstances it can also result in increased atmospheric absorption of shortwave as well. Because clouds interact with shortwave and longwave, this means that the net radiative effect of a cloud depends on the difference of the longwave and shortwave effects. This immediately raises the common problem of computing the difference of two large numbers of similar magnitude – a relatively small error or change in the minuend or subtrahend leads to a big error or change in the difference. For certain individual cloud types (e.g. marine stratocumulus, cirrostratus), this is not a major problem, as either the shortwave or longwave effect dominates. But for the net effect of all clouds, it is a more complicated calculation.

Second, clouds are far more transient than GHGs. Some clouds form and dissipate within a few minutes. Even if all other cloud properties remained the same during a climatic change, a change in the longevity of clouds would change their radiative effects. This transient nature is particularly problematic when it is related to the diurnal or annual cycles. Obviously all shortwave effects can occur only during the daytime, and even then the effects are modulated by solar angle. At higher latitudes, the shortwave effect is also modulated by the time of year. A

change in cloud occurrence frequency can have very different radiative effects depending on the time of day or the time of year they occur.

A third complication, alluded to previously, is the large number of different cloud types, each with different radiative effects. This goes beyond the simple temperature/altitude effect that also applies to GHGs. Some clouds, like cirrostratus, transmit shortwave easily, absorb most incident longwave, and radiate to space at a much lower brightness temperature. These clouds effectively warm the planet. Other clouds, like marine stratocumulus, reflect shortwave strongly, absorb longwave strongly, but radiate at a near-surface brightness temperature. These clouds effectively cool the planet. Other clouds fall somewhere in between. The radiative effect of ice clouds in particular can be very difficult to estimate and simulate because the shortwave effect can depend not only on the physical depth and hydrometeor size/number, but also the shape and vertical orientation. Different cloud types form via different processes, and these processes are not guaranteed to change uniformly with climate change. Perhaps an increase or decrease in the warming-type clouds will dominate, or perhaps a change in the cooling-type clouds will dominate. The situation becomes even more complicated when different cloud types influence each other. For example, in environments marginally suitable for deep convection, the presence of a cirrus layer can reduce or prevent deep convection if the cirrus is thick enough to cool the surface (this only applies during daytime). In marine extratropical environments, an increase in stratocumulus can reduce moisture transfer from the PBL to the free troposphere through strengthening the inversion layer, which reduces cloud formation in the free troposphere. There are a number of other examples of this complication, some involving microphysical feedbacks as well.

A fourth complication is the set of cloud/aerosol interactions. Aerosols can have a direct radiative effect on the atmosphere, where they can scatter shortwave back to space, or enhance atmospheric shortwave absorption under certain conditions. But aerosols can also influence cloud radiative effects by altering the microphysics. Because microphysics is often closely connected with macrophysical properties, aerosols can also influence the macrophysical cloud dynamics and thermodynamics. I am not going into detail on this, but Haywood and Bocher [2000] provides an overview of the topic. Cloud/aerosol interactions are of great interest to both the observational and modeling community. The two atmospheric models described in this thesis, NICAM and SP-CAM, have both been used to study cloud/aerosol interactions [Suzuki et al. 2008, Wang et. al 2011].

By themselves, DCCs (ignoring the anvil) have little radiative effect. They take up only a small fraction of the total surface area, limiting their total radiative effect. However, DCCs also commonly generate expansive cirrus anvils which can cover a surface area multiple orders of magnitude larger than the DCC itself. Convective anvils have a much larger influence on the radiative budget [Randall et. al 1989, Stephens et al. 1990]. The cirrus clouds have a large longwave effect [Fu et al. 1995], but they can also have a large shortwave effect in certain situations [Heymsfield and McFarquhar 1996]. They are often multiple kilometers deep, and can have relatively large cloud ice concentrations for cirrus clouds, and thus they sometimes have large shortwave albedos. In addition to cirrus anvils, DCCs also often produce secondary stratiform clouds which also have surface areas much larger than the DCCs alone. DCCs and stratiform clouds often form into mesoscale convective systems with diameters over 100 km. In the tropics they can grow quite large, with diameters over 1000 km. These secondary clouds can also depend on the diurnal and annual cycles. In the tropics, precipitation often maximizes in the

morning, and cirrus anvils can linger for hours after that. Over land, DCCs usually form during the afternoon, but it some locations (e.g. the US Great Plains), they commonly form at night. At higher latitudes, DCCs occur frequently during the summer, but rarely during the winter. All of these factors, combined with other sensitivities of DCCs to environmental conditions, mean that cloud radiative effects from DCCs are challenging to predict, especially when considering climatic feedbacks.

1.1.4 Meteorological processes

As mentioned before, deep convection often has an effect on the large-scale atmosphere disproportionately larger than the DCCs alone. Deep convection is intimately tied with many larger meteorological processes. I already mentioned mesoscale convective systems, in which DCCs, nimbostratus, and cirrus anvil clouds conspire to produce a meteorological feature much larger than merely a collection of individual DCCs. For brevity, this section will discuss only two examples of this: tropical cyclogenesis, and the MJO.

One of the major questions about tropical cyclogenesis is through what method is planetary vorticity initially concentrated into a tropical cyclone? Often large-scale vorticity can be concentrated into regional bands of relatively high vorticity by the ITCZ. Occasionally the breakdown of the ITCZ preludes tropical cyclogenesis, where the vorticity band is converted into the cyclone vortex [Ferreira and Schubert 1996]. Another mechanism to concentrate planetary vorticity to regional scale is the mesoscale convective vortex. A region of intense widespread deep convection can develop an MCV through ingesting large amounts of low-vorticity air and increasing the vorticity through latent heating (i.e. vertical stretching) [Mapes and Houze 1995, Bister and Emanuel 1997]. But it is still not entirely clear how the regionally enhanced vorticity

becomes a relatively small intense cyclone. Many mechanisms have been suggested, and there isn't space to cover them all. But one idea of particular interest to the topic of this thesis is the vortical hot tower idea [Montgomery et al. 2006].

According to this hypothesis, a tropical cyclogenesis event is preceded by the development of strong DCCs within the larger region of enhanced vorticity. These DCCs ingest large amount of environmental low-vorticity air and greatly increase the local vorticity. Individual DCCs may last only an hour or so, but successive generations of DCCs will cumulatively increase the cyclone-scale vorticity. Simultaneously these DCCs humidify the free troposphere and induce a toroidal circulation on the cyclone scale. After a day or two this process generates a tropical depression, and cyclone-scale intensification processes become dominant. Relevant to this idea is that NICAM has successfully generated relatively realistic tropical cyclones (Fig. 1.3), which is rare for a climate-oriented atmospheric model. What's interesting about this idea is that NICAM simulated a similar process of cyclogenesis, even though NICAM was not designed specifically to study tropical cyclogenesis [Fudeyasu et al. 2010]. While the DCCs in the NICAM cyclone were much larger and weaker than the DCCs simulated by Montgomery et al. (possibly because of NICAM's much coarser horizontal resolution), it still appears that the overall idea applies to NICAM cyclones. If this is realistic, and not just a coincidence, it provides evidence of one more critical link between DCCs and larger meteorological features.

A second process for consideration is the Madden-Julian oscillation (MJO, Madden and Julian [1994]), a 40-50 oscillation in wind patterns and outgoing longwave radiation (OLR) in the equatorial Indian Ocean and western Pacific. Convective clouds are a critical component of the MJO, and not just as passive effects that influence OLR. The mean zonal-vertical circulation strongly resembles the first baroclinic mode associated with DCCs, with strong ascent coinciding

with the OLR minimum, strong low level easterly (westerly) wind anomalies before (after) the OLR minimum, and strong upper level westerly (easterly) wind anomalies before (after) the OLR minimum. Ahead of the OLR minimum and DCC active region, shallow cumulus and congestus clouds moisten the middle troposphere about 10-20 days in advance. Mid-tropospheric humidity is probably a strong controlling factor on deep convection because of the strong convective entrainment at this altitude acting to dry convective clouds [Brown and Zhang 1997, Hohenegger and Stevens 2010]. After the OLR minimum, clouds take more of a stratiform characteristic. The full role of convective clouds in the MJO is not yet fully understood. Several mechanisms have been proposed, such as wind-induced surface heat exchange [Emanuel 1987], frictional wave-CISK [Hendon and Salby 1994], cloud-radiation interaction [Lee et al. 2001], but there is not yet a decisive argument for any of them. Nevertheless, convection is clearly important for the MJO.

Simulating the MJO has long been a sticking point for GCMs [Slingo et al. 1996], Lin et al. 2006). This is still true as of the Intergovernmental Panel on Climate Change (IPCC) Fifth Assessment Report, though there are some measureable improvements [Hung et al. 2013]. Models often produce MJO-like features that have too little variance, and either too high phase or too low phase speed. But some models produce more of a standing wave pattern. There are many different error sources in the models that have been proposed as important reasons for the poor MJO representation, but the limited representation of cumulus clouds is commonly cited. So simulating the MJO has been a major topic of interest for using both NICAM and SP-CAM. NICAM has successfully reproduced the characteristics of an MJO (Fig. 1.4) [Miura et al. 2007]. The experiment realistically simulated the phase speed, variability, general cloud structure, and westerly wind burst of an ongoing MJO event. NICAM produces DCC clusters that are close in

size and frequency to observations, though the 3.5 km resolution version is significantly more realistic than the 7 km version. While this experiment alone does not demonstrate NICAM's ability to spontaneously generate an MJO, Miura et al. [2009] demonstrated that NICAM can do so. But there are not yet any multi-year NICAM simulations that can be used to demonstrate the mean MJO characteristics in NICAM. SP-CAM has also successfully produced the MJO [Benedict and Randall, 2009]. Similar to NICAM, SP-CAM realistically produces many of the meteorological fields associated with the MJO, including their variance with time/longitude. DCCs are somewhat too deep and cold at the OLR minimum (about 20 W m^{-2}), and SP-CAM rains slightly too much (about 2-3 mm). Recent research shows the possibility of further improving the SP-CAM MJO, for example through improved ocean representation [Benedict and Randall 2011].

1.2 Why investigate climate models?

GCMs can help us further investigate the details of climate change. It is an unfortunately common misconception that demonstrating the realism of GHG-induced warming requires a complex climate model. Rather, it can be demonstrated through a relatively straightforward application of fundamental physical laws. Such a calculation was first performed at the turn of the 20^{th} century [Arrhenius 1896]. It is possible to make a crude blackboard demonstration using the graybody approximation (the atmosphere is transparent to shortwave and absorbs all longwave frequencies with a constant absorption coefficient). More detailed demonstrations can be made utilizing relatively simple one-dimensional atmospheric column models. The ability of GHGs to alter global mean temperature is a robust conclusion of practically all mathematical investigations into it, from the most simplistic to the most complex.

1.2.1. Global climate changes

But simply demonstrating a significant connection between GHGs and global mean temperature is not a sufficiently thorough examination of the climate system. A global temperature increase caused by GHGs is more than merely a function of total change in GHG concentration. Increasing temperature triggers a set of climate feedback loops, some of which enhance the initial temperature increase, while others reduce it [Soden and Held 2006, Dessler 2013]. The most basic and obvious one, recognized since the turn of the 20th century, is the water vapor feedback. GHG forcing increases the temperature, which raises the equilibrium humidity according to Clausius-Clapeyron, resulting in increased specific humidity over most of Earth. The increased water vapor enhances the instantaneous greenhouse effect, which raises the temperature further, resulting in further increased humidity, etc. While it may seem simple to calculate the water vapor feedback, recall that the exact feedback is partly dependent on the vertical distribution of water vapor, which in turn is dependent on meteorological processes like deep convection. So constraining the water vapor feedback uncertainty to less than a few Kelvin requires more sophisticated calculations than can be done on a chalkboard. Other feedback processes related to atmospheric physics include the lapse rate feedback, the ice-albedo feedback (at least the precipitation portion), and the cloud feedback. These are difficult to calculate for similar reasons as the water vapor feedback.

Furthermore, GHGs don't simply affect global mean temperature, but also other global mean variables as well. Global mean precipitation is a major topic in climate science, in some ways even more so than global mean temperature [Allen and Ingram 2002]. Water is of course vital to many geophysical and ecological processes, as well as human society. Recall that precipitation rate is related to the latent heating rate, which is in turn related to the tropospheric radiative

imbalance. So in order to predict changes to global mean precipitation, the tropospheric radiative imbalance must be predicted. Again, this is a difficult calculation. Other global variables of interest include cloudiness, circulation, and storm frequency and intensity.

1.2.2 Regional climate changes

Global mean quantities are in a sense abstractions of the climate system. Most geophysical, ecological, and social processes are directly affected by local and regional climate variables, not global [Watson et al. 1998]. Even though the GHG concentration increase is somewhat evenly spread across the planet, that does not mean that the temperature increase will also be spread as evenly. A fairly robust prediction is that land will warm faster than oceans. Oceans can circulate the increased radiative heating over a hundred meters depth of water, while the land can only conduct the heating through the top few centimeters. More difficult to predict are temperature changes associated with regional cloud cover and wind patterns. Just like there are climate feedbacks on the global scale, so they exist on regional scales as well. Changes in regional temperature can influence clouds and wind, possibly triggering feedback loops.

Other climatological variables are affected as well. As on the global scale, regional precipitation is of large concern on the regional scale [Giorgi 2006]. Mean precipitation is important, but so are precipitation frequency and intensity [Stephens et al. 2010]. Even if the mean precipitation for a given region remains constant, an increase in the sporadicity of precipitation events could lead to more intense flooding and drought events. In regions where frozen precipitation occurs, the precipitation phase can also be an important factor to consider. Over land, frozen precipitation affects the magnitude of the ice-albedo feedback. It also can affect the hydrology in regions that use glacial runoff as a source of water during the spring and

summer seasons. A decrease in frozen precipitation amount could lead to a reduction in glacier mass, reducing freshwater availability.

Some regional precipitation changes are thought to be relatively well understood. The best example of this is the "rich get richer" effect for humid versus arid regions [Chou and Neelin 2004, Held and Soden 2006]. An increase in atmospheric humidity, without a corresponding change in atmospheric circulation, would result in enhanced moisture convergence in humid regions and increased divergence in arid regions. Even this mechanism gets complicated when additional factors such as deep convection are included, which can enhance convergence and precipitation beyond what the basic mechanism predicts [Chou et al. 2009]. More complicated are precipitation changes from changes in cyclone activity. Cyclones occur through the interaction of dynamical and thermodynamical processes, so simple models have only limited utility. In addition to cyclone frequency and intensity, it is also possible to change local precipitation via shifting average storm tracks. This results in less precipitation occurring in some regions, and more precipitation in others. Tropical cyclones in particular have been a major point of discussion in climate science. Because traditional climate models have been generally unable to simulate tropical cyclones (the horizontal resolution is too coarse), the use of climate models for addressing this question is still in the opening stages. Extratropical cyclones are less of an issue, and are generally predicted to shift poleward with the jet stream, but again the details are difficult to predict.

It should also be noted that even if long term climate change did not exist, climate models would still have some utility to science and society. Even without a multi-decadal external forcing to consider, there is still a wide range of internal variability within the climate system that extends beyond basic meteorology. For example, on the short end of the variability timescale

is the MJO, mentioned before, which exists on a multi-month timescale. This is slightly too long to be classified as strictly weather, and is too long to be represented with most NWP models. On the longer end of the timescale are multidecadal cycles like the Atlantic Multidecadal Oscillation [Schlesinger and Ramankutty 1994] and the Pacific (inter)Decadal Oscillation [Mantua and Hare 2002]. In between the extremes are the El Nino Southern Oscillation, the annular modes, and others. All of these can be linked with persistent alterations in weather patterns extending up to thousands of miles away from the regions of occurrence, with resulting socioeconomic and ecological difficulties. The basic physics of some of this variability can be understood using simpler mathematical models, but a detailed understanding often requires a climate model to represent the many complex interactions that result in the variability.

1.2.3 Model comparison efforts

Because of the utility of climate models, the climate modeling community has made a strong effort to test climate models against observations and each other. This is generally not an extremely standardized effort, in the way that model evaluation in other engineering and mathematical fields are. Nevertheless, the climate science community has recognized the need for some degree for standardization, and thus has created a number of model intercomparison projects to do this. As this thesis is about atmospheric models, the most relevant project is the Atmospheric Model Intercomparison Project (AMIP) [Gates 1992]. This project involves running different atmospheric models under the same sets of conditions. Specifically, the sea surface temperature, sea ice cover, CO2 concentration, and solar constant are specified for all models, for the time period of 1979 - 1988. A standardized set of data field output is also required to allow for a consistent basis for comparison between all models. Interestingly, clouds

are not well represented in the output list, which includes only cloud cover and cloud radiative forcing. Nevertheless, the resulting quantitative comparisons are used by a wide range of climate science efforts, including the IPCC.

Other model intercomparison projects exist, which test models of other components of the climate system. There are also projects which test coupled model components to better represent the entire climate system, such as the Coupled Model Intercomparison Project, a "sister" program to AMIP [Meehl et al. 2000]. Projects dedicated specifically to clouds are rare. The one most relevant to this thesis is the Cloud Feedback Model Intercomparison Project (CFMIP), begun in 2005 [Williams et al. 2006]. While most of the focus of this project involves cloud radiative forcing and feedback variables, which is not directly relevant to this thesis, part of the project involves comparing model data with International Satellite Cloud Climatology Project (ISCCP) data to examine the realism of simulated clouds. The ISCCP methodology uses cloud albedo and cloud longwave brightness temperature to classify clouds into different regimes, e.g. deep convective, shallow, cirrus, etc. Ideally, it should be possible to use the radiative data generated for CFMIP to identify and characterize deep convective clouds within GCMs, and compare their properties across multiple climate models. Unfortunately, this does not seem to be a major focus of CFMIP so far. So it appears that at the present time, it will be necessary to rely on non-standardized model comparisons to evaluate DCC simulations in climate models. This thesis is one of the many attempts to fill this knowledge gaps.

1.3 Why investigate clouds in climate models?

Clouds remain a major difficulty for climate models. Convective clouds in particular present a large challenge for climate models to simulate effectively. The fact that DCCs have a

disproportionately large effect for their size presents two conflicting needs for a climate model: the need to represent important meteorological processes realistically, and the need to reduce the number of calculations as much as possible to allow for more experiments. The following will present a brief description of the challenges that convective clouds present and some of the proposed solutions to these challenges.

1.3.1 Cumulus parameterization schemes

The effort to represent DCCs in climate models began in the 1960s, when modelers realized that atmospheric models (which were rapidly growing in complexity) could not represent deep convection explicitly [Arakawa 2004]. In order for deep convection to occur in these models, an entire horizontal grid cell, multiple degrees wide, would have to become convective to restore radiative-convective equilibrium. Not only does the real atmosphere not work this way (as discussed previously), but this also creates major numerical problems in the calculations. So deep convection was viewed at the time not so much as an important meteorological process in its own right, but rather as a necessary "bookkeeping" process to keep the models from failing. This was a problem in many atmospheric models used for different purposes, not just those intended for climate research. The earliest attempts were very crude, restricting convection to a limited number of vertical heights, not considering many aspects of moist physics (including none of the liquid/ice phases), and containing other rigid assumptions. Even with their great limitations, they allowed important meteorological processes such as tropical cyclones to be simulated [Charney and Eliassen 1964], and also resulted in better representation of the tropical large-scale environment [Manabe et al. 1965].

Cumulus parameterization schemes became of more sophisticated with time, paralleling other aspects of GCM development. However, in the past couple of decades, progress has slowed [Randall et al. 2003a]. Arakawa [2004] identified multiple challenges facing conventional cumulus parameterizations that must be addressed in order for parameterization efforts to make further progress. First, cumulus schemes do not include the full range of cloud processes that influence real-world clouds. As mentioned previously, cumulus schemes were originally implemented to resolve large-scale energy imbalance problems. So the actual physical local processes that determine cloud characteristics are often only secondary considerations. These processes include microphysics, cloud to cloud interactions (horizontally and vertically), local radiation, entrainment/detrainment (not fixed constants in reality), cumuliform/stratiform interactions, and altering the local planetary boundary layer. Some, but not all, of these processes can be represented indirectly, such as cumuliform and stratiform clouds modifying each the large-scale environment and thus affecting the other. Second, the coarse scale of conventional GCMs greatly limits their ability to represent mesoscale convective systems. These systems are too large, complex, and sporadic to be represented with a universal parameterization scheme. But the large amount of cloud-to-cloud interactions within them can significantly modify the cloud characteristics, and thus the environment/cloud interaction. Mesoscale circulations generated by MCSs have a similar problem, being too small to resolve and too large to rely on turbulence parameterizations.

Third, there is a problem of relating the heating/drying tendency (i.e. Q1 and Q2) from cumulus clouds required by the model and the heating/drying tendency produced by a high-resolution simulation of cumulus clouds (which can be considered the “real” heating/drying tendency). Conventional GCMs, having low horizontal resolution, mix the effects of in-cloud

and environmental heating/drying. This results in a required increase in MSE over much of the upper troposphere and decrease over the lower troposphere, to counter environmental cooling/moistening. But the in-cloud MSE tendency does not resemble this, with the tendency being near zero except just above/below the freezing line (associated with phase changes). Unfortunately the difference between the "real" and required tendencies depends on the horizontal resolution of the GCM, so a cumulus parameterization must be altered as the model resolution increases.

1.3.2. Modern approaches to cumulus representation

Given the difficulties associated with cumulus schemes, it is reasonable that some researchers would seek out possible alternatives. These alternatives may be more computationally expensive than conventional GCMs, but the improved convective processes might be worth the increased expense. One approach is the Global Cloud Resolving Model (GCRM), which is simply a Cloud Resolving Model (CRM) extended globally. These models have a horizontal resolution of a few kilometers, making them capable of resolving larger convective clouds. They cannot represent smaller eddy features within a DCC, and they cannot represent smaller cumulus clouds realistically. Nevertheless, there is mounting evidence that this approach, though extremely expensive computationally, can simulate atmospheric features that give conventional GCMs difficulty (e.g. tropical cyclones, the MJO). The GCRM representative in this thesis is NICAM, and it will be discussed in more detail in Chp. 2.

The other approach investigated in this thesis is the Multiscale Modeling Framework (MMF) [Khairoutdinov and Randall 2003, Khairoutdinov et al. 2005]. This approach creates a hybrid model from a GCM and CRM, where the cumulus parameterization (among other things) is

replaced by a CRM. More specifically, each GCM grid box is linked with its own CRM which simulates subgrid-scale processes for the GCM instead of parameterizing them. The GCM and CRMs communicate with each other frequently, so they are able to influence each other. The GCM grid box provides the large-scale environmental conditions to the associated CRM, and the CRM provides the cumulative effect of convective clouds and other local processes. This is less expensive to run than the GCRM, but still significantly more so than a convectional GCM. SP-CAM will be the representative of the MMF in this thesis, and it will be discussed in further detail in Chp. 3.

An important point to remember is that these alternative approaches should not be considered complete *replacements* for cumulus parameterization schemes. These schemes represent our best conceptual understanding of how convective clouds behave, and how they interact with the large scale environment. Limitations of these schemes represent limitations of our conceptual understanding. Simply discarding them would be equivalent to discarding decades of scientific understanding. And simply accepting the results of the alternative approaches without comparison with cumulus schemes would be similar to treating the alternative models like black boxes, which is contrary to the scientific method. So a full investigation of the utility of the alternative methods would involve a detailed comparison between GCM parameterized convection and convection in the alternative climate models. As mentioned before, this is not a major topic of standardized model intercomparison projects at the moment. Hopefully the methods used in this thesis will have some value in future investigations of this kind.

1.3.3. Observational verification of simulated convective clouds

Testing climate models against reality has always been a tricky challenge. Observations provide only partial knowledge of the climate system. Even with standardized comparison methods, the limited information from observations makes useful comparison difficult. Cloud observations are notably challenging, which does not help the problem with simulating clouds discussed previously. The good news is that cloud remote sensing capabilities have improved significantly in the past decade, concurrent with the introduction of MMFs and GCRMs. In particular, the ability to sense within and through a cloud with high spatial resolution has been made possible with active satellite sensors such as radars and lidars. In the past, it has been difficult to sample every portion of a cloud simultaneously. Visible and infrared sensors cannot penetrate most clouds. Satellite-based vis/IR sensors can only see the cloud tops, and ground-based sensors can only see cloud bases (with a narrow field of view). The presence of a DCC can only be inferred from cloud top characteristics, and almost nothing of its internal structure can be learned. Passive microwave sensors can see through clouds to an extent, but the horizontal and vertical resolutions are too coarse to sample individual convective clouds.

Beginning in the late 1990s, three active cloud sensors were launched to partly fill the blind spots in pre-existing satellite observations. The Tropical Rainfall Measurement Mission (TRMM) carries a Precipitation Radar which can sense the presence and vertical structure of heavier precipitation [Simpson et al. 1996]. This makes TRMM particularly valuable for studying DCCs. However, the radar cannot directly sample the upper regions of a DCC, and other clouds cannot be directly sampled (they can be sampled with a vis/IR and passive microwave sensors, with the limitations discussed previously). TRMM is also limited to observing the tropics and subtropics, as the name implies. CloudSat carries a Cloud Profiling

Radar which can sample most cloud liquid/ice hydrometeors, and light to moderate precipitation [Stephens et al. 2002]. CloudSat cannot detect thin ice clouds, has difficulty detecting very shallow stratocumulus clouds, can cannot penetrate heavy precipitation. Nevertheless, it is useful for sampling almost all convective clouds, and can sample the upper portions of heavily-precipitating DCCs. The Cloud-Aerosol Lidar and Infrared Pathfinder Satellite Observation (CALIPSO) carries the Cloud-Aerosol Lidar with Orthogonal Polarization (CALIOP) instrument which can sample vertical profiles of thin ice clouds, and can detect the cloud top height of other clouds with very high resolution [Winker et al. 2009]. But CALIPSO cannot sample below cloud top for most clouds.

Both CloudSat and CALIPSO fly in the A-Train, a collection of Earth-observing satellites in close proximity which provides multiple overlapping samples. This allows for a far more comprehensive snapshot of the Earth system below than any single satellite can provide. I use this capability in Chp. 2 to sample the tropical oceanic environment, where *in situ* observations are sparse. However, the lack of a TRMM-like satellite in the A-Train is unfortunate, and probably will not be rectified in the near future.

This thesis will use CloudSat as the primary source of cloud observations. CloudSat can sample and vertically profile most convective clouds, the only limitation being the lower cloud in heavily precipitating DCCs. Fig. 1.5 shows an example of a mesoscale convective system observed by CloudSat. This figure displays CloudSat's ability to see past cloud tops deep into an active convective core, and distinguish it from nearby secondary clouds. CloudSat will be discussed in more detail in Chp. 2. CloudSat provides a source of observations for convective clouds can be compared directly with clouds explicitly simulated in GCRMs and MMFs. It's no longer necessary to use proxy measurements of convective activity from vis/IR sensors, and rely

solely on educated guesses of convective internal structure from theoretical studies and field observations. It is also not necessary to examine DCCs in a GCM indirectly via the effect of the cumulus parameterization scheme on a larger-scale grid box. Data from each individual cloud in the model can be recorded and compared with observations. So recent advances in both climate modeling techniques and satellite observation capabilities have opened a new avenue for investigating convective clouds in climate models. That is the primary goal of this thesis.

1.4 Thesis main goal and organization

The main purpose of this thesis is to examine the characteristics of convective clouds, DCCs in particular, in NICAM and SP-CAM, and compare them with each other and observed clouds. The two locations used for this investigation will be the tropical oceans, where many satellite-based and model-based studies have been conducted, and the contiguous United States (CONUS), where fewer such studies have been done. The large difference in climatology between the two regions provides the opportunity to examine convective characteristics in different environments. The time domain is boreal summer, during June/July/August (JJA). In particular I will emphasized the vertical structure of clouds, including vertical location and simulated W-band radar reflectivity, as it has recently become possible to conduct such an investigation using recently launched satellites like CloudSat. In addition, the relationship between convective clouds and their environments will also be emphasized.

Fig. 1.6 and 1.7 shows the spatial resolution difference between SP-CAM and NICAM over CONUS for SAT and TPW, respectively. Obviously NICAM is much higher resolution than SP-CAM, which allows it to explicitly represent smaller-scale meteorological features on the primary grid. The specific day/times chosen for each model in Figs. 6 and 7 include a tropical

disturbance for reference. Note the improved representation of the tropical cyclone in NICAM vs. SP-CAM, similar to what previous work with NICAM has found (e.g. Fudeyasu et al. 2010). SP-CAM produces tropical disturbances, but they only have very weak resemblance of observed cyclones. Also, notice that NICAM occasionally produces small-scale wavy artifacts in SAT near regions with large terrain changes (e.g. the western mountains). These artifacts are not persistent features, and they do not appear to influence seasonal mean SAT.

Fig. 1.8. shows the global mean SAT in JJA for the National Center for Environmental Prediction (NCEP)/ National Center for Atmospheric Research (NCAR) Reanalysis (N/NR), compared with NICAM, SP-CAM version 4 (SPv4), which uses single moment microphysics), SP-CAM version 5 (SPv5, double moment), and the standard Community Atmospheric Model version 5 (CAM5) on which SP-CAM is built. All three CAM-based models have warm biases over the majority of continental regions. There are some differences in Australia, Africa, and the high northern latitudes, but overall the continents are too warm by about 3 K. This bias exists in CAM5 at about the same magnitude, so it is unlikely that super-parameterization can be blamed for the bias. SPv5 is slightly warmer (about 1 K) than the other two over land overall. Fig. 1.9. shows the same as Fig. 1.8. for TPW. For the CAM-derived models, much of the tropics and Northern Hemisphere is far too moist, in some locations over 10 mm too moist. The TPW biases are not limited to land, either. The greatest biases occur mostly over the equatorial Pacific Ocean. A few regions are biased too dry, such as the Pacific cold tongue and South America (which may have major implications for studying the Amazon using the CAM-derived models). Because cloud characteristics are closely tied with atmospheric humidity, the moist bias in the CAM-derived models could potentially influence the cloud characteristics even with perfect model

representation of environment/cloud relationships. Fortunately, for the purposes of studying CONUS, the TPW bias there is smaller, only up to 5 mm at most.

Based on the models' ability to simulate both individual larger convective clouds and the environments they exist within, I have formulated the following set of main questions to attempt to answer with this thesis:

1. How well do the simulated tropical convective clouds in NICAM resemble those observed by CloudSat?

2. How well do simulated continental convective clouds over the contiguous United States in NICAM and SP-CAM resemble those observed by CloudSat?

3. How well do simulated continental convective environments over the contiguous United States in NICAM and SP-CAM resemble observations?

4. What is the effect on improving the microphysics on convective clouds in SP-CAM?

Chapter 2 will discuss the comparison between NICAM and CloudSat within the tropical oceans. Chapters 3 and 4 will discuss a similar, though expanded, comparison between NICAM, SP-CAM, and CloudSat over the contiguous United States. Chapter 3 will focus on the characteristics of the large-scale environments, and Chapter 4 will examine the cloud and precipitation characteristics. Chapter 5 will examine the differences between SP-CAM versions 4 and 5, which include a change from a single moment microphysical scheme (v4) to a double moment scheme (v5). Chapter 6 will be the conclusion chapter, which will discuss the main answers to the questions stated previously.

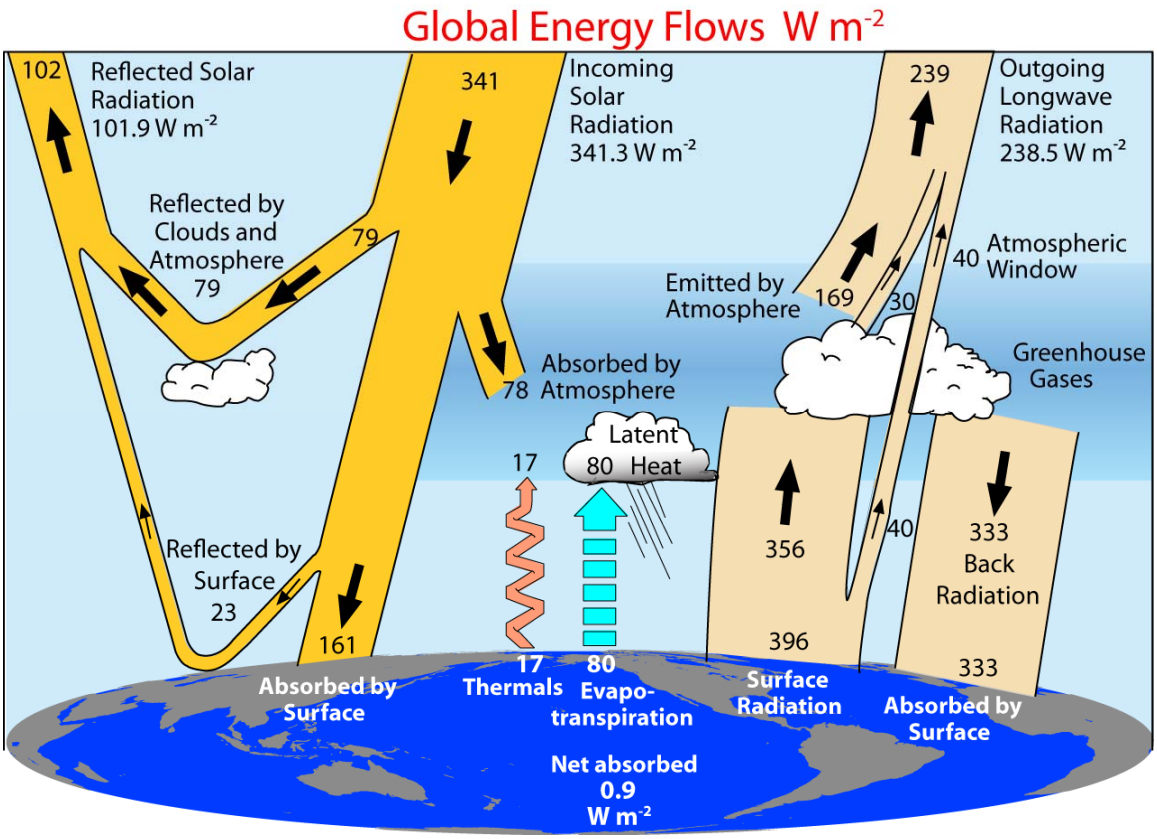

Figure 1.1. The global mean atmospheric energy balance, as calculated by Trenberth et al. 2009 (figure copied from Trenberth et al. 2009)

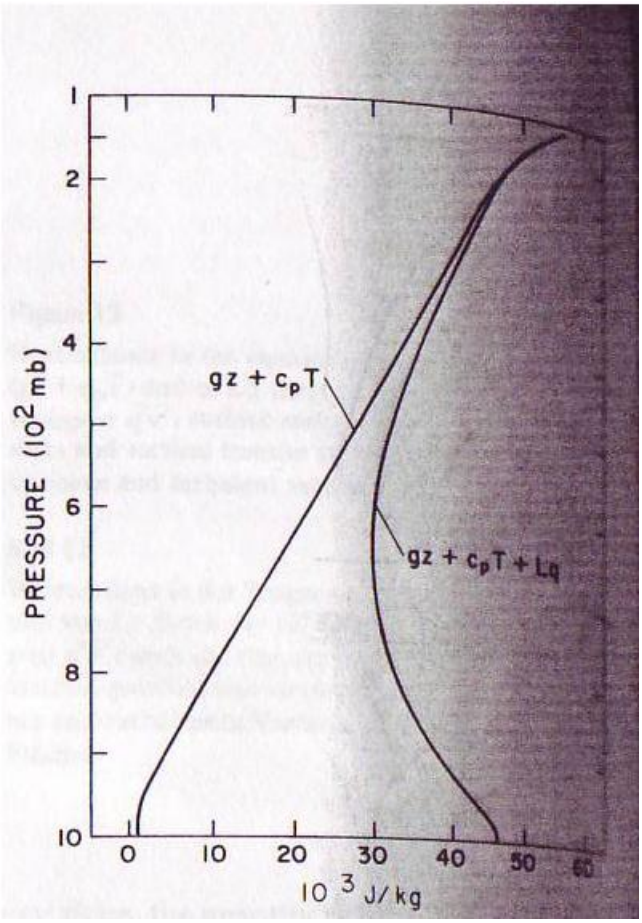

Figure 1.2. The tropical vertical moist static energy profile (figure copied from Riehl and Simpson 1979).

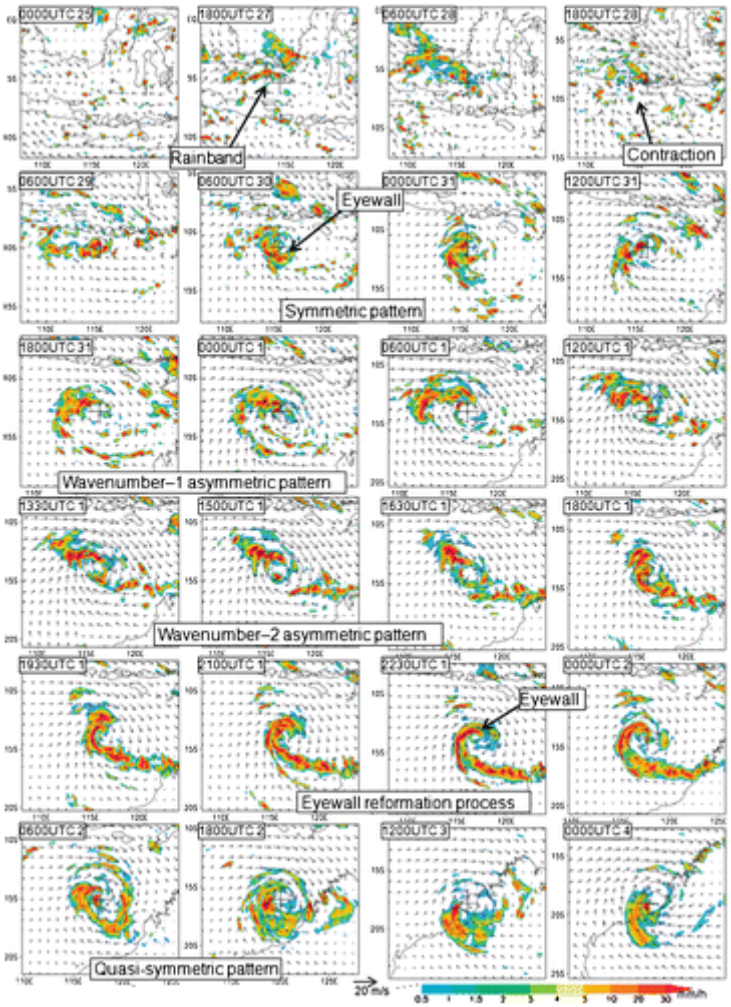

Figure 1.3. Time evolution of tropical cyclone Isobel simulated by NICAM. Rainfall rate (mm h^{-1}) is shaded, and surface (10-m height) winds (m s^{-1}) are shown with vectors. The crosses represent Isobel's center. (from Fudeyasu et al. 2010)

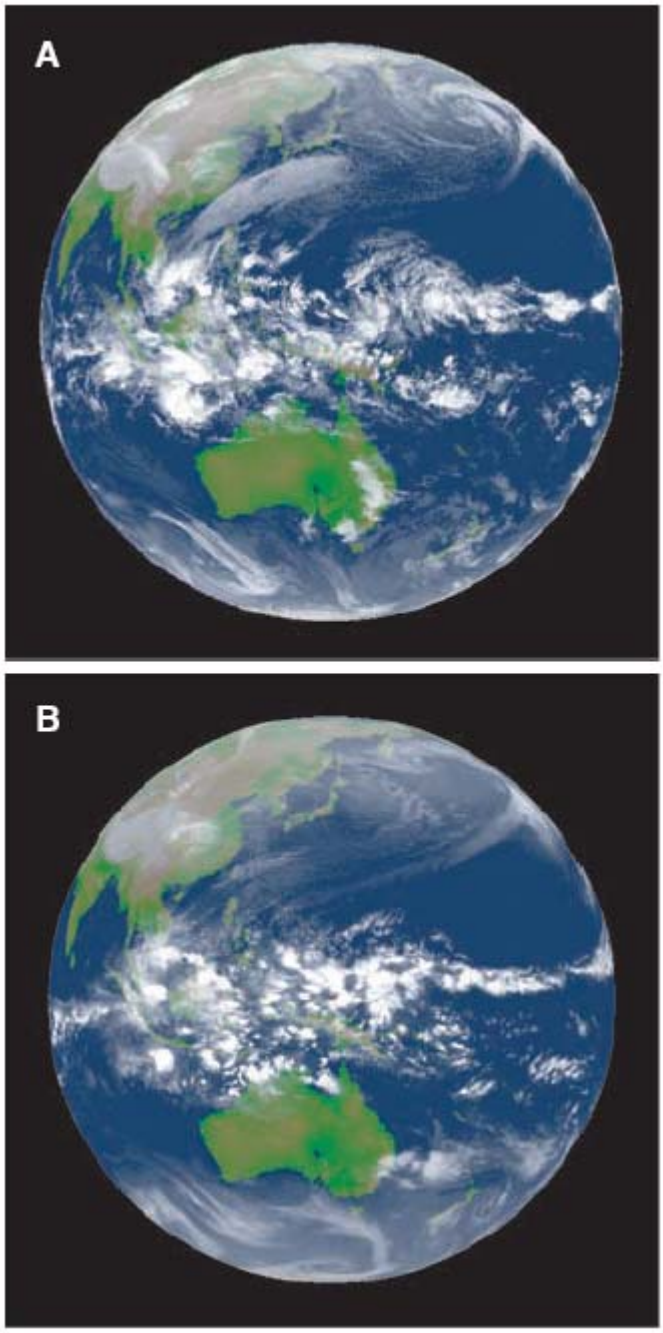

Figure 1.4. MJO event a) observed and b) simulated by NICAM (3.5 km), at 0030 UTC on 31 Dec 2006. Gray shading represent observed/simulated OLR. (from Miura et al. 2009)

a. Radar reflectivity

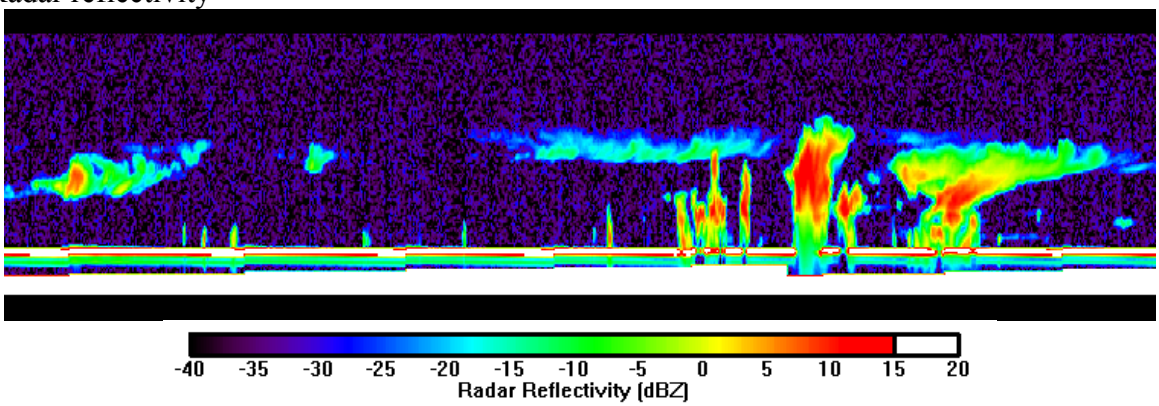

b. Cloud classification

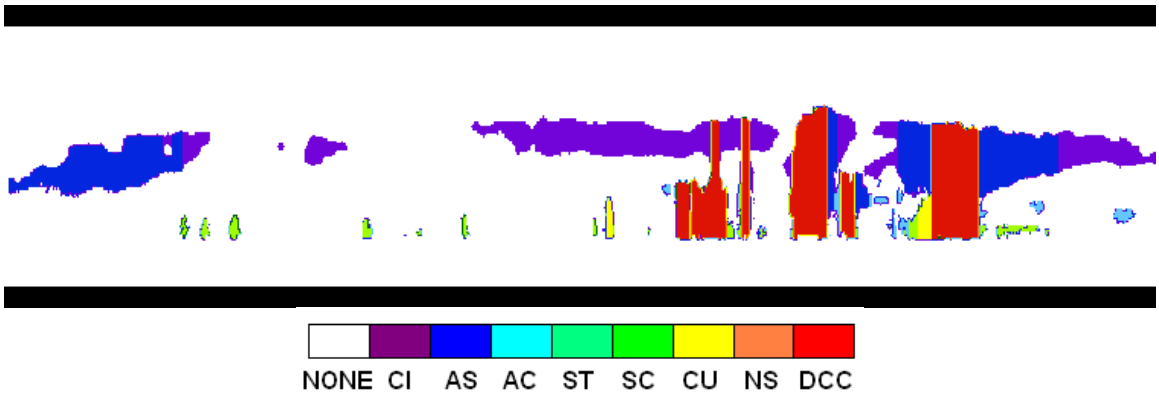

Figure 1.5. Example of CloudSat observation of a mesoscale convective system. The x axis is distance along CloudSat's orbit (2000 km in length), and the y-axis is vertical distance. (a) is radar reflectivity, and (b) is cloud classification according to the 2B-CLDCLASS product.

a. NICAM

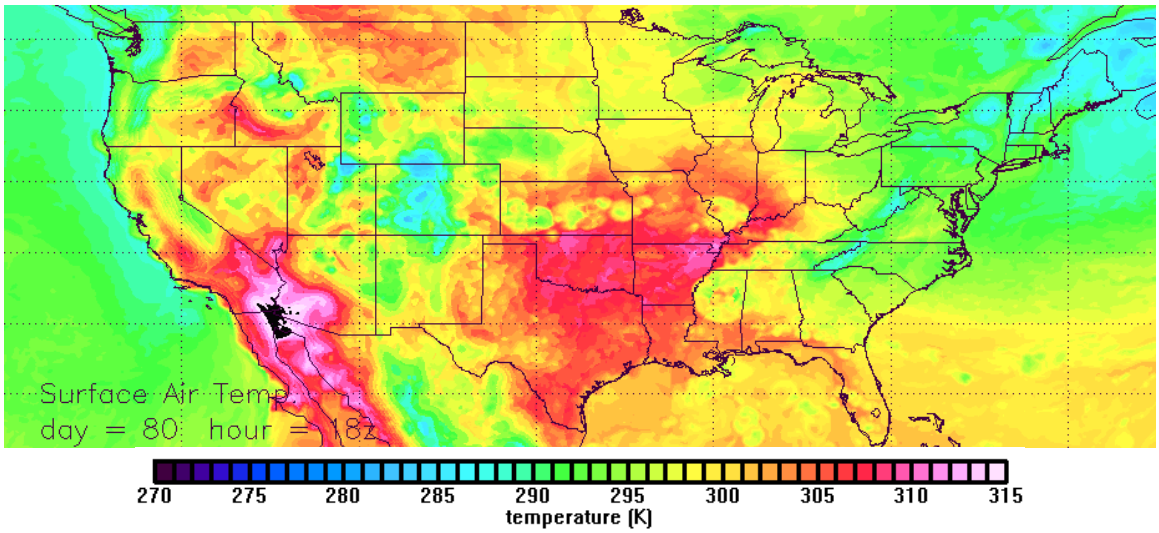

b. SP-CAM

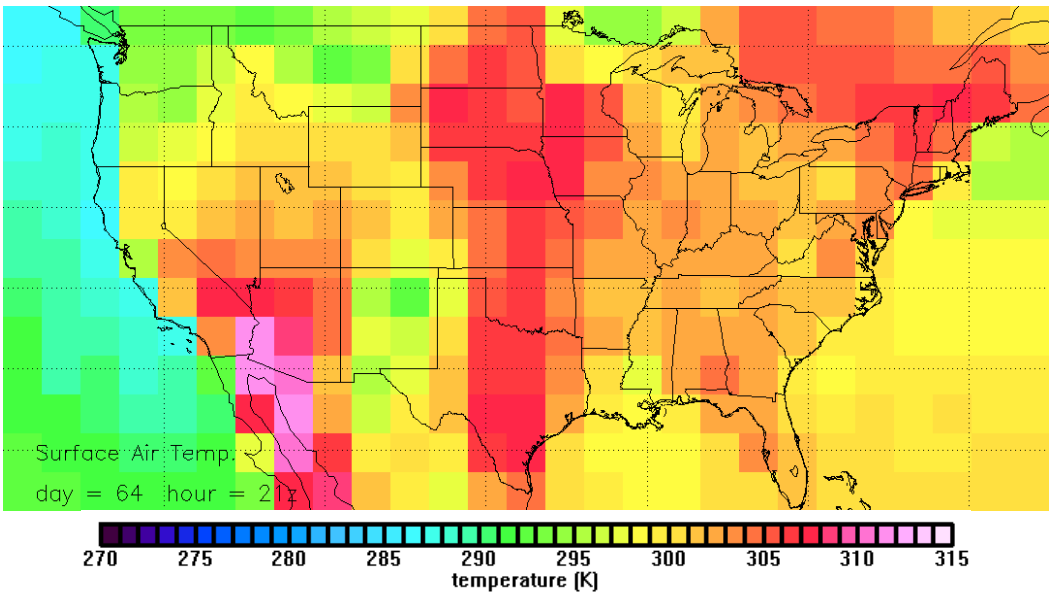

Figure 1.6. Instantaneous surface air temperature of a) NICAM and b) SP-CAM v4 over CONUS for one day in JJA. In both model snapshots there is a tropical cyclone-like feature in the Gulf of Mexico, and active deep convection over the central/eastern US.

a. NICAM

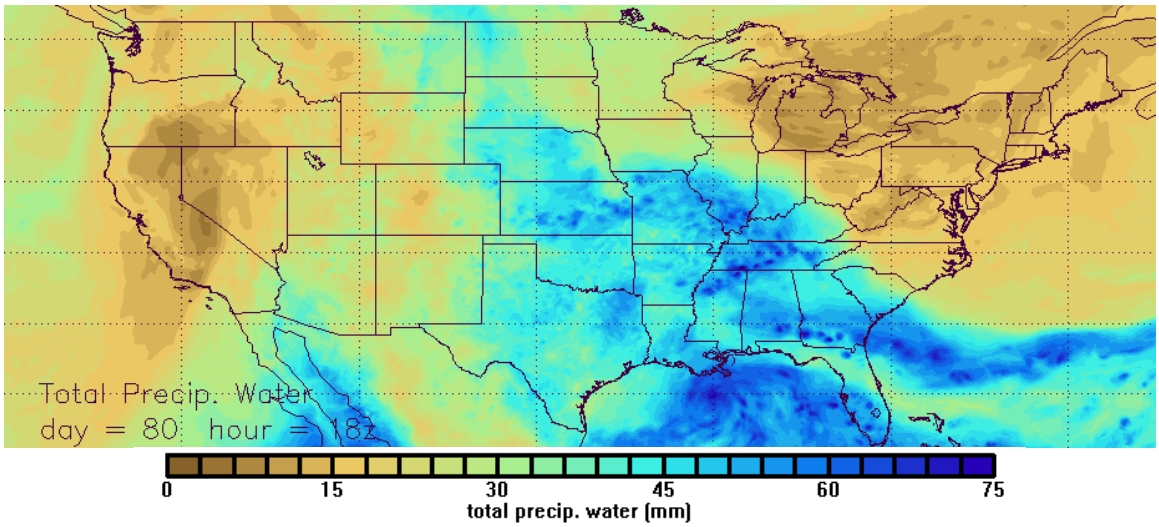

b. SP-CAM

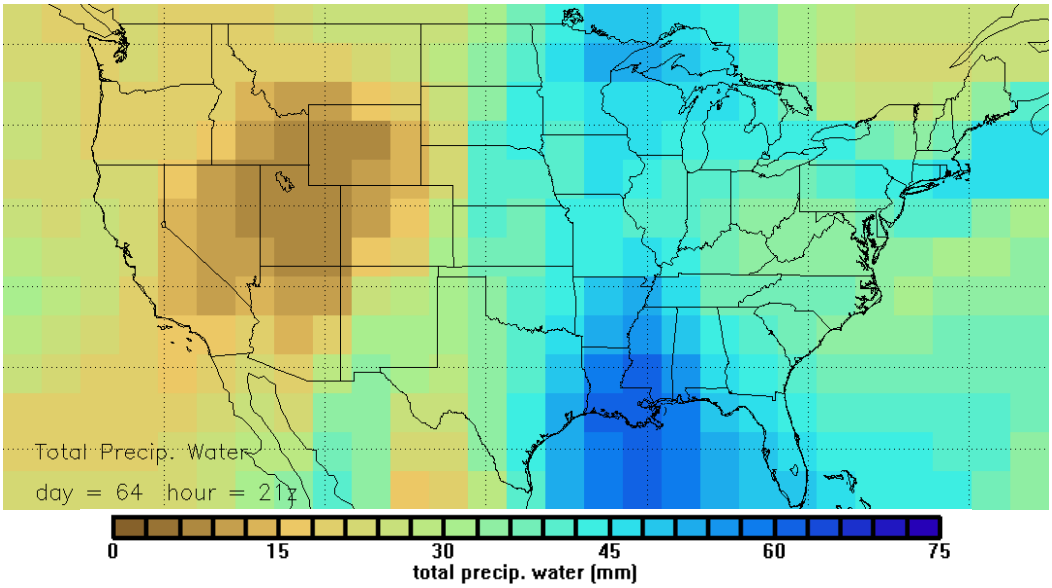

Figure 1.7. Instantaneous total precipitable water of a) NICAM and b) SP-CAM v4 over CONUS for one day in JJA, for the same day/time as Fig. 1.6. In both model snapshots there is a tropical cyclone-like feature in the Gulf of Mexico, and active deep convection over the central/eastern US.

a. N/NR

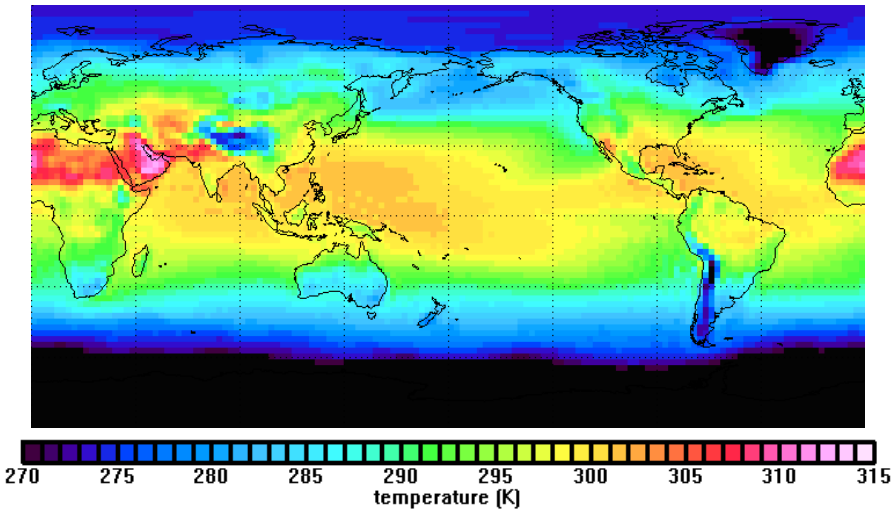

b. NICAM

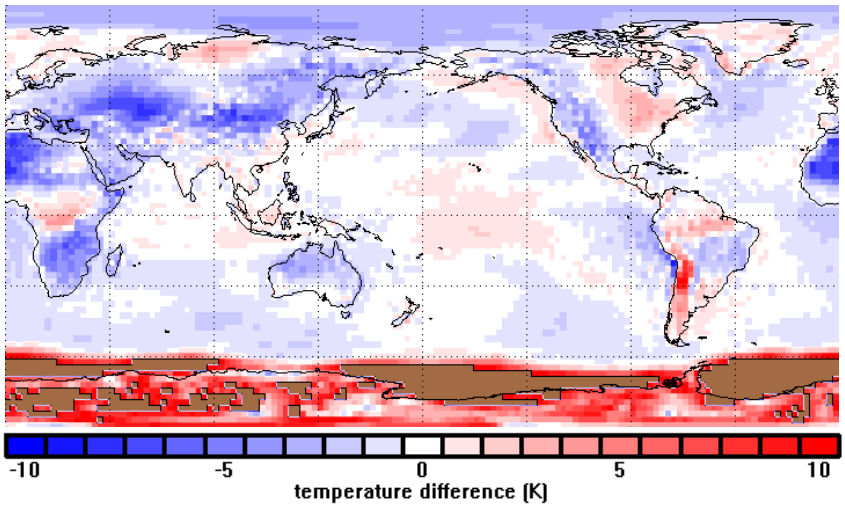

Figure 1.8. Global mean SAT during JJA for a) N/NR, b) NICAM, c) SP-CAM v4, d) SP-CAM v5, and e) CAM5. (a) shows the absolute value, (b) – (e) show the difference between model and reanalysis. Reanalysis is calculated for 2006-2010, and models for a single simulated season.

c. SPv4

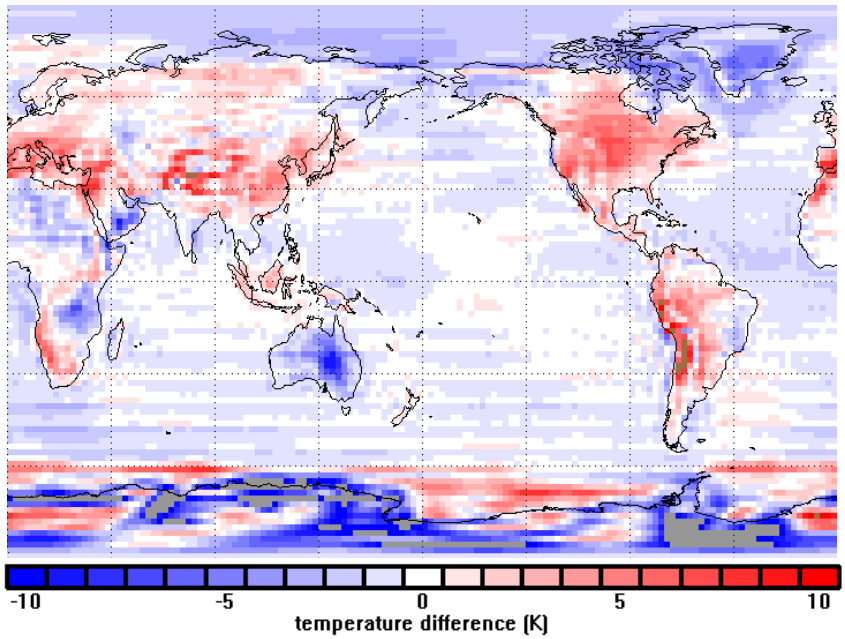

d. SPv5

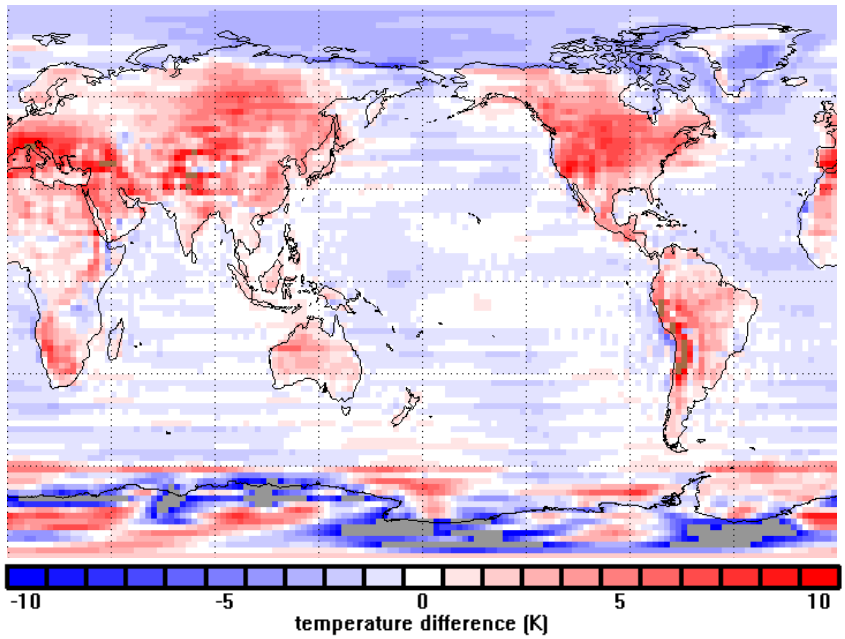

Figure 1.8. (continued)

e. CAM5

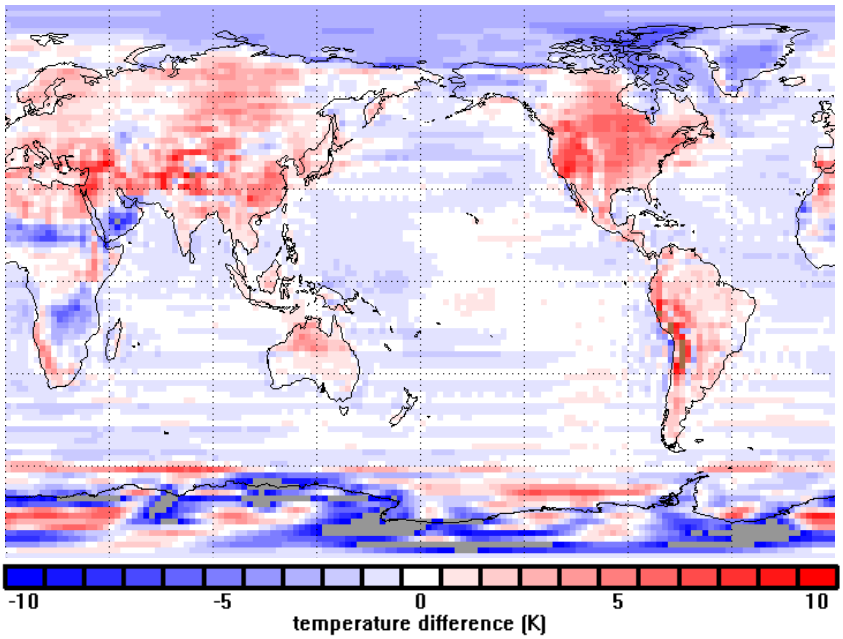

Figure 1.8. (continued)

a. N/NR

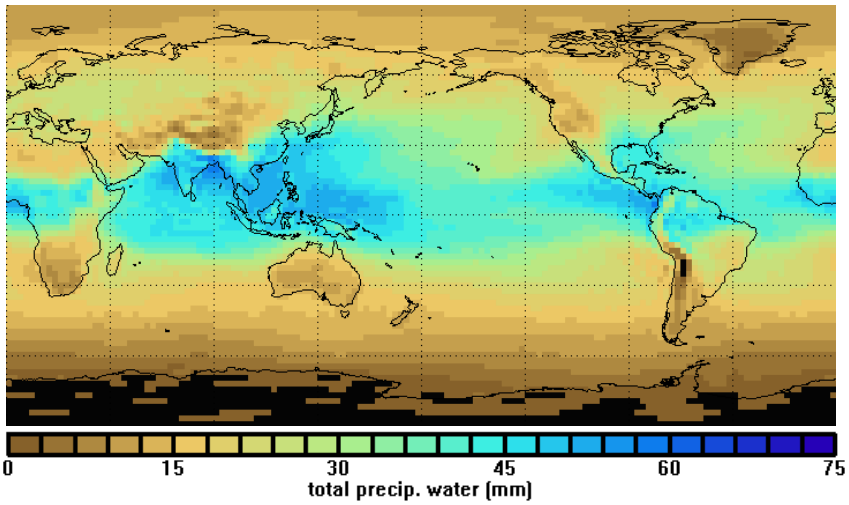

b. NICAM

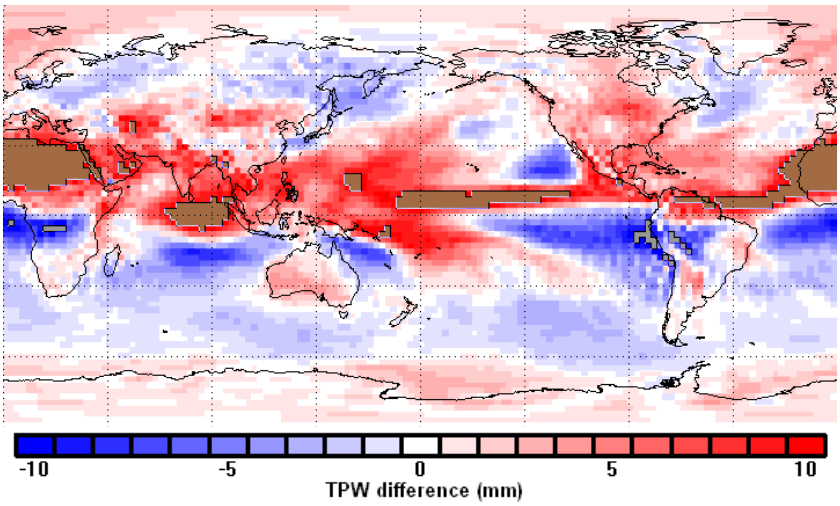

Figure 1.9. Global mean TPW during JJA for a) N/NR, b) NICAM, c) SP-CAM v4, d) SP-CAM v5, and e) CAM5. (a) shows the absolute value, (b) – (e) show the difference between model and reanalysis. Reanalysis is calculated for 2006-2010, and models for a single simulated season.

c. SPv4

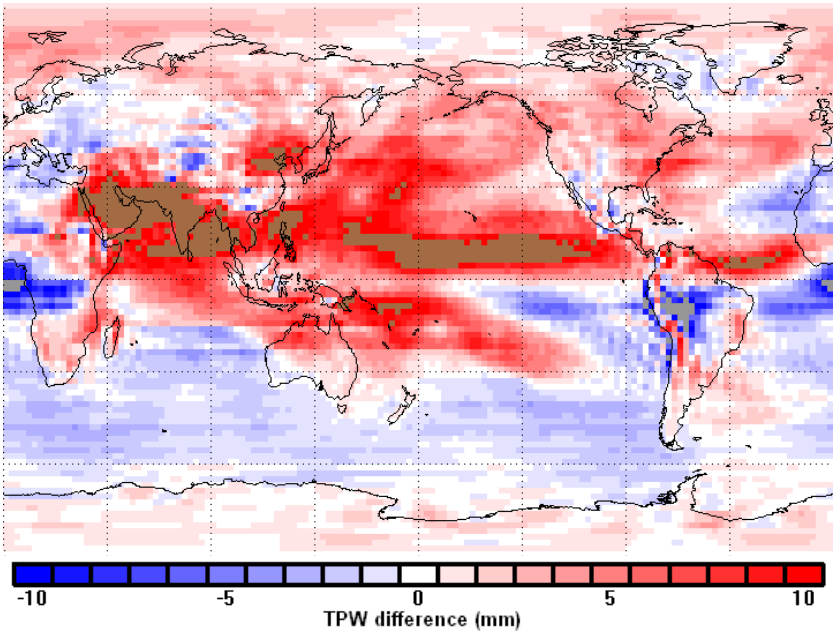

d. SPv5

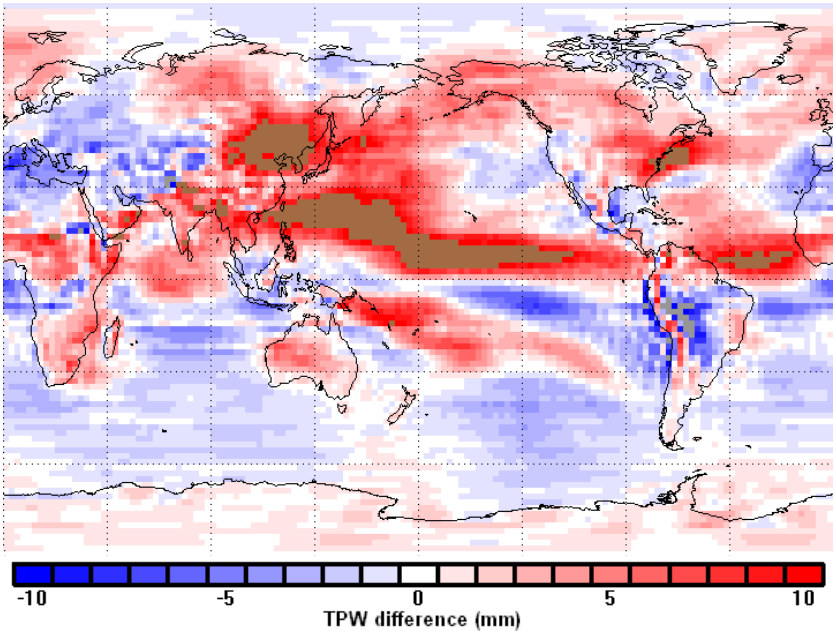

Figure 1.9. (continued)

e. CAM5

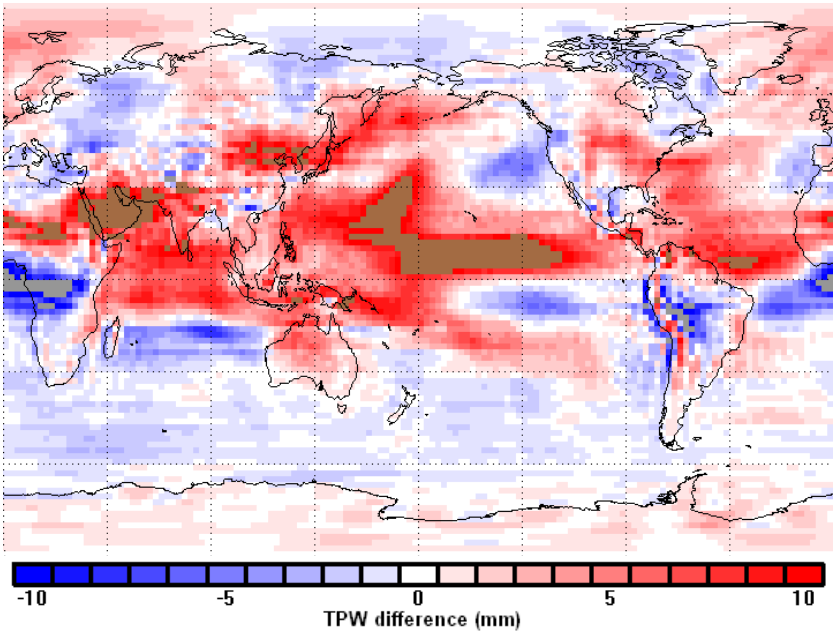

Figure 1.9. (continued)

2. COMPARISON OF OBSERVED AND SIMULATED TROPICAL CUMULIFORM CLOUDS BY W-BAND SPACEBORNE RADAR AND GLOBAL CLOUD-RESOLVING MODEL

2.1. Introduction

One possible solution to the cumulus parameterization problem is to simply remove the need for cumulus parameterizations, by increasing the horizontal resolution enough so that cumuliform clouds (at least the largest ones) can be simulated directly by the model's dynamical core. This is the approach used by NICAM. NICAM possesses a high resolution icosahedral grid to reduce horizontal grid spacing to a minimum of 3.5 km (though 7 km is commonly used). This is small enough to represent entire cumulonimbus clouds directly by the grid, though smaller-scale turbulent processes must still be parameterized. The high horizontal resolution has a significant cost in both vertical resolution (only 40 levels from 0 km to 40 km) and in the total model time. The longest model runs at 7 km resolution are only for a month, and the model runs for 3.5 km are only a week. So NICAM cannot yet be considered a true climate model, even though it has the potential to be one. But as computational power increases with time, NICAM and other GCRMs will become increasing useful and important for the atmospheric and climate science community. Even now, with their limited ability, they are useful for examining certain aspects of local-scale/large-scale interactions important to climate, such as the Madden-Julian Oscillation (MJO), e.g. Miura et al. [2007]. So it is well-worth examining their behavior.

As mentioned before, NICAM has already been used for investigating important topics in atmospheric science. Perhaps most well-known is the aforementioned work on the MJO. Simulating the MJO realistically has been a major difficulty for many atmospheric and climate

models, and at least one likely reason for this is the difficulty of cumulus parameterizations [Maloney and Hartmann 2001]. NICAM has demonstrated a capability to realistically simulate an MJO event already in progress, including a realistic propagation speed, the development of prominent features such as the westerly wind burst, and a reasonable size range for cumulonimbus clouds and mesoscale convective systems. Miura et al. [2009] demonstrated that NICAM is capable of generating an MJO event spontaneously. These studies provide strong evidence that NICAM's non-reliance on cumulus parameterizations is very useful for the ability to handle an existing MJO realistically. NICAM has also been used to investigate the development and life cycle of a tropical cyclone [Fudeyasu et al. 2010]. The high horizontal resolution allows the investigation of the relationship between the individual convective cells within the tropical cyclone and the evolution of the cyclone-scale circulation. It is interesting to note that this relationship appears similar to the proposed "vortical hot tower" path to tropical cyclogenesis, where vigorous convective cells concentrate environmental vorticity and then transfer it to the cyclone-scale circulation [Montgomery et al. 2006]. Finally, NICAM has been used to investigate aerosol/cloud interactions for cumulus, stratus, and stratocumulus by Suzuki et al. [2008]. They used a modified version of NICAM, which included an aerosol transport model, to investigate the realism of aerosol effects in the GCRM. They found that the simulated aerosol effect on the microphysical properties (liquid water path and cloud droplet effective radius) of the aforementioned cloud types is similar to the aerosol effect estimated by satellite observations. While there is some disagreement in the absolute magnitude of the aerosol effect between the observations and NICAM, there is closer agreement between observations and NICAM than observations and traditional GCMs, as described previously.

The A-Train suite of satellites has been used to investigate cloud properties from the observational side [L'Ecuyer and Jiang 2010]. There is a large number of ways to analyze the observational data in a way that can be quantifiably compared with climate model output. One method that has been used frequently in recent research is "conditional sampling": examining the sensitivity of cloud variables to changes in large-scale environmental variables. There had been a few earlier studies utilizing this method to examine the effect of large-scale variables on cloud radiative forcing (CRF). Ramamathan and Collins [1991] used Earth Radiation Budget Experiment (ERBE) and in situ observations to estimate the relationship between sea surface temperature and CRF, and Bony et al. [2004] did a similar study with simulated CRF and 500hPa vertical motion, with the intent to separate dynamical and thermodynamical influences on CRF. CRF is an important quantity to consider for large-scale and global energy budgets, but this is only one important aspect of cloud behavior among many. The A-Train is particularly useful for doing this kind of analysis, given the large amount of available co-located data from the different sensors. The CloudSat [Stephens et al. 2002, Stephens et al. 2008] and the Cloud-Aerosol Lidar with Orthogonal Polarization (CALIPSO) satellites are particularly important for cloud observational studies, as they can observe clouds in situations where traditional VIS/IR sensors cannot (e.g. multiple cloud layers), and can observe vertical profiles of cloud properties with higher spatial resolution than microwave sensors.

One of the earlier studies using CloudSat and another A-Train member (Aqua) was Su et al. [2008], which organized the tropical oceanic CloudSat vertical profiles of cloud water content by various large-scale environmental variables. This method, "conditional sampling", was particularly useful for identifying the transition between shallow clouds and DCCs. In addition, their analysis provided some quantitative knowledge of variability in the vertical structure of

cloud water content (CWC). This is an important piece of information about cloud properties that is not available from other cloud sensors, and is useful for evaluating the cloud properties simulated in GCMs and other models. Su et al. [2011] followed up on the initial study by comparing observations with two traditional GCMs. They found that the GCMs disagreed with each other as much as they did with the observations, particularly on the occurrence of mid-tropospheric clouds. Part of the disagreement was caused by "bogus" atmospheric states, that is unrealistic combinations of environmental variables that bias the average cloud behavior in the GCMs.

Kubar et al. [2011] used CloudSat and CALIPSO to examine the changes in cloud top height with 2m air temperature and the vertical gradient of moist static energy. While this study only uses cloud-top height as the cloud variable, as opposed to CWC vertical profiles, it should be noted that CloudSat and CALIPSO both have the ability to see through higher cloud layers and detect cloud layers below. This allows for a more reliable analysis of cloud top heights, particularly in convectively-active large-scale regions where large cirrus shields can obscure low clouds from traditional cloud sensors. Del Genio et al. [2011] used a similar approach to investigate the relationship between cloud top height and moisture in the MJO environment. They noted that the transition between shallow clouds and deep clouds is best understood in a statistical average sense – individual DCCs can form in a wide range of large-scale environmental conditions, depending on the local meteorology. Su et al. [2008] provided useful insight on this topic, but CWC alone, without filtering for specific cloud types, yields an incomplete representation of all cloud processes. It is necessary to include multiple types of cloud variables for different cloud types in any comprehensive evaluation of simulated clouds in GCMs and other models. Finally, Forsythe et al. [2012] examined changes in vertical cloud

occurrence frequency as a function of total precipitable water anomaly (difference between instantaneous value and weekly climatological mean value). While environmental variable anomalies are a very useful measure in examinations of observational data, they are not practical to use for analyzing model output from modern GCRMs because of the relatively short time domain. They might be useful for analysis of GCMs, though.

Conditional sampling should be a useful way for comparing model data with observational data. Direct comparisons between reflectivity profiles can be difficult because of the problems with simulating realistic attenuation of the radar signal in the reflectivity simulators. So, for example, a higher average maximum reflectivity in the NICAM DCCs versus the observations may not necessarily mean that NICAM DCCs are more vigorous than real life DCCs. It may rather be a problem with the reflectivity simulator's attenuation. This analysis method is one way around this problem – by looking at *changes* in reflectivity with environmental variables in the model and observations separately, and then comparing the model changes with the observed changes, I can remove the ambiguity caused by the conflation of attenuation errors and actual DCC characteristics in the model.

CloudSat has been used previously to examine convective behavior in NICAM. Masunaga et al. [2008] used CloudSat and the Tropical Rainfall Measurement Mission (TRMM) to compare the observed vertical reflectivity profile of tropical clouds in the MJO region with simulated reflectivity profiles from NICAM. They found that NICAM reflectivity profiles generally agree with the observed profiles, except in the frozen portion of DCCs where too much snow is produced. Inoue et al. [2010] confirmed the excess snow production, and found that the model can compensate for the excessive snow by altering other microphysical variables (e.g. the fall speed of snow). Satoh et al [2010] continued this study using a local CRM as a testing bed

for microphysical parameterization schemes. They found that the realism of simulated vertical reflectivity profiles can be improved by implementing more sophisticated microphysical schemes. It should be noted that both of these studies use a limited sample of CloudSat data (11 overpasses of the active MJO region), so their results may not entirely represent the general characteristics of tropical DCCs. Though the previous work with NICAM convection provides substantial evidence that NICAM handles convection more realistically than traditional GCMs, there still seems to be a lack of attention on the behavior of the individual cumuliform clouds themselves. While individual convective cells were examined briefly in the work on tropical cyclones and the MJO [Fudeyasu et al. 2010], there has yet to be an attempt to evaluate the general behavior of cumuliform clouds under a variety of conditions. Such a study is needed for the same reason it is needed for GCMs – so that NICAM can be trusted to produce realistic results in conditions beyond the present day.

This research project seeks to investigate the relationship of clouds and environmental variables in NICAM, specifically cumuliform clouds, in order to identify potential sources of error and uncertainty that may not be immediately obvious when examining larger-scale weather/climate features such as the MJO and tropical cyclones. This involves using the data to answer two principle questions:

1. Do the observed characteristics of DCCs according to this analysis method agree with what has been found by previous observational studies?

2. How well do the characteristics of NICAM DCCs agree with the observed characteristics?

2.2. Data and Methodology

In order to quantitatively compare the cloud properties observed by CloudSat and those simulated by NICAM, the work of Su et al. [2008] is used as a template on which this project is built. In that chapter, the authors derive a relationship of vertical cloud structure and large-scale environmental variables (LSEVs) by binning CloudSat profiles into groups based on the co-located value of each meteorological variable. The meteorological variables are taken from a range of sources, including the Atmospheric Infrared Sounder, the Advanced Microwave Scanning Radiometer for EOS (AMSR-E), Tropical Rainfall Measurement Mission observations, and National Center for Environmental Prediction/National Center for Atmospheric Research (NCEP/NCAR) reanalysis data. The results display how the typical vertical structure for tropical oceanic clouds (displayed as CWC) varies as a function of LSEVs – precipitable water, sea surface temperature, etc. Because of the straightforward nature of the methodology, it should be useful for comparing the observational data with many types of model output, such as NICAM.

To address the main questions of this chapter, the properties of DCCs are divided into two main types: the transition between shallow clouds to DCCs as LSEVs change, and the change of radar reflectivity characteristics of DCCs as LSEVs change. The transition between shallow clouds and DCCs has been studied quite extensively with both observation and simulation, as it is important for certain meteorological features like the MJO and various tropical waves (e.g. Straub and Kiladis 2003, Peters and Bretherton 2006, Del Genio et al. 2011). Because of this, there is a relatively sizable pool of knowledge with which to compare the results of this chapter. Knowledge of the variability of reflectivity properties in DCCs is less well represented in the literature, as it is a presently ongoing topic of research (Luo et al. [2011]

provide one example). So this chapter will present information that is for now more difficult to corroborate with previous research (see section 2.2.2 for more details).

2.2.1 NICAM Description

NICAM is a global cloud resolving model developed by the Frontier Research Center for Global Change/Japan Agency for Marine-Earth Science and Technology for the purpose of advancing climate modeling beyond conventional GCMs. A key property of NICAM is that it does not use a cumulus parameterization scheme. Rather, it simulated cumulus clouds directly using its governing system of equations. This considerably reduces the number of assumptions necessary to represent convection, though many are still necessary (e.g. microphysics, subgrid-scale turbulence). Satoh et al. [2008] describes in detail the mechanics of NICAM.

The dynamical core of NICAM is a set of nonhydrostatic, fully compressible primitive equations placed on a finite volume icosahedral grid. The predictive variables are pressure, density, horizontal momentum, vertical momentum, the sensible heat component of internal energy, and the mass concentration of atmospheric constituents. Because the equations are fully compressible, spurious acoustic and gravity waves are potentially a problem. To avoid this, the model uses a split-explicit integration technique. This technique separates the physical terms in the governing equations into fast components (gravity and acoustic waves) and slow components (everything else). Two time steps are used – a short time step for the fast components, and a long time step for the slow components (about 8 times the length of the short time step). A typical long time step is 30 s.

The icosahedron was chosen because it does not possess the problem of longitudinal convergence near the poles that many other grids do. To create the model grid, first the basic

icosahedron has each triangular face subdivided further into smaller triangles. The number of iterations is referred to as the "glevel"; glevel-0 is the basic icosahedron, glevel-1 has each icosahedral face divided into four triangle, glevel-2 has each face divided into 16 triangles, and so on. Glevel-9 corresponds to 7 km horiz. res., glevel-10 corresponds to 7 km, and glevel-11 corresponds to 3.5 km. Second, a correction algorithm is applied to the resulting grid to transform it from a true icosahedron into an approximate sphere. The governing equations have been altered to adjust automatically to changes in the glevel. Note that because of the way that the icosahedral grid is developed, the horizontal resolution can only be adjusted at discrete intervals; it is not possible to have a 10 km horiz. res.

The vertical coordinate is terrain-following. The vertical grid is Lorenz type, where vertical velocity is staggered from the other predictive variables. 40 vertical levels are used, with the top 5 being damping levels. The vertical resolution changes with height, with a minimum res. of 0.08 km near the surface to 3 km in the lower stratosphere. The number of levels was a trade-off between sufficient res. for useful simulation and computational time [Suzuki, personal communication].

Sea surface temperatures are prescribed according to the simulation (aquaplanet, real Earth for a given year, etc.). Surface heat fluxes are estimated using the method from Louis [1979], and hydrology is treated with a simple "bucket" model. The subgrid-scale turbulence scheme is the Mellor-Yamada scheme with third order closure. Different versions of NICAM use different microphysical schemes. The NICAM versions used in this project include the Grabowski [1998] microphysical scheme. This scheme represents hydrometeors with a very simple single moment bulk microphysical scheme that predicts two hydrometeor classes: cloud water, and precipitating water, both with Marshall-Palmer distributions. The precipitation phase

is determined by ambient temperature, and terminal fall speeds and saturation vapor pressure are assigned accordingly.

It should be noted the NICAM convective clouds are still constrained by the model's horizontal resolution, even at 3.5 km. This resolution is too large for the model to resolve many of the important circulations that occur in real convective clouds. In order for NICAM to resolve these circulations realistically, it would need a horiz. res. of 100 m or smaller [Bryan et al. 2003]. Experiments with NICAM demonstrate that the biggest improvement to NICAM convective clouds occurs when the horiz. res. decreases below 2 km [Miyamoto et al. 2013]. Below 2 km, convective updrafts occupy more than one horizontal grid cell. This causes significant changes in the spatial distribution and frequency of DCCs relative to the resolution – DCCs become relatively fewer in number and further apart. Though it is technically possible for NICAM to operate at even greater horiz. resolutions, the increased computational time required means that this will likely not become commonplace in the foreseeable future.

2.2.2 Data

To begin the study, the results of Su et al. [2008] were replicated with a slightly modified methodology to better fit the goals of this project. The time domain is JJA 2006-2009 during western Pacific MJO events, and the spatial domain is the 15°S-15°N ocean-only region. The meridional domain is smaller than the one used in Su et al. (30°S-30°N) because of the possibility of interference by baroclinic waves within the larger Su et al. domain. Ocean-only is used for now because of the difficulty of the limited coverage of certain data types (e.g. water vapor) over land.

For the cloud vertical structure information, only CloudSat is used. As part of the A-Train (except for a brief time in 2011, when technical issues temporarily forced CloudSat out of formation), CloudSat has a 705 km, 98° inclination orbit, which cross the equator at 1:30am/pm local time. CloudSat follows the Aqua satellite within two minutes, minimizing time lag discrepancies. CloudSat's primary instrument is the Cloud Profiling Radar (CPR), a 94 GHz radar with a 1.1 km wide effective footprint and 480 m vertical resolution, oversampled to create a 240 m effective vertical resolution [Stephens et al. 2002]. The specific CloudSat products used are the 2B-Geoprof Radar Reflectivity and 2B-Geoprof Cloud Mask.

The three LSEVs used presently are total precipitable water (TPW), sea surface temperature (SST), and 500hPa vertical velocity averaged over 2°x2° horizontal areas (W500). TPW and SST data are taken from the AMSR-E instrument onboard the Aqua satellite [Kawanishi et al. 2003], specifically version 5 of the AMSR-E ocean algorithm [Wentz and Meissner 2000, data available at http://www.ssmi.com]. W500 data are taken from the NCEP/NCAR reanalysis [Kalnay et al. 1996]. TPW is binned by 3 mm, SST is binned by 1 K, and W500 is binned by 1 cm s^{-1}. The AMSR-E data must be spatially co-located with CloudSat, but temporal co-location is not necessary because of the short (~1 min) lag between CloudSat and Aqua overpasses. For missing AMSR-E data caused by clouds, a simple linear interpolation is used to fill the missing values. The NCEP reanalysis data must be spatially and temporally co-located with CloudSat, as the data exist only at six hour resolution. No interpolation methods were applied.

It should be noted that these LSEVs are not entirely independent of each other. In particular, TPW and SST are highly correlated [Raval and Ramanathan 1989, Inamdar and Ramanathan 1994, Stephens 1990]. This is a direct result of the Clausius-Clapeyron relationship:

warmer air temperature allows for higher water vapor content. There is a more subtle connection between TPW/SST and W500 – large scale ascent tends to be associated with convectively-active regions and corresponding lower tropospheric convergence, which in turn require relatively high SST and TPW values. Joint PDFs of the three LSEVs from the observed/simulated data used in this chapter (not shown) demonstrate these correlations, though the reanalysis W500 is somewhat less strongly correlated with observed TPW/SST than in the simulation. This is likely a result of a less direct coupling between observation/reanalysis than simulation/simulation. In future studies, it might be useful to examine more sophisticated diagnostic variables which are dependent on these LSEVs (e.g. convective available potential energy). But for this chapter I choose to start with the basic LSEVs so that future research has a platform upon which to build.

Although it is possible to include CALIPSO data to augment the 2B-Geoprof Cloud Mask (increased sensitivity to low clouds and thin cirriform clouds), for now it is not used in order to better facilitate meaningful comparison with NICAM data via the CloudSat Simulator. CALIPSO is commonly used in conjunction with CloudSat because of their complementary capabilities. CloudSat is more useful for observing clouds with higher CWCs and/or deeper vertical extents, while CALIPSO is more useful for examining low-CWC clouds like subvisible cirrus, as well as boundary layer clouds which the CPR has trouble detecting. However, the authors do not have a CALIPSO simulator through which to interpret NICAM output. Furthermore, this study is primarily focuses on the properties of DCCs, which are easily observed by CloudSat. Though CloudSat may have difficulty in observing the fringes of convective anvils, I do not examine these specific features of DCCs. For these two reasons, CALIPSO data are not used in this chapter.

The NICAM simulation, set in early July 2006, included a significant MJO event in the western Pacific. The existence and phase of the MJO may be important in influencing the relationship between clouds and LSEVs in the tropics, so it is reasonable to account for the MJO in the observational data in order to avoid discrepancies between simulation and observations related to the MJO. The temporal domain of the observational data is chosen as the time periods during JJA in which the phase of the observed MJO was close to the phase of the MJO simulated in NICAM. The JJA season is used because the NICAM simulation is set in July. The simulated MJO corresponded with an observed MJO identified as a high amplitude phase 7 event, according to the Real-time Multivariate MJO Index as defined by Wheeler and Hendon [2004]. Phase 7 is defined as the time when the deep convective portion of the MJO has moved east of the Maritime Continent into the western Pacific Ocean. Time periods in the CloudSat data record that correspond to a high amplitude (greater than one) phase 7 MJO during JJA are 3 July – 16 July 2006, 7 July – 13 July 2007, and 8 June – 11 June 2009 (there was no significant MJO phase 7 event in JJA of 2008). This time domain will be called "JJAphase7", and it is time domain used for all observational data shown in the figures for this chapter. For comparative purposes, the full JJA record for 2006 (begins on 15 June because of early CloudSat data availability issues), 2007, and 2009 (called "JJA") was also run through the same procedures as the JJAphase7 dataset, for the purposes of examining differences between the average summer cloud characteristics and MJO-modified characteristics.

This process was repeated for NICAM output. I use the NICAM run from Suzuki et al. [2008]. The time domain is 1-8 July 2006, though this project uses data from only the last four days of the simulation. The model output time resolution is 3hr, and the horizontal resolution is 7 km. In order to compare NICAM output with the observational data, the NICAM output is

partitioned into a series of meridional cross-sections extending from 15°S to 15°N. CloudSat crosses the tropics at an angle close to meridional (~8° from N), so meridional cross-sections are reasonably close to CloudSat cross-sections. In order to minimize the influence of the diurnal cycle, cross-sections are only taken for each time step within 45°-wide zonal domains centered on the longitude corresponding with 1:30am and 1:30pm local time for that time step (e.g., the 9z time step would have zonal domains centered around 67.5°E and 112.5°W). 50 cross-sections are taken within each zonal domain at each time step. Fig. 2.1 shows the meridional domain of all the data, zonal domain of the data for one NICAM timestep, and the orientation of the data cross-sections for one timestep. The meteorological variables in the cross-sections include temperature (skin and atmospheric profile), specific humidity, pressure, TPW, surface precipitation, horizontal wind components, 500 hPa vertical wind, cloud liquid mixing ratio (MR), cloud ice MR, rain water MR, and snow MR.

It should be noted that the NICAM simulation used by Suzuki et al. [2008] included an aerosol model, which is not part of the "standard" NICAM settings. This addition might cause a slight change in behavior of convective clouds in comparison with other NICAM simulations because of changes in the convective microphysical characteristics. However, because the simulated aerosol effect on convective precipitation was smaller than the observed effect, the aerosol effects on other convective characteristics are likely small.

The hydrometeor variables are used to generate a cloud mask via the Quickbeam CloudSat Simulator [Haynes et al. 2007], where currently a value of -30dBZ is used as a minimum threshold for identifying a cloud. The microphysical variables used in the Quickbeam simulation (e.g. drop size distribution, number concentration) were the same as those used in the Suzuki et al. NICAM simulation itself for consistency. The simulated attenuation is not included

in the simulated reflectivity, because of the unrealistic behavior of attenuation for large melting hydrometeors. The simulated DCC reflectivity may also demonstrate some unrealistic behavior in regions of heavy precipitation because of problems simulating multiple scattering by large rain drops [Haynes et al. 2009]. Only data over oceans are used, for consistency. Instead of CWC used as the cloud variable as in Su et al. [2008], this project currently uses cloud occurrence and radar reflectivity as the cloud variables. These variables were chosen because of the unreliability of the current 2B-CWC CloudSat product in conditions of heavy precipitation (discussed by Su et al. [2011]). Because this project has a focus on large cumuliform clouds, such a limitation in the data renders it unsuitable.

2.2.3. Methodology

This chapter seeks to investigate the cloud-LSEV relationship of cumuliform clouds in particular, so it is desirable to reduce the influence of non-cumuliform on the results (e.g. cirrus). One simple way to do this is to include only clouds with a base within or near the planetary boundary layer (PBL). Based on the criteria used in Del Genio et al [2011], I remove all vertical profiles that do not contain a cloud with a base below 2000 m (I will refer to the clouds rooted in the PBL as PBLRCs). Of the remaining profiles, I remove all cloudy bins in each profile that are not connected continuously with the PBLRCs. The remaining profiles are then sorted by each LSEV, and cloud occurrence frequency (COF) vertical profiles are calculated. COF is calculated by summing the number of cloud occurrences in each vertical bin for each LSEV bin, then dividing by the total number of PBLRC profiles for the LSEV bin. This method allows the examination of the sensitivity of cloud vertical growth to the LSEVs without other factors such as changes in cloud cover with LSEV obscuring the relationship. It should be noted that this does

not remove PBLR stratiform clouds from the data. The major stratiform cloud type that may influence these results are the nimbostratus regions of MCSs, and this should be kept in mind when interpreting the deep cloud regions of the various cloud frequency data plots. All the presented COF data have had this procedure applied. The results are shown in Figs. 3, 5, and 6.

To narrow the results further to the properties of DCCs, a cloud identification scheme is necessary that is compatible with both the observational and simulated data. Previous research on the properties of DCCs observed by CloudSat has used the 2B-Cloud Classification product [Wang and Sassen, 2007] in order to identify deep convective clouds and systems. The 2B-CLDCLASS product uses a complex algorithm to determine cloud type from the observed cloud's height, vertical and horizontal extent, reflectivity properties, existence of precipitation, and temperature (the latter is taken from ECMWF data). Such an algorithm would be very difficult to apply to NICAM output without extensive modification, so a highly simplified algorithm designed to detect only DCCs is desirable. The algorithm used in this chapter is based on the tentative cloud classification rules presented in Wang and Sassen [2007, their Table 2]. A vertical profile (both CloudSat and NICAM) containing a cloud is identified as containing a DCC if a) the cloud vertical extent as identified by the cloud mask is greater than 6 km, and b) the reflectivity values for the layer of atmosphere between 15 °C and -15 °C are greater than -5dBZ. The vertical range of the minimum reflectivity has been slightly altered from the range given in Wang and Sassen [2007] (originally -20 °C to 25 °C) in order to improve agreement between DCCs identified by this algorithm and DCCs identified by 2B-CLDCLASS.

This algorithm consistently agrees 2B-CldClass when identifying the "obvious" DCCs - that is, clouds that are several kilometers tall and have high reflectivity values (greater than 5dBZ) extending to within two or three kilometers of the cloud top. However, this algorithm has

difficulty distinguishing between DCCs and other deep clouds which 2B-CldClass identifies as nimbostratus. Fortunately, in the deep tropics these types of clouds are rare, as even the "stratiform" regions of MCSs usually contain high enough reflectivity values over a large enough vertical extent to be classified as DCCs by 2B-CldClass. The most common disagreement between this algorithm and 2B-CldClass arises at the edges of large DCC clusters where reflectivity values can be less than -5dBZ throughout much of the cloud. This occurs because 2B-CldClass assigns cloud type to entire cloud clusters, and this algorithm assigns the DCC type only to individual vertical profiles. Nevertheless, the most important thing for this chapter is that the DCC identification process is *consistent* for both observational and simulation data. The vertical reflectivity profiles are sorted by each LSEV and averaged as with the COF diagrams; these are referred to as deep convective cloud average reflectivity (DCCAR) diagrams. The results are shown in Figs. 8-10.

In order to better quantify the relationship between reflectivity and meteorological variables, it is useful to create indices from the reflectivity data: cloud top height (CTH), maximum reflectivity (MAXREFL), and the distance between the -5 dBZ echo top height (ETH) and CTH (I call this difference N5ETHD). N5ETHD is used in this study to represent the upper DCC vertical reflectivity gradient. An increasing N5ETHD means decreasing vertical reflectivity gradient. While previous studies [e.g. Luo et al. 2011] use 0 dBZ and 10 dBZ ETHs for examining CloudSat data, this study uses the -5dBZ ETH because of the microphysics-related disagreement between CloudSat and NICAM reflectivity in the upper troposphere discussed previously. This disagreement occurs at 0 dBZ, and less so at -5 dBZ (see Fig. 2.6 and section 2.3.2 for discussion about this disagreement), so -5 dBZ is a more useful value to use in a comparative study. CTH in DCCs is a complex function of thermodymanic instability, the level

of neutral buoyancy, and the entrainment of environmental air. In general, it will tend to increase as thermodynamic instability increases, but this is not a rigid relationship [Luo et al. 2011]. MAXREFL is a function of droplet size and concentration, which in turn is thought to be affected by the updraft intensity. N5ETHD also is thought to be related to the updraft intensity, as stronger updrafts are capable of lofting larger cloud hydrometeors higher into the upper troposphere, bringing them closer to the cloud top.

It should be noted that the exact relationship between DCC reflectivity profiles and cloud-scale vertical velocity is a topic of ongoing research. While there are reasonable qualitative arguments for expecting certain relationships between reflectivity and vertical velocity, the science has not yet advanced to the point that I can directly cite peer reviewed research to corroborate this speculation with quantitative analysis. The most relevant research presently is that which has been done with precipitation radars. Zipser and Lutz [1994] found that both the maximum DCC reflectivity and cloud top reflectivity gradient from precipitation radars tends to increase as convective vertical velocity increases (though these results may also be related to other changes in DCC behavior related to land/ocean contrasts). The increased cloud top reflectivity gradient occurs because the high reflectivity values within the DCC occur over a greater depth as a result of large hydrometeors being lofted higher into the upper cloud. Liu et al. [2007] found using TRMM data that higher echo top heights for significant reflectivities (e.g. 20dBZ), and thus a large cloud top reflectivity gradient, is likely associated with more vigorous convection. In fact this may be a more reliable indicator of vigorous convection than cloud top brightness temperature, a more traditional measure of convective intensity. But because of the limited knowledge about CloudSat reflectivity relationships, the reflectivity results will be presented here without an attempt to associate them with physical processes in the atmosphere. A

comparison of reflectivity indices vs. maximum updraft velocity in NICAM (not shown) shows no trend in updraft intensity with increased CTH, an increasing trend of updraft intensity with increasing MAXREFL, and a decreasing trend of updraft intensity with increasing N5ETHD (stronger updrafts tend to occur with more packed cloud tops).

From the changes of these three reflectivity variables with LSEVs I calculate linear trend lines to estimate the average changes across each LSEV. Because of the noisiness of the data on the tails of the sample PDFs, only the central 95% of the data (between the vertical white lines in Figs. 6-9) are used in the trend line calculations. A "significant" result refers to a trend line slope value within the sufficient data range (between the white dashed lines) that is statistically significant according to the 90% confidence one-tailed Student's t-test. The 90% confidence limit is used (as opposed to higher limits) because it provides a roughly even split between the number of significant and non-significant results, so that a meaningful comparison between observations and simulation is possible (e.g. to avoid the trivial "finding" that all relationships are insignificant because confidence limit is too high). The trend line values and significance test results are summarized in Table 2.1.

I also conducted a sensitivity experiment for the definition of DCC by increasing the minimum DCC height to 10 km. 6 km is a rather low altitude for DCC top height in the tropics, and would include both growing DCCs and a small number of cumulus congestus. The results of the 10 km analysis are very similar to the 6 km analysis, with the exception of MAXREFL for TPW, so the results won't be discussed directly other than this one exception.

2.3. Cloud Occurrence Frequency

Before examining the results, it would be useful to discuss what someone might expect to find based on previous research and the general principles of atmospheric physics. It is reasonable to expect deep clouds to become more frequent as TPW increases, because DCCs require relatively high moisture to develop (with the exact value depending on both local climatic and meteorological conditions). Developing DCCs and cumulus congestus also moisten the environment, conditioning the atmosphere for deeper convection [Thayer-Calder and Randall, 2009]. PBL moisture is an important component of CAPE, which in turn is necessary for overcoming the atmosphere's resistance to large vertical motions. Also of particular interest is the idea of midtropospheric humidity acting as a control on vertical cloud growth (e.g. Jensen and Del Genio 2006). Holloway and Neelin [2009] found that most of the variability of TPW (i.e. column water vapor) is directly related to water vapor variability above 850hPa (PBL water vapor is strongly tied with surface interactions and so has smaller variability). If this is true, then larger values of TPW should often correspond with increased midtropospheric humidity, and thus increased vertical cloud growth.

One would also expect deep clouds to become more frequent as SST increases [Zhang 1993]. SST corresponds closely with PBL temperature, which is another important control on CAPE. There is also an association of SST and SST gradients with low level moisture convergence [Lindzen and Nigam 1987]. This, as previously described with regard to TPW, is conducive for deep convection. Previous studies have found a close association with convective activity with SST (e.g. Bony et al. 1997), though there is some question to the precise relationship in the vicinity of tropical warm pools [Liu and Moncrieff 2008].

Finally, one would expect deep clouds to become more frequent as W500 increases, particularly when it becomes positive. As described in Bony et al. [2004], it can be difficult in practice to separate the effects of large-scale vertical velocity and thermodynamics in controlling large-scale convective activity; it is a "chicken and egg" problem. However, a basic argument for the relationship between DCCs and W500 is that subsidence warming (lifting cooling) increases (decreases) vertical stability, and thus suppresses (enhances) deep convection. Also, because of mass continuity, middle tropospheric ascending (descending) motion is associated with convergence (divergence) in the lower troposphere. This convergence/divergence may not necessarily be located within the PBL itself, so I would not expect any correlation between W500 and PBL convergence to be one.

It would be useful to know the average vertical COF for observations and NICAM before applying the conditional sampling technique. Fig. 2.2 shows the vertical COFs for the tropical oceans for four sky conditions: all-sky, cloudy, PBL-R cloudy, and all sky with all clouds but PBLRCs removed. For all-sky conditions, NICAM produces too many shallow clouds and too few mid-tropospheric clouds relative to observations. For cloudy conditions, NICAM produces shallow clouds almost constantly, while CloudSat observes shallow clouds only half of the time. NICAM also produces too many upper tropospheric clouds and too few mid-tropospheric clouds. For PBL-R-only cloudy conditions, NICAM produces too many shallow PBLRCs, and too few deeper PBLRCs. This suggests that PBLRCs do not grow vertically as tall and/or as frequently in NICAM as they are observed to do. Therefore, I should expect to see a deficit in vertical development of PBLRCs when conditional sampling is applied.

2.3.1 TPW

Fig. 2.3 shows the COF plots and sample PDFs for TPW. The PDFs of both all-sky and PBL-R cloudy conditions are shown in order to illustrate the effect of TPW on cloud cover (the ratio of the PBL-R cloud PDF to the all-sky PDF). The observed and NICAM sample PDF curves are shaped quite differently, with NICAM having a roughly Gaussian shape with a maximum value at 36 mm, and the observed PDF being weighted more heavily at high TPW values with a maximum at 57 mm. For both observed and simulated data, the shape of the sample PDF does not change much between the all-sky and PBL-R cloudy conditions, but the PBL-R cloud cover increases noticeably for TPW values above 51mm.

The difference in the shape of the observed and simulated sample PDFs is not easily explained with the results I have presented here. However, I can rule out the possibility of NICAM being unable to simulate PBLRCs realistically. Fig. 2.3c clearly shows that the disagreement in PDF shape for PBL-R cloudy conditions is caused primarily by a more fundamental disagreement between NICAM and observations of the distribution of TPW in all-sky conditions, irrelevant to clouds. It should be noted that Su et al. (2008) showed a TPW all-sky sample PDF that was also skewed towards higher TPW values, so it should not be assumed that the skewness shown here is simply an methodological artifact. Further analysis of why NICAM behaves so unrealistically is beyond the scope of the chapter, but it would be a topic worth investigating.

The observations show primarily lower tropospheric clouds for low TPW values, and a progressive transition to deeper clouds starting at approximately 45-48 mm. This corresponds with results from Su et al. [2008], where the CWC signature for deep clouds begins just below 50 mm, and with Del Genio et al. [2011], where the typical cloud top height begins increasing at

48 mm. This also agrees with tropical precipitation studies, e.g. Holloway and Neelin [2009], where the non-drizzle rain signature (which requires vertical cloud growth) begins around 50 mm TPW. The results make reasonable physical sense: as stated previously, one would expect DCCs to become more frequent as TPW increases.

The NICAM data show a similar progression of COF with increasing TPW. However, the simulated clouds begin transitioning to deep clouds at a higher TPW value of 51-54 mm. A possible explanation for this may be the limited ability of NICAM to simulate deep convection with its horizontal resolution. In the real atmosphere, it is possible for isolated narrow DCCs to form and grow in marginally suitable large-scale conditions, which would inhibit larger DCCs and large-scale convective initiation. But NICAM has a 7 km horizontal resolution, which is too large to realistically simulate these narrow DCCs. Though NICAM can resolve a 7-km or 14 km-wide cloud, it cannot resolve the smaller-scale convective features (e.g. localized updrafts and downdrafts) that are important for building/maintaining observed DCCs. So convective initiation of any sort in NICAM might not occur until the environmental conditions become more than just marginally suitable. There are odd "spike"-like features on the ends of some of the plots, e.g., below 15 mm of the TPW panel. These features are likely numerical artifacts caused by the extremely low number of observations in the outlying regions. There are few observations below 15 mm TPW, so the frequency plot in this region is likely unreliable.

It is difficult to explain the deficit in deeper PBLRCs in NICAM through simple causality, because there is a "chicken and egg" problem associated with clouds and their environment. In this case, on one hand, increased environmental moisture helps clouds develop vertically. On the other hand, cloud growth tends to moisten the surrounding environment, at least until clouds grow large enough to precipitate and induce subsidence drying in the

environment. One possibility is that there is a dry bias in the middle troposphere in NICAM. As mentioned previously, middle tropospheric moisture is an important control in the development of cumulus congestus and DCCs. If the middle troposphere is too dry, deeper cumulus clouds will have more difficulty developing. And if deeper cumulus clouds have difficulty developing, they will be less effective in moistening the middle troposphere.

To test for this possibility, I have applied the conditional sampling technique used for the vertical COF profiles to vertical specific humidity profiles. For the "observed" specific humidity profiles I use the CloudSat ECMWF-Aux product [Partain 2004], which is data from the European Center for Medium-Range Weather Forecasts (ECMWF) global atmospheric model, co-located to CloudSat data in space and time (a description of the ECMWF model is available at http://www.ecmwf.int/products/forecasts/guide/The_ECMWF_global_atmospheric_model.html). I am particularly interested in comparing the "observed" and simulated specific humidity profiles in atmospheric conditions marginally suitable for vertically developing tropical oceanic PBLRCs. "Marginally suitable" is defined as the environmental conditions in which the observations show the transition between shallow and deep clouds occurring; in this case, Fig. 2.3 shows this region to be between 45mm and 60mm of TPW. The results, calculated as NICAM humidity minus ECMWF humidity divided by the number of ECMWF samples, are shown in Fig. 2.4. I find that for tropical ocean atmospheric profiles where the TPW value is between 45mm and 60mm, NICAM has a dry bias of 5-15% between 2-5 km altitude. I hypothesize that this dry bias is related to the deficit of deeper PBLRCs in NICAM discussed previously. Preliminary research by other NICAM researchers have found a similar dry bias, and they speculate that this is related to misrepresentation of shallow/congestus clouds due to subgrid convection (personal communication, A. Noda and M. Satoh, 2012). In the future it may be

possible to remove this dry bias through the use of a subgrid convective parameterization for shallow and cumulus congestus clouds.

2.3.2 SST

Fig. 2.5 shows the COF plots and number of samples for SST. The observed and NICAM sample PDFs have roughly the same shape and mean, with the observations having slightly thicker tails than NICAM. It should be noted that NICAM SST is taken from observations, and is not a prognostic variable, so the similarity between the observed and simulated PDFs is not surprising. PBL-R cloudy cover does not appear to change significantly with increasing SST for either observations or simulation. One might expect for PBLRCs to become more frequent as SST increases because of increased PBL instability, but these results do not support that idea.

The observations show the shallow clouds transitioning to deep clouds beginning at 298 K, with an abrupt increase in the maximum cloud height (i.e. transition to DCCs) occurring at 300 K. This is consistent with Su et al [2008], which shows the deep cloud CWC signal beginning at 300K. Kubar et al [2011] found a similar pattern of a gradual increase in CTH with increasing SST followed by an abrupt increase in maximum CTH. However, they found the abrupt transition at 298 K, not 300 K. It should be noted that their domain was a cross-section of the eastern tropical Pacific, not the global tropical ocean. However, this does not fully explain why this chapter does not find a stronger DCC signature at 298 K. It is possible that there is a disagreement in SST measurements between the AMSR-E product used here and the ECMWF-YOTC product used by Kubar et al [2011].

NICAM data show a pattern of slow increase in CTH with SST followed by the abrupt transition at 301 K, slightly warmer than observations. However, the COF values for mid- and

upper tropospheric clouds does not increase above 25%, unlike the observed COF values. This indicates that DCC occurrence is not as strongly coupled with SST in NICAM as in the real atmosphere.

As with the TPW case, NICAM shows a mid-tropospheric dry bias for regions with SST values marginal for convection (Fig. 2.4). This is not surprising, given the high correlation between SST and TPW.

2.3.3 W500

Fig. 2.6 shows the COF plots and number of samples for W500. The reanalysis and simulated PDFs have a roughly Gaussian shape, though with the observed PDF being noisier. Interestingly, the observed PDF has a maximum W500 probability at 0.002 m s^{-1}, while NICAM has a maximum value at -0.005 m s^{-1}. It appears that the NICAM deep tropics possesses stronger and more common subsidence than the reanalysis show. Su et al. [2008] showed a reanalysis preference for subsidence, as well. This apparent discrepancy in the reanalysis results is not caused by the presence of a strong phase 7 of the MJO, which is associated with enhanced large-scale ascent over the western Pacific, as a similar sample PDF is found for the full JJA dataset (not shown). However, the reanalysis sample PDF for all profiles (cloudy and clear sky, not shown) shows a preference for subsidence similar to NICAM and Su et al. [2008]. This suggests that PBLRCs have at least a weak association with midtropospheric ascending motion in the real atmosphere, which is not simulated appropriately in NICAM. For both observed and simulated results, the PBL-R cloud cover increases slightly with increasing W500 for values above 0.01 m s^{-1}.

It appears that DCCs exist in both ascending and descending large scale regimes for the observations/reanalysis (note the prevalence of the bluer colors for negative w). However, DCCs become more frequent with increasing w beginning at the transition between descending and ascending motion (w = 0). DCCs become more frequent with increasing w until they reach mature DCC height at 0.015 m s^{-1}. This corresponds to the results in Su et al [2008], which shows the deep cloud signal becoming prominent at neutral vertical velocity. Bony et al [2004] found from ERBE data that the transition from a shallow cloud radiative regime to a deep cloud radiative regime begins at about 20 hPa/day, roughly -0.004 m s^{-1}. This is reasonably close to the w = 0 value found by this chapter, and note that Bony et al. did not exclude cirriform clouds from their calculations.

NICAM shows no deep clouds forming in the descending regime – all deep clouds exist in the ascending regime. As with TPW, a possible explanation for this is that the 7 km horizontal resolution does not allow for isolated narrow vigorous DCCs to develop in environmental regimes unfavorable for large-scale convection. The simulated DCCs may be too large and weak to overcome the large-scale subsidence and associated stability. Furthermore, the frequency of deeper clouds does not increase as quickly with increasing w as the observations/reanalysis show. As with SST, this is an indication that DCC frequency is not as strongly associated with increases in w (above w = 0) as in the reanalysis.

It is possible that the observational results have been contaminated with errors in the NCEP/NCAR reanalysis data. Much of the spatial domain for this study covers the remote ocean, where observational wind data are sparse, and thus the reanalysis relies mostly on model estimates. However, in order to fully explain the weak DCC-W500 relationship mentioned above, the NCEP/NCAR reanalysis would have to have a routinely inaccurate estimate of W500

by at least 0.01 m s^{-1}. This possibility cannot be ruled out by the results presented here, but investigating this possibility further would be beyond the scope of this chapter.

As with TPW and SST, NICAM shows a mid-tropospheric dry bias for regions with W500 values marginal for convection (Fig. 2.4). As mentioned previously, W500 is significantly correlated with SST, though not as highly as SST with TPW, so this result is unsurprising.

2.4. DCC Average Reflectivity

Before examining the DCC radar reflectivity vs. meteorological variable plots, it is useful to examine the average vertical reflectivity profile of DCCs. Fig. 2.7 shows the contoured frequency by altitude diagrams (CFADs) of reflectivity for all observed and simulated DCCs. The observed DCC CFAD show the characteristic "arc"-shaped reflectivity profile seen in previous studies (e.g. Masunaga et al. 2008), with a reflectivity maximum of 10-15 dBZ at 4-5 km. The large reflectivity below 0.5 km is contamination from the surface return. The observed local minimum in reflectivity at ~5 km is a "dark band" caused by the melting of larger frozen hydrometeors, which enhances attenuation of the radar signal [Sassen et al. 2007]. The increased reflectivity just below the dim band is the bright band from the recently melted rain drops, though the signal is much weaker for the CPR than it is for precipitation radar. In comparison, the simulated CFAD does not show a strong arc-shaped profile below 5 km. This is because of the non-use of the attenuation by large hydrometeors in QuickBeam [Haynes et al. 2007].

The most notable contrast between the simulated and observed CFADs is the abrupt reduction in reflectivity values starting at ~8 km. This is primarily a problem caused by the Grabowski microphysics scheme used in the NICAM simulation. The Grabowski scheme has only two microphysical variables – cloud water and precipitation, and the water phase (cloud

ice/water, snow/rain) is dependent only on temperature. Importantly, there is no graupel included. Observed DCCs have a significant amount of graupel in the freezing portion of the cloud. Because the Grabowski scheme does not produce graupel, the simulated DCCs instead produce unrealistically large amount of snow in the freezing portion of the cloud [Satoh et al. 2010]. Snow has significantly different reflectivity characteristics from graupel, and this causes the abrupt reduction in simulated reflectivity at ~8 km. The missing dark band is caused by the absence of attenuation in Quickbeam.

2.4.1 TPW

Fig. 2.8 shows the DCCAR plots and number of samples for TPW. Table 2.1 lists the trend slope values and significance test results for TPW and the other LSEVs. The observed and NICAM sample PDFs both have a near-Gaussian shape, with similar means and variances. NICAM has a slightly higher mode (63 mm) and variance compared with the observations (60 mm). Unlike the difference in the PBL-R cloudy PDFs, the difference between the DCC PDFs cannot be explained simply by the difference in all-sky PDFs. If we use the reasoning discussed in section 3.1, one would expect the NICAM DCC PDF to have a lower mean and mode compared with observations because the NICAM all-sky PDF has a lower mean and mode than the observed PDF. This suggests that the disagreement must be related to the simulated DCC behavior in some manner.

The most prominent feature for observed TPW is the near-monotonic increase in the cloud top height with increasing TPW value. This corresponds with a significant trend line slope of 89 m mm^{-1}. This result is consistent with the full JJA dataset. The observed N5ETHD shows a non-monotonic decrease, in which it increases from 51 mm to 60 mm, and the decreases to 69

mm. This results in a decreasing significant trend line slope of -83 m mm^{-1}. This result is also consistent with the full JJA dataset. The observed MAXREFL has no significant trend line slope with the value decreasing from 51mm to 57 mm, and increasing to 69 mm. It should be noted that in the full JJA dataset, there is a non-monotonic increase in MAXREFL with TPW, with a significant trend of 0.11 dBZ mm^{-1}.

The NICAM CTH does not change with TPW, which is curiously very different from the observations. In fact, it appears that DCC CTH is insensitive to all LSEVs. It may be the case that in NICAM, CTH isn't as variable as it is in the real atmosphere. If this is true, this may cause problems for using NICAM to investigate other aspects of tropical convection, such as convective penetration of the tropical tropopause layer, which is important for troposphere/stratosphere interaction [Luo et al. 2008]. The NICAM N5ETHD non-monotonically decreases with TPW, with a decrease from 51 mm to 69 mm, and an increase to 72 mm. The resulting significant trend of -66 m mm^{-1} is consistent with the observations. The NICAM MAXREFL non-monotonically decreases with TPW, with a decrease from 51 mm to 66 mm, and an increase to 72 mm. This results in a significant decreasing trend of -0.087 dBZ mm^{-1}, which again is different from the observations (particularly the full JJA dataset). The NICAM MAXREFL is noticeably larger than the CloudSat MAXREFL. This is related to the lack of attenuation in the Quickbeam simulator, as described in the previous section.

The one major difference in the results of the sensitivity experiment is the observed trend of MAXREFL with TPW. With a 10 km minimum height for DCCs, the observed results for JJAphase7 give a significant increasing trend of 0.184 dBZ mm^{-1}. The NICAM analysis yields the same result as the 6 km minimum height analysis.

2.4.2 SST

Fig. 2.9 shows the DCCAR plots and number of samples for SST. Like with TPW, the SST sample PDFs have a Gaussian distribution with similar means and variances. The NICAM PDF has a slightly lower mode (302 K) than the observations (303 K), and a similar variance. SST does not appear to have as quite an obvious relationship with reflectivity as TPW. While the plots show an obvious increase in observed CTH and MAXREFL with SST, and an increase in CTH for NICAM, there is sufficient "noise" in the data that the t-test values fall just short of the critical values to pass the 90% significance test. While the observations and NICAM may technically agree according to the statistics tests, it may be useful to examine the differences between trend behaviors. The results do not change much with the full JJA record. The only difference between the JJAphase7 and JJA datasets is the observed CTH, which has a significant trend slope value of 91 m K^{-1} for JJA.

2.4.3 W500

Fig. 2.10 shows the DCCAR plots and number of samples for W500. The sample PDFs again have a roughly Gaussian distribution shape with similar means and variances, though the curves are noisier because of the relatively higher number of W500 variable bins - and thus a smaller bin interval - than for TPW and SST. Observed CTH has a general increase with increasing W500, though the increase is very much non-monotonic. This leads to a significant trend slope value of 30,000 m m^{-1}s (or 300 m cm^{-1}s). The observed N5ETHD increases only slightly with W500, and has an insignificant trend slope value of 6500m m^{-1} s (65m cm^{-1} s). This is an unexpected result. As discussed previously, increasing W500 is generally associated with environments more suitable for stronger convective updrafts (e.g. larger CAPE, lower subsidence

warming). If N5ETHD is associated with convective intensity, then N5ETHD should change with changing W500. So the lack of a significant trend is surprising. The observed MAXREFL is highly noisy, and so the calculated trend slope value of 16,000dBZ m^{-1} s is very unrealistic and is almost certainly unrepresentative of the data. It should be noted that the full JJA record also has a significant increase in N5ETHD, with a trend slope value of 12000 m m^{-1}s (120 m cm^{-1} s).

The NICAM CTH shows an insignificant increase with a trend line value of 7600m m^{-1}s (76 m cm^{-1} s). The NICAM N5ETHD shows a non-monotonic decrease with W500, giving a significant trend slope value of 23000 m m^{-1} s (230 m cm^{-1} s). Unlike the observed/reanalysis results, this result is closer to what one might expect. The NICAM MAXREFL shows a decrease with W500, with a significant trend slope value of -29 dBZ m^{-1} s (-0.29 dBZ cm^{-1} s). It should be noted that the NICAM MAXREFL is much less noisy than the observed MAXREFL, despite having a much smaller sample size.

2.5. Conclusions

This study builds upon previous research of using conditional sampling of clouds and LSEVs to evaluate the behavior of atmospheric models. NICAM has an advantage over traditional GCMs of directly simulated DCCs instead of using parameterization, so I focused this analysis on the cloud-LSEV relationship of DCCs in the observations and NICAM. Because no single cloud variable can capture the full relationship between cloud and environment, I used two cloud variables in the analysis. First, I reduced the full dataset of vertical profiles to only the vertical profiles containing PBLRCs. Non-PBLRCs in these profiles were removed. The purpose of this was to examine the transition between shallow clouds and DCCs as related to LSEVs.

Main conclusions from this part of the study are:

1. Do the observed characteristics of DCCs according to this analysis method agree with what has been found by previous observational studies?

The observations presented in this study generally agree with previous similar studies, though there are some minor disagreements over the exact values at which the shallow cloud/DCC transition occurs.

2. How well do the characteristics of NICAM DCCs agree with the observed characteristics?

The NICAM results generally agree with the observations in simulating the general pattern of the transition from shallow clouds to DCCs. There are some small but interesting differences to note, however. Most of the disagreement occurs in situations marginally favorable for deep convection; NICAM appears to resist convection slightly more strongly than the real atmosphere. NICAM and observations both show the increase in COF depth as TPW increases, though NICAM has the transition occurring at slightly higher TPW values than the observations. Both show the increase in cloud depth as SST increases, though NICAM has the transition occurring at slightly higher SST values than the observations, and the COF for DCCs is not as strongly associated with SST as it is for observations. Also, both show the increase in cloud depth as W500 increases, though NICAM underestimates the COF of DCCs in large-scale descent conditions.

For DCCs, the most obvious difference between the observations and NICAM is the insensitivity of the NICAM CTH to changes in the LSEVs. The most notable relationship is found in TPW, where both observation and NICAM respond significantly to increases in TPW. The only insignificance responses are NICAM CTH and observed MAXREFL. The full JJA

record has a significant MAXREFL trend. Both observations and NICAM show only a small response to SST, which is not strong enough to be significant. The only significant response is the observed full JJA CTH. Observations and NICAM have different responses to W500, with the observations having a significant trend with CTH, and NICAM having significant trends with MAXREFL and N5ETHD. The full JJA also shows a significant trend for N5ETHD.

Additional remarks

It is difficult to explain these results simply, because there are many processes that effect both convective behavior and radar reflectivity. However, the results suggest a few possibilities that may be worth looking at in the future. CTH is not simply a function of and convective instability and the level of neutral buoyancy, but also the convective entrainment rate. If the simulated convective entrainment rates are unrealistic, then the simulated CTH may also be unrealistic. Observing convective entrainment rates has historically been a very difficult task, but recently Luo et al. (2010) described a method using A-Train data to estimate the entrainment rates of observed DCCs. It would be interesting to compare observed entrainment rates with those calculated from NICAM. It is also possible that the coarse model vertical resolution of NICAM at the typical DCC CTH, about 1km, prevents NICAM from correctly simulating the cloud/environment interactions that govern cloud top behavior (discussed by Luo et al. [2008]). It would be useful to examine the effect of model vertical resolution at the DCC CTH on the behavior of DCC cloud tops using a local CRM. On the observation/reanalysis side, the lack of significant relationship between W500 and N5ETHD is difficult to explain through simple physical reasons, as mentioned previously. It would be hard to explain this through errors in the

observation/reanalysis integration, because it would require an error in the NCEP/NCAR reanalysis of multiple cm s^{-1}. This question probably merits more investigation.

The 3.5 day time domain in this study leaves some room for improvement in future investigation using larger time domains. A study using a multi-month time domain over a season would help clarify the effect of the short time domain on our results. E.g., does the apparent insensitivity of NICAM CTH to TPW depend on the time domain? There are now multiple NICAM datasets available that would allow such investigations (examples).

As more climate models with cloud-resolving capabilities come into use, the type of analysis used in this study should be considered to evaluate how realistically the simulated clouds behave. It would be very interesting and useful to apply this methodology to other simulations with NICAM. In particular, it would be interesting to examine NICAM runs with 3.5 km horizontal resolution, and compare the effect on DCCs of changing the resolution. This would add information to previous work of this nature [e.g. Inoue et al. 2008]. It would also be useful to use this methodology for other GCRMs, as well as models with cloud-resolving elements, which are also becoming more frequently used in a variety of climate-related research. Because of this, in this thesis, later chapters will include SP-CAM data along with NICAM data.

Another use would be to extend the spatial domain of the analyses to regions outside of the tropics. Most of the literature involving NICAM focuses on the behavior of clouds and related meteorological features in the tropics. While the tropics has a critical role in regulating Earth's weather and climate, the extratropics covers fully half of Earth's surface as well. Using this same analysis method, it should be possible to evaluate the behavior of DCCs in climate models in various extratropical regions. It has been well-established that the behavior of DCCs in the extratropics – particularly over land – is significantly different than their behavior over the

tropical oceans [Lucas et al. 1994]. It may be possible that a cloud-resolving model that behaves realistically over the tropical ocean may not behave realistically elsewhere, with different environmental conditions. One particular place of interest is the continental United States, where the large amount of in situ observations and other measurement methods would offset the limitations of satellite sensors over land. There has already been some research of continental United States DCCs using the A-Train [Luo et al 2011], and it would be reasonable and useful to continue exploring this avenue. So the remaining chapters of this thesis will be set in this region.

Table 2.1. Trend Slope Values and Significance Test Results for the LSEVs by Dataset[a]

	DATASET					
	CS JJAphase7		**CS JJA**		**NICAM**	
	trend slope	sig.?	trend slope	sig.?	trend slope	sig.?
LSEV/REFL.						
TPW						
CTH ($m\ mm^{-1}$)	88.57	y	91.42	y	0.000	n
N5ETHD ($m\ mm^{-1}$)	-82.86	y	-20.00	y	-65.66	y
MAXREFL ($dBZ\ mm^{-1}$)	0.02352	n	0.1127	y	-0.08742	y
SST						
CTH ($m\ K^{-1}$)	144.0	n	168.0	y	354.2	n
N5ETHD ($m\ K^{-1}$)	-72.00	n	48.00	n	-196.2	n
MAXREFL ($dBZ\ K^{-1}$)	0.6245	n	0.01300	n	0.06273	n
W500						
CTH ($m\ m^{-1}s$)	30410	y	14210	y	7638	n
N5ETHD ($m\ m^{-1}s$)	6510	n	11890	n	-23160	y
MAXREFL ($dBZ\ m^{-1}s$)	16210	n	5.926	y	-28.56	y

[a] Listed are the statistics by LSEV (TPW, SST, W500, rows) and by dataset (JJAphase7, JJA, NICAM, columns). Each statistic includes a trend slope value and a yes/no indicator for whether the trend slop value passes the 90% one-tailed t-test.

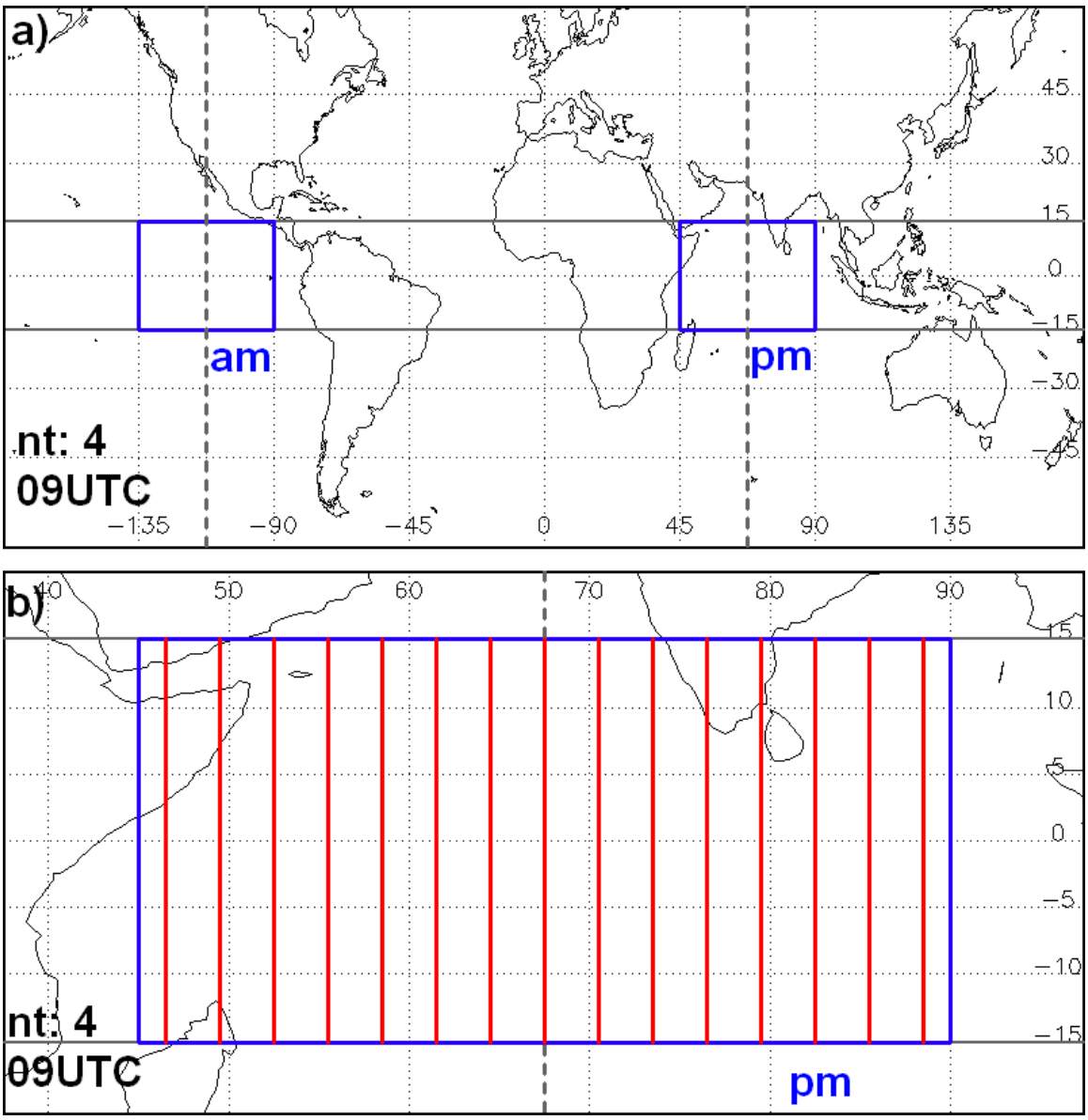

Figure 2.1. a) Global map of the 15°S and 15°N meridional domain boundaries (horizontal solid gray lines), longitudes of 1:30am and 1:30pm local times (vertical gray dashed

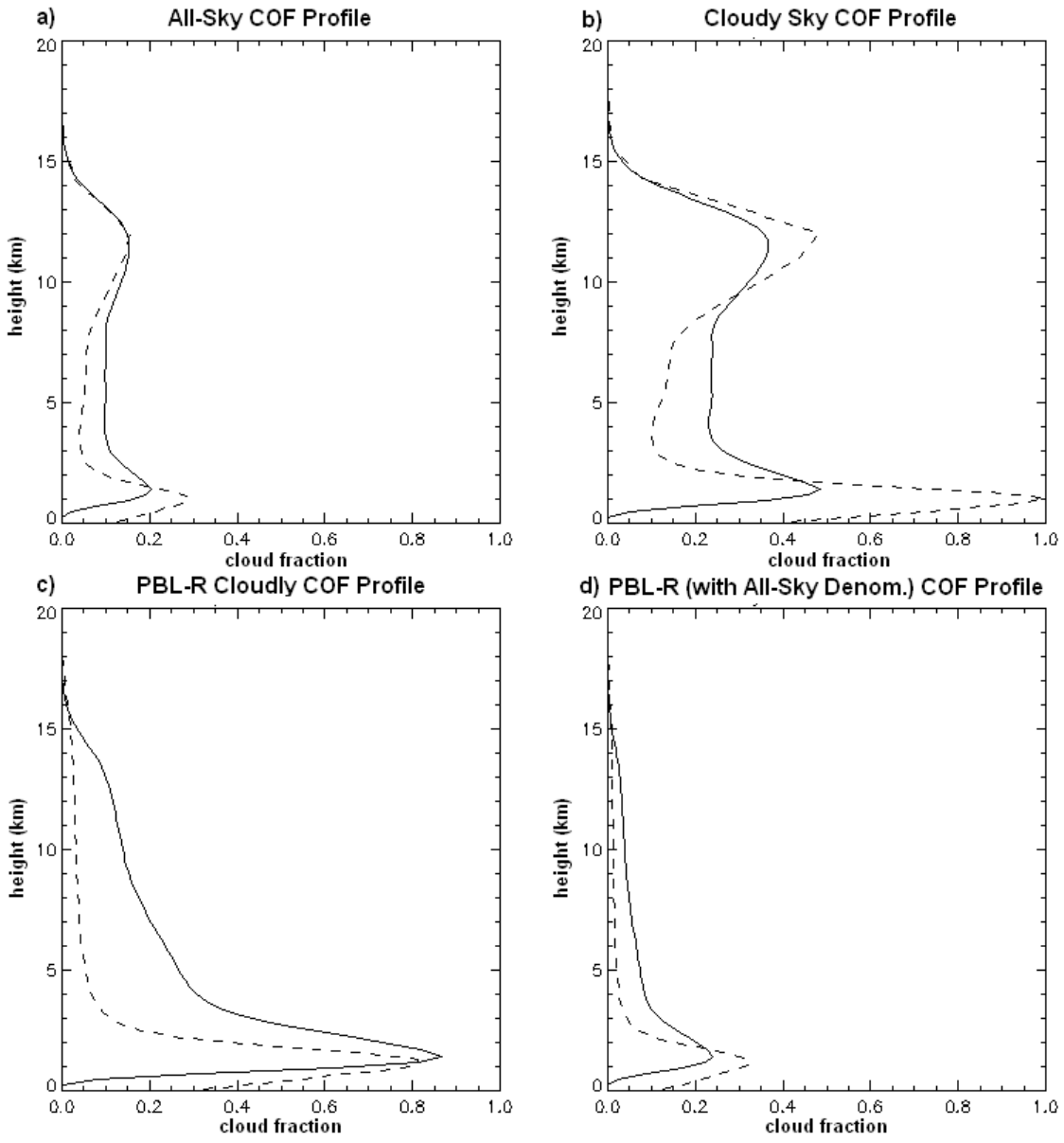

Figure 2.2. Vertical profiles of cloud fraction for a) all-sky conditions, b) cloudy sky, c) PBL-R cloud sky, and d) all-sky conditions where all clouds but PBLRCs are removed. Solid line is observed JJAphase7, dashed line is NICAM. The definition of COF used in panel c is also used in Figs. 3, 5, and 6.

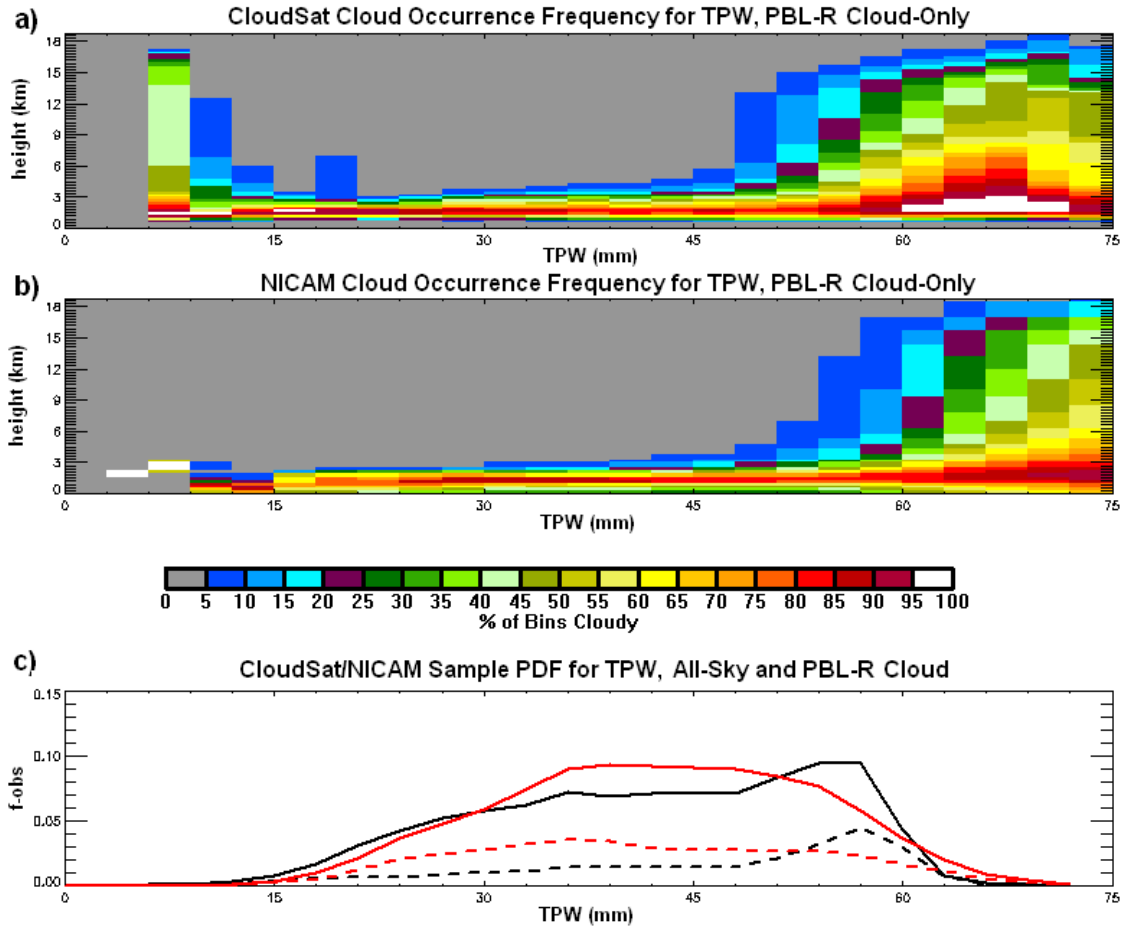

Figure 2.3. a) The vertical frequency of PBL-R cloud occurrence sorted by TPW for the observations; b) the vertical frequency of cloud occurrence sorted by TPW for NICAM; c) the number of samples per TPW bin normalized by the total number of all-sky samples for observations (black) and NICAM (red), in all-sky conditions (solid) and PBL-R conditions (dashed).

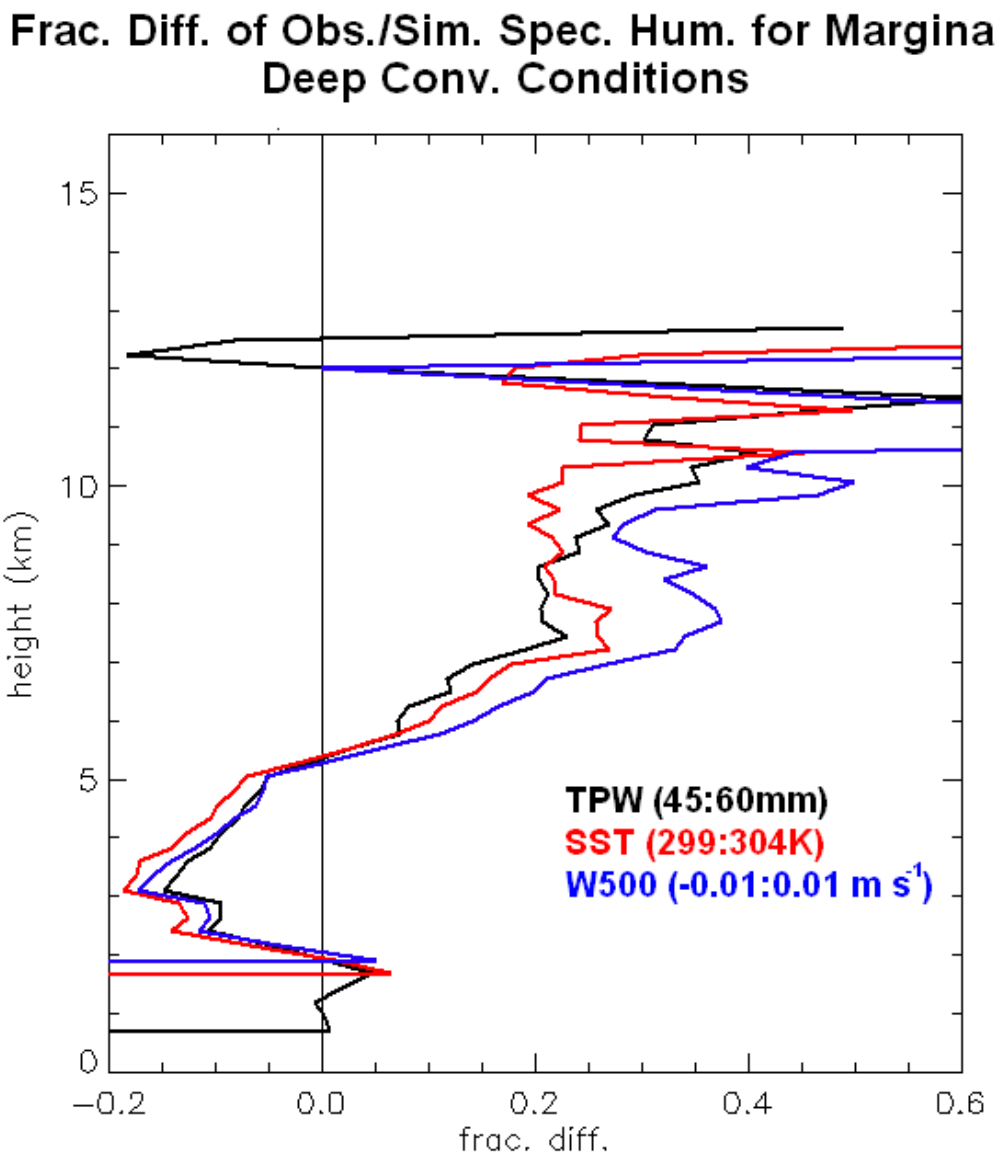

Figure 2.4. The fractional difference in vertical specific humidity profiles between "observations" (from ECMWF) and NICAM for environments marginally suitable for vertical convective development (as indicated by Figs. 3-5). The black line shows the average specific humidity profile for environments possessing TPW values between 45 mm and 60 mm. The red line shows the same for environments possessing SST values between 299 K and 304 K. The blue line shows the same for environments possessing W500 values between -0.01 m s^{-1} and 0.01m s^{-1}.

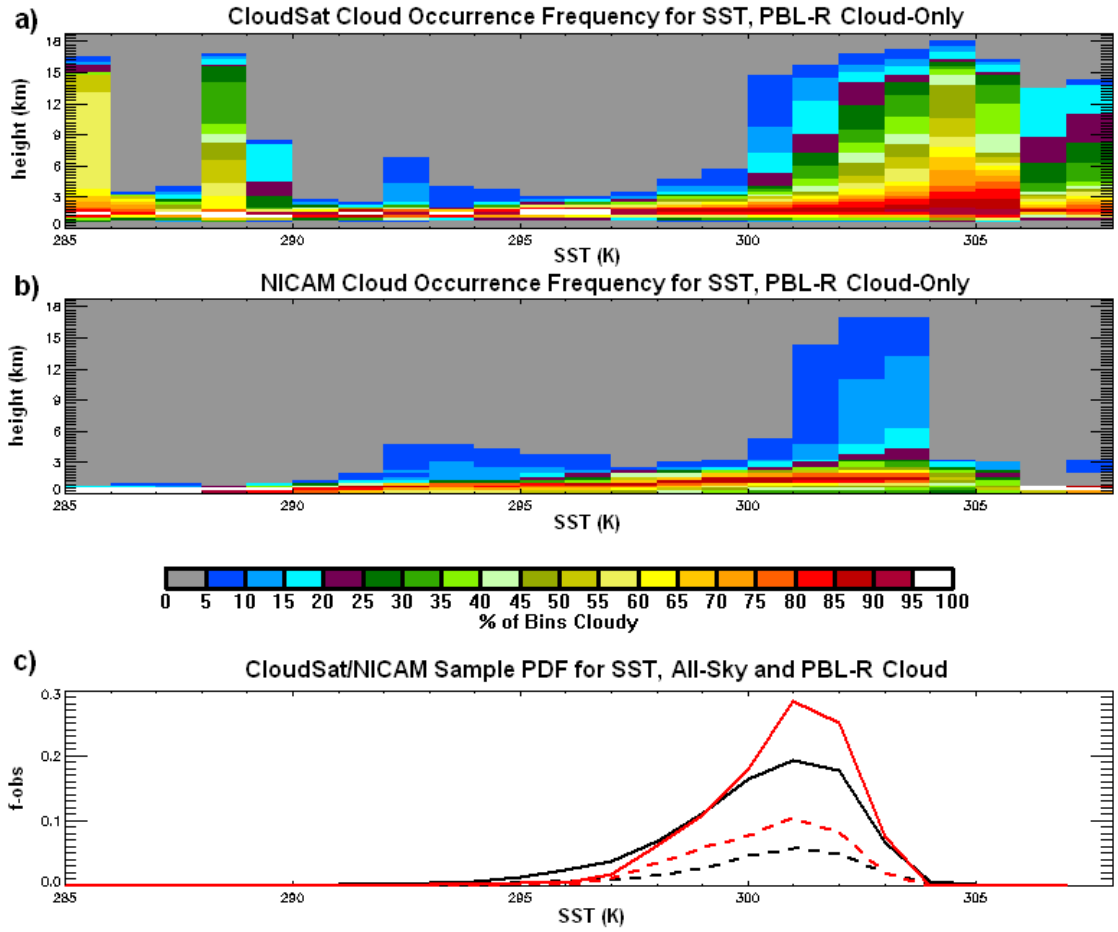

Figure 2.5. Same as Fig. 2.3, but for SST.

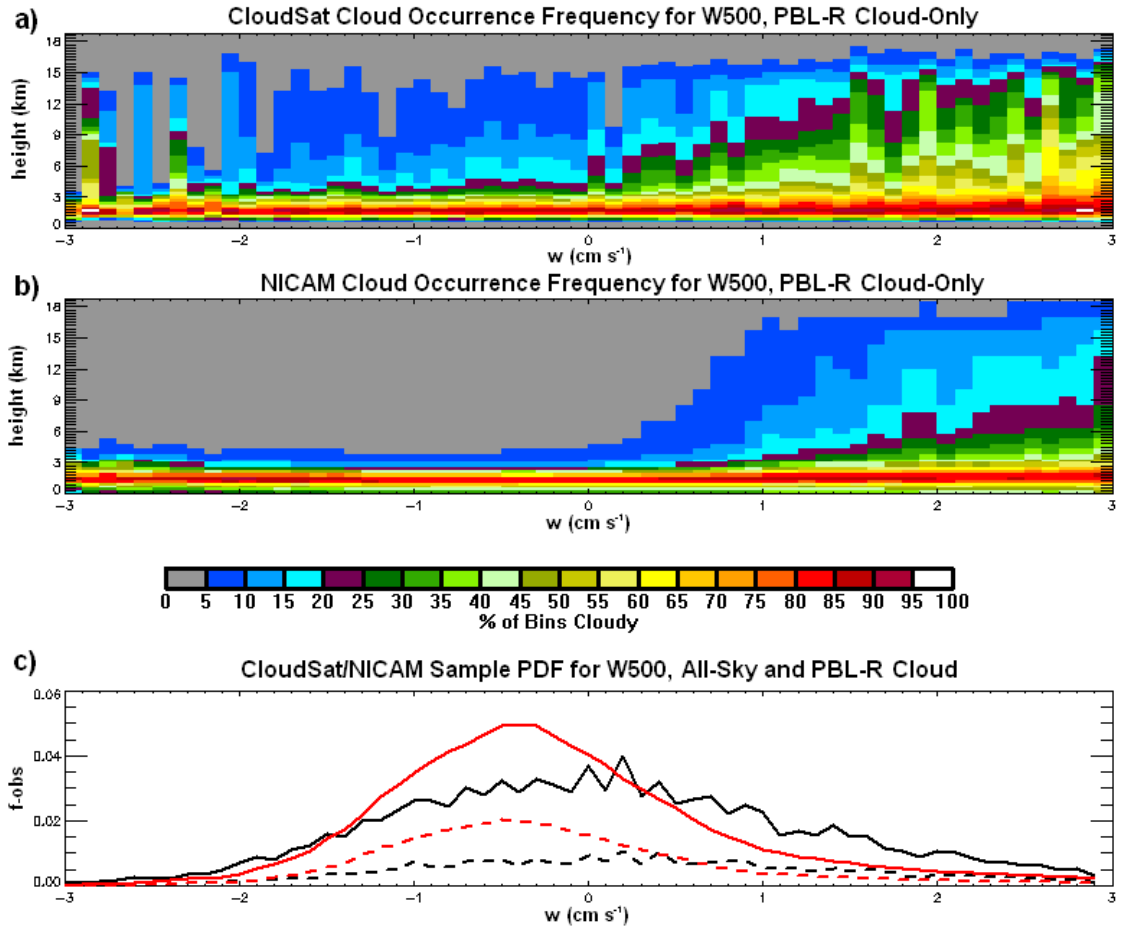

Figure 2.6. Same as Fig. 2.3, but for W500.

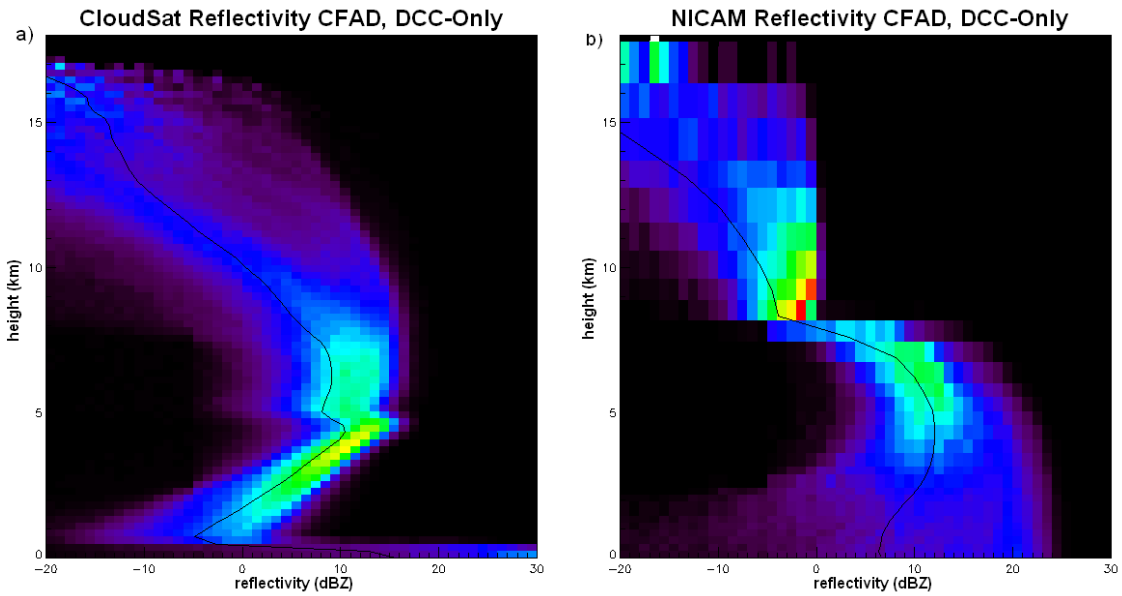

Figure 2.7. The DCC CFADs for (a) CloudSat and (b) NICAM. The black curves near the center of the data are the average reflectivity profiles for CloudSat and NICAM respectively.

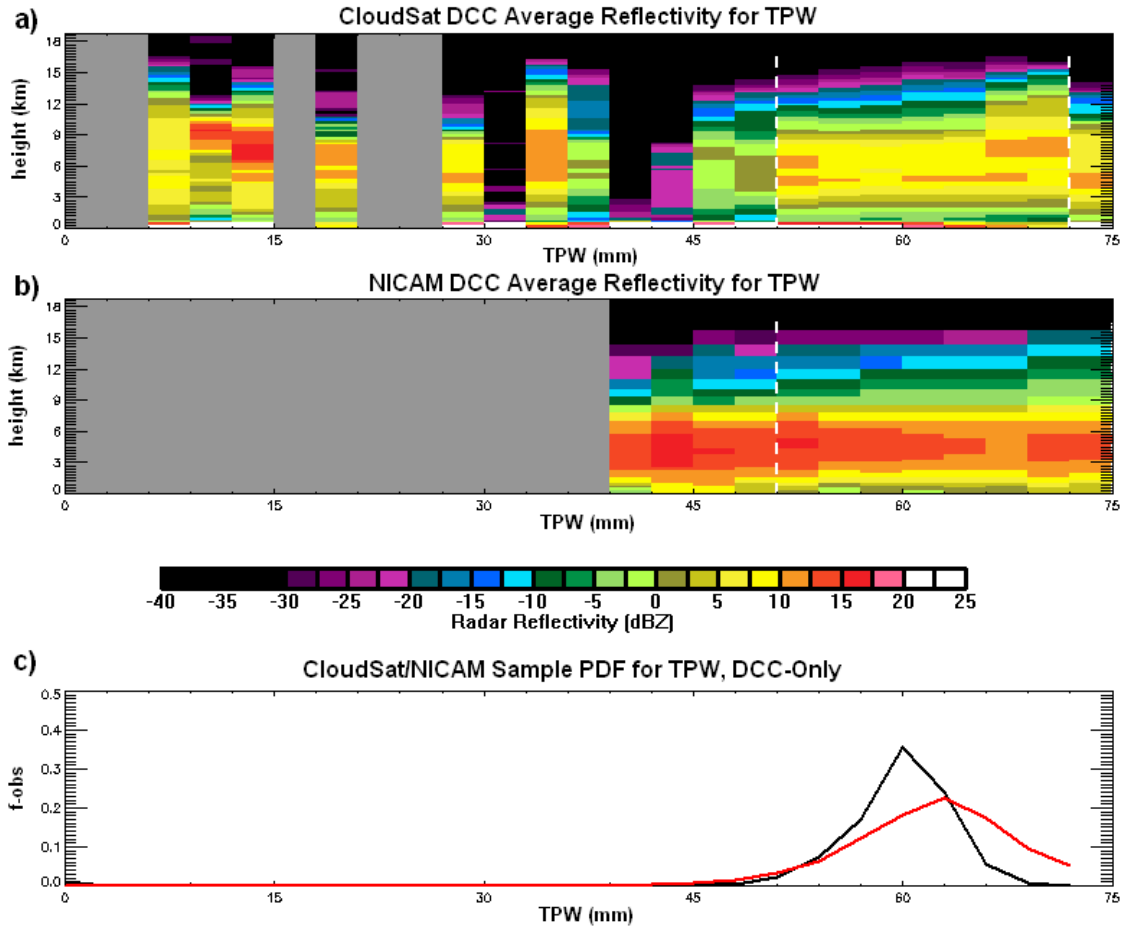

Figure 2.8. a) The average vertical profile of radar reflectivity for DCCs sorted by TPW for the observations, where the vertical dashed lines represent the 98% data range for which the trend line slopes and statistical significance values are calculated; b) the average vertical profile of radar reflectivity for DCCs sorted by TPW for NICAM; c) the number of DCC samples per TPW bin normalized by the total number of DCC samples for observations (black) and NICAM (red).

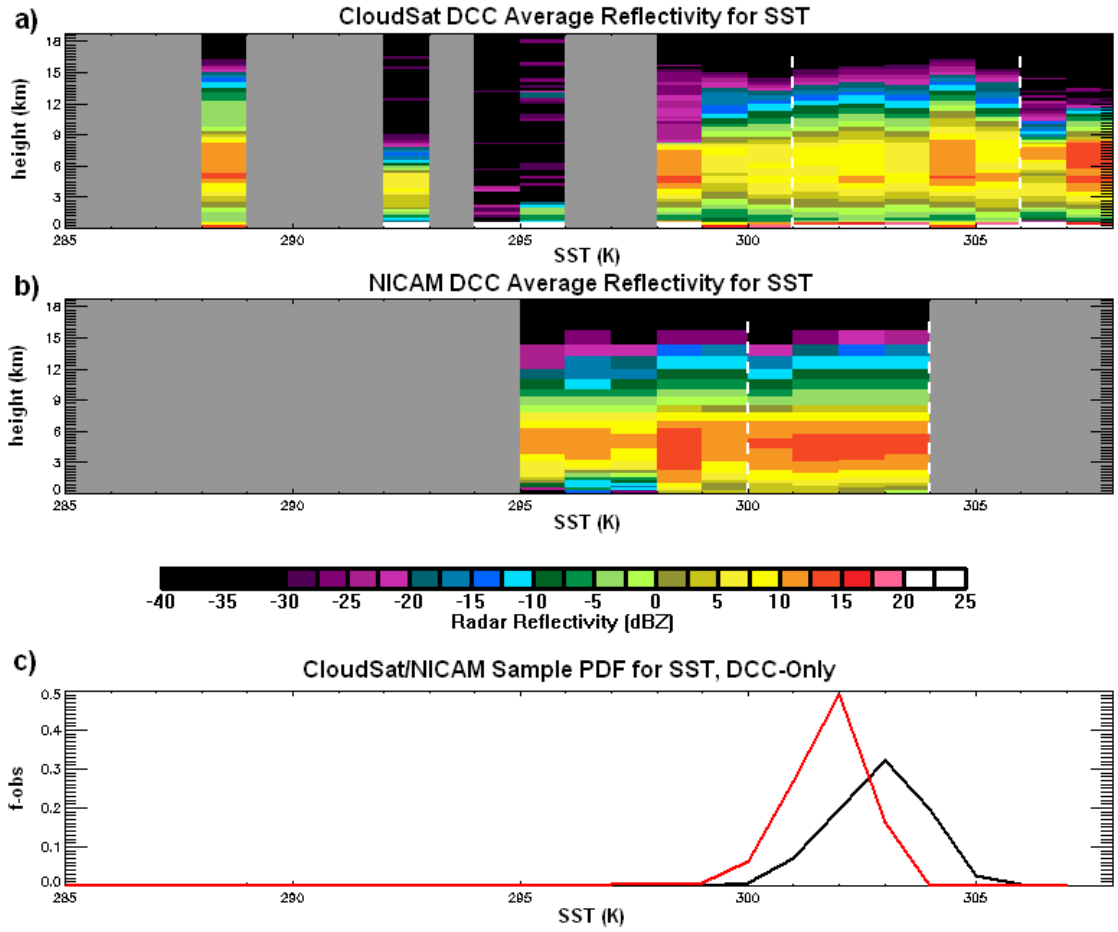

Figure 2.9. Same as Fig. 2.8, but for SST.

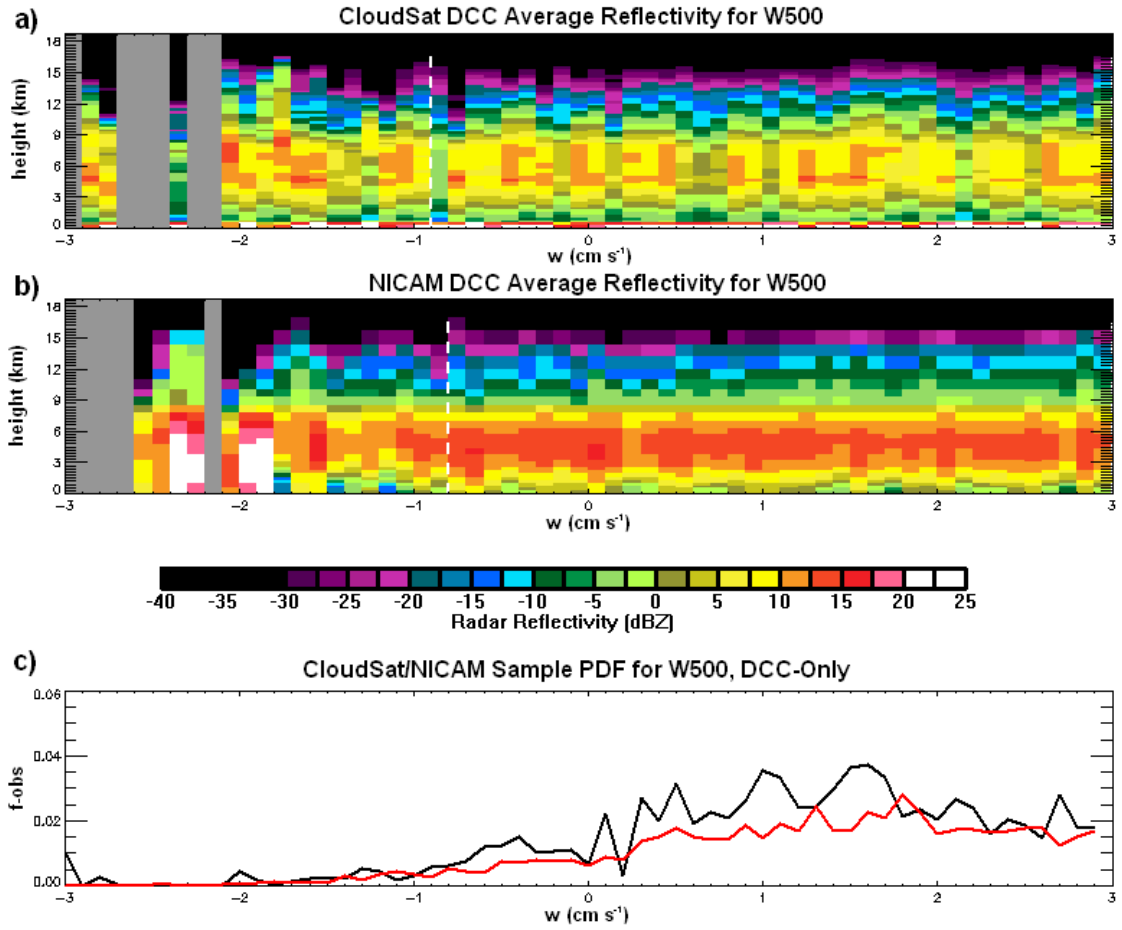

Figure 2.10. Same as Fig. 2.8, but for W500.

3. COMPARISON OF OBSERVED AND SIMULATED CUMULIFORM CLOUDS OVER THE CONTINENTAL UNITED STATES BY SPACEBORNE W-BAND RADAR, GLOBAL CLOUD-RESOLVING MODEL, AND MULTISCALE MODELING FRAMEWORK, PART 1: LARGE SCALE ENVIRONMENTAL VARIABLES

3.1 Introduction

Chp. 2 uses the conditional sampling technique to show the relationship between convective clouds and LSEVs (SST, TPW, W500). This was a continuation of research started several years ago to better characterize clouds and precipitation in the tropics. However, this methodology is not limited to the tropics. It can be applied to the contiguous United States (CONUS) as well, for example. Because CONUS has frequent DCCs during the summer, and because it is monitored by a relatively high-quality and reliable meteorological observation network, CONUS is an ideal location to test the models' abilities to realistically simulate DCCs.

3.1.1 Why investigate the United States?

The tropics are a common location for studying deep convection for several good reasons. The tropics cover half of the Earth, deep convection is frequent at all times of the year, convective systems can grow extremely large (over 1000 km diameter), they can penetrate the tropopause occasionally, and so on. This gives the tropics a very important role in various climatic processes such as cloud feedbacks and stratospheric moisture exchange. Convective systems are the primary weather perturbations in the tropics; they are the rain-makers. In contrast, the extratropics have large baroclinicly-driven perturbations that transport mass and energy horizontally and vertically. They produce much of the cloud cover, too. Nevertheless,

DCCs are a common occurrence over CONUS during JJA. Convective systems are the primary weather perturbations for much of CONUS during this time.

One of the primary motivations for this study is that deep convection over extratropical land has some important differences from convection over tropical ocean. Continental DCCs tend to have larger updraft velocities than oceanic DCCs. Oceanic DCCs have maximum updraft speeds rarely exceeding 10 m s^{-1} [Lucas et al. 1994], while CONUS DCCs have speeds often exceeding 10 m s^{-1}. There are several mechanisms responsible, which are discussed by Lucas et al. [1994], Lucus et al. [1996], and Michaud [1996]. To summarize: First, the depth of the planetary boundary layer (PBL) is usually greater over land than over ocean. Deeper PBLs generate larger turbulent eddies, which are often related with larger DCC core diameter. A larger core can resist the effects of dry air entrainment better than a smaller one. Second, convective inhibition tends to be stronger over land than the ocean. Counter-intuitively, stronger inhibition can lead to stronger convection by suppressing weaker DCCs, preventing them from consuming available CAPE before more vigorous convection can develop. Third, the CAPE vertical profile is different over land than ocean. Unlike what is commonly assumed, it is not necessarily true that increased CAPE over land causes the stronger convection. Rather, the deeper PBL over land, and the lower tropopause in the mid-latitudes, concentrates CAPE into a smaller vertical layer. While this does not affect the theoretical maximum updraft velocity (which is a function of total CAPE alone), it reduces the updraft's vulnerability to dry air entrainment by rapidly accelerating the buoyant air through the mid-tropospheric dry layer.

Because the mid-latitude continental environment is different in multiple ways from that tropical oceanic environment, it is necessary to examine the models' ability to simulate DCCs in

this area. CONUS is a desirable place to test the models because of the high frequency of DCCs during JJA, and because of the relatively high quality of and availability of observational data.

CONUS also has some interesting DCC-related meteorological features that are worth investigating. These include the North American Monsoon and the nocturnal maximum in convective precipitation over the Great Plains. These kinds of features are not unique to CONUS - there are other monsoons, and there is also a well-known nocturnal precipitation maximum in eastern Asia. But these features provide an additional way to test the realism of the models, in the same way that interest is given to simulating tropical convective features like the MJO and the Asian monsoon. The following is a brief description of the convective features in question.

Great Plains Nocturnal Maximum

A prominent observed convective diurnal feature is the nocturnal precipitation maximum over much of the Great Plains, which has an eastward propagation signature [Balling 1985, Riley et al. 1987]. During the warm season, the precipitation maximum along the central Rocky Mountains occurs during the middle to late afternoon. The precipitation maximum in the central Great Plains (western ND/SD/NE/KS) occurs around midnight, and the maximum in the eastern Plains occurs in early morning. Case studies show that this eastward shift often (though not always) occurs in the form of mesoscale convective systems (MCSs) generated by the afternoon mountain convection traveling eastward for several hours through the night [Cotton et al. 1983, Wetzel et al. 1983]. The nocturnal maximum was identified early in the 20th century [Kincer 1916], and was first rigorously characterized by Riley et al. [1987], who used 35 years of hourly precipitation gauge data across the central Rocky Mountains and Great Plains to examine the diurnal precipitation variability. Subsequent analyses using radar and satellite observations have

verified this result [Carbone and Tuttle 2008]. The diurnal variability in total precipitation rate appears to be controlled mostly by precipitation frequency. The maximum precipitation intensity appears to vary relatively slightly with the time of day.

It should be noted that nocturnal convection is not the sole factor in convective diurnal variability for the Great Plains. During the warm season, the Great Plains often experiences afternoon convection associated with local solar heating. This form of convection is often associated with severe weather. Riley et al. [1987] found that the diurnal occurrence frequency for the heaviest precipitation rates (2.5 mm hr^{-1}) maximizes one to four hours before occurrence frequency for all precipitation rates. So the nocturnal maximum is not driven purely by DCCs alone, but also the stratiform precipitation resulting from MCSs.

There does not appear to be a single simple explanation for the nocturnal maximum and its eastward propagation [Carbone and Tuttle 2008]. Perhaps the most intuitive explanation is MCSs being triggered by mountain convection and moving eastward for several hours into the night. But this does not fully explain the observed diurnal pattern. The most obvious problem with this explanation is that it requires MCSs to travel much faster than they are typically observed to do. For example, KS is about 670 km in longitudinal extent. Riley et al. [1987] show a precipitation maximum at the western KS border at approx. 11pm local time, and a maximum at the eastern border at approx. 5am. For a single MCS, this requires a total average movement speed of approx. 110 km hr^{-1} (30.5 m s^{-1}), which is at the very upper range of observed MCS movement speed [Corfidi et al. 1996]. Other analysis techniques used by Riley et al. and others confirm that the early morning precipitation maximum in the eastern Great Plains is not simply a result of long-lived MCSs moving eastward, but also a result of locally-occurring precipitation. However, local surface and PBL forcing cannot be a cause, because their contributions to daily convective

destabilization and inhibition are observed to occur almost entirely out of phase with the observed convective diurnal cycle [Zhang 2003]. Non-local forcings must be the cause. Not only do the observations support this, but modeling studies have also reached this conclusion [e.g. Zhang 2003].

Multiple other explanations have been posited, which include mountain/plains circulations, gravity wave propagation, and the Great Plains LLJ. First, solar heating tends to produce a mountains/plains solenoidal circulation over the Rocky Mountains/Great Plains [Wolyn and McKee 1994]. During daytime, solar heating causes enhanced rising motion over the Rocky Mountains, and thus shifts the region of preferred convection westward. During nighttime, a combination of radiative cooling of the mountains and radiative cooling of the upper troposphere enhances rising motion, and thus convection, over the Great Plains. Dai et al. [1999] examined this behavior using NCEP/NCAR reanalysis data. They found a spatial pattern of diurnal pressure variability across the region. Reanalysis data show the pressure across most of CONUS reaching a minimum at 6pm local time. In universal time, this means the pressure minimum over the Rocky Mountains occurring approx. 1 hr before the Plains minimum. Also, the magnitude of the diurnal cycle over the Rockies is much larger than the magnitude over the plains. These effects combined produce an eastward (low to high) pressure gradient across the Rockies/Plains during the afternoon, and a westward gradient during the midmorning. This pressure distribution is associated with enhanced rising motion over the Rockies and enhanced subsidence over the Plains during the afternoon, and vice versa during the morning. Such diurnally-varying solenoidal circulations exist elsewhere, for example over China. There is evidence from simulation that the circulation alters the regional convective diurnal cycle over portions of China as well, along the mei-yu front [Sun and Zhang 2012].

Second, the Great Plains LLJ can enhance nighttime plains convection through moisture transport and enhanced low level convergence [Higgens et al. 1994]. The LLJ, which is stronger at night, rapidly advects warm moist air from lower latitudes to the Plains region, which helps maintain the convective instability necessary to support nocturnal MCSs. Also, the LLJ tends to turn eastward over the central Plains, creating a convergence zone and thus further enhancing nocturnal MCSs. Of course, the LLJ and the mountains/plains circulation are not entirely independent of each other, and they are not entirely independent of the precipitation they trigger. Pressure tendencies from the mountain/plains solenoid and convective systems can enhance the LLJ, which transport more moisture into the active convective, which alters the regional pressure tendency, etc.

North American Monsoon

The southwest region of North American experiences an annual monsoon, which is associated with a regional precipitation maximum beginning in July and lasting until mid-September [Adams and Conrie 1997]. The monsoon is driven by a thermally-induced low pressure region over central Mexico and the US southwestern desert. During the wet season DCCs are frequent, as is stratiform precipitation and terrain-induced precipitation [Higgins and Gochis 2007]. The moisture flow into the NAM region is generally not continuous, but episodic, commonly (but not always) associated with moisture surges traveling northward from the Gulf of California [Stensrud et al. 1997]. The monsoon is responsible for the majority of the precipitation received in the southern portion of the affected regions, though to the north the relative contribution of the monsoon decreases as latitude increases.

The central monsoon region also experiences a diurnally propagating precipitation signal linked with topography [Becker and Berbery 2008]. In western Mexico, the Sierra Madre Occidental mountain range provide a focus for convective initiation during the local early afternoon (similar to the Rocky Mountains). This convection leads to the development of MCSs which then move westward for the next several hours into the Gulf of California, at a typical rate of ~5ms^{-1}. Unlike the Great Plains nocturnal maximum, this westward movement is associated with a nocturnal maximum of CAPE over the Gulf, which helps to maintain the deep convection. Like the Great Plains nocturnal maximum, the westward movement is also associated with a nocturnal maximum of moisture convergence over the Gulf. The distinct westward propagation occurs in a latitude belt of 20°N to 30°N, and does not occur in Arizona.

The Arizona portion of the NAM region experiences a different diurnal cycle based on different mechanisms. Like the Great Plains nocturnal maximum, the Arizona diurnal cycle is connected with a southerly LLJ which transports moisture into the region. This jet tends to intensify during the local late afternoon, when surface heating in Arizona induces a meridional pressure gradient. Hence, this combined with increased CAPE from solar heating leads to the diurnal precipitation cycle maximizing in late afternoon/early evening. However, there is another important mechanism that strongly influences Arizona precipitation: episodic moisture surges from the Gulf of California. These surges are thought to be triggered by tropical easterly waves and cyclones, which generate a cool moist air mass at the mouth of the Gulf [Fuller and Stensrud 2000]. The resulting lower tropospheric pressure gradient enhances moisture flow into Arizona. The surges can be strengthened by coincident midlatitude disturbances, which further enhance the southerly flow into Arizona. In both model simulations and observations these surges are associated with over half of the total precipitation in Arizona, despite being present less than half

of the time. These surges appear to amplify the existing diurnal precipitation cycle in Arizona, rather than alter the timing. The diurnal cycle of both CAPE and moisture convergence are amplified during surge events, leading to increased precipitation.

3.1.2 Purpose

The main goal of this chapter is to examine the behavior of the LSEVs in reality and the models, and to identify any major unrealistic behaviors of LSEVs in the models. The climatological cloud behavior over CONUS (or any other region) can be broken down into parts: the relationship between cloud and environment, and the frequency of each environment in the region. Chp. 3 seeks to address the latter part, and Chp. 4 addresses the former. In order to understand difference in cloud behavior between observations and different models, we must first understand the differences in environments in which the clouds occur.

3.1.3 Main Questions

The general and specific questions this chapter seeks to answer are the following:

1. How realistically do the models simulate the typical JJA climate over CONUS?
2. Are there significant general biases in temperature, humidity, and circulation?
3. Are there significant regional biases?
4. Are these biases dependent on time of day?
5. Can these biases be explained by observed inter-annual variability?
6. How realistically do the models simulate the diurnal cycle? Magnitude and timing?
7. How realistically do models simulate terrain effects on LSEVs?
8. Are these answers strongly dependent on the observational or reanalysis data used?

3.1.4 Chapter overview

In this chapter I will address these questions using four different analyses of the model and reanalysis data. First, the mean LSEV spatial fields for the CONUS region during JJA will be presented, including the differences between the model and reanalysis fields. Second, I will examine the diurnal cycle of LSEVs for CONUS using planar maps of the diurnal range (the difference between maximum and minimum at each grid point) and the time of the diurnal maximum (the time of day that the maximum in each grid box occurs). Third, I will examine the diurnal cycle for specific subregions of CONUS, using line plots of model, reanalysis, and GPS observational data. This will reveal where certain assumptions about the diurnal cycle (such as its sinusoidal shape) are less realistic. Finally, I will examine a couple of potential causes of disagreements between model and reanalysis. These potential causes are unrealistic model simulation of surface heat fluxes, and unrealistic relationships between terrain elevation and LSEV variability.

3.2 Data and methodology

3.2.1 Data sets

The LSEVs used in Chps. 3-5 are surface air temperature (SAT), TPW, and W500. SAT is used instead of land surface temperature because SAT more closely reflects the link between the surface and atmosphere. SAT is difficult to estimate over remote oceans (SST is much easier to measure remotely), but the dense observational network in CONUS makes the SAT estimates more reliable. In addition, the surface sensible heat flux (SHTFL) and latent heat flux (LHTFL), and net top of the atmosphere shortwave (SWNTOA) and longwave (LWNTOA) will be used briefly.

Five datasets are used in this chapter: The North American Regional Reanalysis (NARR), the NCEP/NCAR Reanalysis (N/NR), SP-CAM, NICAM, and SuomiNet Global Positioning System data. NICAM and N/NR were discussed in Chp. 2, so only the relevant changes will be described here. The other three datasets will be described in detail.

3.2.1.1 NARR Description

The North American Regional Reanalysis (NARR) is an extension of the N/NP. The goal of the project is to provide higher resolution (in time and space) data with higher accuracy for North America and the surrounding regions. Particular attention was given to improved representation of the water cycle in the atmosphere and land. This improvement should be helpful for this project because of its focus on clouds – even if I don't use the cloud and precipitation variables, there will still be benefits for TPW (which is affected by precipitation), and smaller benefits for SAT and other meteorological variables. The temporal resolution is three hour, which is double the resolution of N/NP. This will help in better co-location in time of CloudSat observations and reanalysis data. The spatial resolution varies with location, but is roughly 0.3°, a major improvement over N/NR's 2.5° resolution.

One main improvement of NARR is the inclusion of new data sources. The precipitation data are taken from the CPC Hourly Precipitation (CPCHR) dataset (derived from rain gauges). I use this precipitation dataset directly in the next chapter, and will discuss it in more detail there. Outside of the CPCHR domain, precipitation data are taken from the CPC Merged Analysis of Precipitation (CMAP) six hourly, 2.5° resolution dataset. Radiance data from TIROS Operational Vertical Sounder (TOVS)-1b is assimilated directly into NARR, which removes the need for separate satellite observations of temperature. Improvements were made to the

assimilation of surface observations (temperature, wind, and moisture), and detrimental observation types were removed. In addition, data for snow/ice and SST were added or improved.

Aside from input data, the Eta model component was also improved. In particular, the Noah land surface model was altered in order to better assimilate hydrological data and represent surface processes. When archiving the data for public use, the reanalysis output is remapped from the native Eta grid of 32 km horizontal resolution to a Lambert conformal conic of similar horizontal resolution. This remapping can cause problems for horizontal wind data, but thermodynamic data and vertical wind data averaged over 2.5° should not be affected much.

Because of the improved representation of CONUS over N/NP, and because of higher temporal and spatial resolution, I choose to replace N/NP with NARR for the investigations involving CONUS regions. The meteorological fields of interest are SAT, TPW, W500, surface sensible heat flux, and surface latent heat flux. The latter two will be helpful in explaining why (or why not) the meteorological variables in SP-CAM and NICAM are unrealistic – SAT in particular will be influenced by errors in surface heat fluxes. The higher temporal resolution will be useful in better characterizing the real diurnal cycle, to compare with those of SP-CAM and NICAM. The higher spatial resolution will be helpful for investigating the influence of data resolution on the relationship between terrain and meteorological variables – N/NR has too coarse resolution for this task.

3.2.1.2 N/NP

N/NP remains unchanged from Chp. 2. Because it is the parent version of NARR, I have replaced N/NR with NARR for most applications in Chps. 3 – 5. I use N/NP briefly in this

chapter to compare with NARR in how they represent the relationships between LSEVs and terrain elevation.

3.2.1.3 SuomiNet

SuomiNet is a collection of ground stations across the US that measure meteorological variables, notably TPW, using Global Positioning System (GPS) satellite signals. The signals are affected by multiple atmospheric variables (not all meteorological), and these effects can be used to estimate those variables [Rama Varna Raja et al. 2008]. There are multiple hundreds of stations across the US, and the first ones began operating in 2007. The temporal data resolution is 30 min, though data gaps at individual stations are a somewhat frequent problem. It should be noted that these observations are effectively point measurements. While the satellite beams usually pass through the atmosphere at a non-normal angle (on average about 65° zenith angle), the presence of multiple satellites overhead (usually the case) can be used to correct for the non-normal angle. This makes SuomiNet measurements different from GPS occultation measurements, with the latter being more of a swath measurement than a point measurement. The point measurement nature of SuomiNet means that the data are affected by the usual limitations of point measurements, e.g. influences by locale.

The primary atmospheric effect on GPS satellite beams is beam refraction caused by the ionosphere. The magnitude of refraction is great enough to cause problems for position detection, let alone meteorological measurements. So the GPS satellites broadcast at two different frequencies, which are used by the receivers to identify and correct the ionospheric effects. After this, the atmospheric effect (effectively a signal delay) can be decomposed into a moist effect and dry (or hydrostatic) effect. The dry effect can be calculated using the station

latitude, elevation, and surface pressure. The moist effect is simply the residual. Because the satellite beam usually comes at a 65° zenith angle, the station "point" measurement actually represents an inverted cone beginning at the station and having a radius of 11 km at 5 km altitude (more or less the top of the moist layer). Compared with traditional GCM horizontal resolution, the GPS station measurement is effectively a point measurement. This is not quite the case for finer res. models like CRMs. But with the spatial averaging used in this thesis to compare different datasets, the GPS data are still effectively point measurements.

This thesis uses about two dozen stations to represent different regions in CONUS and northwest Mexico. Table 3.2 lists the station information. As a compromise between the limited temporal data availability and the desire for a robust multi-year climatological diurnal cycle, I only include stations which have at least two full JJA seasons of data. There are no rigorous criteria for selecting specific locations, but for each CONUS subregion I try to pick stations scattered across the subregion, as opposed to all being in only one part of the subregion.

3.2.1.4 SP-CAM version 4

SP-CAM is a Multi-Scale Modeling Framework (MMF), meaning a model which uses multiple spatial scales during operation. SP-CAM consists of two components: a low spatial resolution GCM of the traditional type, and a higher spatial resolution two-dimensional CRM. The CRM essentially replaces the convective parameterization scheme of the GCM.

The main inputs for the model are the atmospheric initial values, prescribed SST boundary values, and other assorted boundary values for topography/aerosols/ozone/etc. The SST climatological values for the early 21st century are supplied by NCAR. The greenhouse gas concentration and radiative effects are also chosen to represent the early 21st century.

For Chps. 3 and 4, I use an SP-CAM run that includes a single JJA period. The time domain is 1 June through 31 August. The following is a description of the model setup for Chps. 3 and 4. This subsection describes the model setup for SP-CAM version 4 (SPv4), with single-moment microphysics. The model setup that includes the double-moment microphysical scheme is slightly different, and will be described in the following subsection.

CAM

The GCM used in SP-CAM for the single moment microphysical scheme is based on the atmospheric component of the NCAR Community Climate System Model version 4 (CCSM4), the Community Atmospheric Model version 4 (CAM4). The horizontal resolution is 2.5° by 2.5°. The vertical resolution is dependent on the height above the surface. It ranges from approx. 150 m near the surface (to better represent the PBL) to approx. one kilometer at the tropopause, to five kilometers in the lower stratosphere. There are 26 vertical levels. The timestep is 600 s (10 min). The prognostic meteorological values are the horizontal wind components, potential temperature, specific humidity, and pressure thickness.

CAM4 uses a Lin-Rood finite volume dynamical core, which was changed from the spectral core used in previous versions of the model. This dynamical system functions similarly to a shallow water system, with a quasi-hydrostatic equation system, but with the addition of thermodynamical and pressure gradient elements. The vertical coordinate is the σ-p hybrid coordinate, which follows the terrain in the lower troposphere and transitions to the pressure coordinate in the upper troposphere. However, the calculation method used by the Lin-Rood method allows the vertical coordinate surfaces to adjust in height during each model time step (and are regridded afterwards), which is part of maintaining the “finite volume” between two

surfaces. These are called “Lagrangian surfaces”, and they allow for the use of a Lagrangian vertical transport scheme. The horizontally-oriented processes are handled with an Eulerian method in physical space (no spectral transforms). A semi-implicit time integration scheme is used to limit the effects of unstable gravity wave activity.

The parameterization schemes in CAM4 are divided into four categories: moist processes, radiation, surface physics, and turbulence. The moist processes are divided into convective and larger-scale prognostic condensation and precipitation. SP-CAM replaces several of CAM4’s parameterization with the CRM. This includes the deep convective, shallow convective, and boundary layer schemes. In addition, the ocean and sea ice coupled models are removed, and climatological values are used instead. The land model, the Community Land Model 4 (CLM4), is still included, as is the stratiform cloud model and the Bulk Aerosol Model (BAM).

CRM

The CRM is based on a version of the Cooperative Institute for Mesoscale Meteorological Studies (CIMMS) LES, modified for use in SP-CAM. The CRM is a two-dimensional model with periodic boundary conditions. The horizontal resolution is four kilometers, and the horizontal domain is 32 grid boxes wide. 24 vertical levels are used, which correspond to the lowest 24 levels (out of 26) of the GCM. The staggered Arakawa C-grid is used, where velocity components are defined at the edges of each grid box, and the other state variables are defined in the center. The time-step is 20 s. The prognostic meteorological variables are wind velocity, liquid/ice moist static energy, non-precipitating water mixing ratio (water vapor + cloud liquid + cloud ice), and precipitating water mixing ratio (rain + snow + graupel).

The CRM uses anelastic approximations of the primitive equations of motion. The vertical coordinate is simply physical height (z). Momentum advection is calculated using a second-order finite difference method. Other quantity advections are handled by a non-oscillatory multidimensional positive definite advection transport algorithm proposed by Smolarkiewicz and Grabowski (1990). Newtonian damping is applied in the lower stratospheric layers to reduce spurious gravity wave effects.

The subgrid-scale model used is based off of the one used in the CIMMS LES, and is similar to the 1.5-order closure scheme used by Deardorff [1980]. Surface fluxes are calculated by applying Monin-Obukhov similarity theory to the surface. This methodology calculates the fluxes as a function of near-surface turbulence generated by vertical wind shear and buoyancy. The radiation scheme, CAMRT, is taken from the CCM3, and is calculated for each vertical column in the horizontal domain. The scheme is calculated only every few minutes (using meteorological quantities time-averaged over the period), because of the large computational expense of each calculation. Cloud water is included in the calculation, but not precipitation.

The single-moment bulk microphysical scheme has five categories of hydrometeors: cloud liquid, cloud ice, rain, snow, and graupel. Cloud water (liquid plus ice) is generated by all water vapor in excess of saturation – supersaturation is not allowed. The saturation vapor pressure is determined by a linear combination of the liquid and ice saturation pressures. The mixture of liquid and ice phases is a function of temperature only. No size distributions, habits, or shapes of the cloud hydrometeors are assigned by the scheme – only the mixing ratios are represented. Cloud ice is allowed to sediment. The drop size distribution of precipitation is calculated with the Marshall-Palmer distribution. Precipitation particles are allowed to form through autoconversion

of cloud water, to grow through collection of cloud water by existing precipitation, and to shrink through evaporation. Accretion of water vapor is not considered.

There are no cloud parameterization schemes in the CRM. The 4 km horizontal resolution limits the CRM's ability to realistically simulate smaller convective clouds, and the limited vertical resolution limits the CRM's ability to simulate PBL-top clouds (where strong vertical gradients of temperature and moisture, important for these clouds, are hard to represent with even 150 m resolution). Larger convective clouds should be simulated more realistically because the spatial scale better matches the CRM's resolution. It should be noted that a 4 km horizontal resolution cannot capture the sub-cloud eddies and turbulent motions for even a DCC. This will cause an inherent limitation of the CRM to simulate deep convection realistically. However, several studies have found that models cannot realistically resolve these smaller eddies until the horizontal resolution approaches approx. 100 m (with an appropriate vertical resolution adjustment). Until the time that 100 m resolution models become feasible, a 4 km resolution model should represent the larger clouds almost as well as models with 1-2 km resolutions.

Unfortunately, because of the 2D nature of the CRM, it cannot simulate some of the more complex convective behaviors, such as bow echoes and supercells. However, larger convective features (e.g. MCVs) can be simulated through the interaction of the CRMs and GCM. This will be discussed in the next section.

CAM/CRM connection

Each separate CAM grid box is assigned a separate CRM to take the place of cloud parameterization schemes. This means that there are 13,824 CRMs running simultaneously with the CAM (which possesses 144 x 96 horizontal grid boxes). Each CRM runs continuously with

the assigned CAM box – the CRM is not restarted for each CAM time step. Rather, during a CAM time step, the CAM "nudges" the CRM's prognostic variables towards the CAM's current condition. This is done through applying the CAM's advection terms to the CRM's prognostic equations. The CRM then runs until the next CAM timestep, where the CRM's prognostic variables are passed back to the CAM in a way similar to how a conventional parameterization scheme would. So the CAM and CRM cannot diverge over time, even though neither is restarted.

It is important to note that the CRMs do not directly communicate with each other. They can only communicate indirectly through influencing the associated CAM grid boxes, which will (theoretically) allow one CRM to influence another. This ability is very important for simulating certain propagating meteorological features like mesoscale convective systems, a common occurrence over CONUS during JJA. Earlier SP-CAM versions had difficulty with this, probably because of the spectral dynamical core used by CAM. The spectral physics would smear out the mesoscale systems so that the propagation mechanisms did not work. But Prichard et al. [2011] showed that an updated SP-CAM with the finite volume dynamical core succeeded in representing propagating convective systems over the Great Plains. The simulation was not perfect, though. Certain important aspects of MCSs like gravity waves and low-level outflow boundaries cannot propagate properly in SP-CAM because the CRMs that resolve these features do not communicate directly. This effectively traps these features in one grid box. Still, propagating meteorological features is a source of difficulty in many GCMs, and the ability to simulate them at all with an MMF approach represents an improvement.

For this study, I obtained data for one JJA season simulated with early 21st century climatology. The data has 2.5° by 2.5° horizontal resolution, and three hour temporal resolution. SAT is calculated from the air temperature at the lowest model layer; it should be noted that this

is not precisely the same as NARR's 2 m air temperature, but it is the closest value available. SAT and TPW are taken from the CRM-level data, and averaged over the one-dimensional horizontal domain. Because of the way the CRM exchanges information with the CAM, the CRM-level mean SAT/TPW is the equivalent to the CAM SAT/TPW. W500 is taken from the CAM-level data.

3.2.1.5 SP-CAM version 5

This chapter will also use SP-CAM version 5 (SPv5). In this version, the primary modification is the change in microphysics from a single moment scheme to a double moment scheme. The single moment scheme only predicts hydrometeor mixing ratio, while the double moment scheme predicts mixing ratio and number concentration. In addition to the microphysics, the radiative transfer scheme has also been changed. Otherwise, the model setup is the same as described in Chp. 3.

The double moment microphysical scheme is based on the scheme presented by Morrison et al. (2005). They originally used four hydrometeor species, but Morrison et al. 2009a updated the scheme with the five species used in SP-CAM. They developed a scheme which predicts mass mixing ratio and number concentration based on Kohler theory, instead of a simple conversion of all supersaturation to hydrometeors like the single moment scheme. Also, ice crystal nucleation processes are represented, both homogeneous and heterogeneous, again different from simple freezing of supersaturation. The changes in droplet size distribution are dependent on the grid-scale vertical velocity and the subgrid scale turbulence. The DSD influences certain microphysical processes like collision-coalescence and contact freezing, and so it is useful to prognose rather than assume. There are also processes that are allowed to vary based on number

concentration, such as sedimentation rate and autoconversion rate. Aerosol concentration is predicted on the GCM level, and aerosol loss from hydrometeors is not represented.

It should be noted that the double moment scheme in SPv5 is not an evolution of the single moment scheme in SPv4. The Morrison et. al scheme was developed independently of the SPv4 scheme, and does not use the same basic assumptions and approximations of the physics. So it will not be possible to do a "pure" single moment versus double moment comparison. The comparison presented here is the best that can be done with the SP-CAM models available at the time of this writing. Perhaps in the future it would be worthwhile to replicate the analysis presented here, but using SP-CAM (or perhaps just the offline CRM) with different double moment microphysics to see the effect on convective characteristics.

The hydrometeor fields are processed through the Quickbeam radar simulator using the same assumptions for hydrometeor distribution as the single moment data. This was done so that the one moment and two moment results could be compared more directly without introducing additional differences from Quickbeam itself. In the future, when comparing different double moment simulations, it would be useful to update Quickbeam's assumptions to more closely match the actual microphysics in the model.

As noted, both the microphysics and the radiation schemes have changed. This means that unfortunately it is not possible to completely attribute differences between SPv4 and SPv5 to the change in microphysics. However, an examination of the mean radiative fluxes at the top of the atmosphere and surface reveal that flux differences between SPv4 and SPv5 are only a few W m^{-2} different at most. The largest difference exists for shortwave net TOA flux, with 330.6 W m^{-2} for SPv4 and 342.4 W m^{-2} for SPv5. Of course these differences are not just dependent on the

radiation scheme, but also dependent on clouds, and thus the microphysics. But it is apparent that the change in radiative scheme has not greatly altered the radiation budgets.

3.2.1.6 NICAM

The NICAM run used in this chapter is similar to the run used in Chp. 2. This run was used as a part of a NICAM boreal summer experiment, which sought to simulate the 2004 boreal summer [ref]. The experiment included a six month run at 14 km horizontal resolution, and a three month run at 7 km horizontal resolution. I use the 7 km run for Chp. 3 and 4. The microphysics scheme used for this run, the Grabowski scheme, is the same as that used for Chp. 2. The time domain for the 7 km run is 1 June 2004 through 31 August 2004, and I use the entire time domain.

3.2.2 Methodology

In order to facilitate better comparisons between different datasets, the higher horizontal resolution datasets (NARR and NICAM) have been degraded to the 2.5° x 2.5° resolution of SP-CAM. The method involves averaging all NARR/NICAM pixels that are within 1.25° of the center of an SP-CAM box. This allows the model maps to be directly subtracted from the NARR maps to better illustrate the differences. This has the side effect of removing local warm and cool regions (e.g. individual mountain ranges). But these local regions can still influence the degraded-resolution maps, and can cause some large differences between the reanalysis and models (e.g. NICAM's cool bias over the western mountains).

I present three types of planar maps for the LSEVs here: mean values, diurnal range of values, and the time of maximum value. The mean value maps are calculated simply by taking

the mean value of the LSEV during the desired time domain at each grid box. The time domain could be all times of day during JJA, or a specific time of day during JJA, or the time of day when the maximum or minimum LSEV value in the diurnal cycle occurs. The diurnal range is calculated by first taking the mean LSEV value for each grid box at every time of day. For SP-CAM, for example, that means calculating eight values for each grid box; one at 00z, one at 03z, etc. Then, from those means, the maximum and minimum mean are identified and differenced. This gives the diurnal range for that grid box. Finally, the time of diurnal maximum is calculated as the time of day when the maximum value identified previous occurs. No sophisticated techniques involving sine curve-fitting, or spatial smoothing and such are used here. This means unfortunately that noise can influence any apparent spatial patterns in diurnal cycle (particularly in the timing). But this approach allows the data to be shown as they are, without forcing them to conform to assumptions like having a sinusoidal diurnal cycle.

Throughout Chps. 3 – 5, CONUS will be divided into multiple subregions in order to more closely examine the data. These subregions are identified here: eastern CONUS (ECONUS), western CONUS (WCONUS), western mountains (WMTN), North American monsoon region (NAM), Great Plains (GPLN), and Mississippi Valley (MSVL). Each of these subregions contain frequent DCCs occurring in different climatological environments, so it will be useful to compare/contrast the behavior of DCCs and LSEVs in these subregions. Table 3.1 gives the coordinates for each subregion, and Fig. 3.1 shows the subregions on a planar map.

3.3 Planar Maps of LSEVs over CONUS

The conditional sampling technique used in Chps. 2 and 4 display the variability of the LSEVs as PDFs taken across the entire spatial domain. In order to give a better sense of the

variability, three kinds of planar maps are presented here: mean values, the diurnal range, and the diurnal time of the LSEV maximum.

3.3.1 24 hr mean values

The following describes the CONUS spatial pattern of LSEV mean values at all times of day for JJA. The magnitude of each LSEV is given for NARR. The model fields are presented as differences between model and NARR. Larger difference values mean the model has a larger magnitude than NARR.

3.3.1.1 SAT

Observations

Fig. 3.2a shows the CONUS mean SAT for NARR during JJA 2006-2010. As might be expected, the spatial temperature variability is controlled primarily by latitude, terrain elevation, and proximity to the ocean. Over ECONUS (where terrain changes are small), the temperature in the southern portion is about 5 – 10 K warmer than the northern regions. The Rocky Mountains are about 10K cooler than the Great Plains a few hundred kilometers to the west. The western coast is about 5 – 10 K cooler than the east coast because of the prevailing westerly wind flow transporting cooler oceanic air over the west coast, and warmer continental air over the east coast. Additionally, the water near the west coast tends to be cooler than water on the east coast because of the ocean circulations.

SPv4

Fig. 3.2b shows the CONUS mean SAT difference between SPV4 and NARR during JJA 2006-2010. Larger values are where SPV4 is warmer. In general, it appears that SPV4 produces a warm bias over the CONUS region. The most noticeable disagreement between SPV4 and the reanalysis is a "hot spot" over GPLN, where SAT is up to 7K warmer than observed. WMTN is also quite warm, with biases of at least 5K being common.

Another noticeable disagreement is that the SPV4 northern latitudes are too warm in the east. A careful examination of the planar plots shows that both southeast Canada and the extreme northwest US are warmer than the reanalysis by up to 5K in the Great Lakes region. The US southeast does not appear to have any major temperature biases, with temperature difference on only 1-2K of both signs.

There is a cool bias of up to 3K in southwest TX and northern Mexico. Northern NAM is biased cool by 2K, though the northern region is up to 4K too warm. The oceans are close to NARR, being only 1 K off at most.

The warm bias over CONUS is not strongly dependent of the diurnal cycle. Figs. 3b and 4b show the bias planar maps for 0z (evening) and 12z (morning). Overall, the morning (CONUS mean bias is 1.67 K) is slightly warmer than the evening (1.34 K). But this is not true for all CONUS regions. North of 35°N, morning is warmer for central and western CONUS, and evening is warmer for eastern CONUS. South of 35°N, central and eastern CONUS actually have a slight cool bias during evening, and a slight warm bias during morning, leading to the small mean temperature bias in the region.

The warm bias in SPV4 cannot easily be explained with interannual variability alone. To demonstrate this, Fig. 3.3 shows the NARR SAT for during JJA of 2012 (a notably warm year

for the central and eastern US), and the difference plots for SPV4 and NICAM. SPV4 is warmer than NARR over most of CONUS. The SPV4 GPLN "hot spot" is still warmer than even the warmest observed years by 3K, and WMTN is warmer in places up to 6K. However, most of TX and the lower MSVL are cooler than NARR by 2K (up to 4K in southwest TX). As can be seen on the NARR map, TX in particular was enduring a major heat wave during 2012. So it appears that for southern and southeastern CONUS, SPV4 is within the range of observed annual temperature variability. For much of the rest of CONUS, though, it cannot be easily concluded that SPV4 is merely simulating a warmer-than-normal year for CONUS.

SPv5

Fig. 3.2c shows the JJA CONUS SAT planar maps for SPv5. SPv5 CONUS in SPv5 is of a similar temperature to SPv4. The GPLN hot spot is similar in magnitude to v4, about 1 K warmer, but extends further south into TX. Other CONUS regions are slightly warmer, by 1-2 K, than SPv4. This fits the global tendency of SPv5 being slightly warmer than SPv4 over land. The ocean temperature is almost identical between SPv4 and SPv5.

An earlier version of SPv5 run for this thesis had a problem of making the land regions much too warm, often 10 K warmer than observed. It was also far too humid over much of Earth, land and ocean, with TPW values often 15 mm above observations. The run presented here obviously does not have this problem, and only has the same warm bias over land that previous SP-CAM versions have, as well as CAM5. It is currently unknown why the older run had such problems. But it is possible that other versions of the older "bad" SPv5 exist elsewhere, so it would be prudent for future research using SPv5 to test carefully for this problem.

NICAM

Fig. 3.2d shows the CONUS mean SAT difference between NICAM and NARR during JJA 2006-2010. Larger values are where NICAM is warmer. In general, NICAM has a cold bias over CONUS. Like SP-CAM, NICAM is too warm in the northeast, though to a lesser extent (up to 4 K). NICAM does not possess a hot spot over the Great Plains. Perhaps the most striking bias in NICAM is the cool bias occurring all across the WCONUS region. Several regions are 4 K-5 K too cool, and northern Mexico is up to 7 K too cool. Compared with SP-CAM, NICAM has higher resolution topography, so ideally NICAM should be able to represent terrain effects more realistically than SP-CAM.

Unlike SP-CAM, the NICAM temperature bias has a notable diurnal component. Figs. 3c and 4c show the bias planar maps for 0z (evening) and 12z (morning). Obviously the cool bias is greater in the evening (CONUS mean bias is -1.72 K) than the morning (0.41 K), across almost all of CONUS. In fact, much of central/eastern CONUS north of 35°N has a weak warm bias during the morning. Interestingly, the warm bias over the Great Lakes is larger during the evening than the morning, when the rest of CONUS has a stronger cold bias.

To show that NICAM's cool bias is not simply a representation of a cool year, Fig. 3.6 shows the NARR SAT for during JJA of 2008 (one of the coolest years in the US during 2000-2010), and the difference plots for SP-CAM and NICAM. The cool bias in NICAM is still obvious, with several regions of WCONUS being 5 – 6 K too cool. Northern ECONUS is still about 5K too warm, even compared with an observed cool year. So it cannot be easily concluded that NICAM is merely simulating a cooler-than-normal year for CONUS.

3.3.1.2 TPW

NARR

Fig. 3.7a shows the CONUS average TPW for JJA 2006-2010 for NARR. The US southeast is the most humid portion of CONUS, with TPW values reaching 50 mm. ECONUS is kept moist by a combination of southerly flow from the Bermuda High and the Great Plains LLJ. The humidity decreases steadily with increasing latitude. The driest region occurs over WMTN, with TPW values around 10 mm. Orographic lifting tends to condense water from air flowing into WMTN, causing the dryness.

SPv4

Fig. 3.7b shows the CONUS mean TPW difference between SPv4 and NARR during JJA 2006-2010. Larger values are where SPv4 is more humid. The SPv4 TPW is generally too high in the east and northeast, and too low in the Great Plains and southwest. The Great Plains are too dry by about 5 mm. This, coupled with the SAT high bias, suggests that the Plains are experiencing a major drought in this SPv4 run. In contrast, the east and northeast are biased both humid and warm. This means that the causes for the biases in SPv4 are complex than the simple "warm/dry and cold/moist" association over land.

SPv5

Fig. 3.7c shows the JJA CONUS TPW planar maps for SPv5. SPv5 TPW is almost identical with SPv4 over much of the US. Over ECONUS, the southeast has become slightly more humid by 3 mm, and the oceans have become slightly drier. The regional TPW minimum over

OR/NV/ID has become slightly drier, by 6 mm. The coastal Pacific has become slightly more humid.

NICAM

Fig. 3.7d shows the CONUS mean TPW difference between NICAM and NARR during JJA 2006-2010. Larger values are where NICAM is more humid. NICAM is obviously too humid across the entire CONUS region, as well as the Gulf of Mexico and the Atlantic. The moist bias is most noticeable in the Great Lakes region (up to 8 mm), the southeast (7 mm), and the southwest and Mexico (9 mm). In contrast, the Pacific west of Mexico is strongly biased dry, up to 7 mm too dry.

3.3.1.3 W500

NARR

Fig. 3.8a shows the mean W500 for NARR during JJA 2006-2010. Again, it should be noted that W500 is not directly observed, and therefore cannot be assimilated into NARR. The values shown here are calculated by NARR's model, so they may not be as realistic as NARR's SAT and TPW. Rising motion tends to occur over FL, New England, WMTN, and NM/AZ. Sinking motion tends to occur over the central US. The ocean near the east coast tends to have rising motion, and the ocean near the west coast has sinking motion (associated with the persistent marine stratocumulus). However, please note that this spatial pattern changes quite a bit during the diurnal cycle. Unlike SAT and TPW, the diurnal cycle of W500 is the same order of magnitude as the mean magnitude itself. This is important for certain meteorological features like the mountain/plains solenoidal circulation. This topic is discussed in more detail below.

SPv4

Fig. 3.8b shows the mean W500 difference between SPv4 and NARR during JJA 2006-2010. Larger values mean SPv4 has larger ascent, or weaker descent. There are some noticeable differences between SPv4 and NARR. SPv4 produces ascent over the US southeast, where NARR shows little vertical motion. The ascent over FL is not present. There is ascent over GPLN in SPv4, instead of descent in NARR. There is descent over New England in SPv4, where there is ascent in NARR. The magnitude of ascent over central WMTN in SPv4 is about the same as in NARR, but there is stronger subsidence in western WMTN. The rising (sinking) motion off the east (west) coast is larger in SPv4.

SPv5

Fig. 3.8c shows the JJA CONUS W500 planar maps for SPv5. SPv5 is similar to SPv4, with ascent over much of WCONUS and southern ECONUS, and neutral/weak descent in a line from TX to the Great Lakes. In SPv5, the ascent over WCONUS extends into Canada, and the ascent over the southeast now extends north along the Atlantic coast into New England. Also, ascent over ECONUS is now limited to the land, as opposed to spread over the ocean in SPv4. Descent is stronger in TX and weaker over the Great Lakes. The mean magnitudes of ascent and descent are similar in SPv4 and SPv5, and there is no evidence of a general strengthening or weakening of vertical motions in SPv5.

NICAM

Fig. 3.8d shows the mean W500 difference between NICAM and NARR during JJA 2006-2010. Larger values mean NICAM has larger ascent, or weaker descent. There are also some

noticeable differences between NICAM and NARR. Overall, it appears that NICAM has a weaker circulation over most of CONUS than NARR does. That is, where there is rising motion in NARR (e.g. central WMTN), NICAM has weaker ascent. The same is true for descent (e.g. GPLN). The major region where this is not true is southern ECONUS, where there is a much broader area of ascent in NICAM than in NARR (where is limited to FL). The ocean off the west coast has stronger descent in NICAM than NARR, but the ocean off the east coast has weaker ascent than NARR. The broad region of ascent in NARR over the ocean doesn't exist in NICAM.

3.3.2 Diurnal range and time of maximum value

The following describes the CONUS spatial pattern of LSEV diurnal cycles for JJA. Both NARR and model data are presented as magnitudes, with no differences shown. NICAM is not included in this section, because the six hour temporal resolution for NICAM data is too low to represent NICAM's actual diurnal cycle. In addition, SPv5 is not included because it is generally similar to SPv4.

3.3.2.1 SAT

NARR

Fig. 3.9a shows the diurnal range of SAT for NARR during JJA 2006-2010, and Fig. 3.10a shows the time of diurnal maximum for the same period. The entire CONUS region east of the Mississippi River has a diurnal range of about 10 K, with a local maximum of 13 K over OK/KS and another maximum of 14 K over the CA Central Valley. Range values east of the Mississippi

River are lower, about 6 – 8 K. Ranges over WMTN are about 10K, which seems a little low. This will be discussed in more detail in the SuomiNet section.

As for diurnal phase, for ECONUS there is practically no variability in phase with location aside from a couple of odd gridboxes. Note that the vertical time changes are the transition between time zones, and are an unavoidable limitation of the three hour temporal resolution. For WCONUS, there is a difference of about three hours between certain locations over land. The max. time difference corresponds generally with the terrain in NARR (see Fig. 3.21a). The higher terrain in western CO/WY, northwestern NM, and eastern AZ, as well as western Mexico, seems to correspond with an earlier max. time, while lower elevations have a later max. time. This association with terrain does not appear to occur as strongly with lower mountains like the Wasatch and Sierra Nevada ranges, and this association does not explain the earlier time over and around Baja California.

SP-CAM

Fig. 3.9b shows the diurnal range of SAT for SP-CAM during JJA, and Fig. 3.10b shows the time of diurnal maximum for the same period. The SAT diurnal range for SP-CAM is lower than NARR by about 5K almost everywhere over land. The two places where SP-CAM's range is close to NARR's range are in southeast Canada and upper New England, and along portions of the Pacific coastline. SP-CAM places a regional range maximum of 8K over the Great Plains (about the same location as the "hot spot"), which NARR does as well. But SP-CAM has a diurnal range over much of WMTN almost as low as over MSVL. NARR has WMTN having a larger (about 3K) range than MSVL, which makes physical sense with WMTN having a drier surface than MSVL.

Compared with NARR, SP-CAM generally has a SAT max. time about three hours later, during late afternoon or evening. There is a more noticeable contrast in the max. time between land and ocean, with the ocean maxing about two or three hours later than land. Curiously, there is an early morning SAT max. over the Atlantic ocean near the southeast coast, as well as over the Gulf of Mexico. This occurs at least six hours later than the NARR maximum. It is currently unclear why there is a discrepancy in the timing. ECONUS east of the MS River and WCONUS near the Pacific coast have max. times close to NARR, but the region between the two are off by three hours. There is no indication of a terrain effect on the max. time over WMTN; the terrain in SP-CAM is greatly smoothed compared with reality, so it is reasonable to not expect realistically large terrain-based effects.

3.3.2.2 TPW

NARR

Fig. 3.11a shows the diurnal range of TPW for NARR during JJA 2006-2010, and Fig. 3.12a shows the time of diurnal maximum for the same period. The values in ECONUS tend to be larger than those in WCONUS. The largest values, up to 3.0 mm, are found along the Gulf coast and southeast Atlantic coast. Values are lowest over most of CA and NV, the northwest portion of the Great Plains, and Baja California.

The time of the diurnal maximum for TPW varies far more with location than it does for SAT. Along the Atlantic coast, TPW maximizes in the evening – in fact, if the NARR can be trusted over the ocean, there appears to be an eastward propagation of the TPW maximum with time. I am not sure why this eastward propagation would exist. It's possible that a sea breeze would moisten the land atmosphere during the day, and dry the sea atmosphere during the night.

But the signal over land extends over 100 km inland, which is a very long range for a sea breeze. Most of the MS Valley and northward has an afternoon maximum, aside from the Gulf coast and part of the Great Lakes region. This would be expected in evapotranspiration dominates the TPW signal – there is not a strong diurnal LLJ here like there is over the Plains. Over the plains there is a mid-morning TPW maximum. This probably corresponds with the LLJ transporting moisture from the south into the region. There is probably also a contribution from the mountain-plains solenoidal circulation, which has its rising branch over the Plains during the night. This is also near the time of the precip. maximum, although the exact time for precip. is closer to midnight.

The northern portion of the western mountains mostly has a maximum in the early afternoon. While evapotraspiration would increase TPW at this time, another likely influence for the timing is the mountain/plains circulation mentioned above. It has a rising branch over the mountains during the afternoon, which would converge moisture during this time. The evening maximum over the Colorado Front Range is an interesting feature, and will be examined in more detail in a following section. The front Range sits in the transition region between the plains and mountains, so the rising branch of the mountain/plains circulation, and associated convection, would affect this region later in the day than the mountains to the west. The morning maximum in the NAM region is odd, and I will discuss this more in a following section. This region might have problems involving the NARR itself, and the morning maximum may not be physical.

SP-CAM

Fig. 3.11b shows the diurnal range of TPW for SP-CAM during JJA, and Fig. 3.12b shows the time of diurnal maximum for the same period. The SP-CAM TPW diurnal cycle in many ways looks very different from the NARR cycle. In general, the max. range is smaller almost

everywhere. The largest ranges are no longer found along the Atlantic coast, but only a small portion of the Gulf coast (near TX/LA). Interestingly, the Great Lakes region has one of the largest ranges in SP-CAM, while it has one one of the smallest in NARR. One similarity is that the NAM region in SP-CAM shows similar ranges to the NAM region in NARR.

As for diurnal phase, ECONUS east of the MS River has an early night max. time, later than NARR. There is some indication of an eastward propagation of the TPW max. with time along part of the Atlantic coast, as in NARR, but the exact timing is different. The Great Plains has a midnight to early morning maximum that shifts eastward with time. This probably is not related to precipitation systems moving east with time, because, as Chp. 4 will show, there is no clear eastward movement of the nocturnal SPREC maximum with time in SP-CAM. One possibility is related to changes in the LLJ from midnight to morning. Prichard et al. [2011] showed that moisture convergence associated with the LLJ tends to increase during the night, and a maximum develops over the eastern Plains (centered over Iowa) during mid-morning. This change in convergence may lead to the TPW max. time shifting east over the night. This question can't be fully answered without a more comprehensive moisture budget analysis over the region (and using an updated version of SP-CAM).

Over the westerm mountains, the max. time occurs several hours after the NARR max. time. I proposed that the NARR max. time was associated with the mountain/plains solenoidal circulation, but there is no evidence of that relationship here. This is not to say that the circulation doesn't exist in SP-CAM, but that it is not evident in the TPW data.

3.3.2.3 W500

NARR

Fig. 3.13a shows the diurnal range of W500 for NARR during JJA 2006-2010, and Fig. 3.14a shows the time of diurnal maximum for the same period. The diurnal range in ECONUS is slightly larger than in WCONUS. Regions with larger range are MSVL, the Great Lakes region, eastern GPLN, southeastern WMTN, and NM/north central Mexico. The phase of the diurnal cycle varies considerably across CONUS. For most of CONUS, there appears to be an eastward movement of maximum ascent beginning over central WMTN during the early afternoon, passing over GPLN during the early morning, and ending at the east coast by late morning. The eastward movement from WMTN to GPLN can be understood in terms of the mountain/plains circulation discussed before. Daytime heating causes rising motion over WMTN during afternoon, which switches to subsidence after dusk. A combination of deep convection and the LLJ causes rising motion over GPLN during the night, which ends at dawn when the LLJ begins weakening and rising motion over WMTN begins. The eastward progression over MSVL is harder to explain, because precipitation maximizes during the afternoon, almost half a day after the W500 maximum. This is discussed in more detail below. The max. time map doesn't show it, but W500 over MSVL actually has a semi-diurnal cycle according to NARR.

New England has a late evening/early morning W500 max. time. This is a few hours later than the early evening maximum in precipitation here (discussed in Chp. 4). Also, the western portion of the NAM region has an early morning W500 maximum, in contrast with most of the rest of WCONUS. This is also out of phase with the precipitation maximum here, which occurs in the evening.

SP-CAM

Fig. 3.13b shows the diurnal range of W500 for SP-CAM during JJA, and Fig. 3.14b shows the time of diurnal maximum for the same period. The diurnal amplitude variability is slightly different for SP-CAM than NARR. The largest range is found near southeast WMTN, which is over twice the range found in NARR. As for ECONUS, the largest ranges are found in the northern half, not southern as in NARR. The spatial phase map shows a clear eastward movement of the W500 max. time from the center of WMTN during early afternoon to the eastern GPLN during early morning. The continuation of this eastward motion to the east coast, as seen in NARR, does not occur in SP-CAM. Rather, there appears to be a southwesterly motion starting around Lake Ontario during the late morning and ending around OH/IN during the evening. There does not appear to be an associated southwesterly movement of the maximum precipitation time corresponding to this. West and north of central WMTN, there is an early morning W500 max. time almost everywhere.

3.4 Diurnal cycle over subregions of CONUS

The planar maps presented above display only certain aspects of the diurnal cycle, and remove other information that may be important. One crucial piece of information for representing the cycle is the "shape" of the cycle. The common assumption that the diurnal cycle in almost sinusoidal may not hold in all locations. Some places may have a semi-diurnal cycle. To use GPLN as an example, while there is a nocturnal precipitation maximum, it does not rain only at night. There is a secondary precipitation maximum associated with afternoon deep convection as well. This could, in principle, affect TPW, as humidity and precipitation are

closely related. So it is worthwhile to examine the diurnal cycles for the CONUS subregions to see if any such deviations from a sine curve exist in the data.

Also, the "observations" of LSEVs presented thus far are actually reanalysis data, which may not always be realistic. This is particularly true for W500, for which there are no direct observations, and has to be diagnosed from radiosonde horizontal wind measurements. This is also somewhat true for TPW, which is hard to observe over land with high temporal sampling. Unfortunately there is little that can be done with W500 beyond looking at other reanalyses. But GPS provides a useful too for checking reanalysis TPW. SuomiNet provides half-hour temporal resolution with an average error of about 1 mm. The main limitation of SuomiNet data is that they consist entirely of point measurements, which can be difficult when trying to calculate areal means. Nevertheless, the high temporal sampling should allow SuomiNet to provide a useful representation of the "true" TPW diurnal cycle, and thus a second data source with which to check NARR. SuomiNet sites also include SAT observations at the same temporal frequency, which is convenient for checking NARR SAT as well.

In this section I will examine the diurnal cycle in five locations: the four CONUS subregions (WMTN/NAM/GPLN/MSVL) as well as Fort Collins (FTCL). Colorado State University operated a SuomiNet station from 2007 to 2012, providing enough JJA seasons to calculate a reliable diurnal cycle for the location. Furthermore, the Front Range sits within the mountain/plains solenoidal circulation, which as seen previously (e.g. Fig. 3.11) is associated with a relatively large diurnal range of TPW. This makes FTCL a good location to compare SuomiNet with NARR and SP-CAM.

3.4.1 FTCL

Fig. 3.15a shows the diurnal cycle of SAT as observed by SuomiNet for JJA 2009-2012 at Fort Collins. Both the four year mean cycle and the cycles for the individual years are shown. The diurnal cycle is what might be reasonably expected, with the maximum occurring in the mid-afternoon (1415 LST), and the minimum occurring at dawn (0530 LST). The range is 11.5 K. The individual years show that while some years are warmer than others, the phase and amplitude of the diurnal cycle is consistent between years.

Fig. 3.15b shows the diurnal cycle of SAT for SP-CAM, NARR, and Suominet for JJA 2009-2012 at Fort Collins. Table 3.3 summarizes the results. For NARR, both the diurnal range (11.0 K) and max. time (1400 LST) are close to SuomiNet. On the other hand, SP-CAM has a range (6.7 K) notably smaller than SuomiNet, and the max. time (1700 LST) is three hours later than SuomiNet. The SP-CAM biases at FTCL are consistent with the CONUS-wide biases discussed earlier, in which SP-CAM underpredicts the diurnal amplitude and has a phase shifted by about three hours from NARR.

Fig. 3.16a shows the diurnal cycle of TPW as observed by SuomiNet for JJA 2009-2012 at Fort Collins. Both the four year mean cycle and the cycles for the individual years are shown. While the mean TPW value at Fort Collins is obviously different for the four individual years, the four year mean and the four individual years all show a prominent diurnal cycle in TPW of about the same phase and range. This supports the claim that the diurnal cycle shown in the planar maps is not just a fluke of the noise, but rather is real. The diurnal range of TPW (3.1 mm) is much smaller than the total range of TPW for all time periods (38.1 mm). The time of maximum TPW is 1815 LST, and the minimum is 0615 LST.

The most reasonable explanation for the diurnal cycle in TPW is that the diurnal cycle of the mountain/plains solenoidal circulation influences the local TPW value. The rising branch forms over the mountains during the early daylight hours, which advects atmospheric moisture towards and converges moisture at the mountains. Precipitation usually begins mid-afternoon, but large virga means that the water stays mostly in the atmosphere. As the rising branch of the solenoid moves over the plains during the night (related to the nocturnal precipitation maximum there), atmospheric moisture is moved away from the mountains. There are other effects like evapotranspiration and such that affect the diurnal cycle, but the details require more data to work out.

Fig. 3.16b shows the diurnal cycle of TPW for SP-CAM, NARR, and SuomiNet for JJA 2009-2012 at Fort Collins. Table 3.4 summarizes the results. Again, the SuomiNet data is sampled at three hour intervals for comparison purposes. First, it should be noted that both NARR and SP-CAM are a little drier than Suominet (by 3 to 4 mm). This is because the former two are not point measurements, but are the average of an area that includes the mountains as well as the plains. Fort Collins is located on the plain, so data that includes the mountains will be slightly drier. SP-CAM shows a diurnal cycle with roughly the same phase as Suominet, though the maximum occurs about three hours later than in Suominet. However, the range 1.29 is notably smaller, about half that of Suominet's. NARR also has a smaller range 1.75. However, NARR has an interesting secondary maximum in TPW at about 0500 LST. It isn't obvious from the data presented why this is the case. One possible cause is from NARR's model having difficulty with the mountain/plains circulation and nocturnal precipitation maximum, for the same reasons that climate models do. This would be an interesting question to investigate in the future. For the data presented here, though, the secondary maximum does not affect the timing of

the diurnal maximum and minimum of precipitation. It may affect the diurnal range, though, by increasing the value of the TPW minimum because it occurs three hours earlier.

3.4.2 WMTN

Fig. 3.17a shows the diurnal cycle of SAT for the WMTN region for SP-CAM, NARR, and SuomiNet. Table 3.5 summarizes the results. Note that the SuomiNet data is taken from four or five point locations, and so it is not an areal average of all points within WMTN. Thus, the mean value of SAT is not intended to reflect the mean SAT over the entire WMTN region. The phases of the diurnal cycle for the three datasets are similar. NARR and SuomiNet have a maximum near 1600 LST and a minimum near 0600 LST. SP-CAM has a phase shifted a little later in the day, with the maximum near 1700 LST and minimum near 0800 MST. There are significantly larger disagreements in the diurnal amplitude. As mentioned before, SP-CAM underestimates the amplitude (about 7 K) relative to NARR (about 10.5 K). However, it appears that NARR underestimates the diurnal cycle relative to SuomiNet (about 13.5 K). The WMTN region tends to have a relatively large diurnal because of the dryness, so the SuomiNet result is not surprising. It is possible that the surface model in NARR does not realistically handle the diurnal cycle of surface heat fluxes in this region. Unfortunately this would be difficult to verify with observational data because of the sparseness of surface heat flux observations. Unrealistic behavior in the PBL model is a similar situation.

Fig. 3.17a also shows the diurnal rate of temperature change (first derivative of Fig. 3.15a). It is apparent that SP-CAM underpredicts both the rate of warming before noon (by about 1.5 K hr^{-1}) and the rate of cooling (by about 1.0 K hr^{-1}) after noon. Interestingly, it appears that NARR

also underestimates the warming rate before noon (by about 1.0 K hr^{-1}). This may help explain why NARR underestimates the diurnal temperature range.

Fig. 3.17b shows the diurnal cycle of TPW for the WMTN region for SP-CAM, NARR, and SuomiNet. Table 3.6 summarizes the results. The diurnal amplitudes of all three datasets are small (smaller than the amplitude at FTCL), and the phases are not all similar. The phase for SuomiNet and SP-CAM are similar, with evening maxima (around 1915 and 1800 LST respectively) and mid-morning minima. NARR shows a different diurnal phase, with a maximum in early afternoon (about 1330 LST) and a minimum near midnight. The diurnal ranges are 0.47 mm for SuomiNet, 1.16 mm for NARR, and 0.79 mm for SP-CAM. The explanation for the diurnal cycle for WMTN is similar to the explanation for FTCL: daytime heating and afternoon precipitation converges moisture over the mountains during the late afternoon, and the switch to divergence during the morning removes this moisture. However, WMTN is a large area as opposed to a point measurement, and not all regions of WMTN are affected strongly by the mountain-plains circulation like FTCL is. So it isn't surprising that the diurnal amplitude of TPW isn't as large for WMTN as it is for FTCL. The NARR results do not fit this explanation, and it would be difficult to deduce what is happening in NARR without more investigation into other aspects of NARR's behavior (e.g. precipitation diurnal cycles).

3.4.3 NAM

Fig 18a shows the diurnal cycle of SAT for the NAM region for SP-CAM, NARR, and SuomiNet. Table 3.7 summarizes the results. The phase of SP-CAM is shifted slightly from the other two, and the amplitude of SuomiNet is larger than the other two. SuomiNet's diurnal range (about 12.3 K) is about 50% larger than NARR (8.4 K) and SP-CAM (7.2 K). Part of this

disagreement is probably because the NAM region includes both land and sea surfaces. The SP-CAM and NARR mean cycles include sea surfaces, while SuomiNet sites are only over land. But even over land, NARR sometimes shows too low of a diurnal amplitude (e.g. WMTN), and SP-CAM frequently does, so the land/sea effect on the data probably isn't the sole cause for disagreement. Both SuomiNet and NARR have a time of maximum at about 1445 LST, while SP-CAM has it later, at about 1700 LST. The time of minimum for NARR and SuomiNet are within an hour, at 0500 and 0600 LST, while SP-CAM has a later min. time at 0800 LST.

The first derivative of the diurnal cycle shows that NARR and Suominet are fairly close in the phase of warming, though NARR's amplitude is of course lower. NARR warming becomes positive about an hour before SuomiNet, but the maximum warming value is only slightly more than half of SuomiNet's (1.25 K hr^{-1} versus 2.25 K hr^{-1}). The warming rates are similar through midday to evening, where the NARR warming rate becomes about 0.75 K hr^{-1} higher than SuomiNet (-1.0 K hr^{-1} versus -1.75 K hr^{-1}). SP-CAM's warming curve is similar to NARR's, but shiften an hour or two later. SP-CAM's warming rate is lower than SuomiNet's from mid-morning until noon (up to 1.0 K hr^{-1} difference), then higher until night time (up to 1.5 K hr^{-1} difference).

Fig 18b shows the diurnal cycle of TPW for the NAM region for SP-CAM, NARR, and SuomiNet. Table 3.8 summarizes the results. The diurnal phase for SP-CAM and SuomiNet are similar, while NARR's is noticeably different. The diurnal range for SuomiNet is somewhat larger than for the other two, though part of that is caused by the unusual afternoon maximum for SuomiNet. SuomiNet's diurnal range is 1.6 mm, but without the afternoon maximum it is closer to 1.0 mm. This is still noticeably larger than SP-CAM's range of 0.4 mm, and slightly larger than NARR's range of 0.9 mm. SuomiNet's time of maximum (1645 LST) is different by several

hours from SP-CAM's (2300 LST) and NARR's (0500 LST). But if SuomiNet's afternoon maximum is ignored, then the main maximum for the day occurs near midnight, similar to SP-CAM.

The reason for the afternoon maximum for SuomiNet is currently unclear. As described previously, there are different diurnal cycles of precipitation across NAM depending on location. For example, for the Sierra Madre Occidental, precipitation tends to occur over the mountains during the afternoon, and moves to the western plains during the evening. It is possible that one or two of the point measurements used in the SuomiNet mean cycles are influenced by this kind of local effect. NARR does not appear to agree with the other two on the cycle phase. Again, explaining why would require additional information.

3.4.4 GPLN

Fig 19a shows the diurnal cycle of SAT for the GPLN region for SP-CAM, NARR, and SuomiNet. Table 3.9 summarizes the results. The phases of all three are slightly offset from the others, and the amplitude of SP-CAM is smaller than the other two. SP-CAM's maximum diurnal range of about 7.0 K is, as with other regions discussed here, noticeably smaller than the others' amplitudes of about 10.9 K. The time of maximum for both SuomiNet and NARR is about 1500 LST, while SP-CAM has a later time of 1745 LST. The time of minimum for all three is about 0600 LST. However, though NARR and SuomiNet have the same time of max. and min., they do not have identical cycles. NARR is about 1 – 2 K cooler than SuomiNet from mid-morning to late afternoon. They are about equal during night and early morning.

The first derivatives show that the warming rates of both NARR and SuomiNet become positive at 0600 LST. However, the maximum warming rate for SuomiNet (about 1.5 K hr^{-1}) is

below the maximum NARR warming rate (about 2 K hr^{-1}), and stays at the max. value for longer in the day than SuomiNet. The warming rates for both stay within 0.25 K hr^{-1} until the next morning, so the abs. temperature diurnal cycles become similar during the later day. SP-CAM's warming rate differs from the other two most during the late morning (by about 1.5 K hr^{-1}) and late evening (by about 2.0 K hr^{-1}), and is closer during early morning and afternoon.

Fig 19b shows the diurnal cycle of TPW for the GPLN region for SP-CAM, NARR, and SuomiNet. Table 3.10 summarizes the results. The diurnal phases for all three are very different, and the amplitude of SP-CAM is much smaller than the other two. The diurnal range of SuomiNet (1.5 mm) is about twice that of SP-CAM (0.8 mm), and slightly larger than that of NARR (1.2 mm). The time of maximum for NARR (1500 LST) and SuomiNet (1615 MST) are close, whereas SP-CAM (0000 LST) has a much later maximum. However, NARR has a secondary maximum occurring mid-morning (0600 MST).

Considering the meteorological processes occurring over GPLN discussed earlier, we might expect there to be a noticeable diurnal cycle in TPW. During the night, the mountain-plains circulation has the rising branch over GPLN, in contrast to WMTN. Furthermore (and related), the Great Plains LLJ transports moist air from the Gulf of Mexico into the plains during night and early morning. Precipitation would reduce TPW by morning, and it would begin to increase again throughout the day by evapotranspiration. There is also the secondary afternoon precipitation maximum to consider, which in principle could dry the afternoon atmosphere temporarily before the solenoidal circulation and LLJ replenish it.

Interestingly, SP-CAM TPW seems to respond to the midnight moistening processes the most out of the three datasets. The magnitude for SP-CAM is small, but the timing seems physically reasonable. SuomiNet appears to respond to afternoon moistening and drying far more

than the midnight processes. This might be an artifact of the point measurement nature of the data. Agriculture can strongly influence local humidity, and of course most evapotranspiration occurs during the afternoon. If one or two of the SuomiNet sites are near agriculture, then this might affect the average diurnal cycle [Changnon et al. 2003, Sandstrom et al. 2004]. NARR also responds to the afternoon processes, but it also has a morning maximum (similar to WMTN). There is no precipitation maximum at this time of day, so it is difficult to say why NARR has a max. at this time.

3.4.5 MSVL

Fig 20a shows the diurnal cycle of SAT for the MSVL region for SP-CAM, NARR, and SuomiNet. Table 3.11 summarizes the results. SP-CAM and NARR have smaller diurnal amplitudes than SuomiNet, and the former two have phases shifted later in the day than the latter. As with other locations, SuomiNet's diurnal range (9.3 K) is noticeably larger than SP-CAM's (5.7 K) and NARR's (7.9 K). Unlike NAM, MSVL does not include large sea surface regions, so this is not a good explanation for NARR have a smaller range than SuomiNet. SuomiNet's time of maximum (1445 LST) is slightly earlier than SP-CAM's and NARR's (both 1600 LST). SuomiNet's time of minimum (0545 LST) is earlier than SP-CAM's (0700 LST), but earlier than NARR's (0400 LST).

The first derivative show that SuomiNet and NARR warming becomes positive within an hour of each other, while SP-CAM becomes positive about three hours later. The peak warming for NARR occurs about two hours later than SuomiNet, and is only about 75% as large (1.5 K hr^{-1} versus about 2.2 K hr^{-1}). SP-CAM peaks about four hours after SuomiNet at slightly over half magnitude (1.25 K hr^{-1}). NARR's warming rate stays close to SuomiNet's until late evening,

where NARR reaches a minimum about two hours after SuomiNet at a little over half the magnitude (-1.25 K hr^{-1} versus 2.1 K hr^{-1}).

Fig 20b shows the diurnal cycle of TPW for the MSVL region for SP-CAM, NARR, and SuomiNet. Table 3.12 summarizes the results. NARR's phase is shifted later than SuomiNet's, and SP-CAM's is shifted later than NARR's. SP-CAM's has a smaller amplitude than the other two. SP-CAM's diurnal range (0.7 mm) is less than half that of SuomiNet's (1.6 mm) and NARR's (1.8 mm). SuomiNet's time of maximum is in the early afternoon (1345 LST), while NARR's is mid-afternoon (1600 LST) and SP-CAM's is in the evening (1900 LST). SuomiNet's minimum is around midnight (0045 LST), while NARR's and SP-CAM's are correspondingly shifted later in the morning (0400 and 0700 LST). While nocturnal precipitation occurs occasionally in MSVL, it is not known for having a strong nocturnal maximum as GPLN is. So SuomiNet's and NARR's cycle phase seems a little more reasonable intuitively than SP-CAM's (if anything, SuomiNet's maximum seems a little too early). NARR also has a mid-morning TPW maximum, a feature seen in the other regions as well. Again, the information presented here is insufficient to determine a likely cause for that maximum.

Interestingly, the first derivatives show that SuomiNet does not begin moistening before the other two, despite having the earliest maximum. SP-CAM begins moistening at the same time, and NARR begins moistening several hours before (though it briefly dries after the morning maximum. SuomiNet moistens rapidly for about two to three hours, then quickly begins drying. The other two moisten over longer periods of time, associated with the maxima later in the day.

3.5 Effect of terrain on LSEVs

As discussed before, terrain plays an important role in weather and climate, altering the flow around and above, and introducing surface/air exchanges well above sea level. Because of the limited resolution of atmospheric models, they can only partially represent terrain effects, which can lead to large errors in regions of highly variable terrain. Even finer-scale models like NICAM cannot fully represent individual mountains and canyons, so no model is entirely immune. Furthermore, the method of transforming the effects of the step-function like shape of terrain in a model grid into the effects of a smooth terrain is a challenging task, and different models have different ways of accomplishing this. In this section we will look at the CONUS terrain maps of NICAM, SP-CAM, and the NCEP/NCAR reanalysis. Then we will investigate the effect of terrain on the LSEVs in WMTN, where terrain elevation changes are large in magnitude and gradient.

3.5.1 Terrain planar maps

Fig. 3.21a shows the terrain in NARR. The reanalysis has an atmospheric modeling component as well as an observational component, so the terrain representation in the reanalysis influences the meteorological fields. NARR has a roughly 32 km x 32 km horizontal domain, which is sufficient to resolve individual mountain ranges, though not individual mountains. This map distinctly shows the Rocky Mountains, the Sierra Nevada and Sierra Madre Occidental and Oriental, the Wasatch, the Appalachians, etc.

Fig. 3.21b shows the terrain height map for SP-CAM, and Fig. 3.21c for NICAM. Immediately noticeable is the lower maximum elevation for SP-CAM (2108 m) than NICAM (3325 m) in WMTN. A cursory look at the two maps shows that SP-CAM does not register the

major ridges and valleys in WMTN. Instead, SP-CAM presents a single large ridge covering WMTN. Also, the Appalachian mountains barely register in SP-CAM, and the Sierra Madre ranges are merged into a single north/south ridge extending from WMTN. While NICAM has much more detailed topography, a careful examination will show that individual mountains do not really exist in NICAM. For an obvious example, Mount Washington in New Hampshire (peak elevation 1,917 m) isn't there.

Fig 22 shows the difference map of Figs. 21b and 21c; positive (red) values are where NICAM is larger than SP-CAM, and vice versa. The difference map is mainly a map of individual mountain ranges and valleys; e. g. the Rocky Mountains, the Sierra Madre Occidental, Central Valley, the Grand Canyon region, etc. The Great Basin is an interesting location where some parts are lower in NICAM than SP-CAM (e.g. western Utah, northwestern Nevada), and other parts are higher (e.g. central Nevada). The Great Basin does not exist as such in SP-CAM.

3.5.2 WMTN examination

Fig. 3.23a displays the scatter plots and regression lines of SAT versus terrain height in WMTN for SP-CAM, NICAM, N/NR, and NARR. The most notable result is that the regression slopes of SP-CAM and N/NP are similar (-1.42 K km^{-1} and -0.74 K km^{-1}, respectively), and the slopes of NICAM and NARR are similar (-3.76 K km^{-1} and -4.14 K km^{-1}, respectively). SP-CAM and N/NP have similar coarse horizontal resolutions, while NICAM and NARR have much higher horizontal resolutions. In addition, the correlations of SP-CAM and N/NP are similar (-0.19 and -0.13), as for NICAM and NARR (both -0.57). The similarity of the coarser and finer resolution datasets suggests that the coarseness of the terrain in both models and reanalyses plays a key role in the sensitivity of SAT to terrain height.

The physical mechanisms for this are not necessarily straightforward. SAT in mountainous terrains is dependent on regional terrain-induced circulations [Mahrt 2006]. During the day, terrain-induced rising motion creates adiabatic cooling at higher elevations, while at nigh drainage flows cause adiabatic warming at lower elevations. Both work to increase the sensitivity of SAT to terrain height. The ability of a model to simulate these terrain-induced flows is directly related to the representation of the terrain. If this explanation is relevant, then we might expect this result.

Fig. 3.23b displays the scatter plots and regression lines of TPW versus terrain height for SP-CAM, NICAM, N/NR, and NARR. We might expect similar results as the SAT results, because of the same horizontal resolution issue. However, the regression slopes of all four datasets are very close (-4.26 mm km^{-1} for NARR to -5.03 mm km^{-1} for NICAM). The correlations are also similar (-0.65 to -0.69), except for N/NR, which is a little lower (-0.57).

This result may seem to contradict the SAT result, but this may not necessarily be so. If the explanation suggested for SAT is true, then the sensitivity of TPW to terrain height should be affected by the same regional circulations as affect SAT. However, TPW is not affected by vertical motion in the column.

It is possible that the terrain influence is affected by the diurnal cycle. For example, if the previous argument about terrain flow is realistic, then the diurnal variation of the strength of the terrain flow would affect the diurnal cycle of the relationship. Fig. 3.24a shows the diurnal cycle of the SAT regression slopes (a1) and correlations (r) for the four datasets. Fig 24b shows the same for TPW. For SAT, first it is clear that the high-res. datasets have smaller (more negative) regression values than the low-res. datasets at all times of the day, and each pair remains close in magnitude at all times of day. So the results described above do not appear to be just a fluke in

the statistics. Second, all four datasets individually show diurnal cycles that are about 10% to 50% of their means. The datasets with three hour temporal resolutions (SP-CAM and NARR) show larger diurnal ranges than the datasets with six hour resolution – this may just be a temporal sampling issue. Three of the datasets show smaller regression values during the evening than the morning. Only N/NR shows smaller regression values during the morning.

3.6 Conclusions

The following are the answers to the questions presented previously, according to the results shown in this chapter:

1. How realistically do the models simulate the typical JJA climate over CONUS?

Biases in SAT are up to 8K for both NICAM and SP-CAM. Biases in TPW are up to 6 mm in SP-CAM and 7 mm in NICAM. Biases in W500 are the same order of magnitude as the mean magnitude in both SP-CAM and NICAM.

2. Are there significant general biases in temperature, humidity, and circulation?

SP-CAM has a warm and moist bias in most locations, and there are some different regions of strong vertical motion. NICAM has a cold bias over much of CONUS, also has a moist bias, and has weaker vertical motions in most locations.

3. Are there significant regional biases?

GPLN and WMTN in SP-CAM are particularly too warm. It is too moist east of the MS River. GPLN and MSVL have ascent where NARR has descent or weak motion. NICAM also has strong ascent over southern MSVL.

4. Are these biases dependent on time of day?

For NICAM, the SAT bias is more negative during the evening than the morning, indicating that NICAM does not warm sufficiently during the day. SP-CAM does not have a major CONUS-wide diurnal cycle in SAT bias, but there are different regional cycles.

5. Can these biases be explained by observed inter-annual variability?

The SP-CAM warm bias cannot be easily explained by inter-annual variability alone, particularly in higher latitudes, because SP-CAM is several Kelvin warmer than the notably warm 2012 JJA. Similarly, the NICAM cool bias cannot be easily explained this way because it is several Kelvin cooler than the notably cool 2008 JJA.

6. How realistically do the models simulate the diurnal cycle? Magnitude and timing?

SP-CAM underpredicts the amplitude of SAT and TPW in most locations. It predicts a SAT max. time a few hours too late in the day, and it predicts the TPW-max time several hours too late in day. It has a much larger eastward progression of TPW max. time across GPLN than NARR does. SP-CAM simulates the shift in rising motion from WMTN to GPLN.

7. How realistically do models simulate terrain effects on LSEVs?

For SAT, the higher horizontal resolution datasets, NARR and NICAM, are more sensitive to elevation than the low res. datasets (N/NR and SP-CAM). The sensitivity of TPW to elevation is similar in all four datasets. The disagreement in SAT sensitivity is not strongly affected by time of day.

8. Are these answers strongly dependent on the observational or reanalysis data used?

NARR does not always agree well with SuomiNet GPS data. The diurnal range in NARR is smaller than SuomiNet for WMTN, and TPW has a persistent morning maximum of unknown causes in multiple locations

Additional comments

These results have some important consequences for Chp. 4. When examining SP-CAM cloud characteristics, keep in mind that the environments that they occur in will often be warmer and more humid than in reality. Large-scale vertical motions are different in some regions, too. While SP-CAM simulates to some degree the mountain/plains circulation for GPLN and WMTN, the vertical motions over MSVL and much of ECONUS are not as well simulated. Clouds in NICAM will occur in more humid but cooler environments, with weaker vertical motion overall (with MSVL being an exception).

As shown in Chps. 2 and 4, changes in environmental conditions of a few Kelvin or a few mm TPW can mean the difference between low clouds and mature DCCs. This transition is particularly sensitive to TPW. The transition for W500 is less abrupt, with DCCs becoming gradually more common as ascent increases in magnitude. But the sign of rising motion strongly

influences DCC development, and the models do not agree with NARR on the sign everywhere. For existing DCCs, properties like cloud top height and intensity (estimated by the reflectivity gradient in the upper cloud) can vary significantly with similar changes in LSEVs. Combining these facts with the conclusions of this chapter suggest the likely possibility that biases in the models' LSEVs can significantly influence the mean DCC behavior in the models. Chp. 4 will continue this discussion.

Table 3.1. Coordinates of CONUS and CONUS subregions

region	abbreviation	Lat. range	Lon. range
Contiguous US	CONUS	25°N – 50°N	130°W – 65°W
eastern CONUS	ECONUS	25°N – 50°N	100°W – 65°W
western CONUS	WCONUS	25°N – 50°N	130°W – 100°W
western mountains	WMTN	35°N – 50°N	120°W – 102°W
North American monsoon	NAM	25°N – 35°N	115°W – 105°W
Great Plains	GPLN	35°N – 50°N	105°W – 95°W
Mississippi Valley	MSVL	30°N – 40°N	95°W – 80°W

Table 3.2. SuomiNet station names, coordinates, and available time domain

Site ID	region	location	year range
SA62	FTCL	105°W, 41°N	2009-2012
P002	WMTN	117°W, 40°N	2008-2012
P019	WMTN	115°W, 43°N	2008-2012
P031	WMTN	108°W, 40°N	2008-2012
P718	WMTN	109°W, 45°N	2009-2012
PTEX	NAM	117°W, 32°N	2011-2012
SA24	NAM	110°W, 31°N	2007-2012
SA27	NAM	111°W, 29°N	2007-2012
CLK5	GPLN	98°W, 45°N	2010-2012
MNSC	GPLN	95°W, 46°N	2011-2012
NEGI	GPLN	98°W, 41°N	2010-2012
PRCO	GPLN	98°W, 35°N	2007, 2012
SGO4	GPLN	97°W, 37°N	2007-2012
KYTG	MSVL	84°W, 38°N	2011-2012
MOCH	MSVL	89°W, 37°N	2011-2012
MSB5	MSVL	91°W, 34°N	2008-2012
P778	MSVL	86°W, 35°N	2008-2012

Table 3.3. SAT diurnal cycle range and max./min. time for different datasets, FTCL

	Range (K)	Max. Time (LST)	Min. Time (LST)
SuomiNet	11.5	1415	0415
NARR	11.0	1400	0500
SP-CAM	6.9	1700	0800

Table 3.4. TPW diurnal cycle range and max./min. time for different datasets, FTCL

	Range (mm)	Max. Time (LST)	Min. Time (LST)
SuomiNet	3.10	1815	0615
NARR	1.75	2000	0800
SP-CAM	1.29	2300	0800

Table 3.5. SAT diurnal cycle range and max./min. time for different datasets, WMTN

	Range (K)	Max. Time (LST)	Min. Time (LST)
SuomiNet	13.4	1615	0515
NARR	10.3	1700	0500
SP-CAM	7.0	1700	0800

Table 3.6. TPW diurnal cycle range and max./min. time for different datasets, WMTN

	Range (mm)	Max. Time (LST)	Min. Time (LST)
SuomiNet	0.48	1915	0645
NARR	0.76	1400	0200
SP-CAM	0.71	2300	0800

Table 3.7. SAT diurnal cycle range and max./min. time for different datasets, NAM

	Range (K)	Max. Time (LST)	Min. Time (LST)
SuomiNet	12.4	1445	0515
NARR	8.4	1400	0500
SP-CAM	7.2	1700	0800

Table 3.8. TPW diurnal cycle range and max./min. time for different datasets, NAM

	Range (mm)	Max. Time (LST)	Min. Time (LST)
SuomiNet	1.59	1645	1115
NARR	0.89	0500	1700
SP-CAM	0.44	2300	1100

Table 3.9. SAT diurnal cycle range and max./min. time for different datasets, GPLN

	Range (K)	Max. Time (LST)	Min. Time (LST)
SuomiNet	10.9	1515	0515
NARR	10.9	1500	0600
SP-CAM	6.9	1800	0600

Table 3.10. TPW diurnal cycle range and max./min. time for different datasets, GPLN

	Range (mm)	Max. Time (LST)	Min. Time (LST)
SuomiNet	1.49	1615	2115
NARR	0.68	1500	0300
SP-CAM	0.59	0000	0900

Table 3.11. SAT diurnal cycle range and max./min. time for different datasets, MSVL

	Range (K)	Max. Time (LST)	Min. Time (LST)
SuomiNet	9.3	1445	0545
NARR	7.9	1600	0400
SP-CAM	5.6	1600	0700

Table 3.12. TPW diurnal cycle range and max./min. time for different datasets, MSVL

	Range (mm)	Max. Time (LST)	Min. Time (LST)
SuomiNet	1.57	1345	0045
NARR	1.75	1600	0400
SP-CAM	0.72	1900	0700

a) CONUS, ECONUS, WCONUS

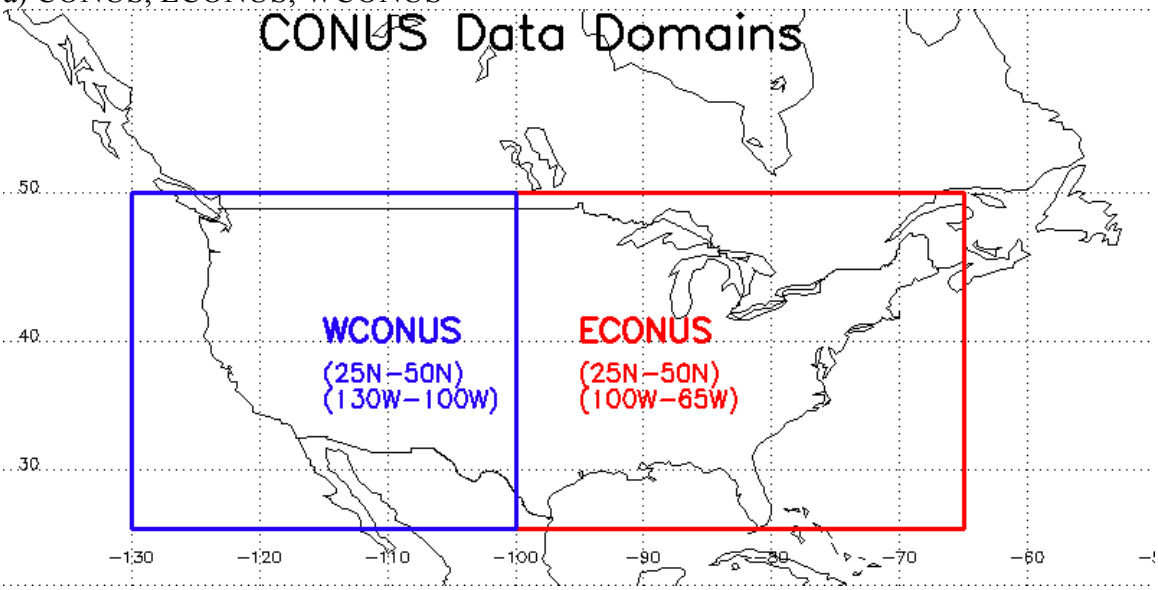

b) CONUS subregions

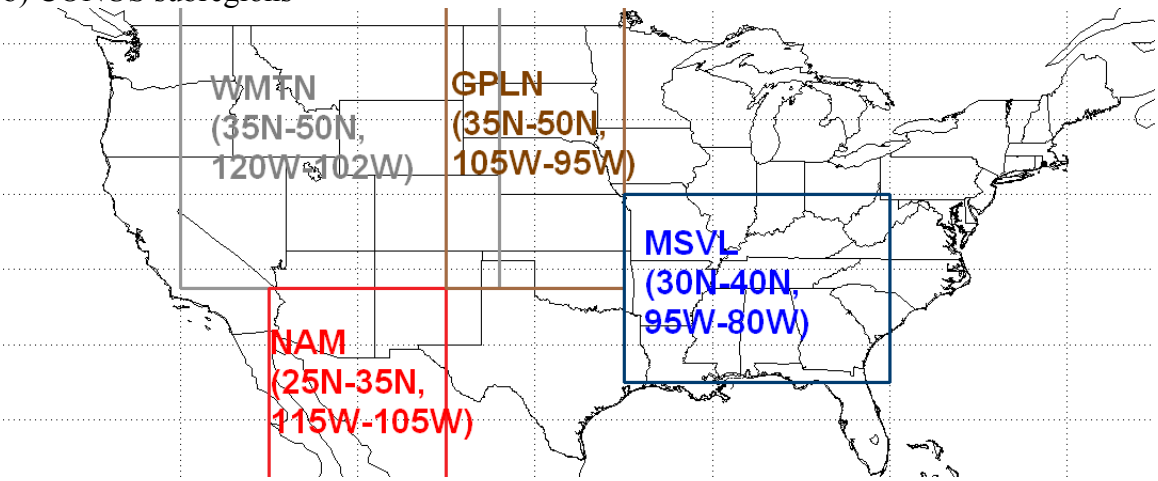

Figure 3.1. Planar maps of a) CONUS, ECONUS, and WCONUS, and b) CONUS subregions (WMTN, NAM, GPLN, MSVL)

a) NARR

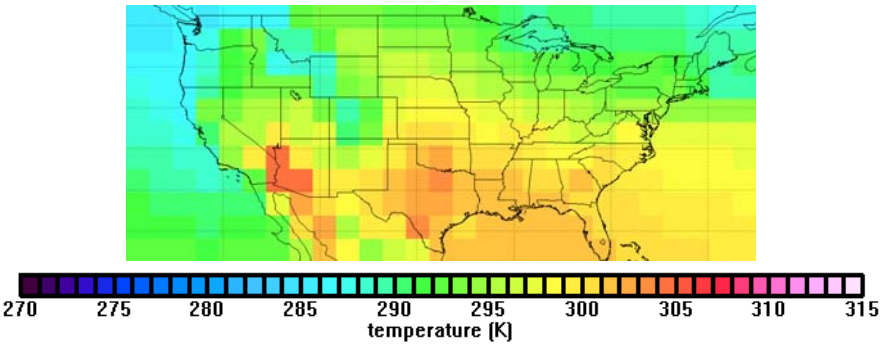

b) SPv4 minus NARR

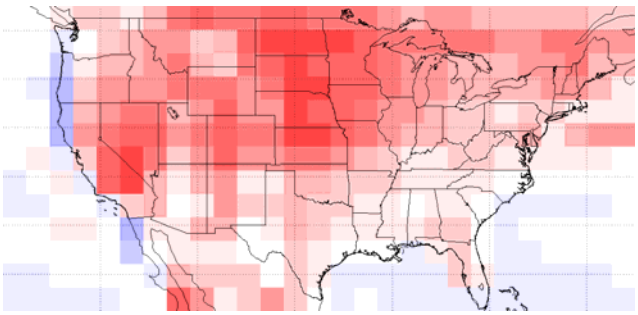

c) SPv5 minus NARR

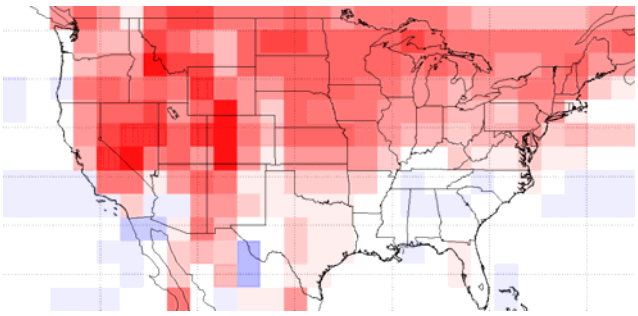

d) NICAM minus NARR

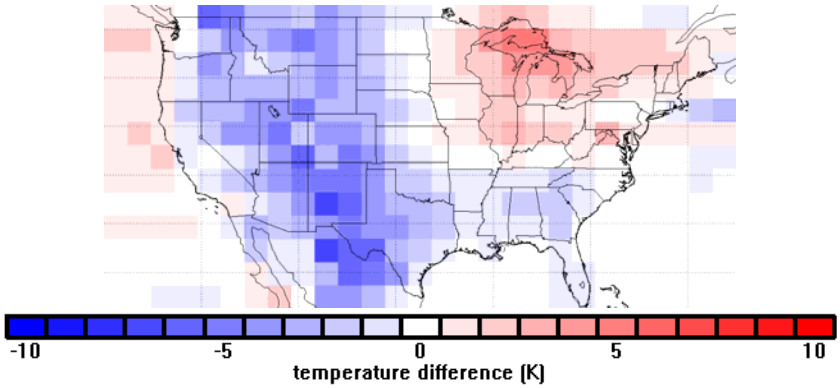

Figure 3.2. a) Mean SAT for NARR, JJA 2006-2010, all times of day. b) Difference between SPv4 and NARR (red means SP-CAM larger than NARR). c) Difference between SPv5 and NARR. d) Difference between NICAM (regridded to 2.5 horizontal resolution) and NARR.

a) NARR

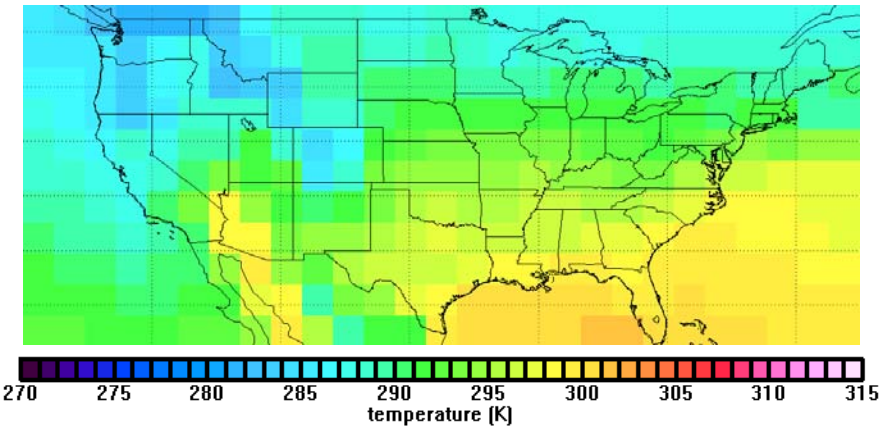

b) SPv4 minus NARR

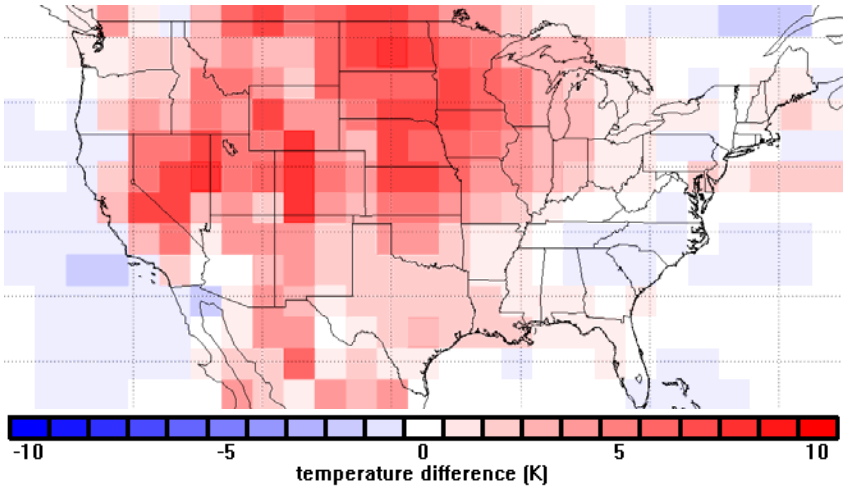

c) NICAM minus NARR

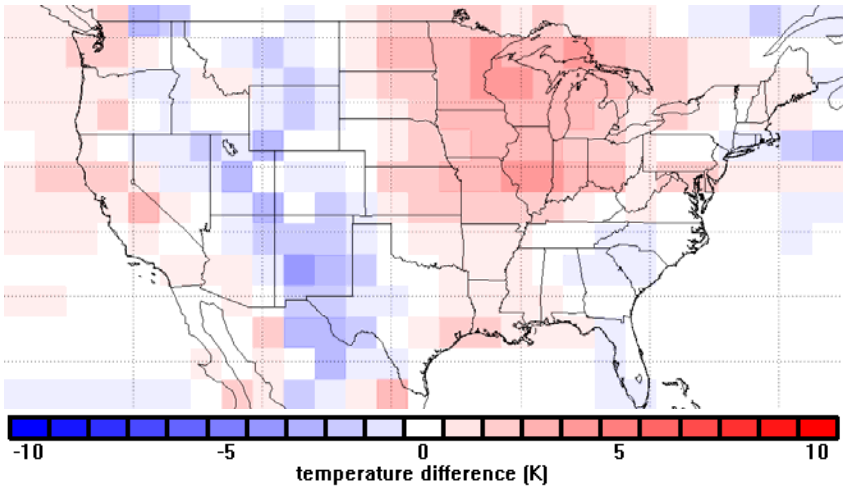

Figure 3.3. As Fig 3.2., but for 12z (morning) only. SPv5 is omitted.

a) NARR

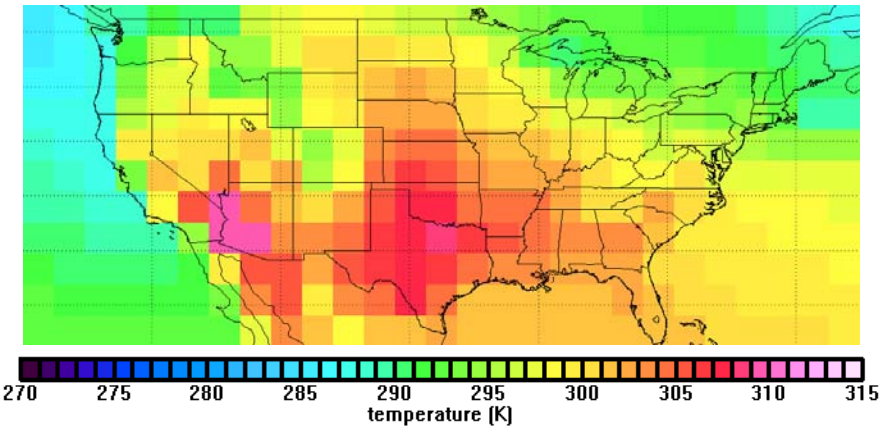

b) SPv4 minus NARR

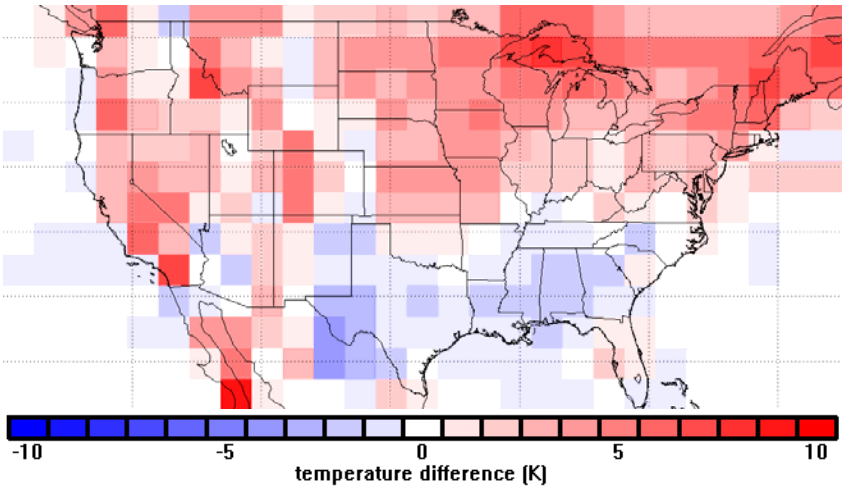

c) NICAM minus NARR

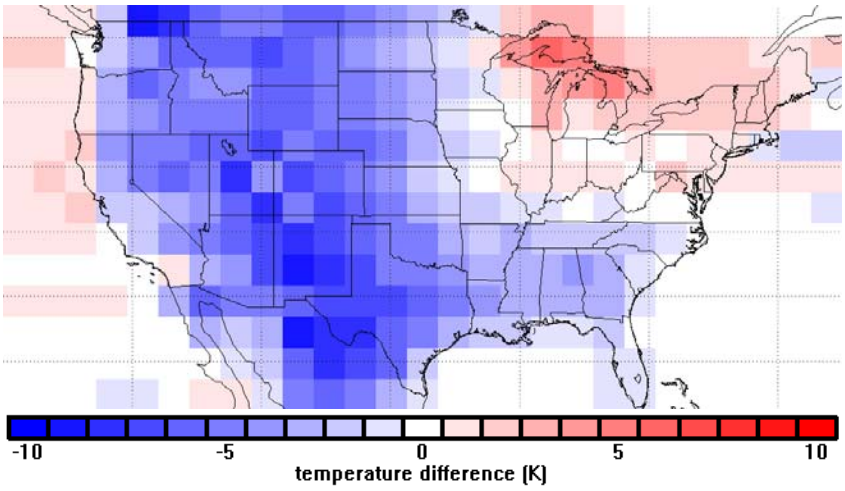

Figure 3.4. As Fig. 3.2, but for 0z (evening) only. SPv5 is omitted.

a) NARR

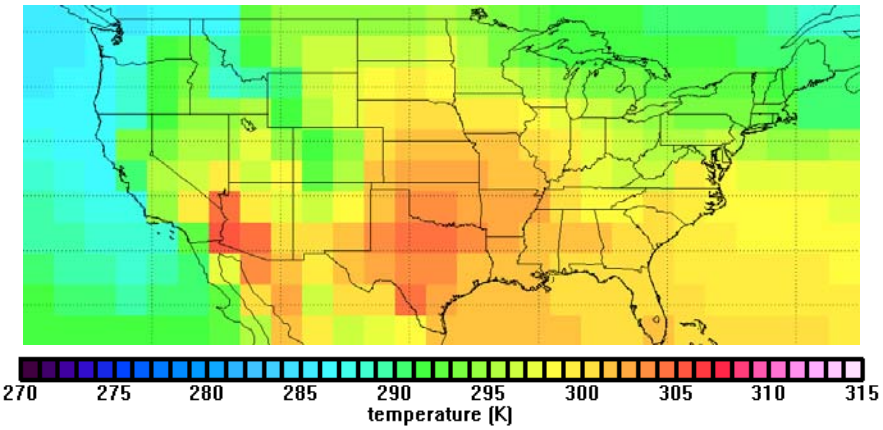

b) SPv4 minus NARR

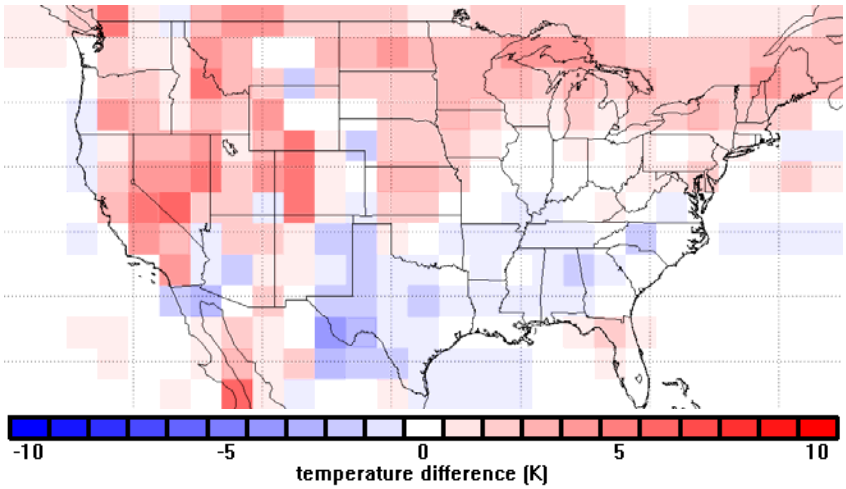

c) NICAM minus NARR

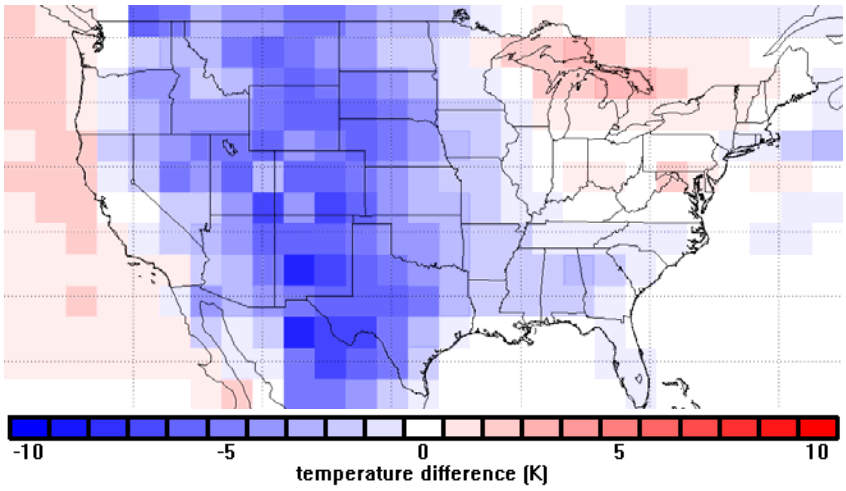

Figure 3.5. As Fig. 3.2, but for the NARR time domain of JJA 2012. SPv5 is omitted.

a) NARR

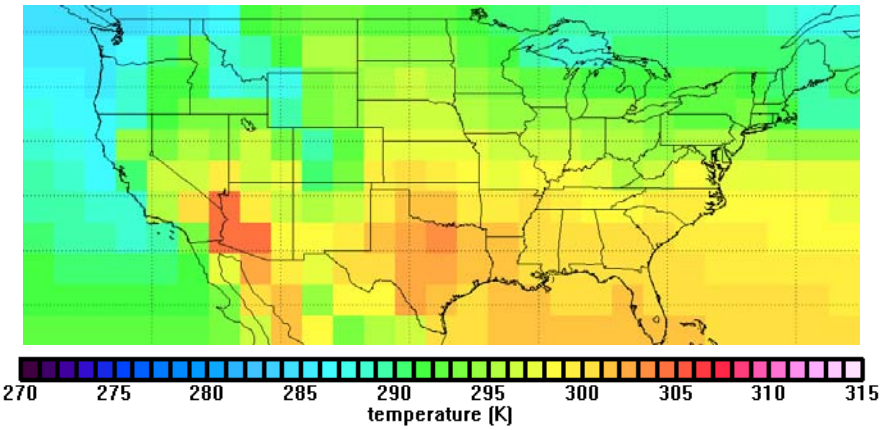

b) SPv4 minus NARR

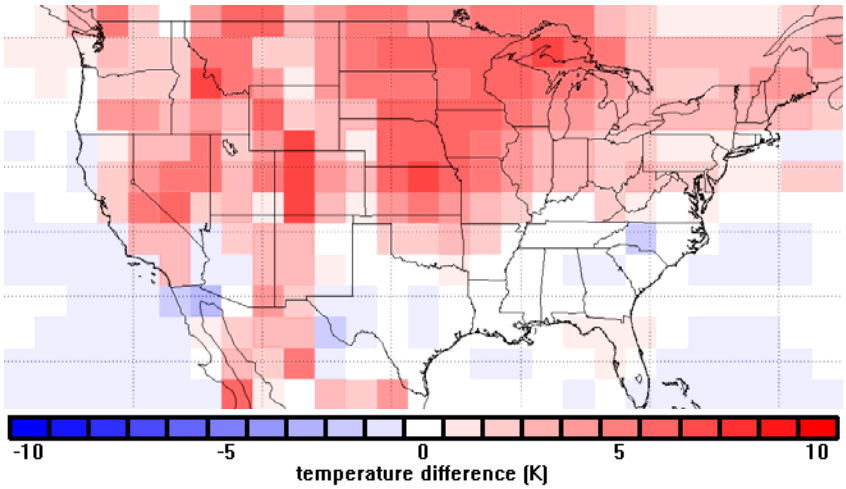

c) NICAM minus NARR

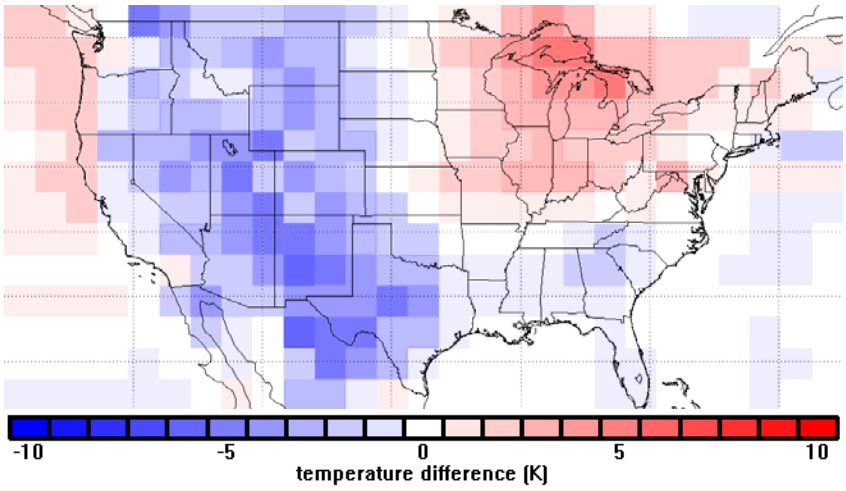

Figure 3.6. As Fig. 3.2, but for the NARR time domain of JJA 2008. SPv5 is omitted.

a) NARR

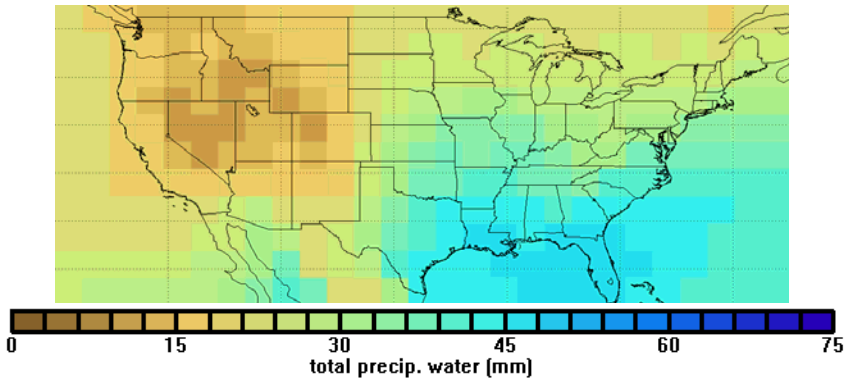

b) SPv4 minus NARR

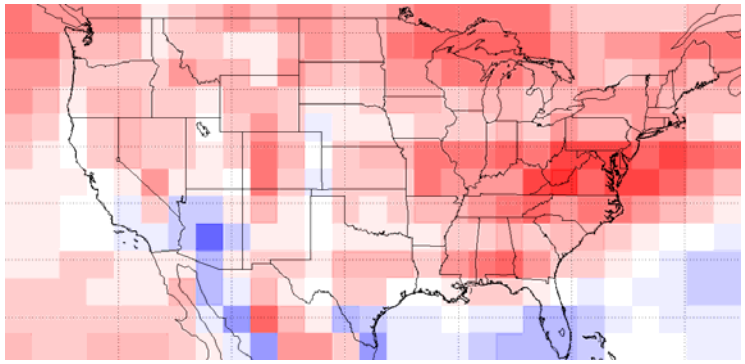

c) SPv5 minus NARR

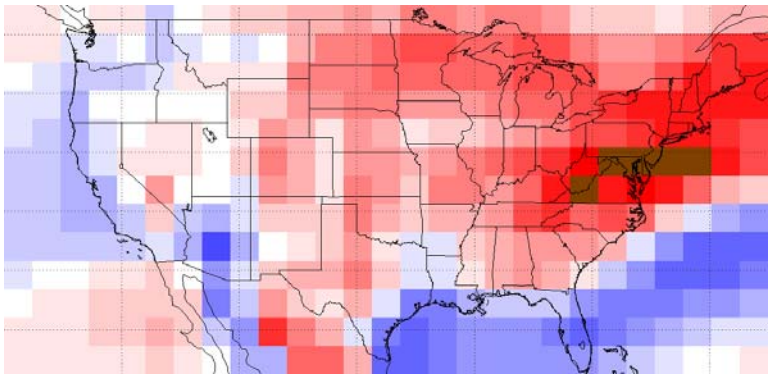

d) NICAM minus NARR

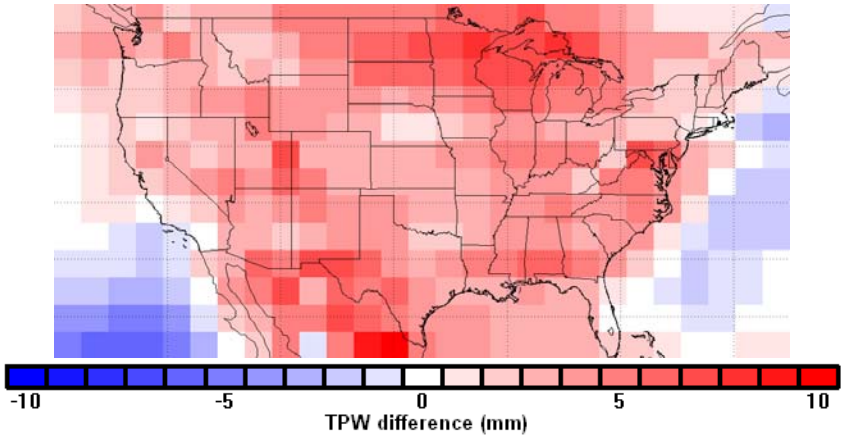

Figure 3.7. As Fig. 3.2, but for TPW.

a) NARR

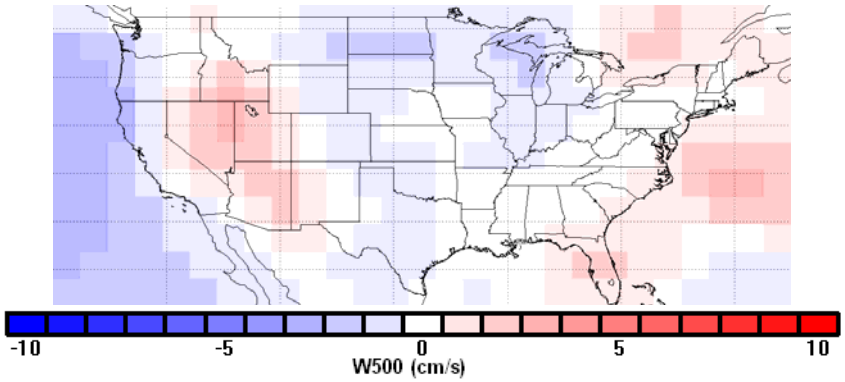

b) SPv4 minus NARR

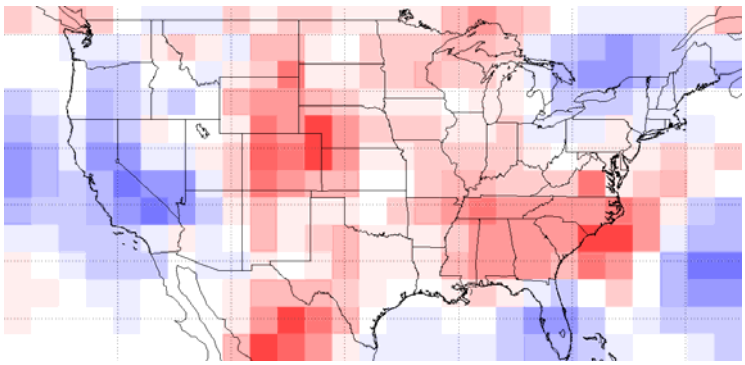

c) SPv5 minus NARR

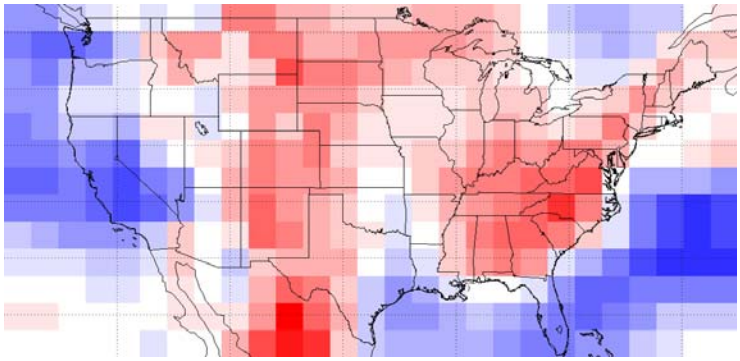

d) NICAM minus NARR

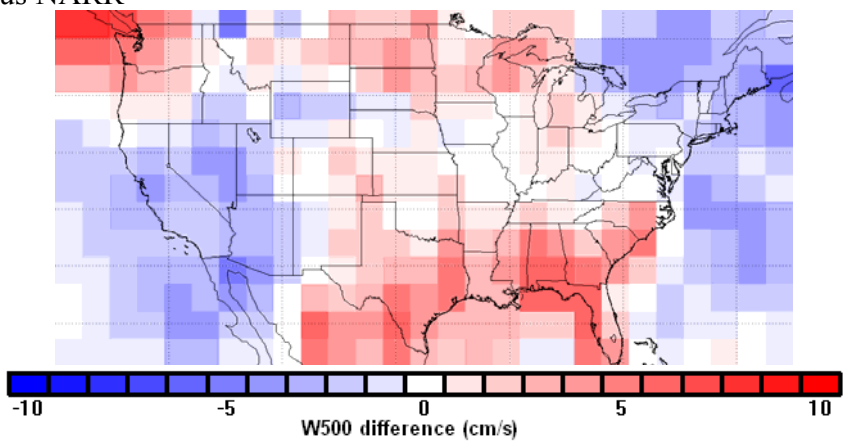

Figure 3.8. As Fig. 3.2, but for W500.

a) NARR

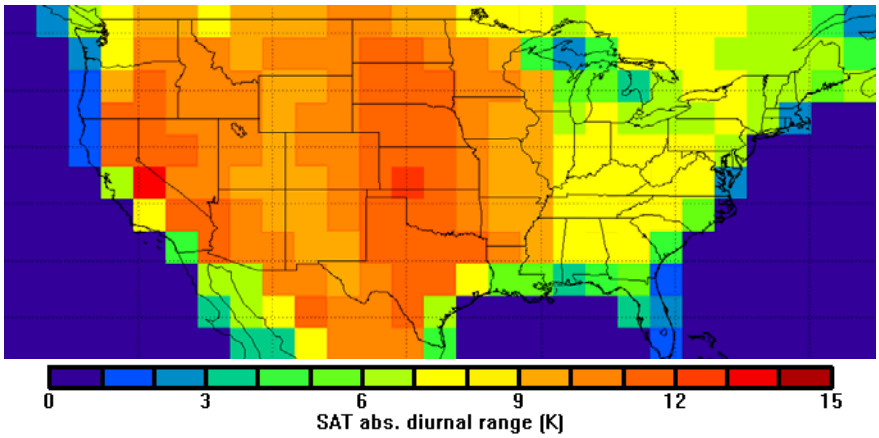

b) SPV4

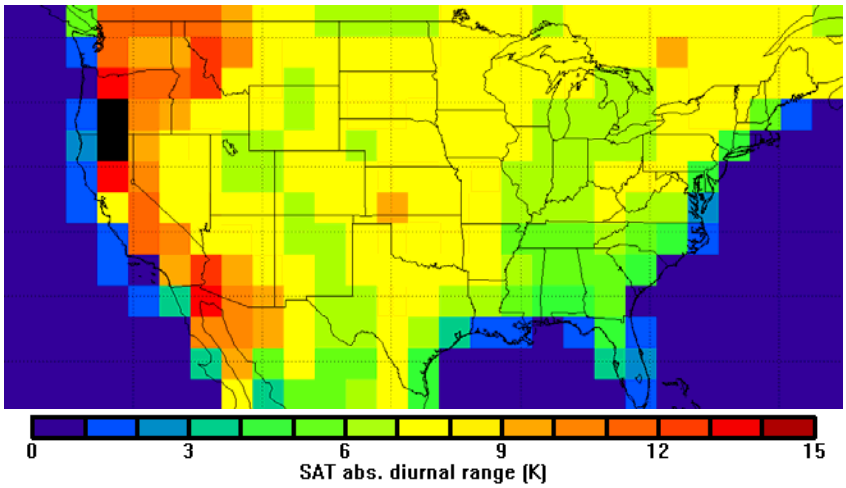

Figure 3.9. SAT diurnal range for a) NARR and b) SPV4. There is no plot for NICAM because the temporal resolution is too low to represent the NICAM diurnal cycle.

a) NARR

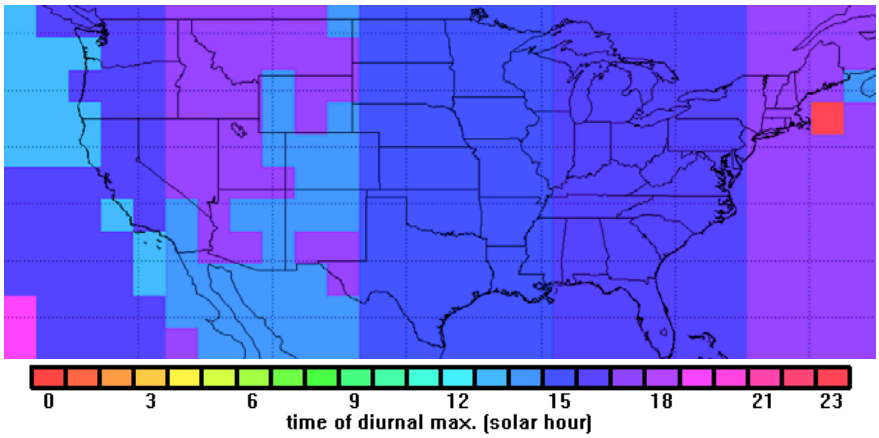

b) SPV4

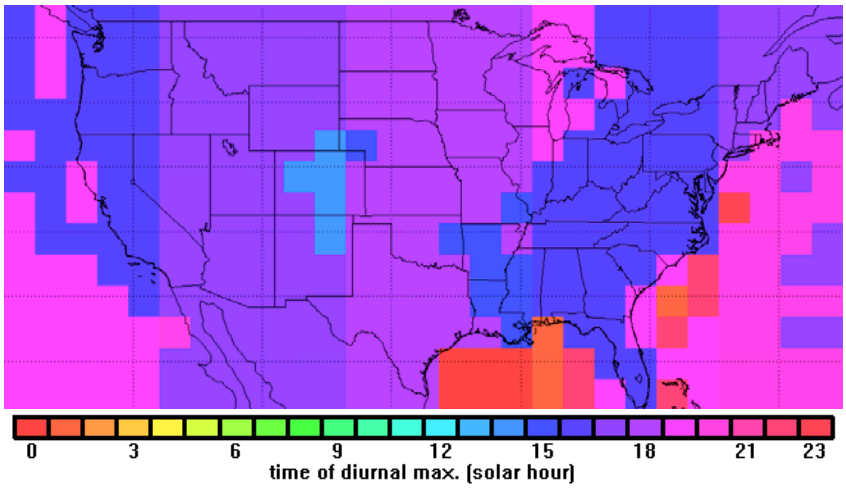

Figure 3.10. SAT diurnal time of maximum for a) NARR and b) SPV4.

a) NARR

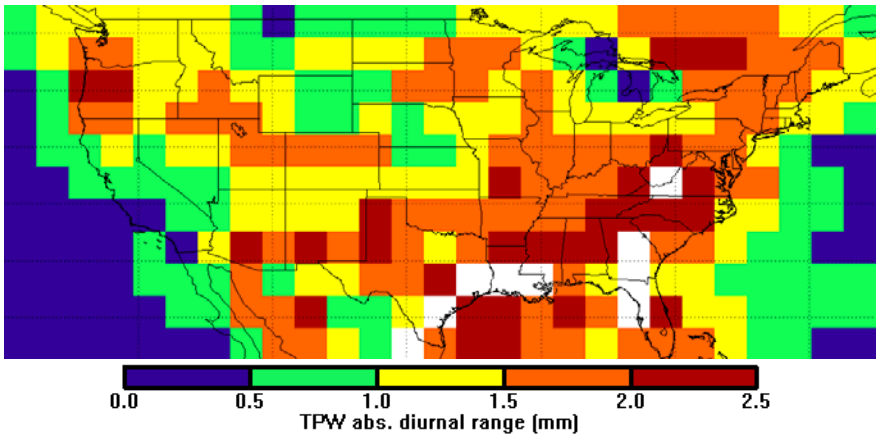

b) SPV4

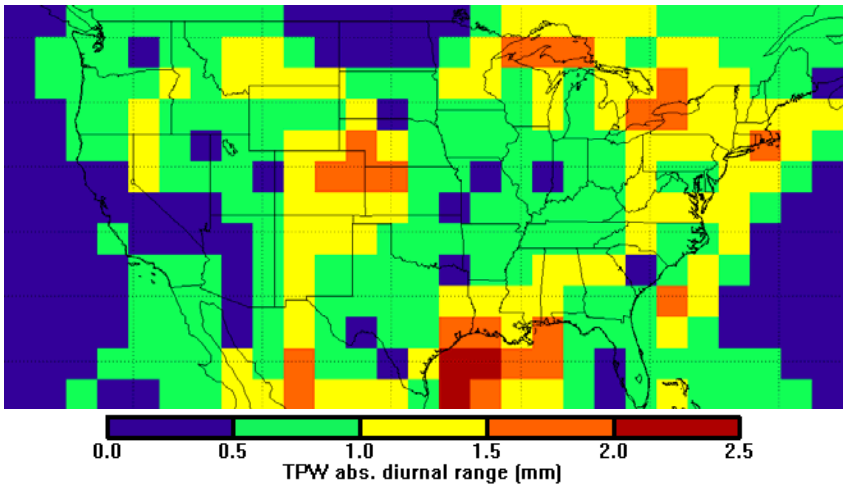

Figure 3.11. As Fig. 3.9, but for TPW

a) NARR

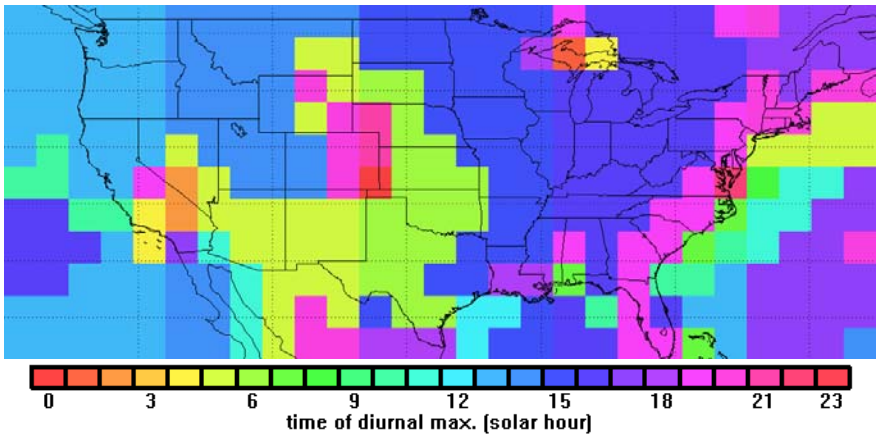

b) SPV4

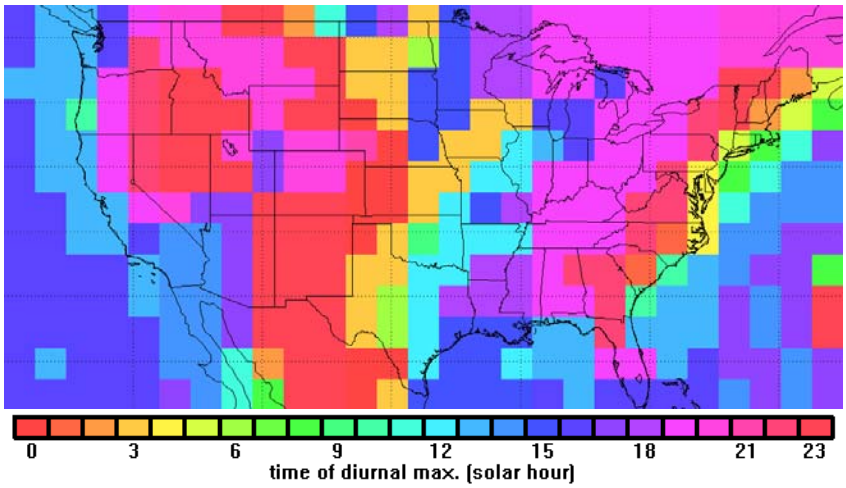

Figure 3.12. As Fig. 3.10, but for TPW

a) NARR

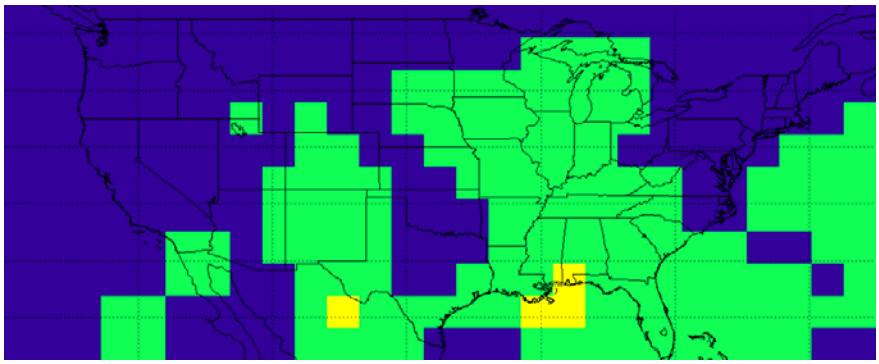

b) SPV4

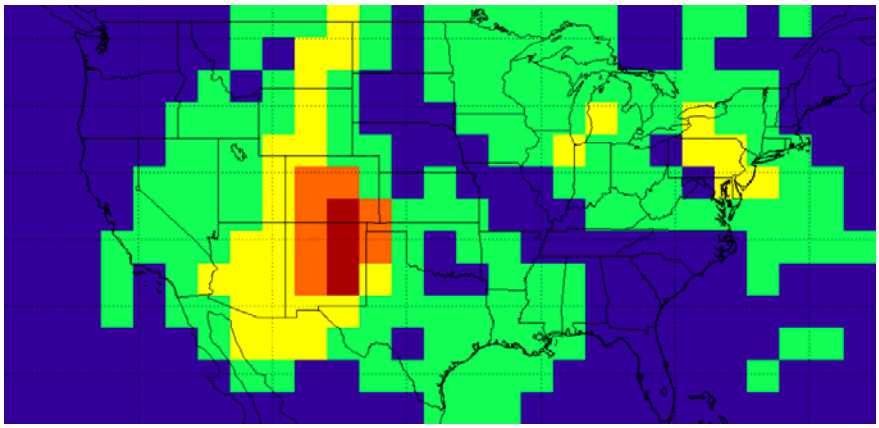

Figure 3.13. As Fig. 3.9, but for W500.

a) NARR

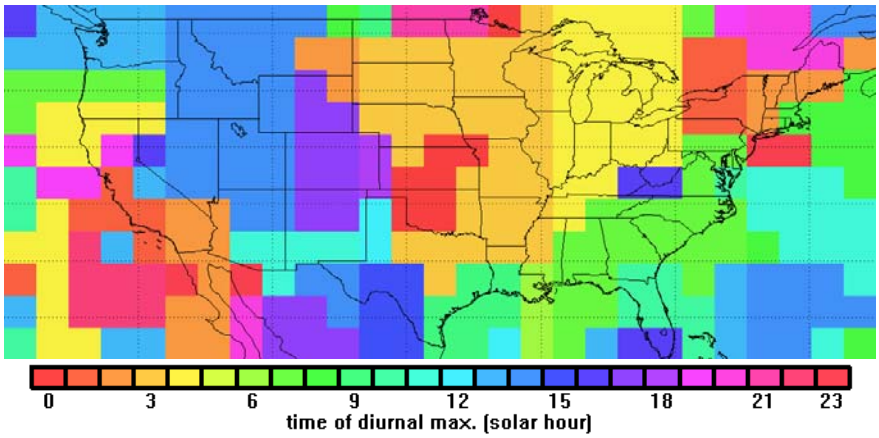

b) SPV4

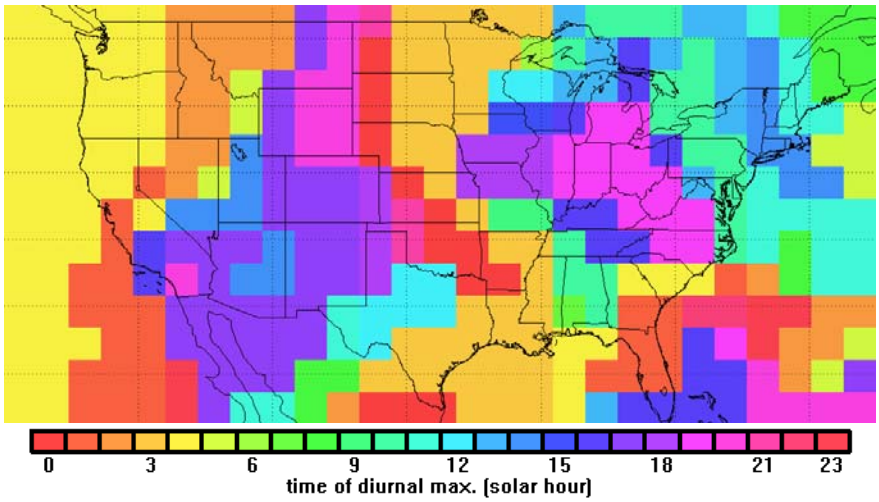

Figure 3.14. As Fig. 3.10, but for W500.

a)

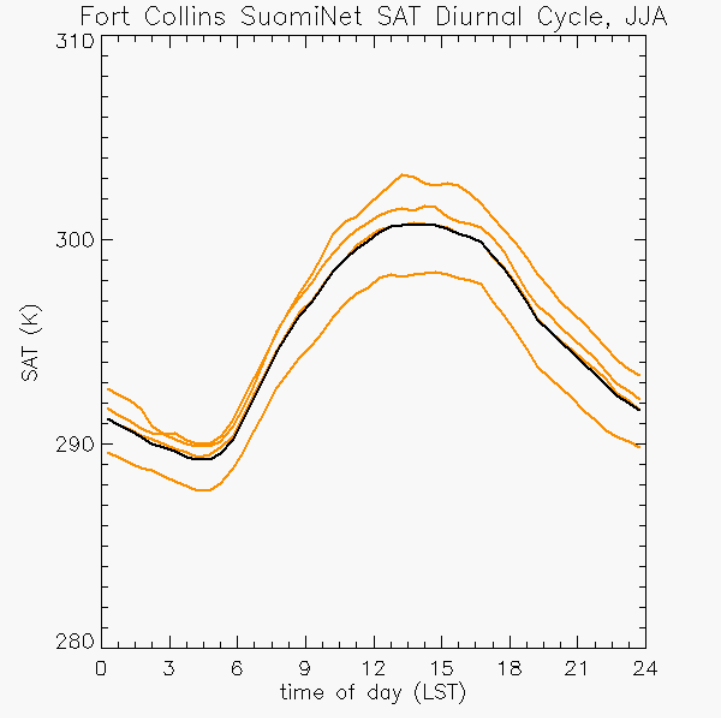

b)

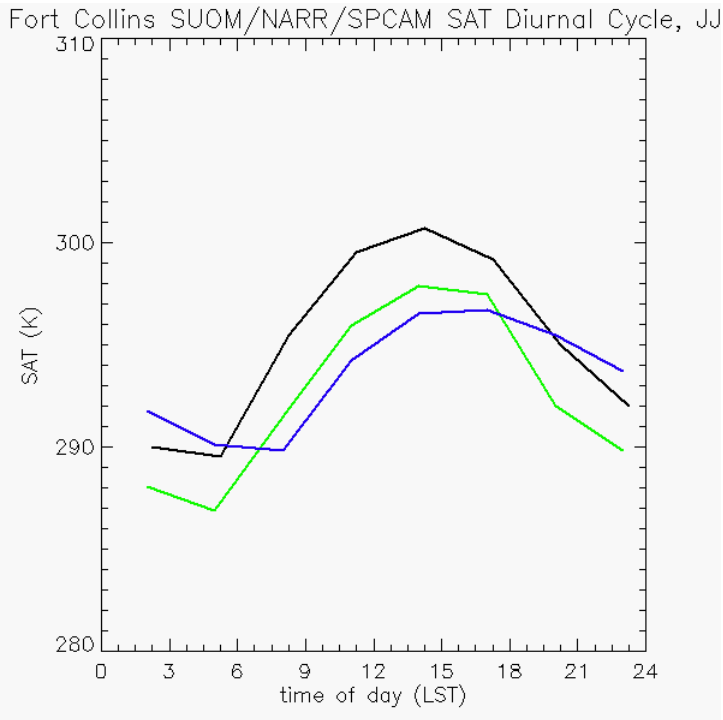

Figure 3.15. The FTCL SuomiNet diurnal cycle of SAT for JJA 2009-2012, with individual years in orange, and the 5-year mean in black. b) The SAT cycle for JJA 2006-2010 for SuomiNet (black), NARR (green), and SPV4 (blue).

a)

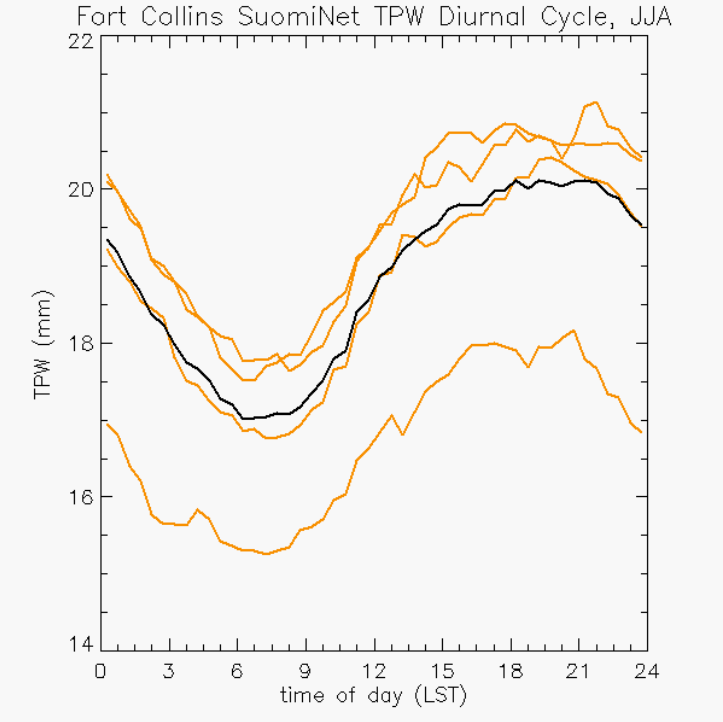

b)

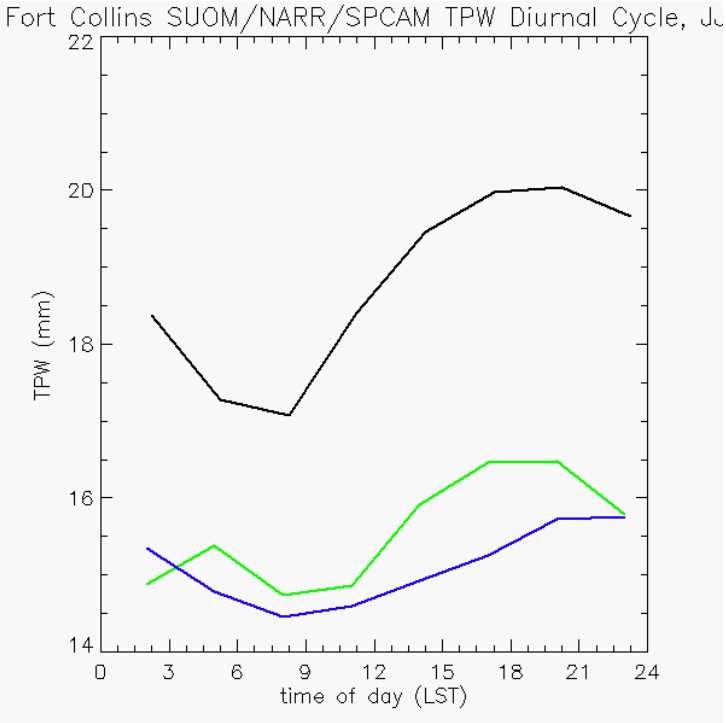

Figure 3.16. Same as Fig. 3.15, but for TPW.

a)

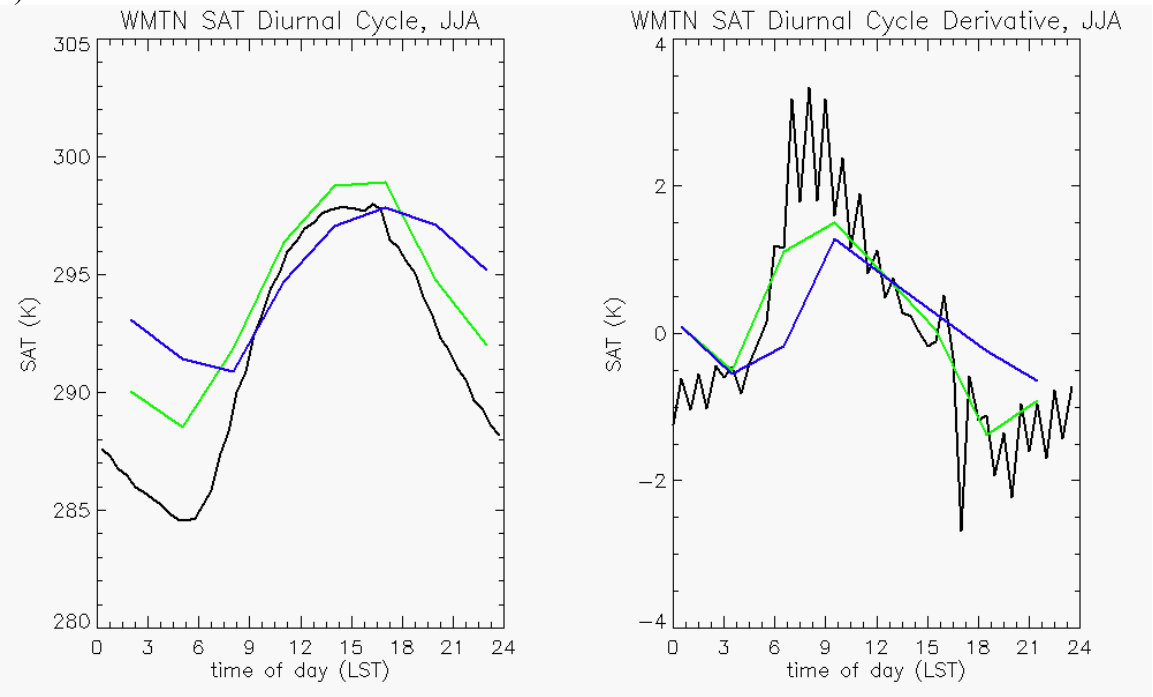

b)

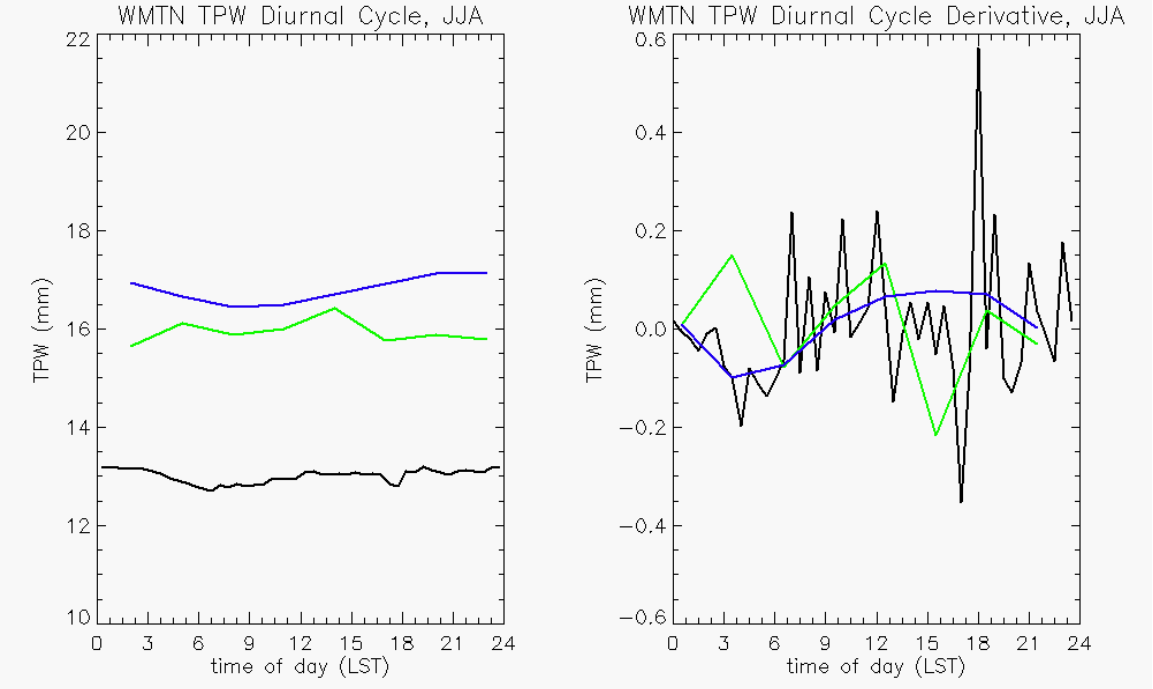

Figure 3.17. The WMTN diurnal cycle of SAT for JJA 2006-2012, with SuomiNet (black), NARR (green), and SPV4 (blue). The left panel is the cycle, and the right panel is the first derivative of the left panel. b) Same as a) but for TPW.

a)

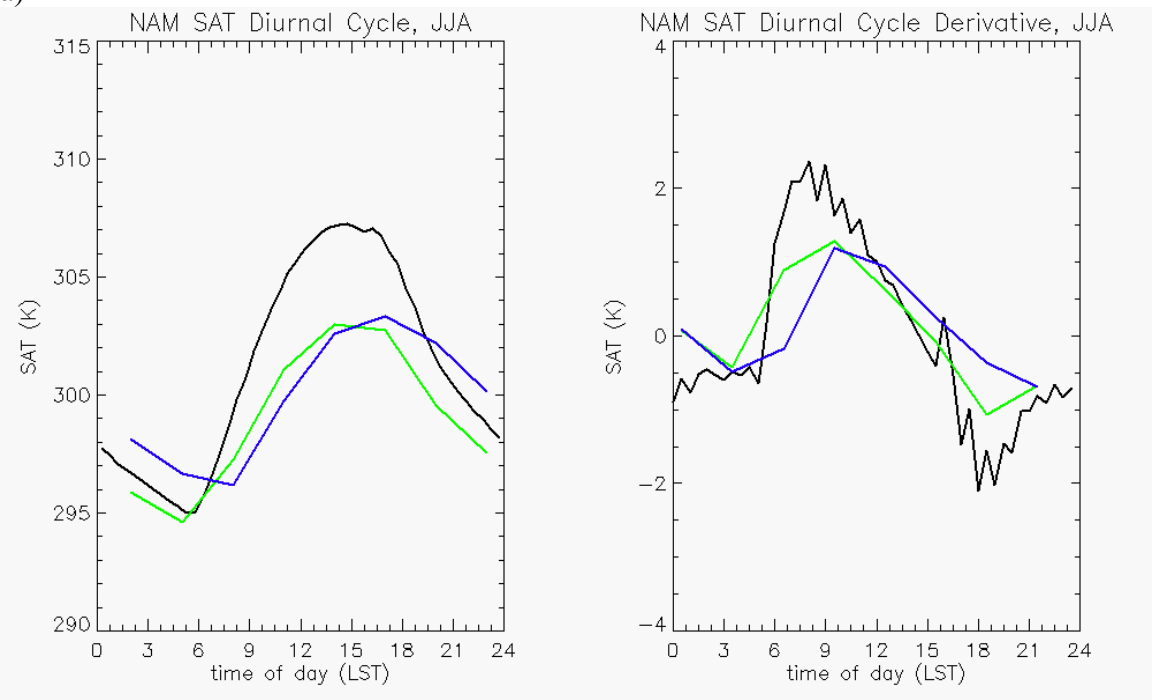

b)

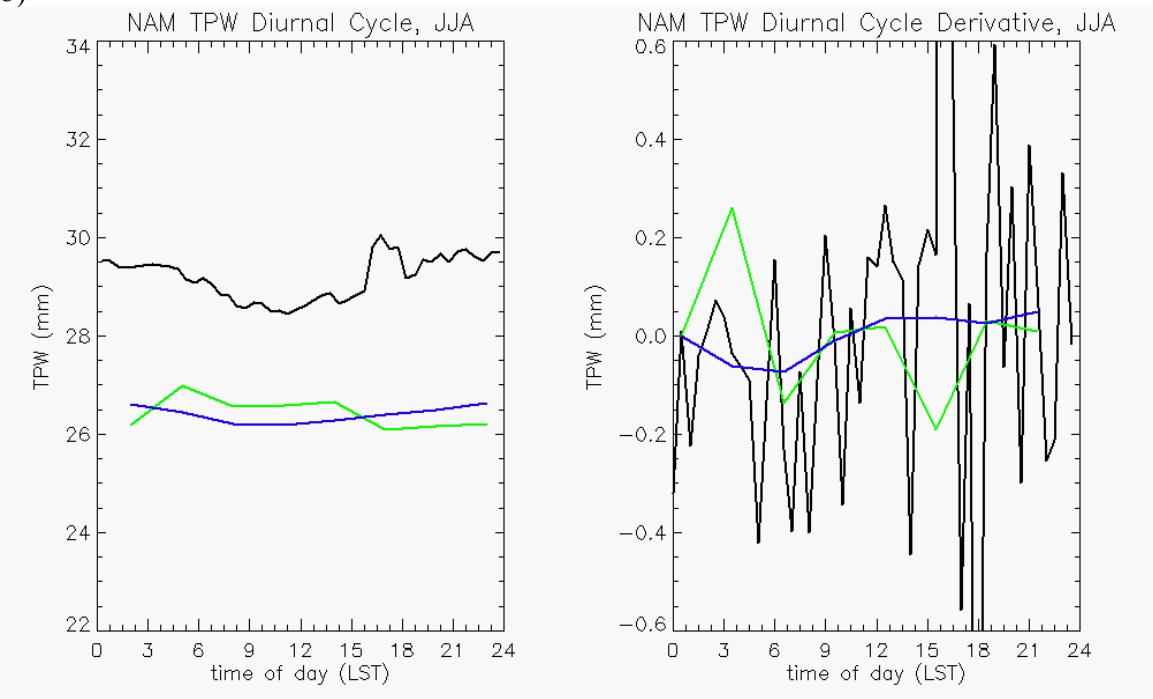

Figure 3.18. As Fig. 3.16, but for NAM.

a)

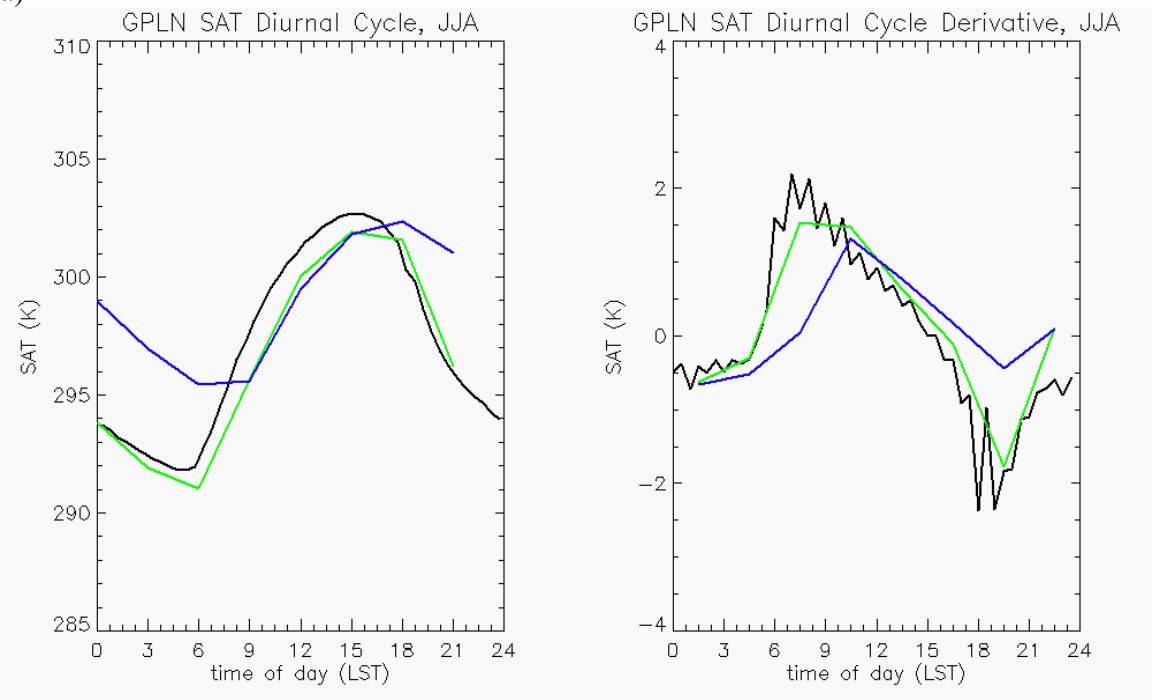

b)

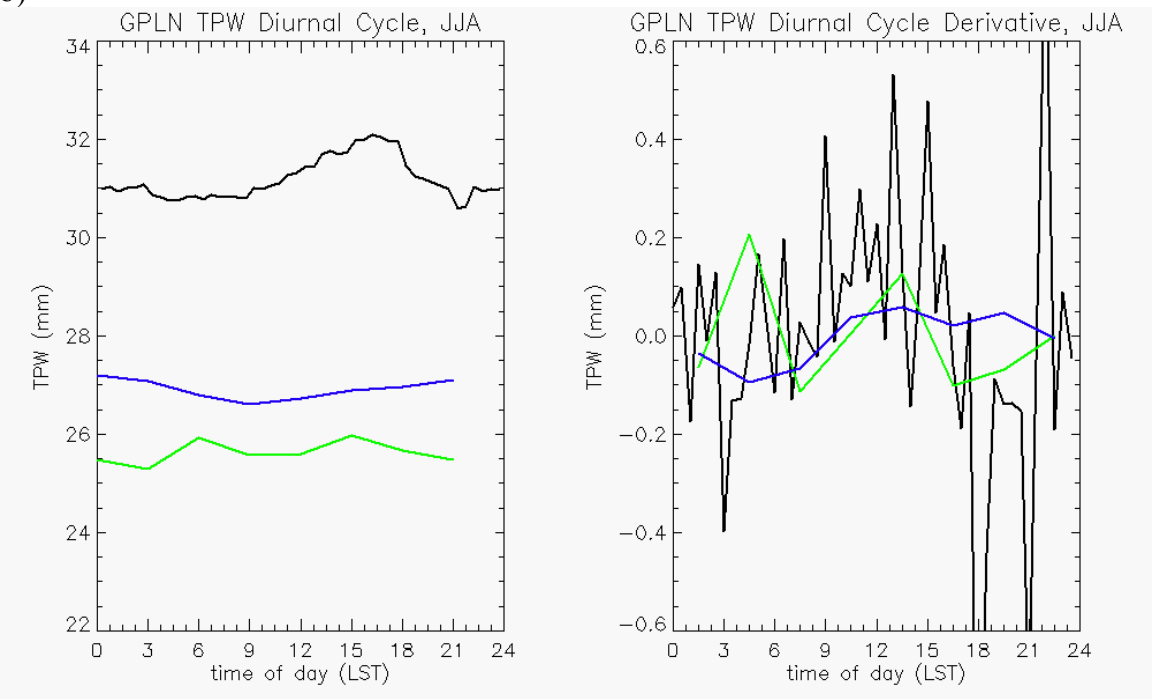

Figure 3.19. As Fig. 3.16, but for GPLN.

a)

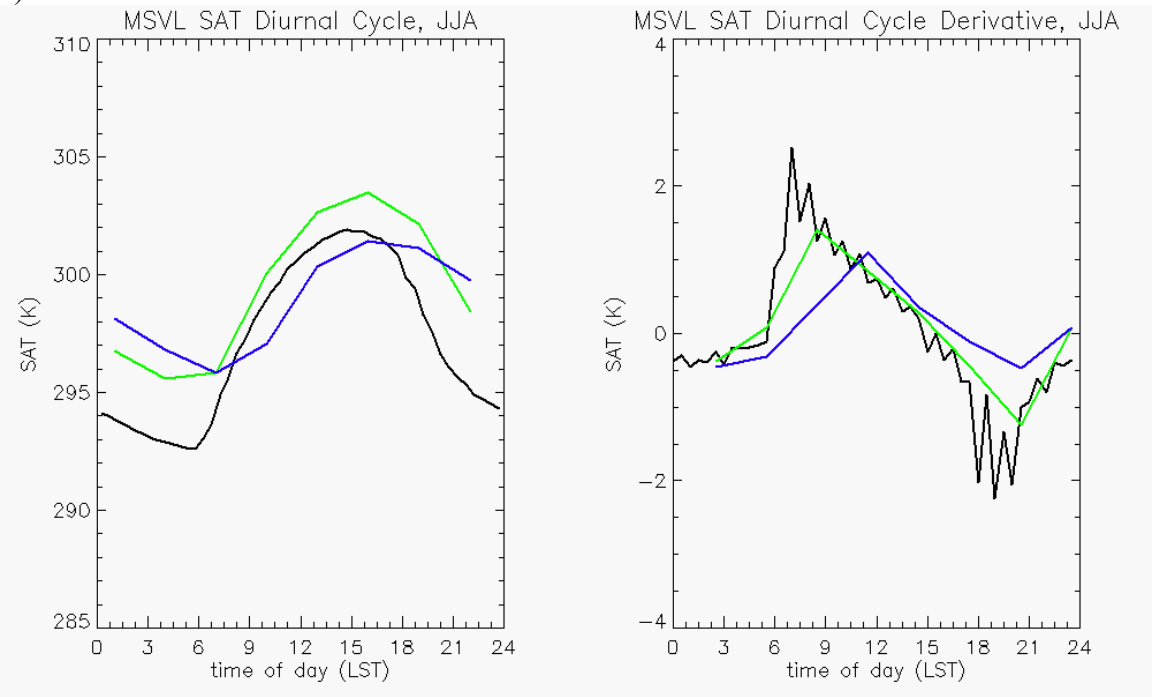

b)

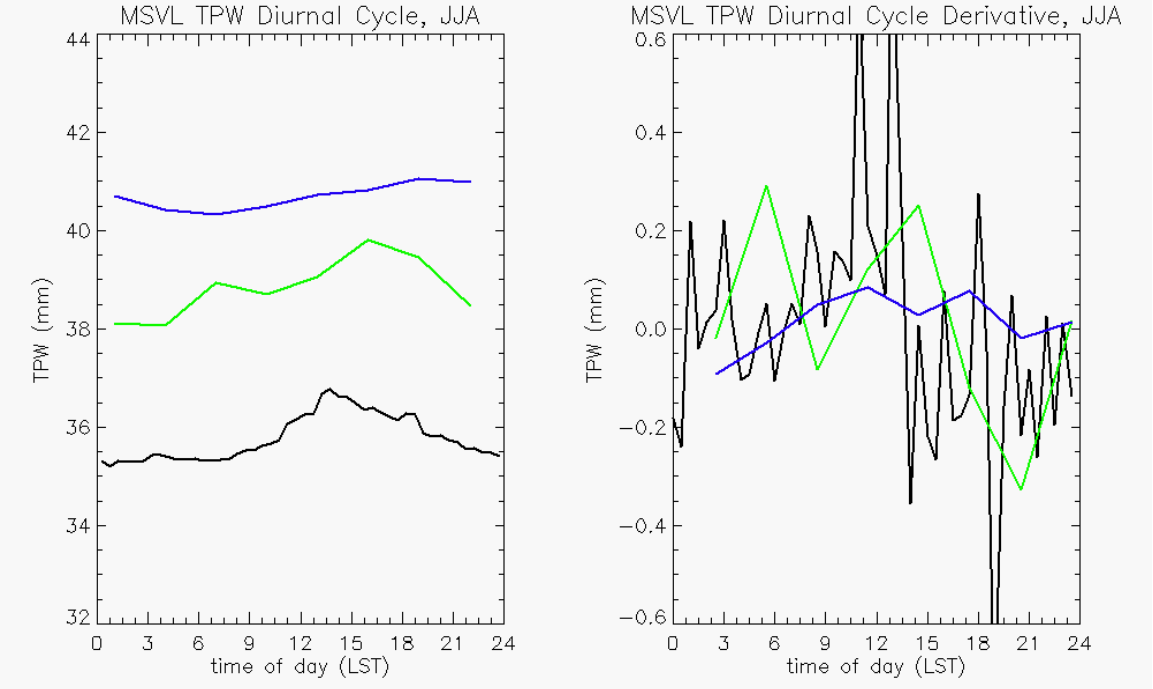

Figure 3.20. As Fig. 3.16, but for MSVL.

a)

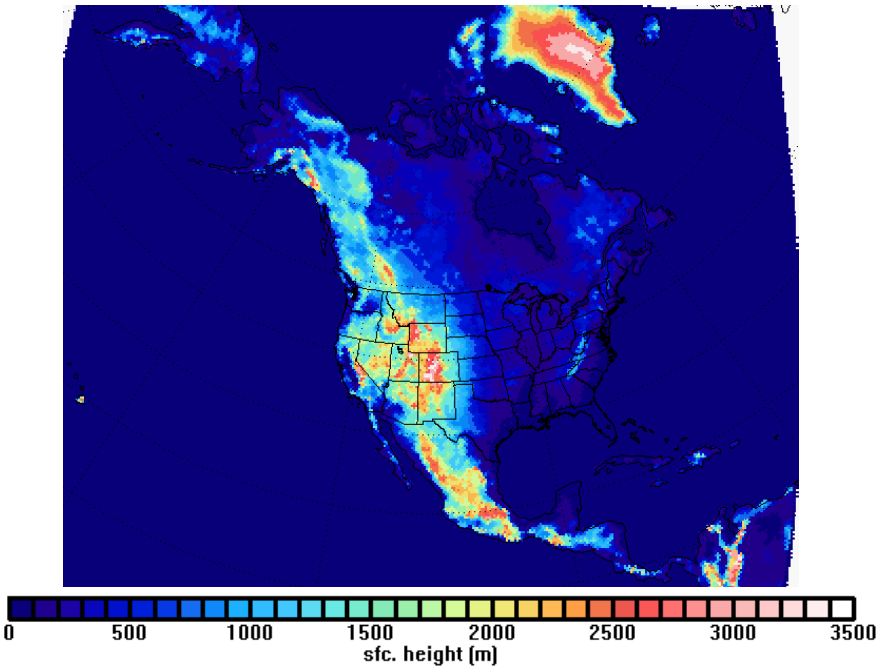

b)

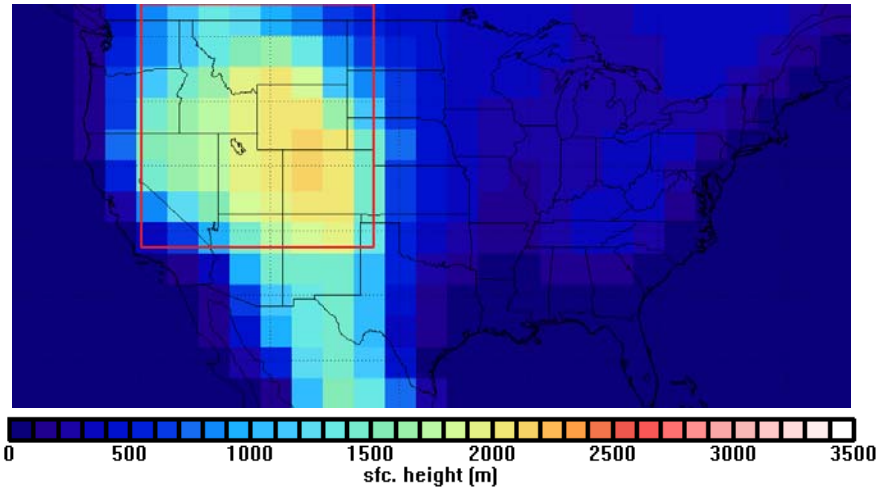

c)

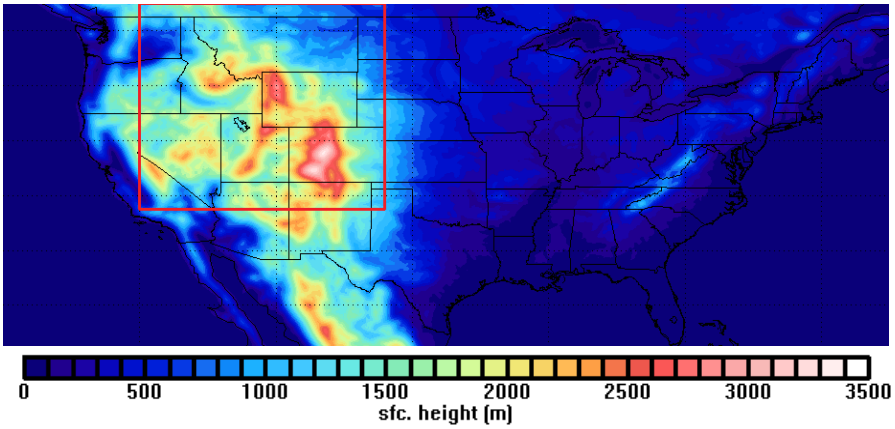

Figure 3.21. Terrain elevation maps of CONUS for a) NARR, b) SPV4, and c) NICAM.

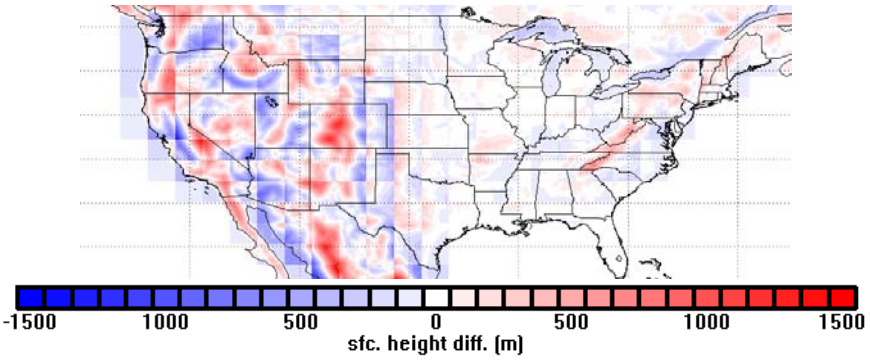

Figure 3.22. Terrain elevation difference map between NICAM and SPV4. Positive (red) values are where NICAM is larger than SPV4.

a)

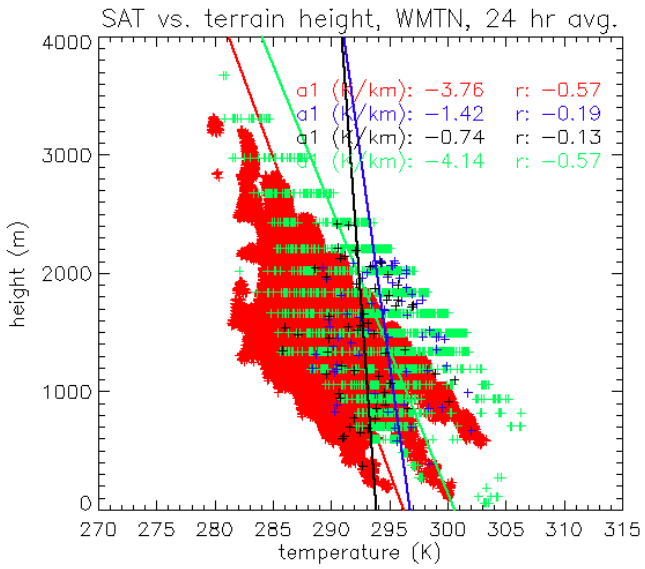

b)

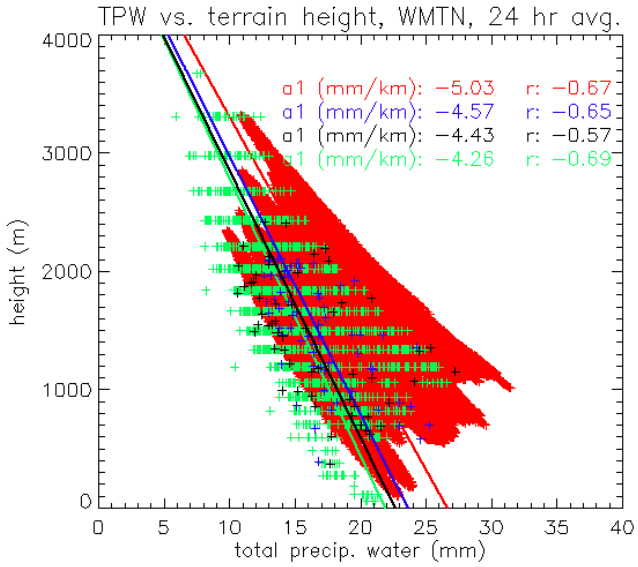

Figure 3.23. Scatter plots and regression lines for WMTN a) SAT and b) TPW for JJA, all times of day. Black is N/NR, green is NARR, red is NICAM, and blue is SPV4. The regression slope (a1) and correlation (r) values for each dataset are listed in the upper right of each plot.

a)

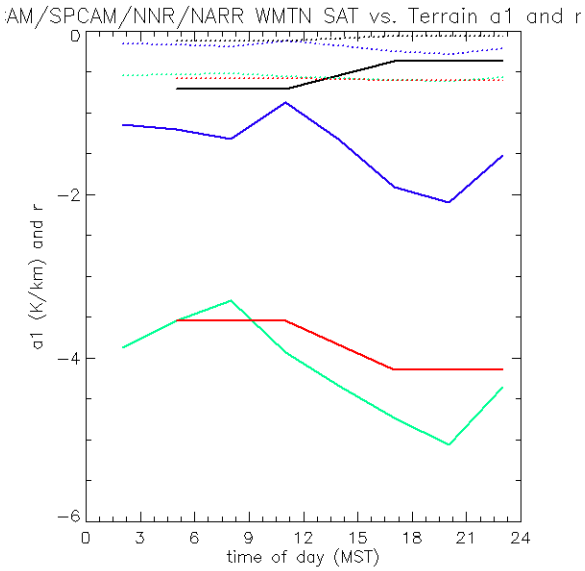

b)

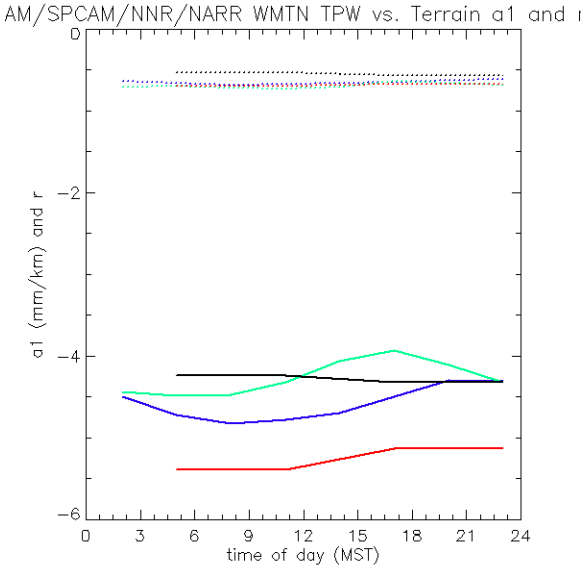

Figure 3.24. The diurnal cycle of LSEV vs. elevation regression slope (a1, solid line) and correlation (r, dotted line) in WMTN a) SAT and b) TPW for JJA. Black is N/NR, green is NARR, red is NICAM, and blue is SPV4.

4. COMPARISON OF OBSERVED AND SIMULATED CUMULIFORM CLOUDS OVER THE CONTINENTAL UNITED STATES BY SPACEBORNE W-BAND RADAR, GLOBAL CLOUD-RESOLVING MODEL, AND MULTISCALE MODELING FRAMEWORK, PART 2: HYDROMETEOR VARIABLES

4.1 Introduction

This section is a continuation of the work started in Chp. 3. Here the observed and simulated cloud variables will be examined. The primary focus will be on the vertical structure of convective clouds, similar to Chp. 2. In addition, a brief analysis of surface precipitation will be presented, as it represents an important link between the atmospheric and surface water cycles.

4.1.1 Previous Studies of CONUS deep convection with NICAM and SP-CAM

NICAM

NICAM has been used little for investigating CONUS convection. Dirmeyer et al. [2012] investigated the diurnal cycle of precipitation simulated by NICAM and other climate models. They used a simulation of global JJA for 2001-2009 (excluding 2003), with a 7km horizontal resolution and the 6-category single moment bulk microphysical scheme. Their analysis particularly focused on the CONUS region and south/east Asia, which both exhibit distinct unusual diurnal variability spatial patterns. The model data were compared with observations from the Global Precipitation Climatology Project (GPCP) and the Tropical Rainfall Measurement Mission (TRMM). Globally, NICAM has the most realistic simulation of the timing of diurnal precipitation maximum, but the magnitude of diurnal variability is slightly too large.

NICAM generally overestimates the magnitude of the diurnal precipitation variability over most of CONUS and the surrounding ocean. The simulated magnitude for Florida is realistic, but it is too large elsewhere. The Great Plains nocturnal maximum is not captured at all. Almost all location in CONUS except the far northwest have a precipitation maximum during local afternoon to evening. All other models tested also do not handle this feature properly, though certain versions of the Integrated Forecast System model from ECMWF display a feature that vaguely resembles the Great Plains nocturnal maximum. This specific failure does not seem to be a symptom of a general shortcoming in NICAM, however. NICAM successfully simulates the timing of multiple key precipitation features over south/east Asia, even where other climate models fail. However, the magnitude of the diurnal variability over south/east Asia is also too large in most regions, including over the ocean.

These results suggest that NICAM land convection is not phase-locked to solar heating the way that other GCMs are, but NICAM is still unable to successfully simulate the meteorological processes that govern the Great Plains nocturnal maximum. All other models used in the paper but one contain convective parameterization schemes, and all these models exhibit the typical phase-lock problem. The super-parameterized Community Climate System Model (SP-CCSM) does not appear to have as severe a phase-lock problem either, though it has other problems with diurnal timing. The paper supports the conclusion that the removal of convective parameterization in NICAM and increased resolution improves its ability to simulate realistic deep convection, but they alone are not sufficient to realistically simulate all aspects of deep convection.

SP-CAM

Prichard and Somerville [2009] investigated the SP-CAM's simulation of the precipitation diurnal cycle. They used the "standard" version of SP-CAM, v3.0, which has a semi-Lagrangian global spectral dynamical core at T42. Similarly with NICAM, SP-CAM does not exhibit the "phase-lock" problem of other GCMs. Diurnal variability over land does not follow as rigidly the solar cycle in a sinusoidal manner, and the timing of maximum precipitation can vary heterogeneously spatially. The diurnal variability in monsoon regions in particular is improved (the CAM-only version has too high an amplitude). Coastal precipitation regions are represented more realistically in SP-CAM. SP-CAM is able to keep the deep convection over land from developing until the afternoon, whereas the CAM-only model develops deep convection as soon as solar heating warms the lower troposphere. Prichard and Somerville interpret this as the SP-CAM simulating shallow convection more realistically than the CAM-only.

Prichard and Somerville focused on the diurnal cycle of the North America region. They found that SP-CAM has a dry bias over the central CONUS, related to an inability to simulate the eastward movement of the Great Plains nocturnal maximum. SP-CAM places a broad local evening precipitation maximum across the Great Plains region. They attribute this inability to the limited capability of SP-CAM to allow movement of long-lived MCSs from the Rocky Mountains to the central Great Plains. Simulating the motion of long-lived MCSs is a difficult problem for SP-CAM, and the MMF approach in general, because of the way convection is handled. The DCCs themselves "live" in the CRM of each grid box, but CRMs in neighboring grid boxes do not directly communicate with each other. They only communicate indirectly by influencing the CAM-level grid boxes. An MCS in the CRM of one gird box cannot directly pass into the CRM of the neighboring grid box. So in a sense a new MCS has to be generated in each

neighboring grid box to simulate the motion of a continuous MCS. This is not a problem shared with NICAM. However, as discussed previously, the causes of the Great Plains nocturnal maximum are more complicated than simply the eastward movement of MCSs. Even if MCSs don't move eastward over long distances in SP-CAM, this is also true for many observed MCSs. The inability of SP-CAM to simulate the eastward movement probably indicates additional problems with SP-CAM than just unrealistic MCS motion. And the similar inability of NICAM to simulate the eastward movement supports the conclusion that MCS motion alone is not a dominant problem.

Pritchard and Somerville also note that the limited representation of topography in SP-CAM may contribute to the unrealistic CONUS diurnal cycle. In reality, the afternoon convective maximum over the Rocky Mountains is related to enhanced solar heating of the steeply-sloped terrain. This is crucial for the development of the solenoidal mountain/plains circulation described previously. In SP-CAM, the terrain has been smoothed to CAM resolution. There is no terrain variation on the CRM scale. This places a major limitation on SP-CAM for handling terrain-related meteorology.

Pritchard et al. [2011] further investigated the issue by using a modified form of the SP-CAM (called SP-CAM3.5), a finite volume dynamical core at 1.9° x 2.5° horizontal resolution. They found that the modified model produces a propagating organized convective signal, unlike the SP-CAM3.0. They argue that DCCs produced within a gridbox on the CRM level create a warming-over-cooling vertical dipole structure (characteristic of mature MCSs) in the CAM gridbox. This triggers baroclinically-generated gravity waves which trigger DCCs in the neighboring gridboxes. In this way a mature MCS can move with time in SP-CAM. There model simulation shows several examples of long-lived MCSs developing over the Rocky Mountains

during afternoon and moving eastward with time. This improvement may help in allowing SP-CAM to simulate the nocturnal maximum realistically, though it remains to be seen how large the improvement will be.

Kooperman et al. [2013] followed up with an examination of MCSs in SP-CAM v3.0, v3.5, and v5. They used a technique modeled on the MJO index developed by Wheeler and Hendon [2004], where an EOF technique is applied to the observed and simulated OLR fields to measure the eastward movement of MCSs over the Great Plains. They found that the SP-CAM variants were all able to simulate eastward movement, and SPv5 most closely resembled the observations. The standard CAM variants did not produce the observed eastward motion. Clearly SP-CAM allows for more realistic simulations of convective system characteristics and behaviors than conventional GCMs, and improved microphysics also improves the representation. However, the realism of individual clouds simulated in SP-CAM remains an open question, and the following chapters will attempt to address it.

4.2.2 SP-CAM single moment and double moment versions

SP-CAM attempts to address the problem of cumulus parameterization by replacing it with a CRM within each grid box. As discussed in previous chapters, the removal of the cumulus parameterization does not remove the dependence on other parameterization schemes. Of these other schemes, the microphysical scheme is perhaps the most serious limitation. Real-life microphysics is highly complex and has a profound influence on cloud properties. And yet the computational representation of it must necessarily be kept much simpler in order to make atmospheric models practical to use. It is a difficult task to balance the increased realism of more

sophisticated microphysics with the increased cost of runtime. This chapter also seeks to investigate the benefits of a more sophisticated microphysics scheme used in SP-CAM.

The two most common options for microphysical schemes are bulk schemes and bin schemes. Bin schemes directly calculate changes in mass and number concentrations for each size hydrometeor without assuming a distribution shape. This method is computationally very expensive, and is used mostly for very specialized applications such as high resolution cloud models. Bulk schemes assume a basic shape for the size distribution for each hydrometeor species, and allow the distribution to change around this basic shape according to a number of variables, called "moments". These moments include the mass concentration of hydrometeors, the number concentration, and the width of the size distribution. A microphysical scheme that predicts one of these variables while holding the others constant is called a "single moment" scheme. A microphysical scheme that predicts two is a "double moment" scheme, and one that predicts all three is a "triple moment" scheme. Ideally, the realism of the microphysical scheme will increase as the number of moments increases (assuming the predicting equations are realistic, something that isn't always easy to verify). But the main cost is computational time. A double moment scheme, depending on the complexity, can cost an order of magnitude more time to run than a single moment scheme, all other aspects of the model held the same (for SP-CAM the cost is about triple). More runtime required means fewer experiments. That's why it is desirable to carefully examine the benefits of increasing the moment number of the microphysics scheme.

Double moment schemes have been used in other atmospheric models, both climatic and numerical weather prediction, to improve the representation of deep convection and convective systems. There have been several reports of the double moment scheme leading to improved

DCCs and associated meteorological systems, though it's not always guaranteed. Swann [1998] compared the simulation of convective case studies in southern England using a CRM with single and double moment schemes. He found that the simulated precipitation radar reflectivity for the double moment simulation matched observations much more closely than the single moment simulation. In addition, the surface precipitation was also affected by the microphysics (observations were not provided). Morrison et al. [2009b] found that simulations of squall lines with the Weather and Forecasting model (WRF) are affected by the double moment scheme. The single moment scheme results in a limited trailing stratiform precipitation region forming from the DCCs, and the double moment scheme resulted in a substantially larger stratiform region, with larger rain rates. This change is attributed to reduced evaporation of stratiform rain, as well as increased evaporation and detrainment from DCCs feeding the stratiform region with more moisture. Dawson et al. [2010] found that the use of a double moment scheme in a large eddy simulation of a tornadic supercell resulted in improved simulated precipitation radar reflectivity as well as weaker cold pool formation. Cold pools are thought to have a critical role in tornadogenesis, so the ability to simulate cold pool formation realistically is very important. Song and Zhang [2011] used double moment schemes in CAM 3.5 single-column simulations of DCCs and found improvements in the convective microphysical properties, as well as enhanced convective detainment to the environment (similar to Morrison et al. [2009b]). So it appears that there is a degree of utility for double moment schemes that could offset the increased computational expense.

There is a major caveat to bear in mind, however. Switching from single moment to double moment microphysics in itself does not necessarily improve simulated clouds if the assumptions in the scheme are unrealistic or are incompatible with the specific model in question. Weverberg

et al. [2013] tested the effect on a single moment, single/double moment hybrid, and full double moment scheme on simulated Pacific tropical deep convection in a CRM. They found that while the different schemes had a large effect on the spatial distributions and size distributions of hydrometeors (and presumably an associated effect on radiation and possibly cloud feedbacks), there was little effect on the mean surface precipitation and updraft characteristics. All three simulation types overpredicted surface precipitation and optical thickness (and presumably vertical mass flux). Weverberg et al. [2012] found that the simulation of squall line surface precipitation and large frozen hydrometeors are highly sensitive to the type of double moment scheme used, including arbitrary thresholds that govern the interaction of different hydrometeor types. Morrison and Milbrandt [2011] found a similar conclusion simulating supercells with WRF. These findings further highlight the need to compare the macrophysical characteristics of simulated clouds with observed clouds, as well as comparing microphysical characteristics between models.

SP-CAM versions 3 and 4 use the single moment scheme described in Chp. 3. As mentioned before, this scheme has a highly simplified treatment of hydrometeors, especially cloud liquid and cloud ice. The notable overproduction of cloud ice is probably caused by this. SP-CAM version 5 utilizes a double moment scheme which includes a more sophisticated treatment of all hydrometeor species. This scheme is described in the following section. The main changes between SP-CAM 4 and 5 are the microphysical scheme and the radiation scheme. This provides a good opportunity to investigate the effects of the double moment scheme on the model without too many other changes obscuring the microphysics-only effects.

4.2.3 Chapter goals and questions

The primary goal of this chapter is to identify unrealistic cloud characteristics in the models. Unrealistic characteristics can be caused for a number of reasons, including unrealistic microphysical parameterizations, unrealistic local (in/near cloud) dynamical and thermodynamical processes, and unrealistic behavior of LSEVs. By conditionally sampling cloud characteristics by LSEVs, we can determine which unrealistic cloud characteristics are not caused simply by unrealistic LSEV behavior.

Specific questions that will be address in this chapter are as follows:

1. How realistic are cloud characteristics in the models? Cloud frequency? Cloud altitude and thickness? Cloud radar reflectivity?

2. How realistically are clouds distributed across CONUS?

3. And related, how realistically is precipitation distributed across CONUS?

4. How realistic is the diurnal cycle of precipitation?

5. What are the relationships between clouds and LSEVs? Do the models simulate them realistically?

6. Can biases in cloud characteristics be explained simply by biases in LSEVs? (E.g. clouds form more often in moist conditions than dry. A model is too dry, and doesn't form enough clouds. Does the model lack clouds simply because it is too dry?)

4.2 Datasets

The datasets used in Chp. 3 are also used here. The models used are NICAM, SPv4, and SPv5 in the same configurations as in Chp. 3, with the same spatial and temporal domains. Cloud observations are taken from CloudSat, over the CONUS region, during JJA 2006-2010, both AM

and PM overpasses. LSEVs are taken from NARR, which are co-located with CloudSat in time and space for the joint CloudSat/LSEV analyses.

One additional dataset is used: the Climate Prediction Center Hourly Precipitation (CPCHP) product. This product uses rainfall data from surface rain gauges and extrapolates the results across CONUS on a 2.5° x 2.5° horizontal grid [Mesinger et al. 2005]. Temporal resolution is one hour, as the name implies. The time domain used is 1982-2002. This is longer than the time domain used for other observations, but it reduces the noise in the diurnal cycle analysis considerably. As noted previously, this product is assimilated into NARR, so NARR and CPCHP are not completely independent of each other.

Also, in order to simulate CloudSat observations of the model atmospheres, Quickbeam is used again. For NICAM, the setup for Quickbeam is exactly the same as used for Chp. 2. For SP-CAM, a variation is used. In the SP-CAM microphysics, hydrometeor characteristics are explicitly simulated in the model for precipitation hydrometeors (rain, snow, and graupel). The distributions used in the model are used in Quickbeam. But for cloud liquid and ice, there are no explicit distributions used in the microphysics. Only the hydrometeor mixing ratios are given, which are used in the conversion equations between cloud water, vapor, and precipitation. In order to simulate the reflectivity for cloud hydrometeors, the NICAM distributions for cloud liquid and ice (taken from the Grabowski microphysical scheme) are used. By doing this, one source of potential difference between the cloud reflectivity profiles of the two models is removed. The same microphysical assumptions are used for both SPv4 and SPv5, even though the microphysical schemes are different between the models. This is done again to reduce the possibility of the radar simulator affecting the simulated reflectivity.

The data here are presented for the CONUS region, as identified in Chp. 3. The CONUS region has been divided into ECONUS and WCONUS subregions, and all data aside from planar maps are presented for each region separately. The reason for this is that CONUS has different terrain between the two subregions. ECONUS is relatively flat, with only a few shorter mountainous regions such as the Appalachian and Ozark mountains. WCONUS contains more mountainous regions such as the Rocky Mountains and Sierra Nevada. Because of this difference in terrain, the results for ECONUS represent a somewhat more "idealized" testing field for model behavior, where terrain influence is minimal. For WCONUS, the terrain could possibly influence the observed results (though in practice this influence is surprisingly small), and the models' limited ability to simulate the mountains (as shown in Chp. 3) could cause additional disagreements between models and observations (though again, in practice they are rather small).

4.3 Cloud and Precipitation Planar maps

Before examining the vertical cloud profiles, it would be useful to examine the spatial distribution of clouds and precipitation in observations and models. Cloud distribution is represented with COF, and precipitation distribution with the rate of surface precipitation (SPREC). The cloud frequency statistics for ECONUS and WCONUS have been compiled in Table 4.1.

4.3.1. Clouds

Fig. 4.1 shows the COF distribution of all cloud types observed by CloudSat and simulated in NICAM and SP-CAM. It should be noted that the CloudSat observations are not meant to represent the full 24 hour mean cloud cover over CONUS. CloudSat passes over CONUS only

during early morning and early afternoon, and it does not sample the entire diurnal cycle. So any cloud cover that is diurnally dependent (e.g. DCCs and anvils) will not be fully represented by CloudSat. CloudSat observes a fairly even cloud distribution across CONUS. COF is higher in upper New England and southeast Canada, the Pacific northwest, southern FL, and the astern portion of the NAM region up (NM/eastern AZ/north central Mexico) into CO. COF is lower in the western half of the NAM region up to northern CA and NV, and the southern Midwest (TX/LA/AK). Unfortunately lack of observations prevents seeing the detail of the marine stratocumulus off the Pacific coastline. A comparison with ISCCP data (not shown) suggests that the CloudSat observations shares roughly the same cloud distribution with other cloud observations, though the mean CONUS COF for CloudSat is lower (likely because CloudSat cannot easily detect high clouds).

NICAM reproduces much of the observed cloud distribution, though there are some notable differences. The mean COF over CONUS is higher (as indicated in Table 3.1). The COF is higher over northern New England, the Pacific northwest, CO, FL, and north-central Mexico as observed. COF is lower over the western NAM region up into CA and the Great Basin region as well. One major difference is the presence of high COF values across TX and the US southeast. The contrast between simulated and observed TX is particularly notable, as TX is observed to have a lower COF than the CONUS mean. Another difference is the extension of the New England high COF westward over the Great Lakes and Canada to the north.

SPv4 likewise produces some of the observed distribution, with some notable errors. The mean CONUS COF is higher than observed, though not as high as NICAM. The high COF over northern New England and southeast Canada, and there is a hint of the higher COF over north-central Mexico. The low COF over the western NAM region, CA and the Great Basin is also

reproduced. But the COF in this region is much lower than observed, and also extends into the Pacific northwest. The low COF over the southern Midwest is largely displaced into the northern Midwest. There is an unobserved high COF in the US southeast, similar to NICAM, but the observed high COF over FL is not simulated.

Over the entire CONUS region, COF has generally increased slightly from SPv4 to SPv5. This increase occurs in most regions, almost equally over ECONUS and WCONUS. The coastal Atlantic is particularly cloudier as well. A couple of regions show decreases, particularly parts of the Pacific northwest.

Fig. 4.2 shows the observed and simulated COF distribution of PBLRCs. CloudSat shows a lower COF value over ECONUS than WCONUS. The higher COF values over WMTN down into central Mexico are highly apparent and not surprising. CloudSat samples the region during the early afternoon, when cumulus cloud formation over higher terrain from terrain-induced upslope flow tends to occur [Orville 1965]. The low COF values in the western Nam region, CA, and the Great Basin are similarly expected, given the climatological dryness of that region. The large region of low COF values covering much of the Great Plains and ECONUS is more difficult to explain. Shallow cumulus fields are a common occurrence over ECONUS during JJA [Rabin and Martin 1996]. While the cloud fraction from shallow cumulus clouds (up to 20%) is less than from all cloud categories (sometimes above 50%), it seems reasonable that they would be more common in CloudSat observations. CloudSat should have little difficulty detecting most cumulus clouds, except perhaps the smallest ones that are less than 1 km in diameter and near the surface (where surface return is an issue). This was a question raised in Forsythe et al. [2012], where analysis of CloudSat data over MSVL revealed a similar puzzling lack of shallow cumulus. This remains an unresolved question.

NICAM and SPV4 both show a different COF distribution, and more closely resemble each other. COF values are higher over ECONUS than WCONUS. This is especially true for SPV4, where almost the entire WCONUS region has COF values below 20%, and the western half has values below 10%. For NICAM, the region of low COF values are limited to west of CO/AZ and south of MT. NICAM has higher COF values across TX and the southeast, corresponding to the high COF values in Fig. 4.1. SPV4 has a similar feature near the southeast Atlantic coastline. For SPv5 the COF has increased, from 0.38 to 0.41. The increase is distributed across most of CONUS and the coastal oceans. WCONUS became cloudier about as much as ECONUS, although it is unfortunately less obvious on the planar map.

For PBLRCs, the overproduction might be partially related to a major limitation of CloudSat: as described previously, CloudSat cannot observe cloud within a kilometer of the surface. This prevents CloudSat from seeing the shallowest stratocumulus layers, as well as most fog. Shallow stratocumulus layers are not common over CONUS during the summer, so it's unlikely that this would be a major source of error in the analysis. Fog possibly might be a significant error source, so it might be useful to examine that statistics for daytime and night time simulations to see if nighttime fog is a problem.

Fig. 4.3 shows the COF distribution of observed and simulated DCCs across CONUS (note the change in color bar). CloudSat observed a higher COF over ECONUS than WCONUS. The details of the distribution are interesting. Previous studies of the CONUS DCC distribution show DCCs being most common over the US southeast (including FL), with the frequency decreasing northward and westward across CONUS [Changnon 2001]. The CloudSat distribution does not show much of an obvious preference for southern ECONUS compared with northern ECONUS. Southern FL has the highest COF across CONUS (almost 10%), but high COF values (6% to

8%) can be found in the northern New England region, as well as the Great Plains and Lake Superior regions. There is a line of low COF values across ECONUS oriented southwest-to-northeast connecting TX with NY. For WCONUS, the eastern NAM region and the Pacific Northwest also have higher COF values. Some of the unusual spatial distribution aspects are just noise in the data, as CloudSat does not pass over all of CONUS with equal regularity. Also, because the data time domain is JJA, convective environments occur more frequently at high latitudes than for the annual time domain [Dai 2001]. But some of it may also be related to the diurnal cycle. Any location that has a DCC maximum several hours removed from early afternoon and early morning would show a low DCC frequency in Fig. 4.3. As discussed in subsection 4.3.2.2, several regions in the US have a late afternoon precipitation maximum (e.g. the US southeast and Atlantic coastline), where the main deep convection would usually occur multiple hours after CloudSat sampled the region. This is not a full explanation, but probably is an important contributor.

NICAM reproduces many of the observed features. There are regional maxima in DCC frequency over the northern Great Plains, the US southeast, north-central Mexico, and southeast Canada extending into northern New England. The Pacific northwest also experiences DCCs. FL is convectively active, though not as frequently as observed. NICAM produces the observed region of low DCC frequency extending from TX to NY – though recall that there is some question as to whether the observed minimum is "real" or just an artifact of CloudSat's diurnal sampling. NICAM does not produce DCCs over the western Atlantic as often as observed. SPV4 also reproduces the DCC frequency maxima over the US southeast and Mexico, and somewhat simulates the DCC maximum over the eastern Great Plains. However, much of the Plains have greatly underestimated DCC frequency. Also, the maxima over Canada/New England and the

Pacific northwest are completely absent. Recall from Chp. 3 that these regions are all warmer and more humid than observed. The absence of DCCs cannot be simply that these environments are too cool and dry to support deep convection, so there must be a more complex explanation.

From SPv4 to SPv5, the frequency of DCCs has increased over CONUS from 0.006 to 0.018, and this increase occurs almost everywhere. This is most noticeable east of the Continental Divide, but even WMTN has a major increase in frequency – from 0.0005 to 0.008. There is a much higher frequency of DCCs in northeast GPLN and up into Canada, and also over in New England. Also, SP-CAM still does not pick up on the high DCC frequency in FL. The model resolution is probably too coarse to represent the necessary mesoscale features (e.g. sea breeze).

4.3.2. Precipitation

This subsection shows the spatial distribution of SPREC. While precipitation is not used directly in the analysis of cloud behavior presented later, it is still of importance scientifically for understanding the influence that the observed and simulated clouds have on the surface water budget. Because CloudSat (or another polar orbiting satellite) is not used to observe SPREC, the data is not limited to specific overpass times of the day. So a diurnal cycle analysis is possible, and will be shown. Unfortunately, NICAM has a six hour temporal resolution, too coarse for diurnal analysis. So the NICAM data will not be used for the diurnal cycle section.

4.3.2.1 Mean

Fig. 4.2 shows the spatial distribution of SPREC for CONUS. Note that the SPREC rate is displayed on a logarithmic scale, because SPREC varies by over an order of magnitude. As may be expected, observed SPREC is higher over ECONUS than WCONUS, with the highest SPREC

rate found over FL and the eastern Gulf Coast. ECONUS receives about an order of magnitude higher SPREC than WCONUS. In WCONUS, the lower precipitation values occur west of western CO, and the Pacific northwest has higher SPREC values than most of WCONUS. As mentioned before, the SPREC values over the oceans should not be trusted, as the data quality over oceans is greatly diminished.

NICAM SPREC is noticeably higher than observed, by up to half an order of magnitude. ECONUS receives more precipitation than WCONUS, as observed. The southeast receives about twice the amount of precipitation as observed, and the precipitation maximum in this region extends farther north and west than observed (away from FL and the coastline). The reduced SPREC in WCONUS occurs further west than observed, west of UT.

SPV4 SPREC is about the same as observed in ECONUS, but much lower than observed over WCONUS. The SPREC maximum over the US southeast is shifted to the north, now over GA/NC/SC and extending westward into MSVL. The western GPLN receive about half the observed SPREC. This bias is co-located with the warm bias over GPLN, so perhaps they are related. The US southwest is extremely dry in SPV4, receiving a full order of magnitude less SPREC than observed. Some of this dry bias occurs within the NAM region, and so this may suggest some difficulty with SPV4 representing the North American Monsoon realistically. It might be worthwhile to investigate this further.

The precipitation over CONUS remains almost identical from SPv4 to SPv5, with a slight increase from 1.82 mm d^{-1} for SPv4 to 1.86 mm d^{-1} for SPv5. However, SPREC increases in WCONUS (from 0.53 mm d^{-1} to 0.73 mm d^{-1}) and decreases in ECONUS (from 2.89 mm d^{-1} to 2.79 mm d^{-1}). Most notably, the unrealistically low SPREC rate in WMTN has increased by

about 0.1 mm d^{-1}, with much of the increase occurring over CA/NV/AZ where the SPv4 SPREC rate is extremely low.

4.3.2.2 Diurnal cycle

Fig. 4.3 shows the average diurnal range of precipitation for JJA. The observations, taken from 1982-2002, show two main local maximums in diurnal range. One is in the US southeast (up to 12 x 10^{-5} mm s^{-1} over Florida and 14 x 10^{-5} mm s^{-1} over Louisiana), and one over the US central Great Plains (up to 7 x 10^{-5} mm s^{-1}). The NAM region does not show a strong diurnal cycle, but there is a noticeable range of 3 x 10^{-5} mm s^{-1} in southwest New Mexico/southeast Arizona.

Fig. 4.4 shows the time of local maximum precipitation for JJA. As mentioned previously, the general pattern for observed precipitation is for it to maximize over land during afternoon, and over ocean during the early morning. This is true over many parts of the US. The maximum occurs during the mid-afternoon (about 3 pm) for WMTN, the southeast, and part of central Mexico. The maximum comes later in the afternoon (about 6pm) for the US northeast, northwest Mexico, and the northwest away from the coastline. The largest noticeable break in the general pattern of timing is, of course, the Great Plains nocturnal maximum, which has a maximum around midnight. There is some indication of an eastward movement of precipitation across the Great Plains throughout the night. There is a clear transition from afternoon precipitation in NM/CO/WY to nocturnal precipitation in TX/OK/KS/NE. There are several pixels of early- to mid-morning maxima on the eastern side of the Great Plains and into the Ohio Valley, but a smooth transition is not as obvious here. There is little evidence of a westward-moving precipitation maximum in the Mexico NAM region.

SPV4 has one large region of high diurnal range covering the entire US southeast, and extending well into the northeast and Atlantic ocean. The ranges are generally larger than observed by about 5 x 10^{-5} mm s^{-1}, though the largest maximum value is only 1 x 10^{-5} mm s^{-1} larger than observed. The observed local maximum over the Great Plains is absent in SPV4. This is probably related to the low bias in precipitation rate over this region. There is a local maximum in range associated with the NAM, occurring over central Mexico. Note that the average precipitation here is larger in SPV4 than observed, and this allows for a slightly larger diurnal range.

The overall pattern is mostly unchanged from SPv4 to SPv5, but the magnitude has increased over much of CONUS. The diurnal range in MSVL has increased by about 5x10^{-5} mm s^{-1}. The local maximum off the southeast coast (near SC/NC) in SPv4 is not present in SPv5. This increase in the diurnal cycle occurs in locations where there has been little change in the mean precipitation rate. This is evidence that the precipitation occurs more often in the convective mode, as DCCs are particularly sensitive to the diurnal cycle. This also coincides with the increase in DCCs.

The diurnal time of maximum precipitation in general agrees with observations, where precipitation maximizes over the oceans near dawn and maximizes over the land during mid afternoon. As noted before, this has been a problem with many GCMs, which maximize precipitation over land too early in the day. The maximum time over much of the WMTN region is 5pm-7pm, which is a little late in the day. One interesting detail that SPV4 partially replicates is the nocturnal maximum of precipitation over the Great Plains. This has been used in previous research as a kind of litmus test for a GCM's ability to simulate regional weather patterns. SPV4 shows a nocturnal maximum in the northern Great Plains and south-central Canada. This region

is not spatially distributed realistically; the real nocturnal maximum extends much further to the south. Also, the CEPPM is not evident at all in SPV4. In fact, if anything, there appears to be an *east-to-west* movement of the precipitation maximum around the Iowa/Minnesota border. Still, the existence of a nocturnal maximum in SPV4 is an improvement over many conventional GCMs.

As with diurnal range, the timing of the maximum remains mostly unchanged from SPv4 to SPv5. Northern GPLN shows a stronger preference for morning precipitation than SPv4 does, indicating that the SPv5 scheme may help in improving the representation of the precipitation diurnal cycle in SP-CAM. There is also a more cohesive eastward propagating signal over GPLN, whereas in SPv4 there was only a hint at best. Note how the max. time in western SD/ND is a few hours earlier than the maximum in MN. Clearly the improved DCC characteristics in SPv5, probably from improved microphysics, allows SP-CAM to better simulate regional convective features, and perhaps even propagating convective systems. However, both the timing of the maximum and the eastward propagation are still not much more realistic than SPv4. The max. time for SPv5 still at least 6 hr after the CPCHP max. time.

Another region of interest is Mexico. During the NAM period (beginning in July), precipitation tends to form over the mountains during the afternoon, and move to the west with time. This movement occurs on a scale large enough that it should be able to be simulated in a GCM. However, SPV4 actually shows a west-to-east movement with time in this region.

4.4. Mean vertical profiles

This section will show the mean vertical profiles of cloud properties over ECONUS and WCONUS. Two cloud types will be examined, as with Chp. 2: clouds rooted in the PBL (PBLR)

and DCCs. The three sets of plots shown are for all-sky (clear and cloudy) conditions, cloudy profiles containing PBLRCs (with cloud layers above the PBLRCs removed), and DCC profiles. The three cloud variables used are cloud occurrence frequency (COF), the average DCC radar reflectivity (DCCAR), and individual hydrometeor species (for models only). For the all-sky case alone, the COF is calculated using both the radar-derived definition of cloud (refl. at least -28 dBZ) and a CWC-based definition (the sum of cloud liquid and cloud ice is greater than 1.0 x 10^{-5} kg kg^{-1}). This is intended to illustrate how different cloud definitions can greatly influence the results. For the other two sets of plots, the radar definition alone is used.

The definitions for PBLRCs and DCCs have changed slightly from Chp. 2. PBLRCs now much have a cloud base within 3,000 m of the surface. Because the PBL can be deeper over land than ocean (particularly over WCONUS during summer), the minimum height has been increased. For DCCs, the altitudes between which reflectivity must be -5 dBZ have been changed to 15°C and 0°C. The reason for this change is that SPv4 poorly represents the vertical reflectivity structure in DCCs (SPv5 shows a large improvement). Above freezing, SPv4 does greatly under-represents the radar reflectivity, leading to an extremely reduced detection of DCCs in SPv4 relative to CloudSat, NICAM, and SPv5. So in order to allow for any meaningful comparison between SPv4 and the other data sources, the definition had to be changed.

4.4.1 All-sky

4.4.1.1 COF

Fig. 4.7 shows the CWC and radar-derived COF for NICAM, SPv4, and CloudSat observations for ECONUS. Fig. 4.8a (right) shows only the radar-derived COF for NICAM, SPv4, and CloudSat observations for ECONUS. Again, it should be noted that CloudSat has

difficulty observing clouds below about 1.5 km above the surface because of ground return, so the large apparent disagreement between observation and the models cannot be easily attributed to errors in the models.

For ECONUS CWC, the models are similar in the lower troposphere, but disagree strongly in the middle and upper troposphere. Both models have a peak of about 1.6 to 1.7 x 10^{-5} kg kg^{-1} in the lower troposphere. The peak for NICAM is slightly higher than SPv4 (2 km vs. 1.5 km). SPv4 produces a shallow layer of high CWC below 0.5 km. This may be fog, or it might be an issue with simulated near-surface processes. This should be investigated further. Above about 3 km, SPv4 produces significantly more CWC than NICAM. SPv4 peaks at about 1.9 x 10^{-5} kg kg^{-1} at about 9km. At this altitude the SP-CAM value is over four times as great as the NICAM value. NICAM has a peak of 0.4 x 10^{-5} kg kg^{-1} at about 10km.

For ECONUS COF, from 1.5 – 3 km, both models overpredict COF by 0.2 – 0.3 (SPV4 moreso than NICAM). Between 3 km and 8 km, SPV4 overpredicts COF by 0.1 at 3 km, and about 0.03 higher up, and NICAM underpredicts COF by up to 0.06 (at 6 km). Interestingly, at about 8 – 9 km, the bias in the models switch signs. SPV4 underpredicts COF by up to 0.03, and NICAM overpredicts COF by up to 0.05.

Fig. 4.8a (right) included SPv5 as well. Below about 6 km, for ECONUS, SPv5 produces fewer clouds observable by CloudSat than SPv4, by up to 10%. For WCONUS, there is little change in COF, though the near surface COF problem is noticeably greater. Above 6 km, SPv5 produces more clouds than SPv4, by almost 20% at 8.5 km. As shown in the following section, this doesn't necessarily mean that the cloud ice overproduction problem is worse in SPv5 than SPv4.Recall that relative to CloudSat, SP-CAM SPv4 produces too many low clouds and too few high clouds. The SPv5 stats, with increased high cloud COF and decreased low cloud COF,

brings SP-CAM closer to the observed COF vertical profile, though the major biases in COF still exist. Also, the maximum height at which high clouds occur is about 1 km greater in SPv5 than SPv4. The increased maximum height of ice clouds in SPv5 brings SP-CAM closer to CloudSat observations than SPv4.

Fig. 4.8a (left) has radar-derived COF for NICAM, SP-CAM, and CloudSat observations for WCONUS. For WCONUS COF, both models overpredict COF by 0.03 in the lower troposphere (up to 3 (4) km for NICAM (SP-CAM)). Note that the NICAM and observational data extend to lower altitudes than SP-CAM data – this is probably because the lower resolution topography in SP-CAM prevents it from representing valleys in mountainous regions. In the middle troposphere up to 11 km, both models underpredict COF; NICAM up to 0.05 at 6 km, and SP-CAM 0.03 – 0.04 throughout the layer. Above 11km, NICAM agrees closely with the observations, with only a small overprediction of about 0.01. SP-CAM continues to underpredict COF right to the tropopause.

It should be noted that CWC and COF values are not necessarily proportional to each other. This is particularly noticeable for SP-CAM, which has a large high bias in CWC in the upper troposphere, and a low bias in COF. This is because the radar is sensitive to the type of hydrometeors in the cloud. A cloud with a given CWC all in small ice crystals will have a much lower reflectivity value than one with the same CWC with much in snow and graupel. Thus, we need to examine the individual hydrometeor vertical profiles to better understand the CWC and COF plots.

4.4.1.2 Hydrometeor species

Fig 9a shows the vertical distribution of QC, QI, QPC, and QPI for NICAM and SPV4. Unfortunately observations cannot be included because of the difficulty in collecting data in multiple situations (such as heavy precipitation. Overall, the liquid hydrometeors (QC and QPC) are in fairly close agreement between SPV4 and NICAM. QC in particular had very close agreement. For QPC, the maximum value in any vertical bin is the same for both models (about 1.2×10^{-5} kg kg^{-1}). However, NICAM tends to produce QPC up to a higher level (about 8.5 km) than SPV4 (about 5 km).

For the ice hydrometeors, the differences between the models are stark. SPV4 tends to produce about three times as much QI as NICAM (2.2×10^{-5} versus 0.8×10^{-5} kg kg^{-1}). In contrast, NICAM produces about twice as much QPI as SPV4 (1.2×10^{-5} versus 2.3×10^{-5} kg kg^{-1}). Furthermore, the shape and location of the vertical distributions are very different. NICAM has a Gaussian curve that peaks at about 10 km, while SPV4 has a curve skewed towards lower altitudes with a peak near 5 km. At the altitude where NICAM peaks, SPV4 has very little QPI. It appears that NICAM tends to transform QI into QPI far more rapidly and often than SPV4. And when QPI forms in SPV4, it tends to fall more rapidly than in NICAM. Part of this may be because SPV4 represents both the snow and graupel forms of QPI, while NICAM does not. Graupel falls more rapidly than snow, which can help explain the lower altitude of SPV4's QPI.

This large disagreement in QI/QPI helps explain the large disagreement in reflectivity-derived COF. QPI is much more reflective than QI. In fact, as mentioned in the CloudSat section, the CPR has difficulty detecting thin high ice clouds. It has little trouble detecting dense ice clouds and snow, however. So if the ice in SPV4 tends to remain in the QI state, and is spread out horizontally so that any local vertical profile has only a small amount of QI in it (that is to

say, the QI isn't all bunched up into a few dense clouds), then the reflectivity value of these clouds will be less than -28dBZ, and the cloud mask will fail to detect it.

For SPv5, QC and QI are reduced at almost all altitudes. QC is reduced by up to 70% at altitudes above 2 km. Below 2 km, SPv5 QC is higher than SPv4 QC, and is much closer to the surface than SPv4. It's not clear from these data alone whether this increase is "real", or if it is a part of the near-surface large QC problem that has been discussed previously. As with SPv4, the problem is much more serious in WCONUS than ECONUS. QI has been reduced greatly, by 75% in maximum magnitude. QI is also limited to the upper cloud in SPv5. In SPv4, QI reaches the freezing level. But in SPv5, QI does not extend below 7 km.

QPC is the variable that has changed the least. There is a 25% reduction in the maximum QPC magnitude in SPv5. Also, QPC extends about 2 km higher into the cloud in SPv5 than SPv4. This difference is more noticeable in WCONUS, where QPC also has a peak maximum altitude about 2 km higher for SPv5 than SPv4. Also, unfortunately, the near-surface high hydrometeor value seems to be affecting WCONUS QPC as well. QPS has changed as much as QI, with SPv5 having a maximum magnitude about 600% that of SPv4. Also, QPS in SPv5 is shifted lower in the cloud than in SPv4. In SPv4, QI and QPS occur about in the same location in the cloud, just having different magnitudes. In SPv5, QPS is clearly staggered from QI. This is hopefully an indicator that QPS in SPv5 actually falls realistically after being generated from QI aloft, whereas it appeared not to do so in SPv4. The flip in relative magnitude between QI and QPS also indicates that SPv5 does not have the problem of converting QI to QPS that SPv4 appears to have. SPv5 ice hydrometeors have vertical profiles much closer to NICAM than SPv4.

4.4.2 PBLRC

4.4.2.1 COF

Fig. 4.8b (right) shows the radar-derived PBLR-only COF for NICAM, SP-CAM, and CloudSat observations for ECONUS. Recall that this is calculated as the number of samples at each vertical level divided by the total number of PBLR cloud samples. It shows where a PBLR cloud occurs when one occurs, and not necessarily how frequently one occurs. The observed vertical profile maximizes at near 0.8 at 1.6 km altitude. It decreases relatively slowly up to about 3.5 km, and then decreases more rapidly and steadily up to the tropopause. The relatively slow decrease up to 3.5 km might be caused by frequent shallow cumulus, which are common over ECONUS during summer afternoons. There is no clear distinction between the top of cumulus congestus clouds (which are a few kilometers tall at most) and DCC clouds. The slight kink in the curve at 10 km is too high to be caused by congestus.

Both NICAM and SPV4 show PBLRCs occurring less frequently above the PBL than observed. NICAM shows the PBLR cloud bases occurring at about the same altitude as observed with the same frequency, but drops off rapidly with altitude with a nearly exponential decay. SPV4 has fewer PBLRCs at all altitudes. The COF drops off nearly constantly until about 8 km to about 0.01, and then slowly above that. This rapid dropoff in SPV4 COF up to 8 km may have an important effect on identifying DCCs, because the definition of DCC used in this chapter includes the cloud being at least 8 km deep. This will be discussed in the next subsection.

Below 6 km, SPv5 COF has decreased by up to 10% relative to SPv4. However, above 6 km, COF has increased greatly. The problem with SPv4 PBLRCs not growing above 8 km appears to have been resolved in SPv5. 20% of SPv5 PBLRCs grow to at least 10 km height. The maximum altitude to which PBLRCs grow in SPv5 is about 15 km, which is close to the observed

maximum height. So in terms of PBLR cloud altitude, SPv5 represents a great improvement over SPv4. On the other hand, the unrealistic representation of shallow PBLRCs in SPv4 persists in SPv5. If anything, it is slightly worse, as shallow clouds are even shallower and closer to the surface in SPv5 than SPv4. The inability to improve shallow clouds with SPv5 is understandable given the model limitations discussed in Chp. 4: the 4 km horizontal grid spacing in the CRM is too large to effectively simulate smaller shallow clouds.

Fig. 4.8b (left) shows the radar-derived PBLR-only COF for NICAM, SP-CAM, and CloudSat observations for WCONUS. The same main conclusion from ECONUS holds for WCONUS, that NICAM and SP-CAM both underpredict the vertical development of PBLRCs, though SPv5 is more realistic than SPv4. SP-CAM produces very few clouds that grow above 8.5 km tall. Both SP-CAM and NICAM have an unusual large COF value below 1 km, as with the all-sky case. CloudSat cannot detect clouds that close to the surface, so it isn't possible to tell if there is any physical relevance to the near-surface model values.

CloudSat has a COF maximum at about 5.5 km. Below this is a region of relatively high COF down to about 3 km. Similarly with ECONUS, this layer may indicate where shallow convective clouds tend to form. Both SP-CAM and NICAM have a COF maximum at about 3 km, and don't possess a layer of high COF like CloudSat does (NICAM has one less than 1 km thick). This is not a surprising result. While NICAM and SP-CAM have sufficient horizontal and vertical resolutions to resolve DCCs (though maybe not simulate all relevant processes), the spatial resolution is still too large to simulate shallow convective clouds. So, the simulated COF vertical profiles in the lower troposphere are correspondingly unrealistic.

Fig. 4.8b also includes a sensitivity test for SPv4, with the cloud detection reflectivity threshold reduced from -28 dBZ to -39 dBZ. The purpose of this test is to help determine

whether the apparent lack of deeper clouds in SPv4 is simply the result of the microphysics influencing the results. It is possible that a poor microphysical scheme could fail to produce a realistic snow content in the upper convective cloud, reducing reflectivity and thus rendering the upper cloud invisible to CloudSat. Lowering the reflectivity threshold allows the simulated CloudSat to detect even thinner ice clouds, such as an unrealistically low reflectivity convective cloud. The results show little change in the upper PBLR cloud COF, suggesting that the low COF is not merely an issue of bad microphysics. This result will be tested using other cloud metrics, but the preliminary result is that the lack of deep PBLRCs in SPv4 is "real".

4.4.2.2 Hydrometeor species

Fig. 4.9b shows the vertical profiles of hydrometeors within PBLRCs over ECONUS for NICAM and SP-CAM. Fig. 4.10b shows the same for WCONUS. First, the liquid hydrometeors, QC and QPC, are largely the same between the all-sky and PBLR cloud-only scenes. This should not be much of a surprise, given the definition of PBLR cloud – they would be the primary contributors to low level hydrometeors in the mean vertical profiles. Second, the frozen hydrometeors, QI and QPI, are notably different between the all-sky and PBLR cloud-only scenes. This is also reasonable, because cirrus clouds and convective anvils have been removed from the statistics. For SPV4, QI is still higher than NICAM, though the vertical distribution peaks lower in the troposphere because of the limited vertical growth of PBLRCs in SPV4. QPI has decreased even further than in the all-sky case, even at lower altitudes (below 8 km) where the limited vertical growth should not be an issue. The decreased QPI from all-sky to PBLRCs can be explained by the fact that SPV4 has difficulty transitioning QI to QPI. If this is true, then long-lived ice clouds, cirrus and convective anvils, would be required to allow enough time for

QI to convert to QPI. Short-lived convective clouds, especially those outside of long-lived MCSs, would not allow enough time for QI to convert to QPI. These results do not verify this hypothesis, but only are consistent with it, so further analysis with higher temporal resolution data (perhaps from an offline CRM) is desirable.

Regarding SPv5, for QC and QPC, the conclusions for the all-sky case are relevant for PBLRCs also. For QI, the effect of the increased height of the tallest PBLRCs can clearly be seen in the upward shift in the QI altitude. SPv5 QI does not have the odd "bird beak" shape that SPv4 has, with a rapid reduction at 8 km. For QPS, the large increase seen with all-sky scenes is even larger for PBLRCs, with about a 1000% increase in maximum magnitude. Again, PBLRCs in SPv5 now look much closer to NICAM than SPv4.

4.4.3 DCC

4.4.3.1 COF

Fig. 4.8c (right) shows the vertical COF for DCCs over ECONUS. DCCs are taller in the two models than in observations. By definition, DCCs must be at least 8 km tall, so that's why there is a drop off in COF from 1.0 in CloudSat and NICAM at about 9 km altitude. About 50% of observed DCCs grow to 12 km height. For NICAM, 50% grow to about 13 km height, and for SP-CAM, 50% grow to 14.5 km. SPv4 shows an unusual minimum in COF at about 8.5 km. It's not obvious what causes this, but it is possibly related to the low reflectivity values at this altitude (discussed shortly). The most obvious change between SPv5 and SPv4 is that SPv5 lacks the reduction in COF at 8 km. It appears that DCCs in SPv5 develop vertically well beyond 8 km, often enough that contamination from other cloud layers is not a major problem. In addition, DCCs are on average about 1 km shorter in SPv5 than SPv4 and the observations.

Fig. 4.8c (left) shows the vertical COF for DCCs over WCONUS. The profiles are similar to ECONUS, and the model DCCs are taller than the observed DCCs. NICAM CTH is slightly closer to the observed CTH over WCONUS than ECONUS. The observed and NICAM DCCs are slightly shorter by 0.5 km (50% grow to 12.0 km and 12.5 km, respectively) than over ECONUS. SPv4 DCCs are slightly taller than over ECONUS by about 500 m (50% grow to 15 km). The minimum COF at 8.5 km for SP-CAM occurs in WCONUS as well. SPv5 does not possess the 8 km COF minimum. They are also slightly shorter than SPv4.

4.4.3.2 Radar Reflectivity

Fig. 4.11a (right) shows the vertical mean reflectivity profile for observed DCCs over ECONUS. The profile has the characteristic arc shape for DCCs also seen in Chp. 2. The maximum reflectivity is about 9 dBZ at 4 km altitude. Below this, reflectivity decreases towards the surface because of attenuation from precipitation. The reflectivity spike near the surface is ground interference, which should be disregarded. There is a slight dark band at about 5 km altitude, caused by attenuation from melting ice near the freezing level. The mean reflectivity decreases rapidly with altitude starting at about 6 km. However, at about 10 km there are two distinct maxima in reflectivity, one at about 10 dBZ, and the other below zero dBZ. The larger reflectivity arc is caused by larger ice particles, including graupel and even hail. The smaller reflectivity is caused by snow. It is interesting that there appear to be two distinct arcs, rather than a single continuous arc smeared out between the two reflectivity ranges. Perhaps this indicates two general modes of deep convection, with one possessing large ice particles in the upper cloud, and the other possessing mostly snow. Note that the minimum reflectivity signal for

the real CloudSat CPR (as opposed to the simulator) is about -28 dBZ, so the large maximum at this reflectivity above 12 km is simply this minimum.

Fig. 4.11a (left) shows the vertical mean reflectivity profile for observed DCCs over WCONUS. The vertical profile over WCONUS is very similar to the one over ECONUS. The maximum reflectivity magnitude is slightly lower at 8 dBZ, and the altitude is about 1 km higher. The rate of reflectivity decrease in the upper cloud is about the same. The double reflectivity maxima in the upper cloud also exists, though at a slightly higher altitude of 11 km. The ground interference is not as noticeable for WCONUS because terrain elevation changes smear it out over the lowest two kilometers or so.

Fig. 4.11b (right) shows the vertical mean reflectivity profile for NICAM DCCs over ECONUS. Similarly with the results in Chp. 2, NICAM shows low reflectivity above 8 km altitude. The problem does not appear quite as severe in NICAM as in SP-CAM, though it is still obvious in the plot. The rest of the NICAM CFAD is quite close to CloudSat. The maximum NICAM reflectivity (8 dBZ) is 1 dBZ lower than observed. The upper cloud above 12 km has higher reflectivity (by 5 dBZ) than CloudSat (this might be influenced by CloudSat's -28 dBZ reflectivity floor). There is no hint of a dark band at the freezing level in NICAM, because of the limited microphysics. But the primary difference between the two is the missing graupel signature above 8 km.

Fig. 4.11b (left) shows the vertical mean reflectivity profile for NICAM DCCs over WCONUS. NICAM behaves similarly over WCONUS as ECONUS. The near-surface reflectivity is lower because of terrain. Interestingly, the upper cloud reflectivity is slightly lower for WCONUS than ECONUS, even though the CTH is greater. This may be evidence that DCCs

are slightly weaker over WCONUS than ECONUS in NICAM, which is not observed. Admittedly, the differences between the two regions are small.

Fig. 4.11c (right) shows the vertical mean reflectivity profile for SPV4 DCCs over ECONUS. SPV4's vertical reflectivity profile is very different from observation. As a whole, reflectivity is lower than observed. The lower cloud reflectivity is smaller than observed, by about 3 dBZ. SPV4 produces the very low reflectivity in DCCs above 5 km, even more so than NICAM does. This low reflectivity is not seen in observations. This makes two CRMs that have the same problem with DCCs. In Chp. 2, I argued that the NICAM discrepancy was caused by the lack of graupel in the NICAM microphysics, leading to the overproduction of snow in the upper cloud. This was based on an argument made by the NICAM team in one of their papers looking at CloudSat simulations of the MJO. It is reasonable to expect that the problem would be less severe in SPV4 because of graupel. But that doesn't appear to be the case. This calls into question the explanation proposed for NICAM's discrepancy. As will be discussed in the next subsection, this error is probably caused by unrealistic behavior of graupel in the version of SPV4 used in this analysis.

There is one other obvious possible answer: Quickbeam. Both reflectivity analyses share Quickbeam in common, so Quickbeam could be the common cause for the problem. But there is a problem simply assuming this solution. Quickbeam has problems in simulating reflectivity in very heavy rain and hail (because of multiple scattering in real life), and in thin ice clouds (because of complexities involving ice crystal shapes and orientations). But the middle to upper portion of a DCC does not contain very heavy rain and thin ice clouds. Hail exists at this altitude is some observed DCCs, but far from all of them. Graupel, snow, and cloud liquid/moderate rain

are not problems for Quickbeam. Furthermore, this analysis uses the microphysical assumptions for graupel/snow/rain directly from the model physics, so that isn't the problem either.

Fig. 4.11c (left) shows the vertical mean reflectivity profile for SPV4 DCCs over WCONUS. Overall, aside from the lower number of samples over WCONUS than ECONUS, the reflectivity profile over WCONUS is almost identical to the profile over ECONUS. The biggest difference is that the reflectivity in the lower cloud (including the maximum) is about 2 dBZ lower than ECONUS. The low reflectivity in the middle/upper cloud occurs for WCONUS as well. The strong similarity between the two profiles suggest that even with the low sample size, the profile shapes are not merely statistical flukes.

Fig. 4.11d shows the DCCAR CFAD for SPv4 and SPv5 simulations over ECONUS and WCONUS. The most noticeable difference between the two is that the middle to upper cloud reflectivity has increased greatly, up to 20 dBZ at 8 km. Reflectivity is still below the observed, and is closer to NICAM reflectivity. There is no longer a reflectivity minimum between the freezing level and the cloud top, but only the same rapid decrease with height seen in NICAM. In addition to the middle cloud, the cloud top reflectivity is lower for the double moment than single, by about 5 dBZ, which corresponds to the decreased CTH seen in the COF data. Finally, the reflectivity below the freezing level has changed little in the double moment data. The maximum reflectivity, 5 dBZ, is slightly smaller than the single moment, which is in turn smaller than observed or in NICAM. The height of the double moment maximum reflectivity (ignoring the near-surface maximum) also occurs about 1 km higher than the single moment height

One interesting feature of the double moment results occurs at 10 km altitude. To the right (higher reflectivity) of the mean reflectivity value, there is a region of low frequency (blue color) extending out to about 5 dBZ. This superficially resembles the hail/graupel arc at the same

altitude in the observation CFAD. NICAM, which does not have graupel, also lacks this kind of feature. It's possible that SP-CAM may be "attempting" to replicate the double arc feature seen in the observed CFAD. Of course limitations in the microphysics probably preclude a full representation. But this feature may be a hint that the double moment scheme with graupel is capable of representing certain convective processes that the single moment scheme cannot.

The overall story for WCONUS is the same for ECONUS, with the reflectivity vertical gap in the middle/upper cloud being absent in the double moment data. Upper cloud reflectivity decreased slightly, like ECONUS. The lower cloud reflectivity has decreased by 2 dBZ. As with ECONUS, the double moment height of the maximum reflectivity (ignoring the near-surface maximum) occurs about 1.5 km higher than the single moment height. The low frequency high reflectivity (blue) region at 10 km exists in WCONUS as well.

The double moment CFAD supports the conclusion suggested by the COF vertical profile that the double moment scheme allows SP-CAM to represent DCCs much more realistically than the single moment scheme over CONUS. The relatively continuous reflectivity arc from the cloud base to cloud top suggests that most DCCs, if not all, extend upwards many kilometers above the freezing level and the semi-arbitrary 8 km definition. So upper cloud properties will almost always be directly related to the DCC itself, and not contaminated by high level clouds like the single moment data. The lower reflectivity of the lower cloud is curious, though. It is probably related to decreased QPC concentration at this altitude (see the next section), but it opens the question of why improved microphysics would reduce rain intensity.

4.4.3.3 Hydrometeor species

Fig. 4.9c shows the hydrometeor species in DCCs for NICAM and SP-CAM over ECONUS. SP-CAM QC is about the same magnitude as NICAM, but spread over a slightly greater vertical extent. SP-CAM QI, like with the other QI results, is much greater in magnitude than NICAM, and also distributed over a larger altitude than NICAM. SP-CAM QPC has about half the magnitude to NICAM, and the maximum altitude for QPC is about 2 km lower than NICAM. The lower magnitude for SP-CAM may explain the slightly lower maximum reflectivity for SP-CAM. NICAM and SP-CAM QPI have similar altitudes, but NICAM has a much greater magnitude than SP-CAM. Again, this may support the idea that SP-CAM has difficulty with the transition from QI to QPI, while NICAM has no such problem. In fact, that NICAM's QPI is much larger than its QI suggests that NICAM may have the opposite problem, producing QPI too quickly from QI. It's possible that the vertical gap between QPC and QPI in SP-CAM may be the cause of the unusually low reflectivity occurring at about the same altitude. NICAM does not have such a gap in its hydrometeor profiles, so there is no corresponding major reflectivity gap in NICAM DCCs.

Fig. 4.10c shows the hydrometeor species in DCCs for NICAM and SP-CAM over WCONUS. The same comments and conclusions for ECONUS apply to WCONUS.

Fig. 4.12 shows the mean hydrometeor profiles in DCCs for SP-CAM, all in one graph. For SPv4, Perhaps the most interesting feature involves graupel. The mixing ratio of graupel is extremely low (almost imperceptible on the graph), much lower than cloud ice or snow. However, the minimum altitude at which graupel occurs is at 11.5 km. In comparison, snow occurs down to 4.5 km, which is near the freezing level. While there is currently no observational evidence to show the realistic distribution of graupel in most DCCs, it is a

reasonable first guess that graupel would not be restricted to the cloud top in a real DCC. Graupel particles usually have a higher mean density than snow particles of equivalent mass, and this would allow them to fall from their origin height into the lower cloud more easily then snow. It is surprising to see graupel limited to the cloud top.

This questionable behavior of graupel is likely related to, if not the direct cause of, errors in the simulated DCC radar reflectivity. As mentioned before, graupel scatters the 3 mm radar beam more effectively than snow. Recall that for NICAM, the low reflectivity in the upper/middle DCCs was likely caused by a lack of graupel altogether in the microphysics. If, for SPV4, graupel is not present in the upper/middle cloud as it is in reality, then SPV4 will produce a low reflectivity in the upper/middle cloud just like NICAM does.

For SPv5, there are notable changes in every hydrometeor species, especially for the ice phase. QPC extends higher into the cloud for SPv5. Both the height of the maximum magnitude and the height of the top for each are about 1 km greater than SPv4. The maximum magnitude for QC has decreased by about 30%, and about 20% for QPC. This corresponds with the decrease in lower cloud reflectivity. Both QC and QPC have small near-surface maxima in SPv5 that weren't present in SPv4.

QI has decreased in magnitude by about 75% in SPv5, and does not occur below 8 km. QPI has in turn increased in magnitude by over 100%, and has shifted lower in altitude by about 3 km. The QPI vertical distribution is skewed towards lower altitude in SPv5, which was not apparent in SPv4. Apparently in SPv5 the snow density increases as it descend through the cloud until it reaches the melting layer. Whereas in SPv4 QI and QPI occupied the same vertical extent of the cloud, in SPv5 the maxima are separated by about 5 km. Another major change in SPv5 is

the much greater presence of QPG, which has a slightly larger maximum magnitude than QI. QPG now extends almost all throughout the cold cloud layer, only missing at the very top.

This result explains some of the reduction of cloud ice seen in the all-sky data. A significant amount of the cloud ice that occurs over JJA CONUS originates from DCCs (though perhaps not to the extent that it does in the tropics). Even if cirrus clouds over CONUS are not directly attached to DCCs, the water composing the cloud ice likely originated within a DCC, because other modes of vertical transport are weaker during JJA. But in SPv5, the cloud ice is clearly being converted to precipitation more efficiently than in SPv4. Furthermore, the skew in snow towards lower altitudes indicates that snow is falling more rapidly from high altitudes in SPv5 than SPv4. Removing water from the upper cloud more efficiently prevents the water in the snow from eventually reforming into cloud ice. So this is a partial answer to the cloud ice problem. A more complete answer would require a more formal water budget analysis, which is beyond the scope of this work.

The changes in hydrometeors also help explain the changes in radar reflectivity in DCCs, particularly the removal of the middle cloud minimum seen in SPv4. The large increase in graupel concentration and vertical distribution is a major factor, as graupel is highly reflective. This also is probably related to changes in snow. Snow occurs with a higher mass concentration, and it also is found lower in the cloud than in the single moment scheme. The combination of graupel and snow helps remove the vertical gap in reflectivity seen in the SPv4 scheme. Rain may also play a role, as it extends about 1 km higher into the cloud than in SPv4. All these changes result in the vertical gap in highly reflective hydrometeors just above the freezing level in SPv4 being filled in SPv5, which removes the reflectivity gap.

4.5 Vertical profiles of cloud/precip. variables sorted by LSEV

Now the data presented in the previous section will be subdivided based on LSEV, as in Chp. 2. First the results for PBLRCs are presented, and then the results for DCCs.

The conditional sampling technique applied to single LSEVs in Chp. 2 will be used in this chapter as well. For PBLRCs, the COF will again be used to show vertical growth. Likewise, for DCCs, the DCCAR will be used to show vertical structure. The DCCAR is further quantified by three variables: cloud top height (CTH), the difference between the CTH and the -5 dBZ echo top height (n5ETHD), and the maximum reflectivity in the column (MAXREFL).

MAXREFL is used here to represent the properties of the lower cloud, below the freezing level. Recall that in Chp. 2, the radar attenuation from rain drops was not simulated in Quickbeam. MAXREFL is located near the top of the attenuation region in the lower cloud, so MAXREFL was unreliable in Chp. 2. But attenuation is simulated for NICAM and SP-CAM over CONUS, so MAXREFL is more reliable for use in this chapter.

For each hydrometeor radius, assuming a liquid hydrometeor (ice has additional complications), the radar reflectivity is proportional to the number concentration of hydrometeors, and to the sixth power of the hydrometeor radius. Because reflectivity is far more sensitive to radius than number concentration, a change in reflectivity with an LSEV probably represents a change in hydrometeor radius. Unfortunately, there is no simple way to relate changes in hydrometeor properties with LSEVs. Both number concentration and drop size distribution are controlled by a number of microphysical and macrophysical processes. Microphysical processes influencing number and DSD include the activation of cloud condensation nuclei, vapor deposition, and collision-coalescence. These can be influenced by a number of macroscale characteristics, including temperature, humidity, the vertical velocity and

entrainment rate of the DCC, and even the environmental aerosol characteristics. So while changes in CTH and N5ETHD may be explainable with relatively simple conceptual arguments, MAXREFL cannot be. Nevertheless, the results for MAXREFL are presented here as a means to compare the observed behavior of the lower DCC with simulations.

The TPW and SAT data for observations and NICAM have been averaged over 100 km areas to better represent the environmental state they clouds occur in, rather than locally influenced conditions. W500, by definition, is averaged over a 2° by 2° area. For SP-CAM, all three LSEVs represent the mean conditions within one GCM box (2.5° by 2.5°). TPW is binned by 3 mm, SAT by 1 K, and W500 by 0.001 m s^{-1}.

4.5.1 PBLRC Occurrence Frequency

4.5.1.1 TPW

Fig. 4.13 shows the mean vertical COF profiles of PBLRCs sorted by TPW over ECONUS, and the corresponding sample PDF of TPW. For observations, the vertical depth of PBLRCs clearly increases steadily as TPW increases. This stands in contrast with the behavior of tropical PBLRCs discussed in Chp. 2. In the tropics, PBLRCs are shallow for lower TPW values, but rapidly transition into deep clouds above a threshold TPW value (about 50 mm in the tropics). The lack of this rapid transition for ECONUS suggests that there isn't the relatively clear distinction between cumulus congestus and DCC clouds here that there is in the tropics. This corresponds with the mean vertical COF profile shown in 4.3.2.1, which does not have any indication of an altitude where congestus clouds often terminate.

NICAM agrees with the observations that low COF values increase steadily as TPW increases. This is again in contrast with the tropics. However, high COF values do not increase

steadily. They remain at low altitude until about 50 mm, above which the altitude increases slightly. So, while the maximum possible CTH of PBLRCs increases steadily with TPW, the typical CTH does not. This behavior indicates that NICAM's problem with producing too shallow clouds occurs in all moisture environments, and is not strongly related to an inability of NICAM to reporduce the TPW/PBLRC relationship. Note that at the highest TPW values, the CTH is actually higher than observed. 18 km is taller than the typical tropopause height, so these PBLRCs might be examples of stratospheric penetrating DCCs. But according to the sample PDF, these tall clouds are extremely rare. PBLRCs tend to form at higher TPW values in NICAM than observed. This appears to be caused simply by the mean TPW values for ECONUS in NICAM being higher than observed.

For SPv4, the CTH generally increases with increasing TPW, like observed. However, there is a small rapid increase in CTH beginning above 55 mm, much moreso than NICAM. Even at high TWP values, PBLRCs to not grow as tall in SP v4 as observed. This is consistent with the mean vertical COF profile shown in 4.3.2.3. As with NICAM, PBLRCs tend to form at higher TPW values in SP v4 than observed. Again, this appears to be caused by a high bias in mean TPW values over ECONUS.

SPv5 displays a transition from shallow clouds to deep clouds at about 50 mm, similar to NICAM and unlike the observations. Below 50 mm, SPv5 produces low COF values (blue colors) much higher in altitude than SPv4. However, the higher COF values (green and above) actually have a lower maximum altitude in SPv5. This probably accounts for the decreased COF values at low altitude in the mean vertical profile discussed previously. Out of the three models, SPv5 is closest to the observations above 45 mm. Below this, it has the same lack of deeper clouds as SPv4.

Fig. 4.14 shows the results for WCONUS. The distribution of observed vertical COF with TPW is similar to ECONUS, where mean CTH increases steadily as TPW increases. The CBH decreases slightly from 0 mm to 30 mm. This is probably caused by the lowest TPW values occurring over higher terrain. The sample PDFs for both all-sky and PBLR cloud-only are drier than for ECONUS, as we would expect, and they are also skewed towards lower TPW. There is little obvious preference of PBLRCs for higher TPW.

For NICAM, the low COF values (below 0.2) increase in altitude steadily with increasing TPW values. The higher COF values increase in altitude more slowly until about 60 mm TPW, where they increase in altitude rapidly. The increase is much greater than with ECONUS. It is reasonable to expect deep clouds occurring at the highest occurring TPW values, but caution should be used when trusting the results from such a low sample size at these high TPW values. This discrepancy between NICAM and CloudSat, if real, occurs both in ECONUS and WCONUS. Because it occurs in both locations, it may not be a fluke, but represent a systematic unrealistic behavior of PBLRCs in NICAM over the extratropical continents. The sample PDFs show NICAM being more humid than observed, but otherwise resembles the observed PDFs closely. As observed, NICAM PBLRCs have a slight preference for higher TPW values.

For SPv4, the COF distribution by TPW resembles the observations, expect with CTH being lower than observed. There is an odd disagreement between 15 mm and 30 mm, where it appears that few deeper PBLRCs are observed. Only a thin layer near the surface occurs with high frequency. It seems that the algorithm used for detecting PBLRCs might be tripped up by the high CWC that occurs often near the surface in SPV4 (discussed in section 4.3). But the missing deeper PBLRCs don't affect the sample PDF for PBLRCs noticeably. The sample PDFs resemble the observed and NICAM PDFs, but even more humid. PBLRCs seem to favor higher

TPW values a bit more strongly in SPV4 than observed. Notice that the PBLR cloud fraction is at least 50% starting at 30 mm TPW, and drops to near zero below 10 mm.

For SPv5, most of these statements for ECONUS apply for WCONUS. There are a few differences to note, though. The shallow cloud frequency at lower TPW values is affected in SPv4 and SPv5 by the near-surface COF values described previously. At higher TPW values, clouds in SPv5 actually have a higher maximum altitude than in SPv4. So increased cloud depth in the mean vertical COF profile arises from an increase in depth in the deepest PBLRCs in addition to other factors. So WCONUS resembles the observations slightly more than ECONUS. But the transition between shallow and deep clouds in SPv5 is still quite abrupt.

The lack of shift to higher moisture in the SPv5 PDF is important for understanding the deeper PBLRCs in SPv5. Note that SPv4 actually produces clouds deeper than 8 km above 60 mm. However, the sample PDF is very small above 60 mm. This means that these deeper clouds contribute very little to the mean vertical COF profile shown in 5.5. In comparison, the SPv5 PDF is not more humid than SPv4 above 60 mm, where the clouds are, as with SPv4, much deeper than 8 km. Rather, the deeper clouds form more commonly in drier environments in SPv5, which are much more common. So the deeper clouds factor in much more to the mean vertical COF profile. This is an important clue to why the mean vertical COF profile has become more realistic at higher altitudes – the mean TPW environment is not more humid. These results are a reassuring indicator that improvements in the PBLR cloud representation are not merely the result of unrealistic changes in the mean convective environment. Note that SPv4 actually produces clouds deeper than 8 km above 60 mm. However, the sample PDF is very small above 60 mm. This means that these deeper clouds contribute very little to the mean vertical COF profile shown in 5.5. In contrast, SPv5 produces deep clouds at lower TPW values, and yet the

mean environment is not more humid in SPv5 than SPv4. This is an important clue to why the mean vertical COF profile has become more realistic at higher altitudes – the TPW/cloud relationship now more closely resembles observations. This is relevant for the conundrum described earlier: the possibility that mean cloud properties become more realistic, but the mean environment becomes less realistic. That does not appear to be the case for the transition from single moment to double moment microphysics.

4.5.1.2 SAT

Fig. 4.15 shows the mean vertical COF profiles of PBLRCs sorted by SAT over ECONUS, and the corresponding observed sample PDF of SAT. Generally, CloudSat observes PBLRCs to increase in depth as SAT increases. As with TPW, and unlike the tropics, there is no abrupt change in the rate of increase as SAT increases. So with SAT as well, there does not appear to be an obvious distinction between shallow modes and deep modes of PBLRCs. Above 305 K, the higher COF values decrease rapidly in height with increasing SAT. This is probably indicative of an important difference between the tropical oceans and the extratropical continents. Over the extratropical continents, during the summer, the highest SAT values tend to occur in high pressure regions, where subsidence hinders convective cloud growth and allows more insolation to warm the surface. In the tropics, higher SATs (and SSTs) are usually associated with increased ascent, which enhances cloud growth. So we might expect that PBLRCs would not grow vertically as much with the highest SAT values.

It's also notable that PBLRCs occur over a large range of SAT values, about 30 K. This is different from the tropics, where the narrow range of climatological SST values (SAT is closely related to SST in the tropics) leads to a narrow range of SST values at which PBLRCs form.

The distribution of PBLRCs by SAT in NICAM looks notably different from observations. First, between 280 K and 305 K, the lower COF values increase steadily with increasing SAT. This is similar to observations. They also fall above 305 K, which again resembles observations. However, the higher COF values (above 0.2) do not increase with increasing SAT. It appears that most PBLRCs are insensitive to SAT below 300 K. Third, starting at about 303 K, both the CTH and the cloud base height increase as SAT increases. Some of this might be related to low sample size, but the coherence of the distribution pattern (i.e., there are no "spikes" in the distribution), plus the same result showing up in SP-CAM, cast doubt on the possibility that this is a sample size issue alone.

Both issues are unexpected, and I don't have an explanation for them currently. There is a possibility that the models become too dry to support DCCs when SAT is high. It would be useful then to look at joint PDFs of SAT and TPW to see what happens with humidity at high SAT. It could also be possible that mid-tropospheric humidity is too low in the models at high SAT. Recall that this is a problem for NICAM in the tropics (see Chp. 2).

Also, the sample PDF for NICAM is different from observations. The standard deviation of SAT is smaller in NICAM, so that most samples occur only a few Kelvin from the mean of 299 K. NICAM noticeably underpredicts lower SAT values. Furthermore, NICAM lacks the higher SAT values (above about 307 K) that are observed. This affects the SAT values at which PBLRCs form in NICAM – they tend to form over a much narrower range of values than observed. The sample PDF for NICAM over ECONUS looks closer to the sample PDF for NICAM over the tropics than the observed sample PDF over ECONUS. Recall that the NICAM COF distribution for TPW also resembles the NICAM tropics more than the observed ECONUS

region. This could be just a coincidence, of course, but it might also indicate that the simulated ECONUS atmosphere behaves more like the tropics than is observed.

SPV4 produces some of the same unusual features that NICAM does, though it is not exactly the same. Namely, it has the same odd reduction in CTH at about 298 K, and the increase in CBH above 305 K. The low COF values remains at low altitude at all SAT values. The higher COF values (above 0.2) increase with SAT until 295 K, then decrease rapidly until 300 K, and then increase again. In this sense SPV4 is the opposite of NICAM – most PBLRCs are sensitive to SAT, but the maximum CTH is only weakly sensitive.

The SPV4 sample PDF resembles NICAM's PDF more closely than the observed PDF. The main difference is that for the all-sky PDF (solid line), SPV4 produces the observed higher SAT values. Because SPV4 produces the higher SAT values, but underpredicts the lower SAT values, SPV4 produces a mean SAT warmer than observed for ECONUS. This was shown in Chp. 3. However, the sample PDF for PBLRCs (dashed lines) has few PBLRCs forming above 307 K. This is similar to NICAM, and results in a low PBLR cloud fraction at higher SAT values (more like the observations).

SPv5 still does not represent the relationship between SAT and vertical COF realistically, just like SPv4 and NICAM. Both SPv4 and SPv5 have the odd reduction in CTH around 300 K. SPv5 shows a general increasing slope in low frequency CTH as SAT increases for ECONUS, which is an improvement over SPv4. WCONUS shows an abrupt change in CTH at 290 K, whereas nothing of the sort appears in observations. SPv5 CTH is higher at all SAT values than SPv4. The SPv5 sample PDF is almost identical to SPv4 PDF. SPv5 maintains the same unrealistically narrow PDF with from SPv4.

It seems that all models have a similar tendency to behave unrealistically above 305 K. While the data presented here can't prove that the cause for these discrepancies is the same in both models, the similarity in these discrepancies suggests a similar cause. This is certainly worth further investigation.

Fig. 4.16 shows the same results for WCONUS. The observed COF distribution for WCONUS resembles that for ECONUS fairly closely. CTH increases with increasing SAT (though more slowly than ECONUS) up to above 306 K, where it decreases rapidly. The deep clouds above 313 K might just be statistical artifacts from low sample size, though it cannot be demonstrated conclusively from these data. CBH decreases slightly from 275 K to 381 K because of lower SAT values occurring at higher terrain. The sample PDFs show the same relatively wide distributions of SAT as ECONUS does, with PBLRCs slightly favoring lower SAT values.

NICAM displays the same odd COF distribution over WCONUS as for ECONUS. The low COF values increase in altitude with SAT until 295 K, then decrease. There is an unobserved increase again starting at 302 K. Higher COF values increase in altitude beginning at 305 K, and CBH also increases with increasing SAT. This behavior above 300 K occurs over ECONUS as well, and it isn't related to terrain height, since higher terrain usually has lower SAT. Because this odd behavior occurs in both halves of CONUS, it probably isn't merely a statistical quirk, but rather indicates a real unrealistic process or set of processes in NICAM.

The sample PDFs for NICAM are noticeably different from observations. Both PDFs are narrower than observed, with more SAT values occurring near the mode (290 K). This narrower PDF is also seen in ECONUS, and like ECONUS it somewhat resembles the sample PDF of SST in the tropics. The PBLR cloud-only PDF is noticeably shifted towards lower SAT values.

Notice that the PBLR cloud fraction is at least 0.5 below 286 K, while it is below 0.25 above 293 K. This preference for lower SAT values is larger than observed.

SPV4 shows a discontinuity in the COF distribution at about 288 K. There is a span of "missing" deeper PBLRCs from 283 K to 291 K, which is similar to the "missing" clouds discussed for TPW. Above 300 K SPV4 resembles NICAM closely, with CTH and CBH increasing with increasing SAT. Again, it seems a reasonable first guess that whatever is happening in NICAM to cause this is also happening in SPV4.

The all-sky sample PDF for SPV4 has a bimodal shape, unlike any other sample PDF shown in this section. In fact, the SPV4 looks something like a hybrid between SPv5 and the observations. It has the large width of the observations, and a secondary peak at 295 K, like the observations. The PBLR cloud-only PDF is not bimodal, and strongly favors lower SAT values. Notice that the PBLR cloud fraction below 288 K is at least 0.75, while above 293 K it is below 0.25.

Most of the statements for ECONUS hold true for WCONUS. The increase in CTH with increasing SAT is lower for WCONUS. The change in the sample PDF is also similar with ECONUS.

4.5.1.3 W500

Fig. 4.17 shows the mean vertical COF profiles of PBLRCs sorted by W500 over ECONUS and the corresponding observed sample PDF of W500. For CloudSat, there is a steady increase in CTH from about -0.03 m s^{-1} to about 0.3 m s^{-1}, above which the clouds are consistently deep. As with TPW and SAT, this contrasts somewhat with tropical PBLRCs. In the tropics, while PBLRCs can grow deep in large-scale subsidence conditions, most PBLRCs will not develop

vertically in subsidence regions. They will only grow in ascent conditions. Over ECONUS, PBLRCs will often develop vertically in subsidence conditions as well as ascent conditions, though they will usually grow taller as vertical motion increases positively.

The sample PDF is important to notice here, too. The all-sky PDF (solid line) is nearly symmetrical for subsidence and ascent conditions, but with a slight preference for subsidence. However, the sample PDF for PBLRCs (dashed line) is skewed towards ascent, with a mode of 0.01 m s^{-1}. PBLRCs form preferentially in ascent conditions. This is different from the tropical oceans. In the tropics, both the all-sky and PBLR cloud sample PDFs slightly favor ascent. There is no major difference in the distribution of the two PDFs, but only magnitude. This indicates that in the tropics, PBLRCs favor ascent only because the mean climate does. But over ECONUS, the PBLRCs favor ascent while the climatological mean slightly favors subsidence. This will be important when examining the models.

In contrast with CloudSat, NICAM generally does not produce deep clouds frequently in subsidence conditions. Vertical growth only begins increasing with W500 above 0 m s^{-1}. These two features resemble NICAM's simulation of PBLRCs in the tropics. One other interesting feature is the increase in low COF values as subsidence increases (below -0.02 m s^{-1}). And the lowest COF values (0.05 to 0.10) change very little with W500. The higher COF values don't increase in altitude at all, so this feature only involves infrequent PBLRCs. Unfortunately, it isn't obvious what causes this from the presented data. This suggests the need for further investigation.

The sample PDF is also different from the observed PDF. The all-sky PDF has a smaller width than the observed PDF, and it more strongly favors subsidence. The PBLR cloud PDF resembles the all-sky PDF strongly, and does not obviously favor ascent conditions strongly as

observed PBLRCs do. Careful examination shows that NICAM PBLRCs do in fact favor ascent slightly more than the all-sky climate. Above 0.02 m s^{-1}, the PBLR cloud fraction is above 0.5; the cloud fraction is never this high in subsidence conditions. Still, PBLRCs favoring subsidence in NICAM is very different from observations. Once again, NICAM's behavior over ECONUS resembles its behavior over the tropics. In the tropics, the all-sky sample PDF in NICAM favors subsidence (unlike observations), as does the PBLR sample PDF. The behavior of PBLRCs in NICAM over ECONUS more closely resembles their behavior in the NICAM tropics than over the observed ECONUS.

SPV4 resembles NICAM in that vertical growth happens mostly in the ascent regime. While the low COF values increase with increasing rising motion for all W500 values, the higher COF values (above 0.2) increases only above 0 m s^{-1}. The odd vertical growth of low COF values in strong subsidence seen in NICAM does not occur in SPV4.

The sample PDFs for SPV4 resemble NICAM's, but with an even smaller width, and favoring subsidence more strongly. The PBLR cloud PDF slightly favors ascent relative to the all-sky PDF, as with NICAM, though still does not favor ascent nearly as strongly as observed. Though these data are insufficient to prove it, it seems likely the unrealistic physics (whatever they are) in NICAM that causes unrealistic behavior in NICAM's PBLRCs may also be causing the same unrealistic behavior to manifest in SPV4.

Overall, the COF distribution for SPv5 resembles the one for SPv4, except that deep clouds are taller. The same general statements apply for WCONUS as well as ECONUS. The sample PDF for SPv5 remains almost unchanged from SPv4. This means that changes in the mean dynamical environment (at least in the free troposphere) cannot explain the improvement in the mean vertical COF profiles.

Fig. 4.18 shows the same results for WCONUS. As with ECONUS, observations show deeper PBLRCs in subsidence conditions as well as ascent. The lower COF values increase in altitude with increasing W500 to -0.005 m s^{-1}, then remains steady. The higher COF values increase in altitude up t0 0.025 m s^{-1}, then remains constant with height. The all-sky sample PDF is nearly symmetrical around 0 m s^{-1}, with a slight preference for subsidence, as with ECONUS. PBLRCs slightly favor ascent conditions, though not as obviously as ECONUS.

The NICAM COF distribution resembles the ECONUS distribution very closely. PBLRCs do not usually develop vertically in subsidence conditions, but only is ascent conditions. The high altitude low COF values in strong subsidence occurs for WCONUS as well as ECONUS, so it may not be just a statistical fluke. There is no immediate intuitive reason why strong subsidence would favor low amounts of deep PBLRCs, so further investigation would be necessary to determine why it occurs in NICAM. As with ECONUS, the sample PDF for all-sky conditions shows that NICAM prefers subsidence more strongly than is observed. Also, PBLRCs slightly prefer ascent conditions. Unlike ECONUS, NICAM agrees with the observations in that the preference for ascent over WCONUS is only weak.

As with NICAM, the COF distribution in SPV4 looks very similar between ECONUS and WCONUS. The most noticeable difference is that the "missing" cloud issue seen with WCONUS TPW and SAT occurs for W500 too. Here it occurs between -0.02 m s^{-1} and 0.0 m s^{-1}. The occurrence of this problem for all three LSEVs, and the way in which it occurs over a single discrete range of LSEV values, indicates that there is a systematic cause for this somewhere in SPV4's physics. This probably is not a mere statistical fluke. The sample PDFs also resemble ECONUS closely, with the all-sky PDF favoring subsidence more than observations and

NICAM, and the PBLR cloud-only PDF not strongly favoring ascent. The conclusions for SPv5 over WCONUS are similar to ECONUS.

4.5.2 DCC Radar Reflectivity

4.5.2.1 TPW

Fig. 4.19 shows the mean vertical DCCAR profiles sorted by TPW over ECONUS and the corresponding observed sample PDF of TPW. Table 4.2 displays the trends in CTH, N5ETHD, and MAXREFL. CTH increases steadily as TPW increases. This is similar to the tropics, though with about 30% higher slope. N5ETHD increases slightly. which is curiously the opposite of the tropics, which has a decreasing trend about twice the magnitude. MAXREFL increases slightly as well. There are no apparent major jumps or discontinuities in the DCCAR distribution with TPW. The sample PDF for DCCs is shifted to higher TPW relative to all-sky conditions.

Recall that earlier I discussed that N5ETH and N5ETHD may be inversely related to convective updraft velocity. Stronger updrafts loft larger hydrometeors higher into the cloud. It is reasonable to expect that higher TPW may lead to stronger updrafts, because of higher convective instability and reduced dry air entrainment. Increasing N5ETH indicates stronger vertical velocities. But the observations suggest that because N5ETHD decreases with increasing TPW, then perhaps convective updraft velocities decrease with increasing TPW, at least in the upper cloud. This is a very odd result, and is not at all intuitive. Why would individual DCCs be weaker in high moisture environments over midlatitude continents, while being stronger in the same situation over the tropics? However, this result does not necessarily mean that deep convection overall decreases in intensity, depending on the definition of "intensity". For example, the convective mass flux of an average DCC might increase if the cloud horizontal

diameter increases, even if the maximum vertical velocity in the cloud decreases. It is not possible to determine this from the current data, though it may be possible to use CloudSat to do this. There is already work being done on using CloudSat to estimate the horizontal scale of individual DCCs [Bacmeister and Stephens 2011].

Another possibility is that DCCs organize differently in higher TPW environments than lower. Environmental moisture influences buoyancy, which is a key variable in influencing convective organization [Weisman and Klemp 1982]. In general, higher moisture leads to heavier precipitation from the deep convections as a whole, and the individual DCCs will tend to cluster in to MCSs and squall lines. But there is not much work existing on how individual DCCs are affected by the kind of convective system they occur within. Perhaps in some kinds of MCSs, individual DCCs are weakened because the presence of many neighboring DCCs reduces the importance of each DCC in reducing convective instability. On the other hand, perhaps certain kinds of MCSs produce a protected environment for convective development, so that individual DCCs in the center are shielded from external inhibiting factors. Of course, DCCs also tend to cluster in the tropics in regions of high TPW, which complicates the situation. In order for this possibility to be realized, DCCs would have to cluster differently over the tropics than the midlatitudes in high TPW environments. It is an open question.

A third possibility is problems with the hypothesis itself. Perhaps the hydrometeor microphysics is affected by stronger updrafts. A stronger updraft would theoretically loft larger particles higher into the updraft, and also loft supercooled liquid particles higher (which have a larger reflectivity with respect to ice). But what if stronger updrafts reduces the particle size? Reflectivity is strongly related to particle size (to the 6^{th} power), so even a small reduction in size would noticeably reduce reflectivity.

NICAM CTH increases steadily with increasing TPW, similar to CloudSat, though with a lower slope value. This is quite different from NICAM's behavior in the tropics, where DCC CTH is strangely insensitive to TPW (unlike CloudSat). N5ETHD increases with increasing TPW, which again is similar to CloudSat. The same questions asked about the CloudSat result also apply here. MAXREFL increases slightly with TPW, again similar to CloudSat. As with the observations, NICAM shows no major discontinuities in the DCCAR distribution by TPW. The DCC sample PDF is biased considerably moister than observed. This is probably a result of NICAM being much moister than observations. DCCs obviously prefer more humid environments relative to all-sky conditions in NICAM as well.

The reflectivity profile for SPV4 is very different from CloudSat or NICAM. The larger reflectivity is confined below the freezing level, and the reflectivity in the middle to upper cloud is very low. In fact, it almost looks like there are two separate cloud layers at lower TPW values, separated by a very tenuously thin cloud. It's possible that the vertical reflectivity profile for SPV4 DCCs is so different from CloudSat and NICAM that the algorithm that identifies DCCs is being contaminated by high clouds. This would be a secondary high cloud layer above the DCCs that is in close enough proximity to the high reflectivity core that it is included in the reflectivity profile. This means the statistics shown in Table 4.2 are of dubious use. Nevertheless, for a consistent methodology, they will be included and discussed.

CTH decreases as TPW increases, which is the opposite sign from CloudSat and NICAM. Examining the DCCAR distribution, it is clear that the linear trend does not capture the full situation as well as it does for the other two data sources. At lower TPW values there appears to be two vertical maxima in reflectivity with two associated CTHs. The lower reflectivity maximum has a CTH that increases with height as TPW increases. The upper reflectivity

maximum (which may be partially caused by contamination from secondary high cloud layers) has a CTH which decreases with increasing TPW. The two reflectivity maxima merge around 60 mm. N5ETHD decreases as TPW increases, which is of opposite sign from CloudSat and NICAM, and of larger magnitude. Careful examination of the DCCAR distribution shows that this is a result of the upper reflectivity maximum occurring at lower TPW values having a large upper cloud reflectivity gradient. When the two reflectivity maxima merge at 60 mm, this large gradient disappears. Ignoring the upper reflectivity maximum, the reflectivity gradient associated with the lower reflectivity maximum does not obviously decrease as TPW increases. Thus, again, the regression statistic is questionable. MAXREFL increases as TPW increases, similar in sign and magnitude (though a bit larger) to CloudSat and NICAM. So perhaps while SPV4 has difficulty simulating DCCs above the freezing level, it behaves more realistically in the warm cloud layer. Like observed and NICAM DCCs, SPV4 DCCs favor more humid conditions relative to the all-sky sample PDF. SPV4 DCCs tend to form at higher TPW values than observed because SPV4 is more humid than observed.

The most obvious change between SPv4 and SPv5 is that almost complete removal of the reflectivity minimum near 8 km. There is only a slight hint of it at low TPW values, and the observed DCCAR distribution has similar off features in the tails of the sample PDFs (likely statistical artifacts). This indicates right away that the improvement of vertical DCCAR for SPv5 is not merely the result in a change in the mean humidity environment. Nevertheless, SPv5 still does not reproduce the relationship between DCCAR and TPW realistically. CTH generally does not increase with increasing TPW. For ECONUS and WCONUS the increasing slope occurs only below 45 mm, with rapid decrease above 45 mm. N5ETHD increases with increasing TPW, which is observed. However, N5ETH decreases with increasing TPW, which is not observed.

This decreasing slope is about the same for WCONUS as ECONUS. If there is a connection between N5ETH and convective updraft strength as proposed, it seems that SP-CAM DCCs weaken with increasing TPW, even more severely than the observations hint at. MAXREFL decreases as TPW increases, which is inconsistent with observations. Recall that SPv4 did not have a major problem with the lower cloud even though the upper cloud had serious problems. The sample PDF for SPv5 is shifted to less humid than SPv4 (moreso for ECONUS than WCONUS), more than can be explained by changes in the mean humidity. For ECONUS, the humidity decrease makes the sample PDF slightly more realistic, though it resembles SPv4 much more than observations. Again, this doesn't appear to be a major factor in the vast improvement of the DCCAR mean profile shown in 5.5.

The weakening of DCCs in moist environments is likely related to errors in the TPW/SAT relationship. Fig. 4.27 in Chp. 4 shows that SAT decreases as TPW increases in SPv4, especially in the vicinity of DCCs. Reduced SAT suggests the possibility of reduced CAPE, which would reduce convective updraft strength. Perhaps the causes of the unrealistic TPW/SAT relationship should be investigated further.

A preliminary analysis of mine of maximum DCC updraft velocity versus TPW confirms the possibility of DCCs weakening with increasing TPW. Maximum vertical velocity over ECONUS decreases steadily from 1.3 m s^{-1} at 27 mm to 0.35 m s^{-1} at 69 mm. WCONUS has a similar decrease. The mean maximum updraft velocity is less than 1 m s^{-1}, which is also curious. CONUS DCCs tend to be among the most vigorous on Earth [Zipser et al. 2006], with maximum updraft velocities of at least a few m s^{-1}. Of course it is not entirely reasonable to compare the maximum updraft velocity of a simulated DCC in a CRM with 4 km horiz. resolution with the much finer resolution of aircraft observations during field experiments. The vigorous updrafts in

observed DCCs tend to not form monolithic multi-kilometer columns of ascending air, but rather often form into extremely turbulent, highly localized updrafts and downdrafts on the order of 1 km diameter or smaller [Carptenter et al. 1998]. But the low updraft velocities in SPv5 are still surprising. This is a topic that needs to be investigated further.

Fig. 4.20 shows the same results for WCONUS. Table 4.3 displays the trends in CTH, N5ETHD, and MAXREFL. The DCCAR distribution for WCONUS resembles ECONUS closely, though shifted to lower TPW values because of the drier environment. CTH increases as TPW increase, which is the same sign as CloudSat over ECONUS, but about half the magnitude. The rate of increase is not as steady at all TPW values as for ECONUS, with CTH maxima at 30 mm and 50 mm. N5ETHD also increases as TPW increases. Again, as with ECONUS, this result is not intuitive and difficult to explain easily. MAXREFL increases with TPW, again similar to ECONUS. The sample PDF shows that, like with ECONUS, DCCs strongly prefer more humid environments relative to the all-sky PDF.

Like CloudSat, the NICAM DCCAR distribution for WCONUS looks very similar to ECONUS. As with ECONUS, CTH increases steadily with increasing TPW, a bit larger than ECONUS. Also, N5ETHD increases with increasing TPW, again very similar to ECONUS NICAM. MAXREFL increases with increasing TPW, about three times the magnitude over ECONUS. And as with all the TPW results, NICAM WCONUS DCCs strongly prefer more humid environments relative to the regional climatology.

SPv4 produces the same unrealistic DCCAR distribution over WCONUS as over ECONUS. There appears to be two main vertical reflectivity maxima separated by a region of very thin cloud. CTH decreases with increasing TPW, slightly less in magnitude than ECONUS. And as with ECONUS, this decreasing CTH is associated with the upper reflectivity maximum. The

lower reflectivity maximum seems to have an associated CTH that increases as TPW increases. N5ETHD decreases with increasing TPW, also a slightly smaller magnitude than ECONUS. Again, this seems to be associated with the upper reflectivity maximum, and not the lower maximum where the higher reflectivity is located. MAXREFL increases with TPW. As with ECONUS, this is close to the CloudSat MAXREFL trend. It appears that SPV4 simulates the lower cloud realistically. The DCC sample PDF again favors high humidity relative to the all-sky state.

4.5.2.2 SAT

Fig. 4.21 shows the mean vertical DCCAR profiles sorted by SAT over ECONUS and the corresponding observed sample PDF of SAT. Table 4.2 displays the trends in CTH, N5ETHD, and MAXREFL. CTH increases steadily as SAT increases. This is similar to observations in the tropics, with a slope of slightly higher magnitude. It is interesting to note that DCC CTH does not appear to decrease at high SAT (above 305 K), even though PBLR cloud CTH decreases at high SAT. This implies that mature DCCs are not strongly inhibited by the subsidence associated with the high pressure systems that often accompany high SAT values, once they develop. N5ETHD increases with increasing SAT, similar to ECONUS TPW, and the opposite of tropical SST. The increase in N5ETH suggests updrafts strengthening with SAT, but N5ETHD suggests the upper cloud updraft does not strengthen. This increasing tendency occurs at almost all SAT values, not just at high SAT values. It might be reasonable to expect DCCs to weaken at high SAT values because of increased subsidence, but the implied weakening trend at all SAT values is hard to explain easily, as discussed previously. MAXREFL decreases slightly as SAT increases, the opposite of CloudSat in the tropics. There is not an easy explanation for this,

either. Reflectivity increases as hydrometeor size and number increase. Higher available water vapor allows hydrometeors to grow larger and in more numbers, but the relationship with SAT is not as obvious. The main relationship is through relative humidity, which is reduced as temperature increases but absolute humidity remains constant. It's possible that the relative humidity in the lower to middle cloud decreases as SAT increases, which would lower radar reflectivity as SAT increases. This possibility will be examined later. The sample PDF shows that observed DCCs do not favor higher or lower SAT relative to the all-sky sample PDF, as they favor higher TPW. The DCC-only sample PDF has a similar mean and width to the all-sky PDF.

For NICAM, CTH increases with increasing SAT. This is similar to CloudSat, though with a larger slope. This is also similar to NICAM in the tropics, where NICAM has a positive slope about twice the observed. N5ETHD increases with increasing SAT, about three times as large as observed. It is also of the opposite sign and smaller magnitude as NICAM in the tropics. MAXREFL increases with increasing SAT, which is the opposite of observations, and different from the insignificantly small slope in the NICAM tropics. Another noticeable difference between the observations and NICAM is that for high SAT values, CTH actually decreases with increasing SAT. This indicates that in NICAM, mature DCCs are inhibited by the subsidence associated with high SAT values. This result is questionable, though, because of the low sample size in NICAM at high SAT values. The sample PDF for NICAM DCCs favors lower SAT values relative to the all-sky PDF. This result works in tandem with the decreasing CTH at high SAT values, where DCC formation and growth are inhibited by the environment.

For SPv4, like with TPW, the DCCAR distribution with SAT is very different from observations or NICAM. There are two distinct vertical reflectivity maxima, with a region of thin cloud in between. CTH increases with increasing TPW, slightly less than CloudSat. This increase

is associated with the upper reflectivity maximum. The lower reflectivity maxima seems to have an increasing CTH at a similar rate as the upper reflectivity maximum. N5ETHD increases as SAT increases, with the same sign, but a greater magnitude, than CloudSat. This increasing slope is associated with the upper reflectivity maximum. However, a careful examination of the lower reflectivity maximum shows that there is also an increasing slope (i.e. decreasing reflectivity gradient) associated with the lower maximum as well. MAXREFL decreases with increasing SAT. This is the same sign as CloudSat, but twice the magnitude. There is also an increase in CBH with SAT at high SAT values, like with NICAM. The sample PDF does not strongly favor higher or lower SAT relative to the all-sky PDF. DCCs tend to form in a narrower range of SAT values in SPV4 than observed. This is probably just because the all-sky PDF is narrower for SPV4 than observed.

The reflectivity minimum issue in SPv4 is missing in SPv5 for SAT as well. CTH increases with increasing SAT as observed, though with a smaller slope. N5ETHD decreases with increasing SAT, and N5ETH also increases. This is an interesting result, when compared with the TPW results. While SPv5 DCCs appear to weaken with increasing TPW, when we might expect them to strengthen with greater available humidity, they appear to strengthen with increasing SAT, which we might expect, and even moreso than observed. It would be very interesting to do a more thorough sensitivity study of DCCs in the CRM and analyze their responses to variations in SAT and TPW. MAXREFL decreases slightly with increasing SAT for ECONUS, which is consistent with observations and SPv4. Again, SPv4 did not have major problems with the lower cloud properties. But this is not true for WCONUS, where MAXREFL increases with SAT. The SPv5 sample PDF is also quite interesting. It shares its mode with SPv4, but it is noticeably wider than SPv4, with a broader tail in warmer environments, and

looks more like the observations. This change in shape cannot be explained by changes in the all-sky mean SAT variability, because the SPv5 PDF has the same unrealistically narrow shape as the SPv4 PDF.

It's interesting that the SPv5 scheme seems to reproduce the relationship between SAT and DCCs much more realistically than SPv4 even when both the all-sky mean SAT and the SAT/PBLR cloud relationships are so unrealistic. I don't have a good explanation for this seeming contradiction at the moment. But regardless of the cause, this may be good for SP-CAM. Because DCCs have such a disproportionally large effect on the large-scale environment for their frequency of occurrence, then errors in DCC characteristics could cause serious problems for a lot of different large-scale features in SP-CAM. Conversely, if DCCs behave realistically, then they may be able to reduce some of the effects of unrealistic behavior from other features in the model, e.g. PBLRCs.

Fig. 4.22 shows the same results for WCONUS. Table 4.3 displays the trends in CTH, N5ETHD, and MAXREFL. The DCCAR for WCONUS looks similar to ECONUS, but with a couple of noticeable differences. CTH increases as SAT does, which is the same sign as for ECONUS, but about half the magnitude. This increasing slope isn't continuous for all SAT values, as there are maxima in CTH at 291 K and 306 K. The decreasing trend above 306 K falls in line with the idea that convective clouds may have difficulty developing in very hot environments, as discussed earlier. This idea seems to show up in the DCCAR for CloudSat WCONUS, which makes it more puzzling that it does not show up in ECONUS. The biggest difference between WCONUS and ECONUS is that WCONUS N5ETHD actually decreases as SAT increases. This is the opposite sign of ECONUS, though a much smaller magnitude. A close examination of the DCCAR reveals that the N5ETH stays about the same distance from the CTH

for most SAT values, so this isn't a case of statistical noise interfering with the linear regression. So the strengthened updrafts may reach closer to the cloud top over WCONUS. The MAXREFL decreases with increasing SAT, similar to ECONUS but with larger magnitude. A close examination of the DCCAR shows that this is mainly caused by relatively large MAXREFL values occurring at the lowest SAT values, below 285 K. There appears to be little trend above 285 K. As with ECONUS, the sample PDF does not show a strong preference of DCCs for higher or lower SAT values. There is an absence of DCCs above 310 K, which suggests that both the formation and vertical development of DCCs are inhibited by extreme high SAT values.

The DCCAR for NICAM WCONUS looks similar to that for ECONUS. CTH increases with SAT generally, with about the same magnitude as ECONUS. However, CTH decreases with SAT at high SAT values, as with ECONUS. The CTH maximum occurs at about 299 K, a few Kelvin cooler than ECONUS (because WCONUS is cooler on average). N5ETHD increases with increasing SAT, again with the same magnitude as ECONUS. MAXREFL increases with SAT, about three times the rate for ECONUS, and again in disagreement with observations. As with ECONUS, the sample PDF favors the lower SAT values relative to the all-sky PDF. Also note that NICAM WCONUS DCCs form at much lower SAT values than observed DCCs, because NICAM has a major cold bias in the WMTN region.

SPV4 WCONUS looks similar to ECONUS in that there are two distinct vertical reflectivity maxima at all SAT values. The regression slopes are slightly different, though. CTH increases slightly with increasing SAT. This is about 10% the magnitude of SPV4 ECONUS. The N5ETHD increases slightly with increasing SAT. This is also much smaller in magnitude than ECONUS, and also the opposite sign of CloudSat WCONUS. MAXREFL decreases as SAT increases, about half the magnitude of both CloudSat WCONUS and SPV4 ECONUS. The

sample PDF is strongly shifted towards higher SAT values relative to the all-sky PDF. Recall that the all-sky PDF for SPV4 WCONUS has two frequency maxima, resulting in a bimodal distribution. It appears that DCCs in SPV4 WCONUS only occur near the higher SAT mode, not the lower.

Unfortunately it is difficult to tell of the differences between SPV4 ECONUS and WCONUS regression slopes actually represents a significant difference in DCC behavior in different parts of CONUS, or if it is simply a result of contamination by other cloud types. A close examination of the DCCAR distribution reveals that for the lower reflectivity maximum, the associated CTH does not change much with increasing SAT, but N5ETHD increases (the reflectivity gradient increases). This increase in N5ETHD occurs because of a decrease of N5ETH. This may be indicative of SPV4 DCCs becoming less vigorous at high SAT values, which would be consistent with other results for SPV4 and other data sources discussed previously. A close examination of the SP-ECONUS DCCAR reveals a similar increase in N5ETHD and decrease in N5ETH. This might be evidence that the lower DCC behaves similarly in ECONUS and WCONUS, even if the upper cloud behaves differently.

As for SPv5, most of the statements for ECONUS hold true for WCONUS. The increase in CTH with increasing SAT is lower for WCONUS. The change in the sample PDF is also similar with ECONUS.

4.5.2.3 W500

Fig. 4.23 shows the mean vertical DCCAR profiles sorted by W500 over ECONUS and the corresponding observed sample PDF of W500. Table 4.2 displays the trends in CTH, N5ETHD, and MAXREFL. In general, there do not appear to be any obvious, nearly monotonic changes in

DCCAR as W500 increases. Like with the tropics, there appears to be only a weak association at best between W500 and the vertical reflectivity structure, unlike with TPW and W500. The CTH for CloudSat decreases as W500 increases, which is the opposite sign from the tropical observations, and a larger magnitude. A careful examination of the DCCAR distribution shows that CTH does not decrease steadily with increasing W500. Below about 0.0 m s^{-1}, CTH decreases relatively rapidly with increasing W500. Above 0.0 m s^{-1}, CTH decreases relatively slowly. This maximum in CTH in neutral vertical motion conditions is not observed in the tropics. There is not an obvious answer why CTH would decrease as large scale ascent increases. One might think intuitively that because ascent aids the formation and development of DCCs, that CTH would increase with increasing ascent. Or at very least it would not decrease. The N5ETHD decreases as W500 increases, which is also of the opposite sign of CloudSat in the tropics, and has a larger magnitude. A close examination of the DCCAR distribution reveals that above 0.0 m s^{-1}, the N5ETH stays relatively constant as the CTH decreases, leading to higher upper cloud vertical reflectivity gradient. So while DCCs may become shorter in large ascent conditions, their vertical velocities may not be inhibited in the same manner. MAXREFL increases with increasing W500. There is an odd reduction in reflectivity occurring at 0.0 m s^{-1} in the DCCAR. Unfortunately there is no obvious explanation for this. It cannot be merely an issue of insufficient sampling, according to the sample PDF. The sample PDF shows that DCC formation strongly favors the ascent regime relative to the all-sky PDF, and even more so than the PBLR cloud PDF. So while CTH inexplicably decreases in strong ascent regimes, the frequency increases substantially.

For NICAM, CTH increases with increasing W500, which is the opposite sign from CloudSat and a similar magnitude. Note that this increasing slope is not immediately obvious

from looking at the DCCAR plot. Below -2.0 m s^{-1}, CTH actually decreases as W500 increases. This is possibly related to the low frequency of tall PBLRCs NICAM produces in strong subsidence regimes. But these strong subsidence conditions are not included in the regression calculations because the sample PDF very low here. Above -2.0 m s^{-1}, CTH increases slowly and non-monotonically with increasing W500. N5ETHD decreases with increasing W500 as well. Interestingly, the CTH and N5ETHD slopes are exactly the same. This is because the difference between the CTH and the N5ETH stays constant with W500 for all W500 values above -2.0 m s^{-1}. The vertical resolution of NICAM at this latitude is more than 1 km, so it is difficult for NICAM to represent small changes in height at this altitude. That's why the seemingly odd coincidence occurs. MAXREFL decreases as W500 increases. Aside from MAXREEFL, it appears that NICAM represents the W500/DCC relationship somewhat well.

The sample PDF for DCCs is very strongly shifted into positive vertical motion. This is interesting because the all-sky sample PDF favors subsidence more than observed, and yet the DCC PDF favors ascent more than observed. There is an odd maximum in frequency occurring at 0.0 m s-1, which coincides with a slight discontinuity in the DCCAR distribution. This maximum is not seen in observations or SP-CAM. Unfortunately it is not possible to tell with the currently available data why NICAM DCCs might have this preference for both neutral vertical motions and strong ascent.

For SPv4, the same unrealistic DCCAR distribution discussed previously occurs with W500 as well. CTH increases very slightly with increasing W500. This is the negative of CloudSat, and with a much smaller magnitude. N5ETHD decreases at MAXREFL decreases, again the opposite sign from CloudSat with smaller magnitude, and the same sign and magnitude as NICAM. The disagreement between SP-CAM and CloudSat over MAXREFL should be noted here. Recall that

with TPW and SAT, SP-CAM simulated the lower cloud realistically even when the upper cloud was represented unrealistically. But with W500, both the upper and lower cloud are not represented well. It appears that both models do not simulate the relationship between W500 and DCC vertical structure very well. The sample PDF is shifted to the right even more than NICAM relative to the all-sky PDF. There is no preference for 0.0 m s^{-1} as with NICAM.

SPv5 DCCAR appears to be fairly insensitive to W500 in the upper cloud relative to observations, especially for ECONUS. The observed decrease in CTH and increase in N5ETHD are not seen in SPv5, but rather have opposite sign with a much smaller magnitude. The change in MAXREFL is of the opposite sign, and similar magnitude. The sample PDF for SPv5 is shifted to slightly lower W500 values than SPv4, though it is still higher than observed. This corresponds with the increased frequency of DCCs in SPv5, as DCCs can occur more frequently at W500 values that rarely occur in the mean all-sky environment.

Fig. 4.24shows the same results for WCONUS. Table 4.3 displays the trends in CTH, N5ETHD, and MAXREFL. Like with ECONUS, the changes in DCCAR with increasing W500 are small over WCONUS, and they do not change monotonically. CTH decreases with increasing W500, which is slightly larger than observations over ECONUS, but the same sign. N5ETHD decreases with W500, the same sign as ECONUS, but smaller. MAXREFL increases, again with a similar sign and magnitude to ECONUS. Whatever the reasons are for the regression slopes having their signs and magnitudes, the reasons seem to be somewhat consistent between ECONUS and WCONUS. As with ECONUS, the DCC sample PDF favors ascent relative to the all-sky PDF, though not quite as strongly.

For NICAM, CTH increases similarly to ECONUS and opposite to the observations, according to the regression. A careful examination of the DCCAR reveals a similar pattern

between ECONUS and WCONUS, with CTH decreasing with increasing W500 in subsidence regions, and increasing in ascent regimes. Only the decreasing slope in subsidence is observed. N5ETHD and N5ETH both increase, the latter of which is different from ECONUS. This indicates strengthening of DCCs as W500 increases. The MAXREFL decreases slightly with increasing W500, which is the same sign as NICAM ECONUS, though about a tenth the magnitude. And as with NICAM ECONUS, this is the opposite sign of CloudSat. The sample PDF again shows a strong preference for strong ascent, and an unrealistic preference for 0.0 m s^{-1}.

It's interesting to note that while ECONUS and WCONUS CloudSat results are somewhat similar (with N5ETHD being not so close), those for NICAM are not. Perhaps this should be considered additional evidence that NICAM does not represent the relationship between W500 and DCCs well, or the effect of terrain on DCCs well. IF terrain is an issue for DCCs, it may possibly be an issue for SAT as well, as SAT is much too low over WCONUS.

For SPv4, the same unrealistic double vertical reflectivity maxima seen elsewhere are present here too. CTH decreases as W500 increases, which is lower in magnitude and opposite sign than SPv4 ECONUS, though it has the same sign as CloudSat WCONUS. This decreasing trend is associated with the upper reflectivity maximum. A close examination of the DCCAR shows that the CTH associated with the lower maximum actually increases slightly with increasing W500. MAXREFL increases as W500 does, which is opposite in sign and a smaller magnitude than SPv4 ECONUS. But, it is the same sign and slightly smaller magnitude as CloudSat WCONUS. As with SPv4 ECONUS, the WCONUS sample PDF strongly favors large ascent conditions, more so than observations and NICAM.

As for SPv5, WCONUS CTH is much more sensitive to W500 than ECONUS, with N5ETHD particularly so. CTH increases with increasing W500, the opposite sign and same magnitude as observed. The N5ETHD decreases very rapidly, and N5ETH correspondingly increases rapidly. A careful examination of the plot reveals that this deepening and strengthening only occurs in strong ascent regimes, of at least 0.04 m/s. This makes SPv5 do almost the opposite of the observations, something also seen with TPW. There is no other evidence of a systematic change in N5ETH with W500.

4.6 Conditional sampling of LSEVs

The preceding sections have identified multiple inconsistencies in clouds between the real and simulated atmospheres. A full diagnoses of why these inconsistencies exist is beyond the scope of this chapter. However, it may be possible to use the conditional sampling technique on the LSEVs themselves to see if there are any identifiable connections between simulation errors in cloud behavior and errors in environmental conditions. One example would be simulated clouds not growing vertically at high SAT because of unrealistically low TPW. So it will be useful to check each LSEV's occurrence frequency relative to the other LSEVs in order to determine such issues in the models.

So this section will present the three LSEVs sorted by each LSEV. The sampling technique is the same as used in the preceding section. The results are presented in line plot format instead of 2D contour format, with the mean value of the dependent variable plotted.

4.6.1 SAT

Fig. 4.25 shows various non-cloud meteorological variables sorted by SAT over ECONUS, partitioned into all-sly/PBLR cloud-only/DCC-only categories. Fig. 4.26 shows the same for WCONUS. Recall the models' inability to realistically represent the SAT/PBLR cloud relationship. It's reasonable to consider that possibly the models do not realistically relate changes in SAT with changes in humidity or large-scale ascent/descent, which would hinder the ability to represent the SAT/PBLR cloud relation. But Figs. 25 and 26 show that there are not major differences in the SAT/TPW and SAT/W500 relationships. For ECONUS, the observed TPW for all-sky and PBLR-cloud only increases with SAT until about 300-302 K, then remains roughly constant. For DCC-only, SAT increases until 308 K, then decreases. Not surprisingly, observed and simulated DCC environments tend to be more humid for a given temperature than non-DCC environments. Both models follow the same general pattern for all-sky and PBLR cloud-only, though SP-CAM peaks a few K lower than observed, and actually becomes drier than observations at high SAT values. Neither model shows PBLR CTH increasing/decreasing with SAT in the same manner as TPW, so something other than humidity errors must be responsible for the unrealistic simulated SAT/PBLR cloud relationships. For DCC-only, NICAM is over 10 mm more moist than observed until about 305 K, and the increase in TPW (and by proxy CTH and MAXREFL) corresponds to the observed SAT/DCC relationship. SP-CAM curiously shows a decrease in TPW as SAT increases for DCC-only. This may be another symptom of SP-CAM's inability to simulate DCCs realistically, requiring unrealistically high humidity for DCC formation at lower SAT values. The situation for WCONUS is similar to ECONUS, except that observations and NICAM do not have a maximum TPW value near 300 K for all-sky and PBLR cloud-only conditions.

The all-sky SAT/W500 relationship for ECONUS shows little difference between observations and models. Observed PBLR cloud-only W500 is slightly larger than for both models. For NICAM, there is no obvious decrease in W500 at 300 K where PBLR CTH decreases, so strong subsidence at high SAT values is not an obvious cause for the lack of deep clouds in NICAM at high SAT values. SP-CAM W500 matches the observed W500 near 295 K for PBLR cloud-only, whereas the SP-CAM CTH is still much too low. W500 tends to be larger in observed and simulated DCC environments than non-DCC environments. The DCC-only W500 for SP-CAM is 2 cm s^{-1} too high at almost all SAT values, and does not appear to restrict vertical DCC growth in SP-CAM. For WCONUS, W500 for SP-CAM PBLR cloud-only samples increases to about 1 cm s-1 greater than observed above 294 K, with no similar increase in CTH. NICAM PBLR cloud-only W500 is consistently lower than observed. For DCC-only, SP-CAM again has notably higher W500 than observed, which does not appear to resolve the lack of vertical DCC growth in SP-CAM. Recall that observed DCCs are relatively insensitive in vertical structure to W500, so differences in SAT/W500 relationships between the models and observations shouldn't be strongly related to differences in SAT/DCC relationships.

4.6.2 TPW

Fig. 4.27 shows various non-cloud meteorological variables sorted by TPW over ECONUS, partitioned into all-sky/PBLR cloud-only/DCC-only categories. Fig. 4.28 shows the same for WCONUS. Observations show that generally SAT increases as TPW increases until about 55 mm, for all three data categories. NICAM generally reproduces this, though it is a bit too cool above 40 mm. SP-CAM is about 2-3 K too warm below 40 mm, and the same magnitude too warm above 40 mm. SP-CAM does not show the observed all-sky sensitivity of SAT to TPW

above about 25 mm. The situation is almost the same for the PBLR cloud-only relationships for both models and the observations. However, because the simulated SAT/PBLR cloud relationships are so unrealistic, it is difficult to say what kind of differences in the TPW/SAT relationship would result in the simulated lack of deep PBLRCs in SP-CAM, or the lack of deeper clouds in drier environments in NICAM. The most that can be said is that, hypothetically if NICAM and SP-CAM produced the observed SAT/PBLR cloud relationship, then the lack of large cool biases in the simulated TPW/SAT relationships would not contribute to a lack of deep clouds in either model.

The TPW/SAT relationships for DCC-only shows larger differences between models and observations. NICAM is generally cooler than observations by about 5 K below 50 mm. According to the SAT/DCC relationship, this should result in lower MAXREFL and CTH below 50 mm if the TPW/SAT relationship was a significant source of errors. NICAM MAXREFL is indeed lower than observed MAXREFL below 50 mm, but the same is true above 50 mm. So it is unclear whether lower MAXREFL below 50 mm is related to too low SAT or just a result of a generalized lower MAXREFL in all convective environments as a result of microphysical errors. NICAM CTH is not notably lower than observed CTH below 50 mm. SP-CAM has the most different TPW/SAT relationship, however. SAT below 45 mm is much larger than observed, up to 20 K in drier environments. If SP-CAM DCC vertical profiles were more realistic, this could potentially correspond with a decrease in CTH and MAXREFL with increasing TPW. This fact might be relevant if DCCs in SP-CAM improve with the double-moment microphysical scheme.

The situation is a little different with WCONUS. For all-sky and PBLR-only categories, NICAM and SP-CAM are cooler than observations at most TPW values by about 5 K. If NICAM and SP-CAM produced a realistic SAT/PBLR cloud relationship, this might result in

lower CTH for most TPW values, and could help explain the lack of deeper clouds in the TPW/PBLR cloud relationship. This possibility cannot be confirmed with the unrealistic SAT/PBLR cloud relationships, though. The large differences in TPW/SAT relationships for DCC-only exist in WCONUS as well, though they are more pronounced for NICAM and less pronounced for SP-CAM. Interestingly, in NICAM's case, MAXREFL is about 5 dBZ too low below 50 mm, and CTH is about 1 km too low. Low MAXREFL and CTH are consistent with low SAT for NICAM, so it is possible that the cold bias in the TPW/SAT relationship might contribute to errors in CTH and MAXREFL in drier DCC environments.

For ECONUS W500, the all-sky TPW/W500 relationship is close for models and observations, except for SP-CAM above 60 mm, which has a 2 cm s^{-1} high bias. NICAM W500 is about 1 cm s^{-1} too low at all TPW values, so this cannot explain the lack of deep clouds in only drier environments. SP-CAM shows a high bias in PBLR cloud-only W500 above 50 mm. This should encourage deep cloud development. While SP-CAM PBLRCs become deeper above 50 mm, they are still too shallow compared with observations. So the TPW/W500 biases in SP-CAM cannot explain the lack of deep clouds. For DCC-only, observations don't show any major increases or decreases in W500 with increasing TPW, but DCC-only W500 is larger than all-sky. NICAM shows W500 decreasing with increasing TPW, and SP-CAM shows increasing W500 with increasing TPW above 30 mm. For NICAM, the DCC vertical profile is mostly insensitive to W500, so it is reasonable to expect the error in the TPW/W500 relationship to have little effect on DCCs.

There are a few differences between WCONUS and ECONUS. First, there is no obvious increase in observed W500 with TPW for all-sky conditions. The models replicate this difference. Second, the difference between PBLR cloud-only W500 for observations and models

is not as large for WCONUS as for ECONUS. Third, NICAM as well as SP-CAM has higher W500 than observed for most TPW values in DCC-only conditions. Aside from that, the main conclusions for ECONUS still hold for WCONUS. The lack of deep PBLRCs in NICAM at lower TPW values and SP-CAM at all TPW values cannot be explained by low biases in W500.

4.6.3 W500

Fig. 4.29 shows various non-cloud meteorological variables sorted by W500 over ECONUS, partitioned into all-sky/PBLR cloud-only/DCC-only categories. Fig. 4.30 shows the same for WCONUS. The observations show that SAT maximizes in weak subsidence regimes, which is reasonable given that high SAT values tend to form in high pressure regions. This is particularly true for DCC environments. This also corresponds to the SAT-sorted W500 discussed earlier. This occurs in all three environments, and is particularly strong in deep convective environments. TPW is more interesting in that not all environments have the same relationships. The mean and PBLRC environments both show TPW increasing as ascent becomes stronger. But in DCC environments, TPW is highest in weak subsidence, and decreases in ascent regimes. This corresponds with the tendency for PBLRCs to grow deepest in ascent environments, but DCCs to grow taller in weak subsidence (both cloud types grow taller with higher TPW values). It isn't clear how to interpret this. It could be that DCCs require more humidity in weak subsidence environments to develop and overcome the subsidence effects.

The models generally capture the W500/SAT relationship of SAT being highest in weak subsidence. SPv4 in particular reproduces the strong DCC environmental tendency for high SAT in subsidence, though NICAM does not do so as much. The models also reproduce the increase in TPW as ascent increases for the mean and PBLRC environments, and both show an even

stronger relationship than observed. However, the models do not reproduce the different behavior of the DCC environment. NICAM shows no sensitivity of TPW to W500, and SP-CAM has TPW increasing with W500. This may help explain why the models have problems with the W500/DCC relationship for DCCAR. The sensitivity of DCCs to TPW should lead to unrealistic simulated W500/DCC relationships if the simulated W500/TPW relationship is unrealistic.

The observed W500/SAT and W500/TPW relationships are generally similar to ECONUS, with the main difference being that SAT maximizes in weak ascent rather than descent for the mean and PBLRC environments. NICAM does not reproduce this difference, and resembles the ECONUS results. SP-CAM shows an error with the mean environment, where there is a minimum in weak subsidence, and higher SAT values in strong ascent and subsidence. The reason for this is not presently clear, but it is possible that the limited terrain resolution in SP-CAM may lead to such an error – this may need to be investigated further. The PBLRC and DCC environments more closely match observations.

The W500/TPW observations show the same difference between the mean/PBLRC environments and the DCC environment. The models also generally fail to reproduce the observations in DCC environments. It appears that whatever the cause is for the observed TPW maximum in weak subsidence for DCC environments, the models do not capture the relevant physical processes well.

4.7. Vertical profiles of other cloud indices

The radar identification technique for clouds is a relatively new and potentially useful technique for characterizing simulated cumulus clouds and comparing them with observations. However, it is an imperfect technique for reasons discussed previously. So it would be useful to

briefly examine other simulated cloud characteristics and compare them with the radar-derived results. Unfortunately, the vertical structure of thick clouds and multi-layer clouds is very difficult to observe, so I am currently limited to model intercomparison studies. Furthermore, NICAM data is not available to me for latent heating studies, so only SPv4 and SPv5 can be examined here for that.

This section will examine two cloud properties in relation to the radar-derived results: the mean convective vertical velocity profile, and the mean cloud latent heating rate (CLHR) profile. In-cloud vertical velocity can be taken directly from the CRM grid-level data. Latent heating data are more difficult to handle. SPv4 and SPv5 do not output heating data on the CRM grid, but only the GCM grid. Furthermore, the latent heating rate is not directly given – only the total diabatic heating rates and the radiative heating rates are given. So to calculate the latent heating rate, the difference between the total and radiative heating rate is used as a proxy for latent heating. This should be reasonable for convective environments, where latent heat release is on the order of 10 K/day or even 100 K/day within DCCs. The grid issue is resolved by assigning the same latent heating rate for each cloud within the same GCM gridbox (as identified on the CRM grid), and then weighting the mean by the number of clouds within that GCM box.

4.7.1 Vertical velocity profiles

Fig. 4.31 shows the vertical velocity profiles for PBLRCs and DCCs. For the ECONUS PBLRC mean, all three models show two maxima in the vertical profile – a shallow maximum at 1-2 km which is likely associated with shallow cumulus (or the models' attempt at representing them), and a second maximum at 7-8 km likely associated with DCCs. Interestingly there is no maximum representing cumulus congestus, which would probably occur at 3-5 km altitude. This

is consistent with the lack of cumulus congestus suggested by the radar-derived data. Vertical motion within SP-CAM shallow clouds appear stronger than in NICAM, but weaker in deeper clouds. Interestingly, there appears to be little difference between SPv4 and SPv5. This is curious because it appears at face value to be inconsistent with the radar-derived results, with SPv4 deep clouds apparently limited to 8 km and SPv5 deep clouds extending multiple kilometers above that frequently. This apparent discrepancy will be discussed further with regard to the CLHR results.

The 95% results roughly mirror the mean results, though with a less smooth curve because of the data sparsity. SPv4 has larger vertical velocity than SPv5, and this will be discussed in the DCC paragraphs. It's interesting that NICAM has a lower vertical velocity than SPv4, unlike the mean values. It isn't obvious why this should be the case, especially when viewed in conjunction with the DCC results.

The WCONUS results have one major interesting difference from the ECONUS results. SP-CAM shows strong sinking motion from 2-6 km altitudes. It is not obviously clear why this exists. It's possible that downdrafts in the drier WCONUS troposphere could enhance some tendency in SP-CAM to generate stronger downdrafts. This tendency could not be solely linked to microphysics errors in SP-CAM because of the change in microphysics from SPv4 to SPv5. There is some evaporative cooling in SP-CAM in the lower troposphere (discussed in the next subsection), but not throughout a deep enough layer to easily explain the sinking motion. This is probably another topic that would be worth investigating in the future.

As for DCCs over ECONUS, all three models show the same general shape of the idealized Gaussian distribution of velocity, with a maximum in the middle troposphere and smaller positive values above and below. However, the DCC profiles show distinct differences between

the three models. The absolute magnitude of velocities in all three models seems rather low at first glance, with mean velocity less than 1 m/s, and even the 95% velocities of a few m/s. But keep in mind, as mentioned previously, that the model velocities are taken at multi-kilometer horizontal resolution. They cannot be easily compared directly with observed vertical velocities, which for the Great Plains can be well over 10 m/s within turbulent updrafts. This problem has been noted with previous studies using NICAM [ref]. For the mean profiles, NICAM has the largest magnitude of the three models, at 7 km altitude. NICAM also shows a shallow layer dominated by downdrafts below 2 km. Keep in mind that the mean velocity is calculated from DCCs in all phase of development and decay, so the existence of downdrafts in the mean profile does not mean that all DCCs have downdrafts in the lower cloud. SPv5 has the same general shape as NICAM, but with about half the magnitude of velocities, and a deeper region of downdrafts in the lower cloud.

SPv4 is particularly interesting, as it has a magnitude greater than SPv5, though below NICAM, but the altitude of the maximum velocity is about 2-3 km higher than the other models. This probably is not related to a difference in the latent heating profile (discussed further in the next subsection), but it could be related to the microphysical deficiencies in SPv4. Snow falls more quickly than cloud ice, and thus induces a greater restraint on the convective updraft. So the absence of midtropospheric snow in SPv4 means less resistance to the convective updraft, and thus a higher altitude velocity maximum in SPv4. As for the larger velocity magnitude in SPv4, recall that DCCs are much less frequent in SPv4 than SPv5. If the large scale convective forcing in both models are similar, this means that each DCC in SPv4 would have to have a higher vertical velocity than in SPv5 to maintain the same large scale convective mass flux. If this argument is true, then it makes sense that SPv4 would have higher velocity than SPv5. This

also makes the NICAM result interesting, as NICAM has a larger horizontal resolution than SP-CAM. NICAM DCCs are more frequent than SPv4, so this suggests that large scale DCC activity in NICAM is larger than in SP-CAM. There is currently little research that explains why this is the case if it is, so this is a topic worth further investigation.

The 95% results are mostly the same as the mean results, except that the downdrafts are obviously absent as a consequence of the methodology, and that NICAM and SPv4 are closer in absolute magnitude. The 95% curves appear to be shifted about 1 km higher in altitude from the mean curves, indicating that the most vigorous DCCs are slightly taller than the average DCC.

It should be noted that there is no evidence of a vertical velocity hole in SPv4 DCCs in the middle troposphere. This confirms the idea that the radar reflectivity hole discussed previously is caused by microphysical errors and not errors in macrophysical properties.

The results from WCONUS DCCs are broadly consistent with the results from ECONUS DCCs. The most obvious difference is that the difference in velocity magnitude between NICAM and SP-CAM is notably greater than for ECONUS. This reinforces the question of large scale convective forcing discussed previously, especially since deep convection over WCONUS is largely controlled by the North American Monsoon, a tricky climatological feature to simulate. The vertical velocity maxima over WCONUS appear to be about 0.5 to 1 km greater in altitude than for ECONUS. This may be a result of the higher terrain over much of WCONUS combined with a higher lifted condensation level compressing the DCCs into a shallower depth of troposphere.

4.7.2 CLHR profiles

Fig. 4.32 shows the CLHR profiles for PBLRCs and DCCs. Recall that there is no NICAM data for CLHR. For the ECONUS PBLRC mean, There are two main maxima in CLHR that correspond with the vertical velocity maxima – one at 1 km which represents shallow clouds, and one at 7 km representing DCCs. Again, there is little evidence of cumulus congestus in both models. As with vertical velocity, there is little difference between SPv4 and SPv5, at least for the mean values. This means that SPv4 has significant CLHR above 8 km, which as with vertical velocity appears to be inconsistent with the radar-derived results. I do not have a good explanation for the discrepancies at the moment. Perhaps it would be useful to do a more thorough sensitivity study with the radar-derived results to make sure that the latter results are reliable. This is a topic worth further investigation. Whatever the answer is, it appears that the apparent lack of frequent very deep clouds in SPv4 does not have a major effect on the upper troposphere CLHR profile produced by them.

The 95% results show the same general distribution shape as the mean data. There are two minor differences. There is a minor maximum in both models at 13 km, near the cloud top, which is more evident in SPv4. Also, there is a tertiary maximum at 17 km, above the cloud top. It isn't immediately obvious what causes these maxima, but the latter is very likely not latent heating. The SPv4 CLHR is larger than the SPv5 rate. For the deeper clouds, the explanation for this is the same as for the vertical velocity difference between DCCs (discussed earlier). For shallow clouds, the formation rate in SPv5 is slightly higher than SPv4 (see Table 4.1), which may contribute to this difference.

WCONUS has three notable differences from ECONUS. First, in the mean profiles, there is slight cooling occurring in the lower troposphere for both models. Because this occurs in both

models at a similar magnitude, it cannot be easily concluded that this is a simple microphysical issue, as the microphysical schemes are different. As discussed with the vertical velocity data, it may be related to SP-CAM's tendency to produce stronger downdrafts than NICAM in DCCs, particularly in the drier WCONUS convective environment. Second, the 95% magnitudes for both models are similar, and in fact SPv5 is slightly larger at higher altitudes. This will be discussed further in the DCCs, and it may be related to problems with SPv4 simulating the large scale convective forcing over WCONUS. Third, the mid-tropospheric maximum for SPv5 occurs 1-2 km higher than for SPv4 in both the mean and 95% data. This occurs in the DCC-only data as well, discussed below.

The DCC CLHR vertical profiles for ECONUS resemble the vertical velocity profiles closely, with a maximum at 7 km and negative values below 2 km. Both models show the typical shape associated with the first baroclinic heating mode. However, there is also evaporative cooling occurring below 2 km, likely associated with the downdrafts seen in the vertical velocity profiles. As with vertical velocity, SPv4 has larger positive and negative values than SPv5. The 95% values resemble the mean values in vertical structure, except that the region of large heating in the middle troposphere appears to be shifted slightly higher in altitude by about 1 km. As with vertical velocity, no CLHR hole is apparent in SPv4 in the middle troposphere, which supports the claim that the reflectivity hole is a result of microphysical errors rather than macrophysical deficiencies. Interestingly, there is no obvious offset in altitude between SPv4 and SPv5, unlike with vertical velocity. There is no demonstrable reason for this difference at the moment, but it is consistent with the idea presented previously that increased drag from increased snow in SPv5 lowers the vertical velocity in the upper cloud, not a change in the vertical heating profile.

WCONUS is interesting because it looks rather different from both the ECONUS CLHR and WCONUS vertical velocity profiles. The main difference is that SPv4 and SPv5 are much closer together than in the other results. In fact, the 95% curve for SPv5 has a larger maximum value than SPv4. This appears to be at odds with the argument made for ECONUS that the value for SPv4 is larger because there are fewer DCCs in SPv4 to contribute to large scale convective activity. Because of the large difference in DCC frequency between SPv4 and SPv5, these results taken together mean that SPv4 has less large scale convective activity than SPv5 over WCONUS. As suggested previously, a likely cause for this is a nearly dead North American Monsoon in SPv4. The large scale forcing needed for vigorous deep convection in this region just does not exist in SPv4 for whatever reason.

4.8 Conclusions

From these results, it is possible to answer the questions posed at the beginning of this chapter with some confidence:

1. How realistic are cloud characteristics in the models? Cloud frequency? Cloud altitude and thickness? Cloud radar reflectivity?

SPv4 greatly overproduces cloud ice relative to NICAM, and underproduces precipitating ice. However, because CloudSat is relatively insensitive to thin ice clouds, this bias is not evident from radar-simulated cloud identification. Both SPv4 and NICAM do not grow PBLRCs (detectable to CloudSat) vertically as often as observed. SPv4 in particular has great difficulty growing clouds deeper than 8 km. NICAM DCCs have a similar vertical structure to observed DCCs, but the lack of graupel in NICAM reduces the reflectivity above the freezing level. SPv4

does not reproduce the observed reflectivity profile in the upper cloud, instead producing a vertical layer of very low reflectivity above the freezing level. The lower cloud reflectivity structure is closer to observations, but is slightly too low.

For SPv5, deep PBLRCs (detectable by CloudSat) have increased in frequency, and low clouds have decreased in frequency. This brings SP v5 closer to CloudSat observations, though the biases from v4 still persist to an extent. PBLR clouds no longer are limited to an 8 km maximum height, and commonly (with a 20% frequency) exceed this height. The maximum CTH for PBLR clouds now matches observations fairly closely. Shallow clouds show little improvement from SPv4 to SPv5, but there are good reasons to expect little improvement. The overproduction of cloud ice appears to have been resolved in v5. Cloud ice concentration has greatly decreased, and snow has greatly increased. There is also a separation in altitude between cloud ice and snow, indicating that snow falls more realistically in v5. These improvements lead to a large improvement in the SPv5 DCCAR, with the reflectivity hole in SPv4 missing in SPv5.

Using other cloud variables to test this finding leads to mixed results. The vertical velocity profiles for SP-CAM seem to support the idea that PBLRCs have difficulty growing deeper than 8 km, as vertical velocity above this altitude are low. This appears to be the case for SPv5 as well, even though the radar-derived results suggest an improvement above 8 km. However, the CLHR profiles show significant heating in SP-CAM well above 8 km, for both versions. The interpretation for this is not presently clear. However, one good bit of news from this result is that the microphysical errors in SPv4 do not appear to cause problems with the convective latent heating in the upper troposphere.

Both NICAM and SP-CAM produce too many clouds, including PBLRCs, relative to CloudSat over both ECONUS and WCONUS. Part of this result may be CloudSat's insensitivity

to very low clouds. NICAM produces a number of DCCs comparable to observations. However, SP-CAM produces far too few clouds, especially over WCONUS.

2. How realistically are clouds distributed across CONUS?

NICAM and SP-CAM both produce more clouds than observed by CloudSat, though CloudSat observations may miss some clouds (mainly cirrus clouds). NICAM produces too many clouds over the US southeast and south, and SP-CAM produces too few clouds over the Pacific coastline. Both models produce more PBLRCs than observed (almost double), and the spatial pattern is notably different. CloudSat observes more PBLRCs over WCONUs than ECONUS (particularly over the western mountains), while both models produce more clouds over ECONUS. There is an open question about CloudSat's ability to detect PBLRCs over ECONUS, though. In contrast, both models produce fewer DCCs than observed, especially SP-CAM over WCONUS (15% of the observed frequency). NICAM reproduces a majority of the observed DCC spatial distribution, but SP-CAM does not produce DCCs over much of GPLN, southeast Canada/northern New England, and all of WCONUS (including NAM).

3. And related, how realistically is precipitation distributed across CONUS?

NICAM produces too much precipitation, by up to half an order of magnitude, across CONUS. SP-CAM produces slightly too much precipitation over ECONUS, and far too low precipitation over WCONUS (by up to an order of magnitude). SP-CAM does not correctly place the southeast SPREC maximum over FL, and the lowest SPREC is found in part of the North American Monsoon region, calling into question SP-CAM's ability to simulate the Monsoon. SPv5 improves precipitation in WCONUS, but still has difficulty with the Monsoon.

4. How realistic is the diurnal cycle of precipitation?

SP-CAM reproduces the diurnal precipitation range fairly realistically, though it misses the regional maximum over the Great Plains. SP-CAM is not phase-locked to the solar cycle like many traditional GCMs are, and produces an afternoon precipitation maximum like observed. SP-CAM also produces something that slightly resembles the Great Plains nocturnal precipitation maximum, though it does not reproduce all of the details. SPv5 appears to improve the representation of the nocturnal maximum from SPv4, including a stronger easterly propagation signal.

5. What are the relationships between clouds and LSEVs? Do the models simulate them realistically?

Observed PBLRCs increase in height steadily as TPW increases. NICAM cloud height increases with TPW similarly to observations, but with an absolute COF magnitude too low at all TPW values. SPv4 behaves somewhat similarly, but the COF magnitude is even lower at all TPW values. SPv5 appears to improve the COF values to almost the observations above 45 mm, but not below. Observed PBLRCs increase steadily with increasing SAT until a certain threshold value, and then decrease in height (presumably hot environments inhibit cloud growth over extratropical continents). Both SP-CAM and NICAM fail to represent the observed relationship, with NICAM reproducing the observations slightly more closely than SP-CAM. Observed PBLRCs increase steadily as W500 increases, and vertical development occurs in subsidence and ascent conditions. NICAM and SP-CAM fail to develop most PBLRCs vertically in subsidence regions, and NICAM produces the occasional deeper PBLR cloud in strong subsidence

conditions for unknown reasons. Furthermore, the observed preference for PBLR cloud formation (regardless of height) in ascent conditions is not seen in either model.

NICAM's lack of vertical PBLR cloud development seems to occur because NICAM does not grow clouds frequently at lower W500 values, and at all TPW values as well. While SPv4 shares the same problem, SPv5 grows deep clouds more frequently (almost realistically) in more humid environments. This change from SPv4 is likely responsible for SPv5's increase in the mean COF of deep clouds over CONUS.

Observed DCCs increase in height as TPW increases, the N5ETH increases, the upper cloud reflectivity gradient decreases, and the maximum reflectivity increases. This suggests that observed DCCs get deeper and stronger as TPW increases, though the stronger updraft does not reach the cloud top. NICAM predicts these changes fairly closely, but SPv4's mean DCC reflectivity profile is too different from observations to simulate the relationship realistically (or at least it is too difficult to tell what is happening through simple regression statistics). Observed DCCs increase in height with increasing SAT over ECONUS, the N5ETH increases, the gradient decreases, and the maximum reflectivity also decreases. Over WCONUS, cloud top height is diminished at high SAT values. NICAM represents the upper cloud sensitivity to SAT relatively well, but not the maximum reflectivity. NICAM also shows an unrealistic preference of DCC formation at cooler SAT values. SPv4 again has difficulty for the same reason as with TPW. Observed DCCs decrease in height as W500 increases, the gradient increases, and the maximum reflectivity increases as well. Neither NICAM nor SPv4 represent the relationships between DCCs and W500 well.

For SPv5, the improvement in DCC vertical structure is not attributable merely to changes in the mean convective environments, as the improvement occurs in all environments that produce

DCCs. The relationship between LSEVs and maximum reflectivity (representing the lower cloud) has worsened between v5 as v4, though it is hard to interpret what this means for cloud behavior. The relationship between the upper cloud and SAT is represented fairly realistically, but not for TPW or W500. CTH is insensitive to increasing TPW and W500. N5ETH suggests that DCCs weaken unrealistically with increasing TPW.

To summarize, the three models both have major difficulty with the relationship between PBLRCs and SAT. They also have some difficulty reproducing the relationship between W500 and DCCs. Both models also have difficulty developing PBLRCs vertically in environmental conditions marginally favorable to convection (lower TPW, negative W500).

Conditional sampling also reveals that the algorithm for detecting DCCs may not work well in SPv4 because the DCC reflectivity profile in SPv4 is so different from the observed profile. There might be contamination from high clouds as a result of the low cloud reflectivity decreasing rapidly at the freezing level. This possible source of error is not obvious from the mean reflectivity profile alone, without conditional sampling.

6. Can biases in cloud characteristics be explained simply by biases in LSEVs?

Generally, the biases in LSEV/LSEV (e.g. SAT/TPW) relationships are not sufficient to explain the errors in LSEV/PBLR cloud and LSEV/DCC relationships. One possible except to this is for WCONUS, where a cold bias in drier DCC environments may contribute to slightly shorter DCCs with lower MAXREFL. Errors in mid-tropospheric humidity, tropopause height, and level of neutral buoyancy do not correspond with errors in LSEV/cloud relationships, though the LNB analysis may need to be extended to draw more reliable conclusions.

Additional comments

These results also help answer one question involving unrealistic cloud behavior in SP-CAM. Previous studies have identified a persistent problem with older SP-CAM versions producing too many high clouds over the tropics, with the mean CWC at this altitude being too high [Benedict and Randall 2009]. Others have proposed that this problem might be related to overactive DCCs over the tropical oceans [e.g. Zhang et al. 2008]. Well, the version of SP-CAM used in this chapter, SPv4, also produces too many high clouds over CONUS, as has been shown. This high cloud anomaly exists even though SPv4 produces too few DCCs over CONUS. So the answer cannot be something as simple as too much deep convection. Whether or not it is true over the tropical oceans, it is not true over CONUS.

So what could be the answer? These results suggest that the microphysics plays a major role in the error. The vertical hydrometeors profiles in and (possibly) above SPv4 DCCs shows that SPv4 does not change cloud ice into snow nearly as rapidly as NICAM. It stands to reason that if SPv4 does not easily remove cloud ice in the turbulent conditions of a DCC, it will have the same problem in a calmer environment. The excess high clouds over CONUS could be the result of cloud ice, produced by the few DCCs that form in SPv4, that simply persists for a long time without an efficient mechanism to erode it. Alternately, it might be the case that the cloud ice over CONUS might originate in the tropics, and is simply advected over CONUS via the subtropical jet. The SPv5 results show that by changing only the microphysics and radiation schemes, the problem is apparently resolved, or at least greatly reduced in severity. Cloud ice is transformed to snow and graupel much more efficiently in SPv5. This change should also affect the properties of non-convective ice clouds in SPv5 as well. Given their role in cloud/climate interaction, this possibility should be investigated further.

With this chapter, I conclude the analysis of the NICAM data currently available to me. The results presented here were created from an older version of NICAM using simplified microphysics. The NICAM team have since implemented more advanced schemes into the model that show some promise for improving the model [Tomita 2008, Satoh and Matsuda 2009]. It's my hope that other researchers using current versions of NICAM will see the utility of the conditional sampling technique presented here, and will use it in analyzing the more current NICAM versions.

Table 4.1. Number of samples and frequency of occurrence for each meteorological scene[a]

ECONUS	DATASET: CS		NICAM		SPv4		SPv5	
	number	freq.	number	freq.	number	freq.	number	freq.
Scene								
all-sky	1939443	1.000	19114095	1.000	771328	1.000	771328	1.000
cloud	663221	0.342	9431935	0.493	291193	0.377	321878	0.417
PBLRC	314737	0.162	6762888	0.353	257214	0.333	270275	0.350
DCC	44722	0.023	365516	0.019	7872	0.010	23506	0.030

WCONUS	DATASET: CS		NICAM		SPv4		SPv5	
	number	freq.	number	freq.	number	freq.	number	freq.
Scene								
all-sky	1867720	1.000	17061990	1.000	671232	1.000	671232	1.000
cloud	580845	0.311	7652487	0.448	149225	0.222	171818	0.255
PBLRC	353356	0.189	4599897	0.269	81363	0.121	98374	0.146
DCC	22784	0.012	228877	0.013	1342	0.001	6244	0.009

[a] Listed are the number and frequency of samples for all-sky (clear plus cloudy), cloud-only, PBLR cloud only, and DCC only (rows), by dataset (CloudSat, NICAM, SP-CAM, columns). The frequency of samples is the number of samples for each scene type divided by the number of all-sky samples.

Table 4.2. Trend Slope Values for the LSEVs by Dataset over ECONUS[a]

	DATASET			
	CS	**NICAM**	**SPv4**	**SPv5**
	slope	slope	slope	slope
LSEV/REFL.				
TPW				
CTH ($m\ mm^{-1}$)	117.80	61.82	-64.00	-35.23
N5ETHD ($m\ mm^{-1}$)	36.92	13.67	-65.33	-47.61
MAXREFL ($dBZ\ mm^{-1}$)	0.03808	0.02871	0.02671	-0.00542
SAT				
CTH ($m\ K^{-1}$)	163.63	191.81	120.00	101.47
N5ETHD ($m\ K^{-1}$)	32.49	109.93	96.00	-58.10
MAXREFL ($dBZ\ K^{-1}$)	-0.03580	0.07750	-0.08687	-0.14566
W500				
CTH ($m\ m^{-1}s$)	-58022	45640	-2909	15272
N5ETHD ($m\ m^{-1}s$)	-48791	45640	-8727	21818
MAXREFL ($dBZ\ m^{-1}s$)	241.84	15.47	-146.65	-225.05

[a] Listed are the statistics by LSEV (TPW, SAT, W500, rows) and by dataset (CloudSat, NICAM, SP-CAM, columns).

Table 4.3. Trend Slope Values for the LSEVs by Dataset over WCONUS[a]

	DATASET			
	CS	**NICAM**	**SPv4**	**SPv5**
	trend	trend	trend	trend
LSEV/REFL.				
TPW				
CTH ($m\ mm^{-1}$)	63.73	77.43	-49.33	37.33
N5ETHD ($m\ mm^{-1}$)	34.28	27.31	-48.00	-61.33
MAXREFL ($dBZ\ mm^{-1}$)	0.04052	-0.85840	0.02807	0.1602
SAT				
CTH ($m\ K^{-1}$)	95.52	114.68	5.27	79.44
N5ETHD ($m\ K^{-1}$)	-5.08	54.37	9.23	-108.61
MAXREFL ($dBZ\ K^{-1}$)	-0.1015	0.1860	-0.15979	-0.1559
W500				
CTH ($m\ m^{-1}s$)	-77802	94362	32000	80000.0
N5ETHD ($m\ m^{-1}s$)	-19780	34194	16000	-156000.0
MAXREFL ($dBZ\ m^{-1}s$)	206.48	155.54	342.30	166.48

[a] Listed are the statistics by LSEV (TPW, SAT, W500, rows) and by dataset (CloudSat, NICAM, SP-CAM, columns).

a) Observation

b) NICAM

c) SPv4

d) SPv5

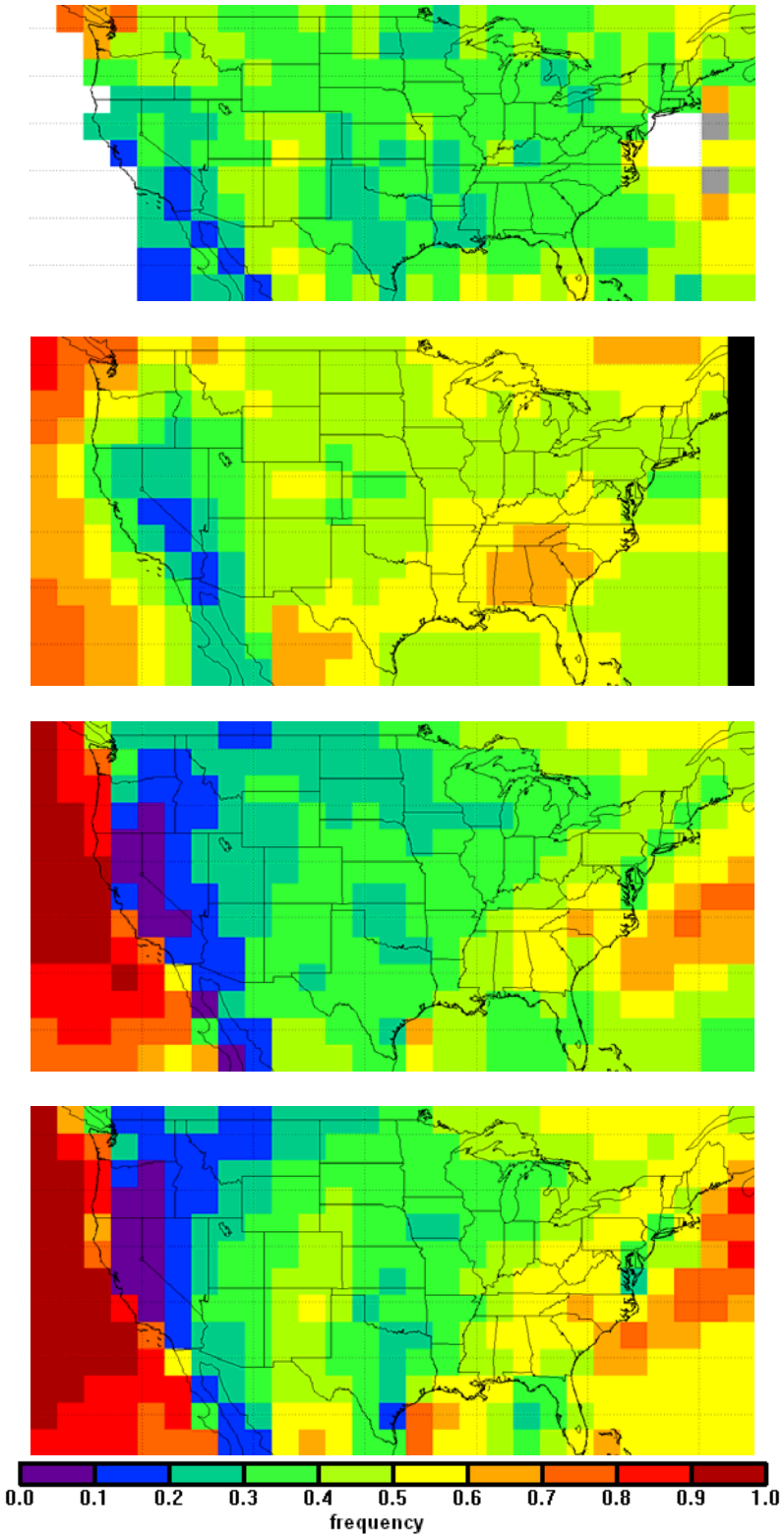

Figure 4.1. COF spatial distribution for all cloud types at 6z and 18z over CONUS for a) observations, b) NICAM, c) SPv4, and d) SPv5. For CloudSat, white areas represent regions with no data, and gray areas represent areas with less than 100 samples.

a) Observation

b) NICAM

c) SPv4

d) SPv5

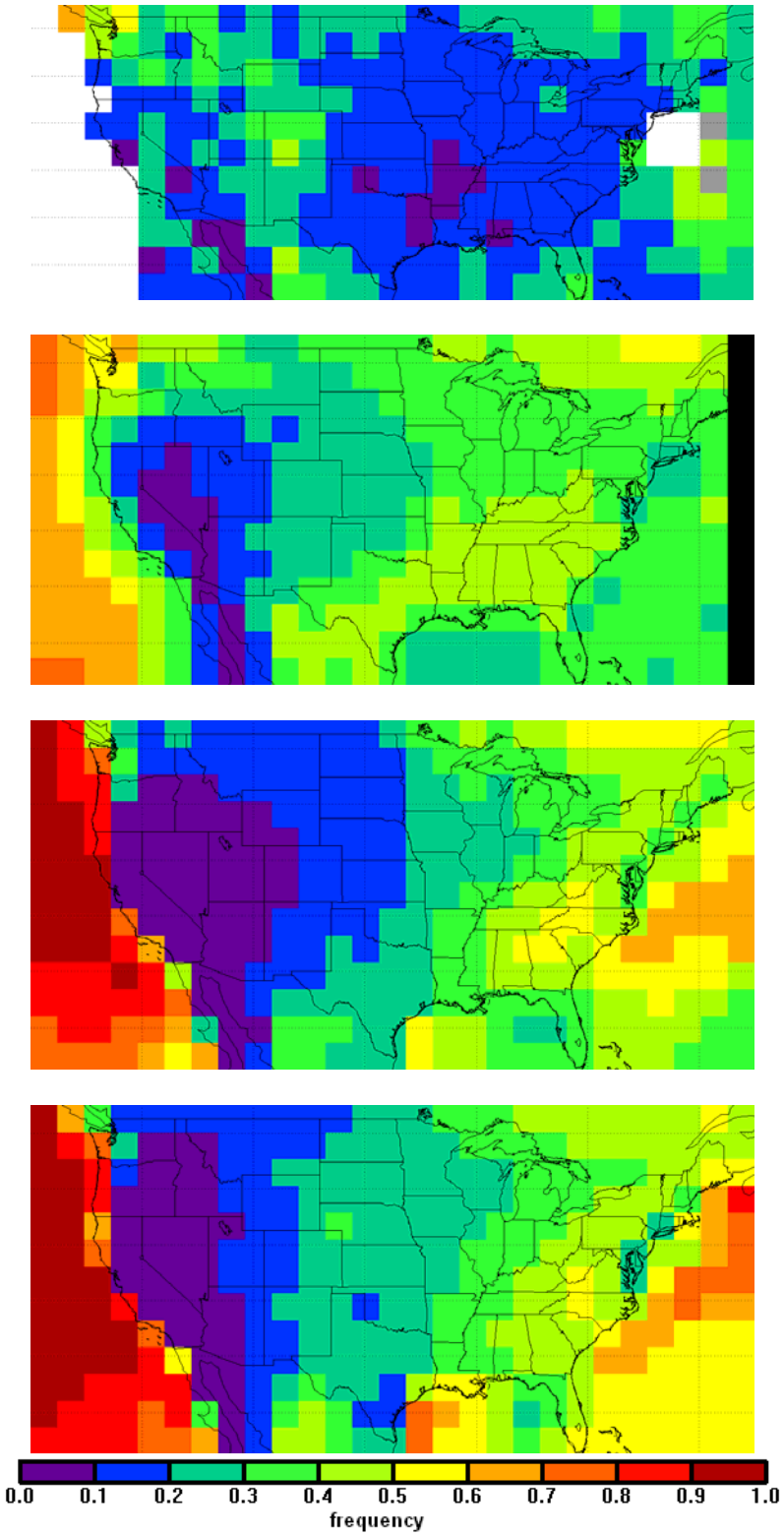

Figure 4.2. Same as Fig. 4.1, but for PBLRCs.

a) Observation

b) NICAM

c) SPv4

c) SPv5

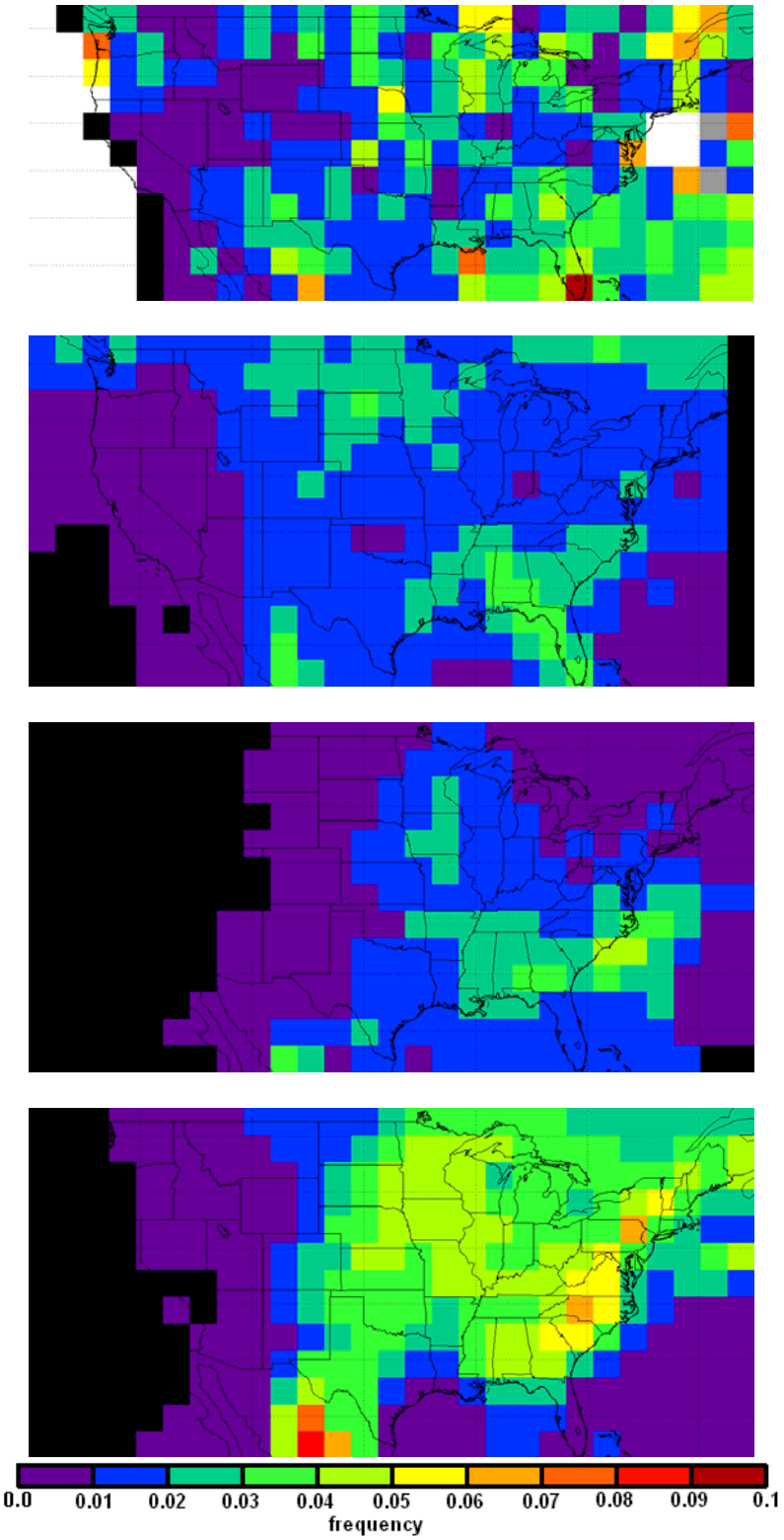

Figure 4.3. Same as Fig. 4.1, but for DCCs. Note the change in color bar.

a) Observation

b) NICAM

c) SPv4

d) SPv5

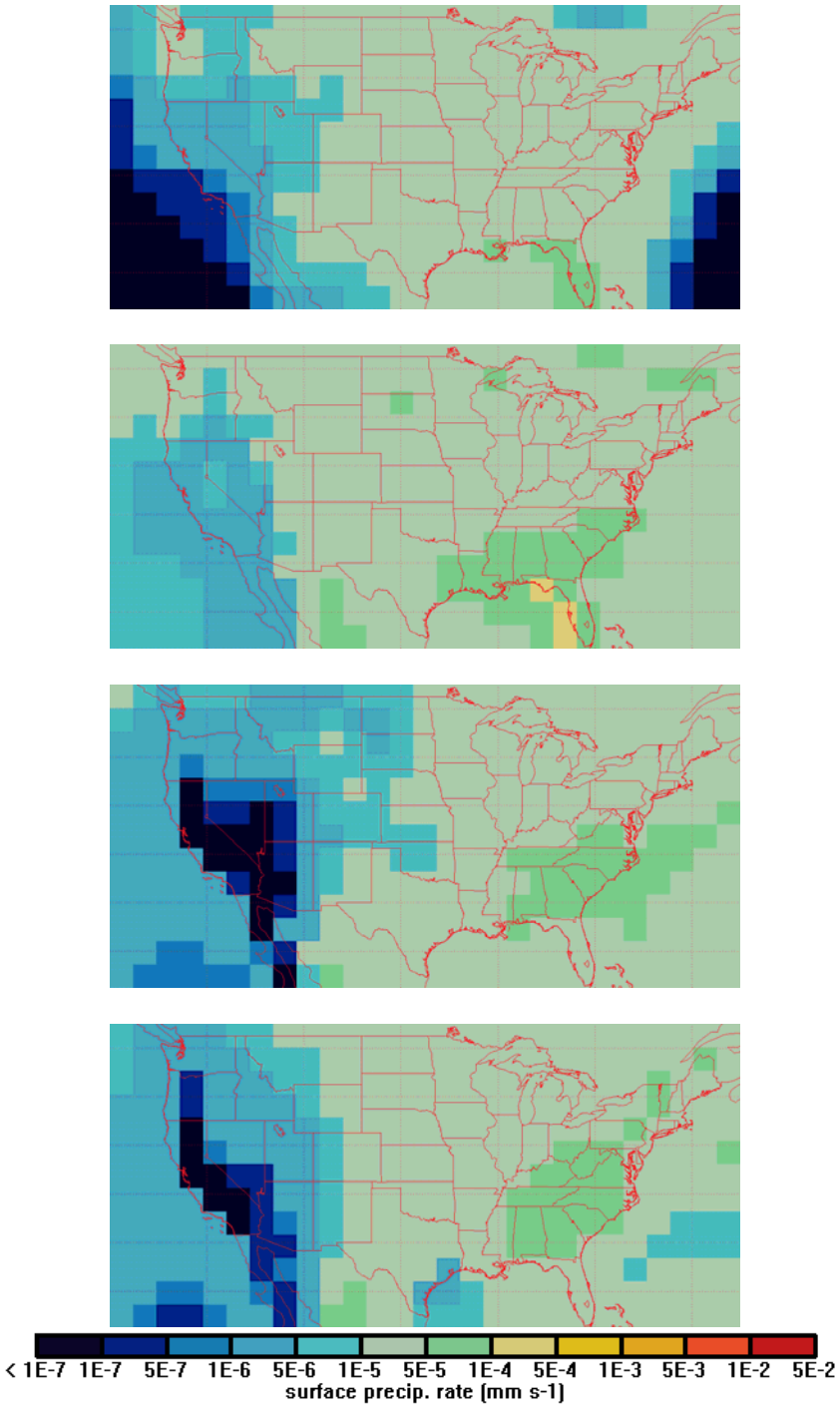

Figure 4.4. SPREC spatial distribution at all times over CONUS for a) observations (from CPCHP), b) NICAM, and c) SPv4, and d) SPv5.

a) Observation

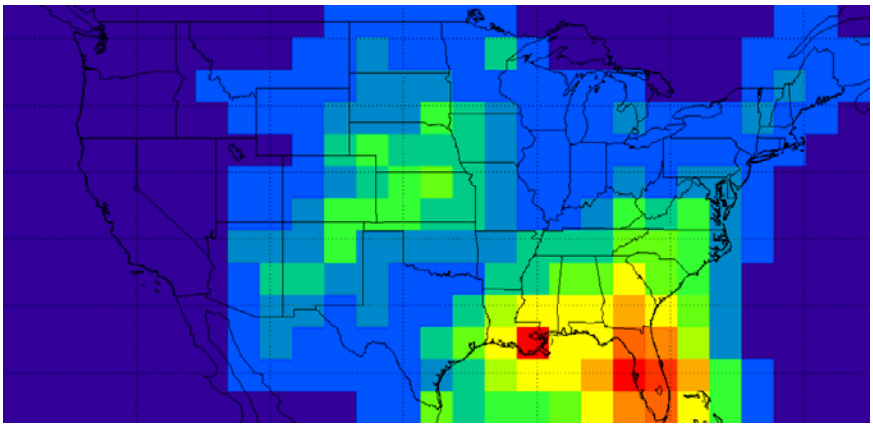

b) SPv4

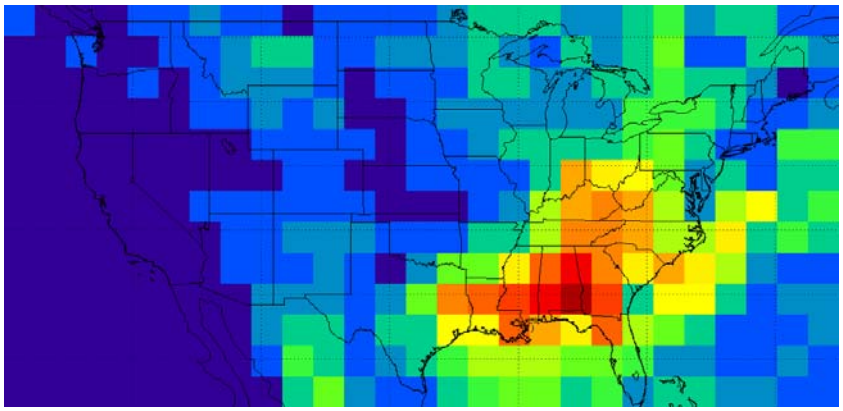

c) SPv5

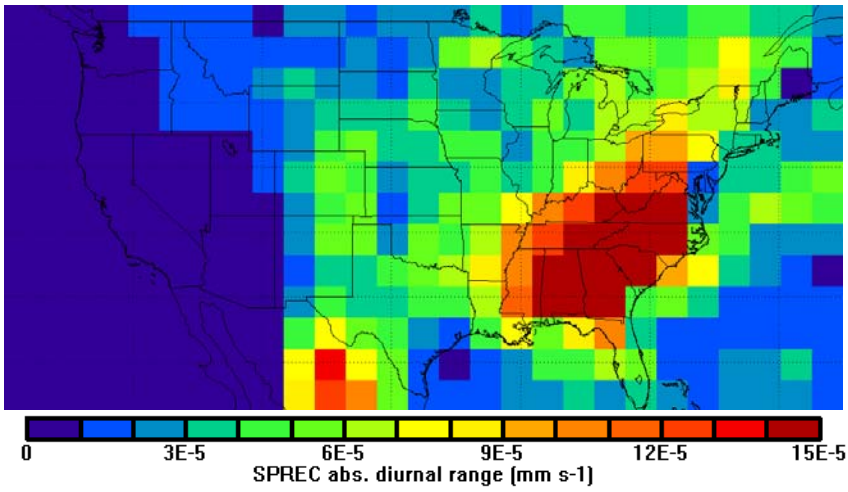

Figure 4.5. SPREC diurnal cycle spatial distribution over CONUS for a) observations (from CPCHP), b) SPv4, and c) SPv5.

a) Observation

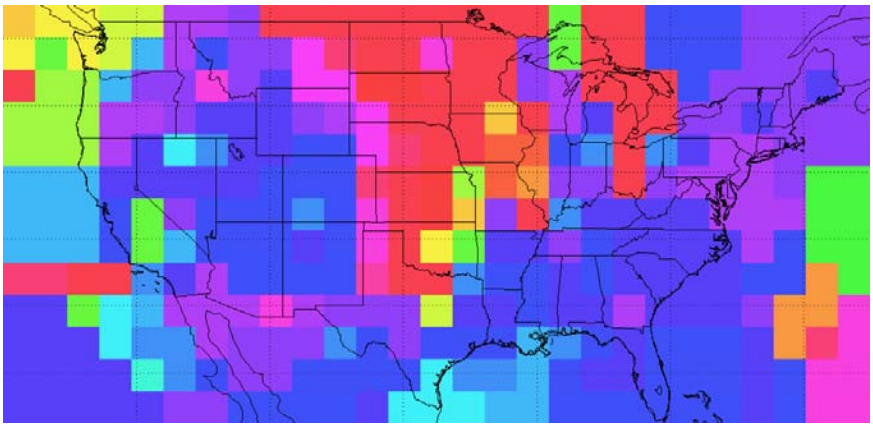

b) SPv4

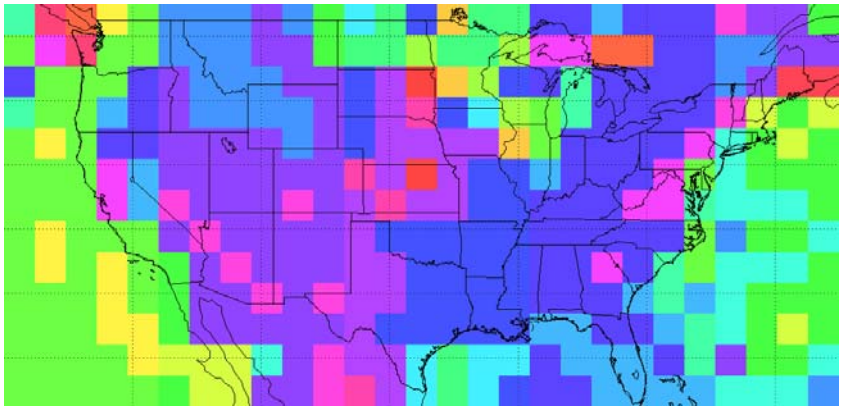

c) SPv5

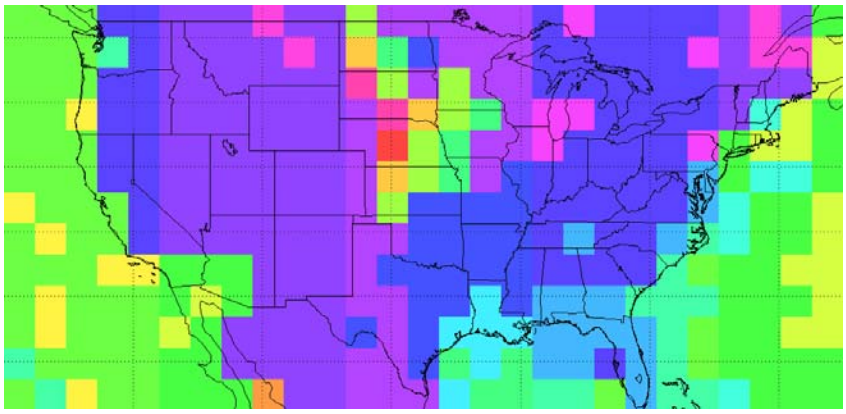

Figure 4.6. SPREC diurnal cycle spatial distribution over CONUS for a) observations (from CPCHP), b) SPv4, and c) SPv5.

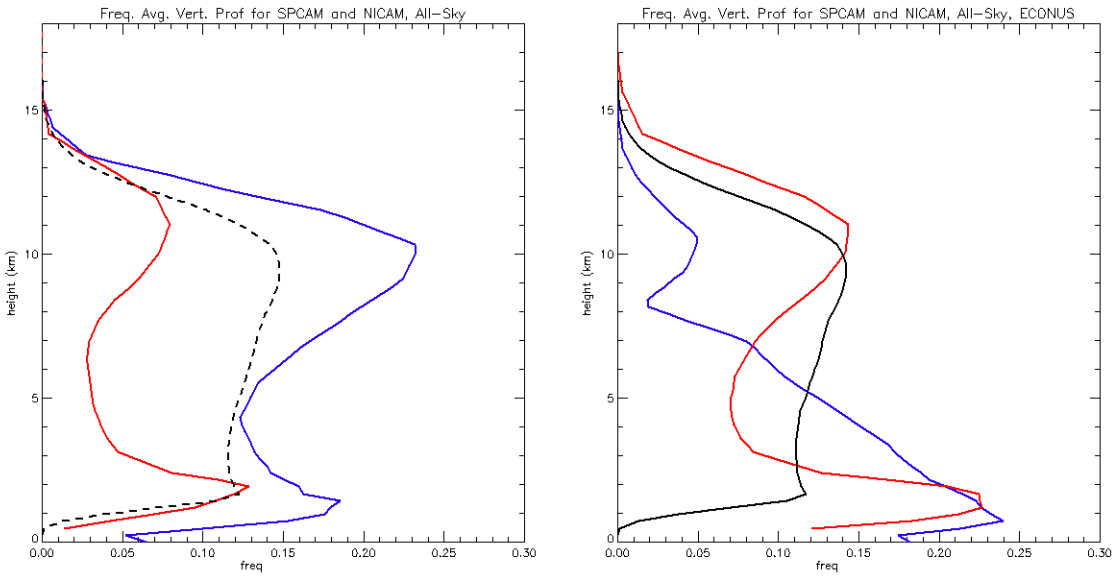

Figure 4.7. COF vertical profiles over ECONUS for all-sky scenes. Left is the COF profile using the CWC-based definition of "cloud", and right is the same profile using the radar-based definition. CloudSat is black, NICAM is red, and SPv4 is blue. The dashed line for CloudSat on the left indicates that CloudSat uses the radar-based definition only, and so is not a direct comparison to the models.

a. all-sky

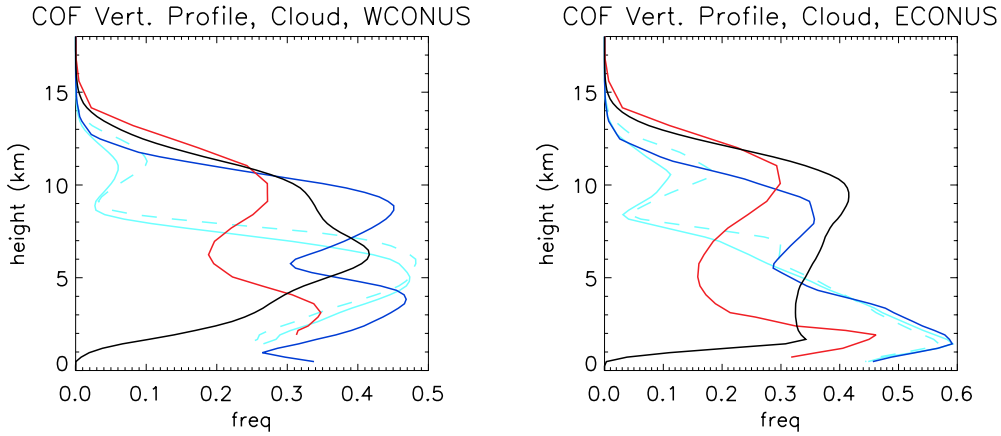

b. PBLR Cloud-only

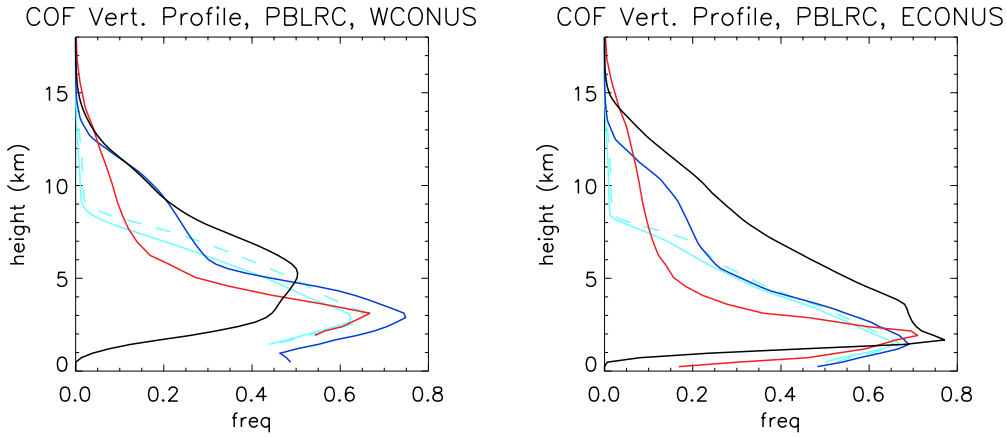

c. DCC-only

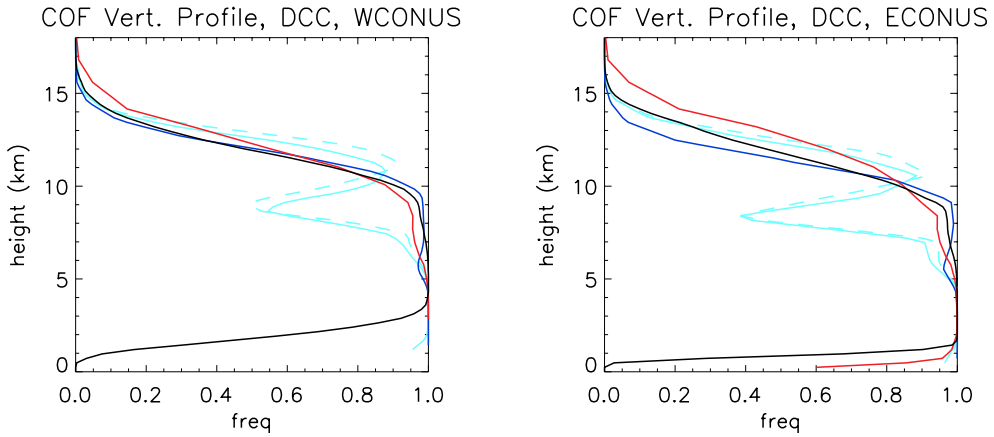

Figure 4.8. COF vertical profiles over WCONUS (left) and ECONUS (right) for a) all-sky, b) PBLR cloud-only, and c) DCC-only. CloudSat is black, NICAM is red, and SP-CAM is blue. The COF is normalized by the number of clouds observed, so the plots effectively show the altitude at which a cloud occurs when it occurs.

a. all-sky

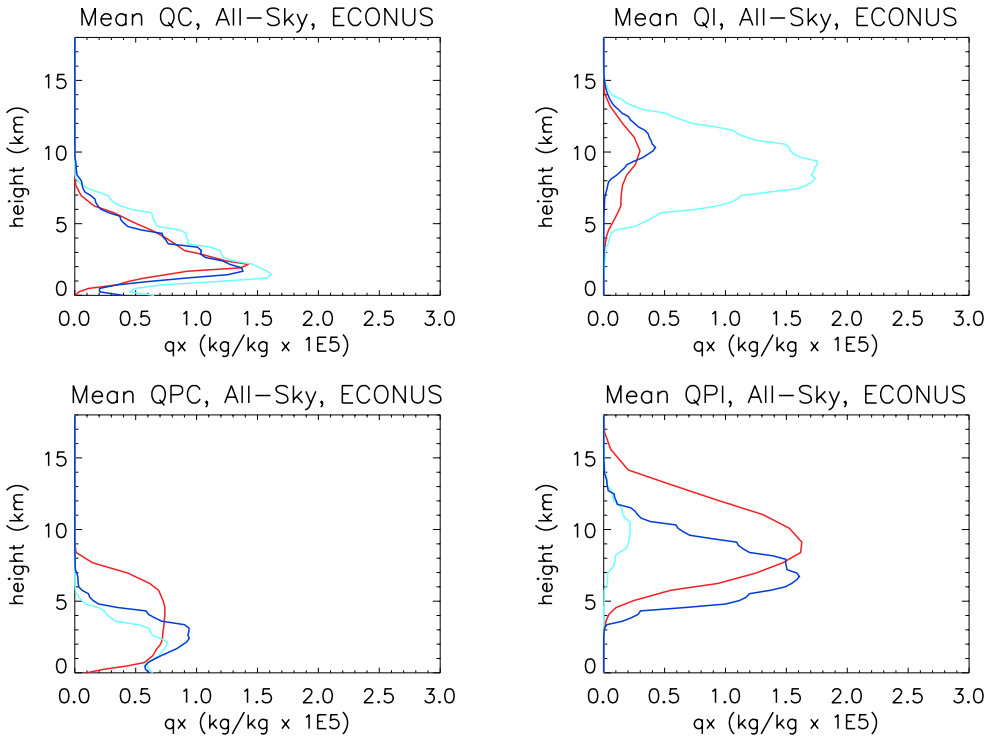

b. PBLR Cloud-only

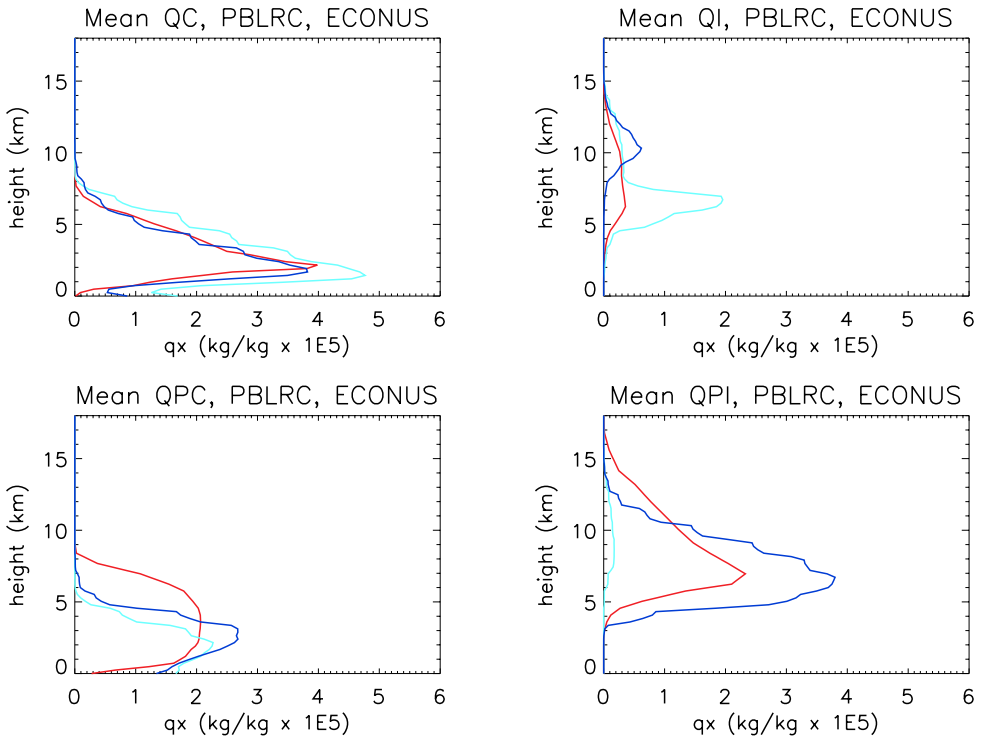

Figure 4.9. Simulated hydrometeor vertical profiles over ECONUS for a) all-sky, b) PBLR cloud-only, and c) DCC-only. NICAM is red, SPv4 is light blue, and SPv5 is dark blue.

c. DCC-only

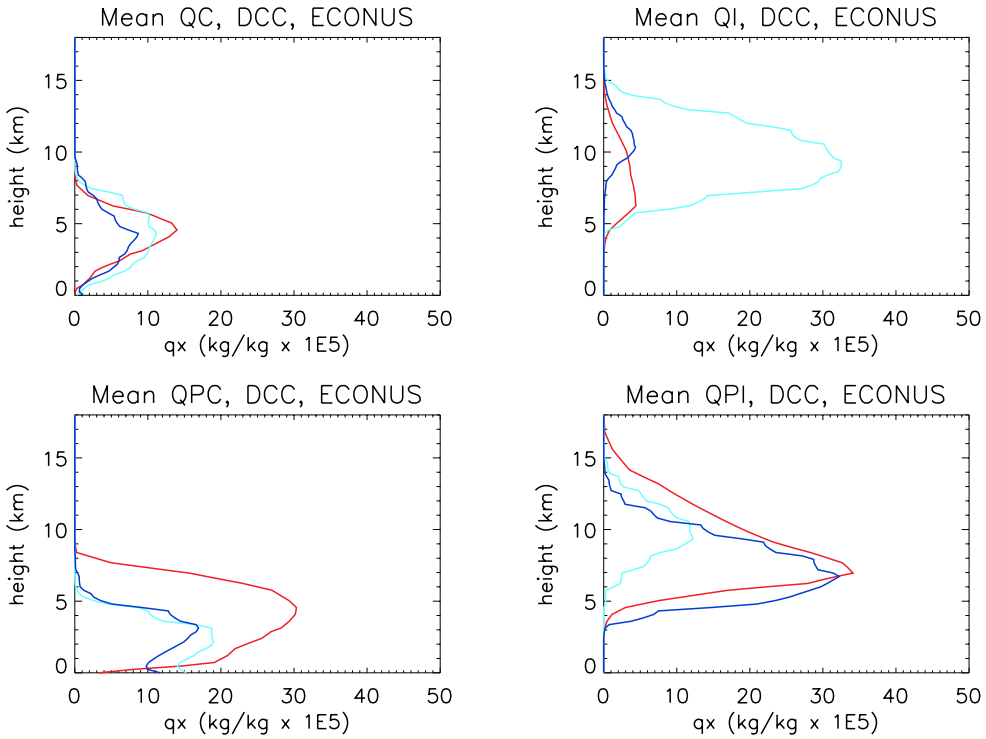

Figure 4.9. (continued)

a. all-sky

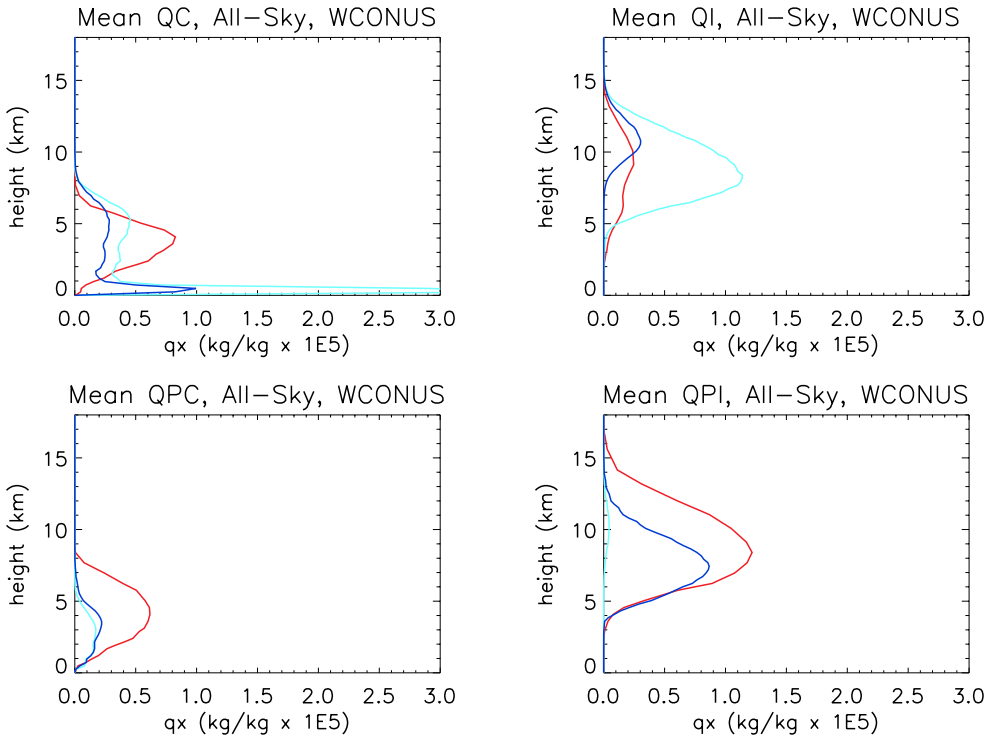

b. PBLR Cloud-only

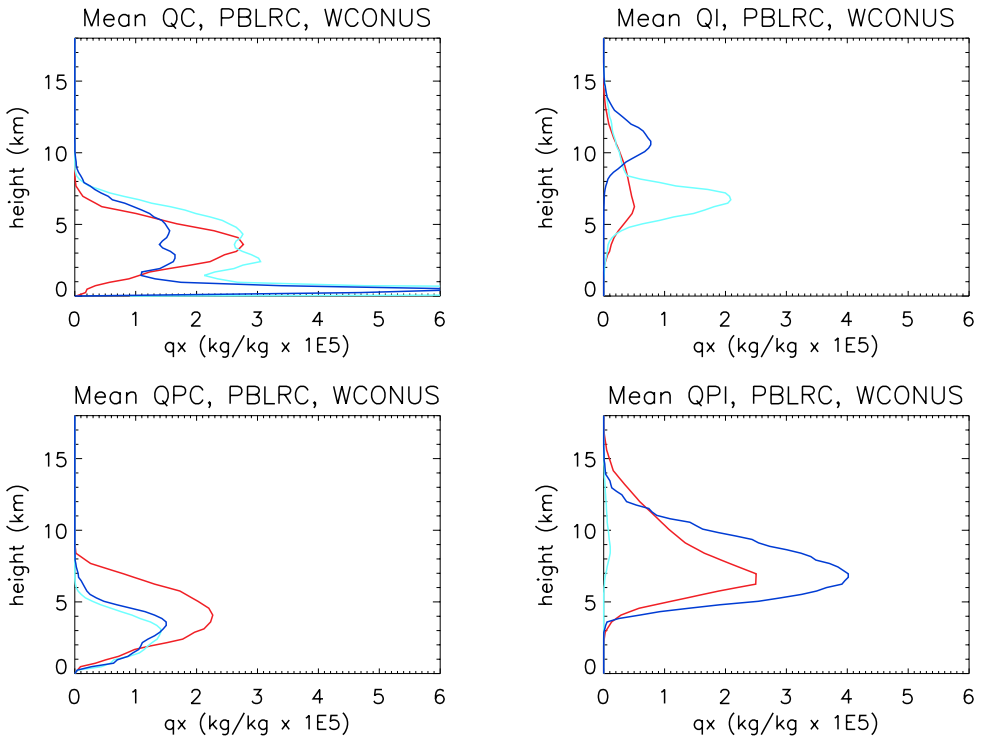

Figure 4.10. As Fig. 4.9, but for WCONUS.

c. DCC-only

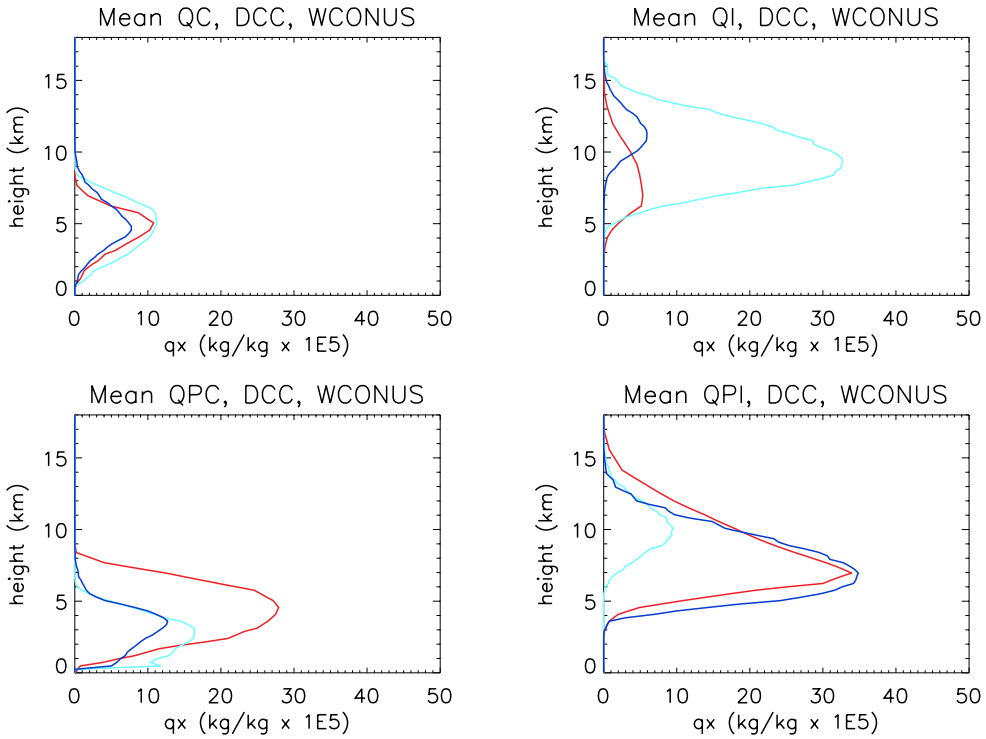

Figure 4.10. (continued)

a) CloudSat

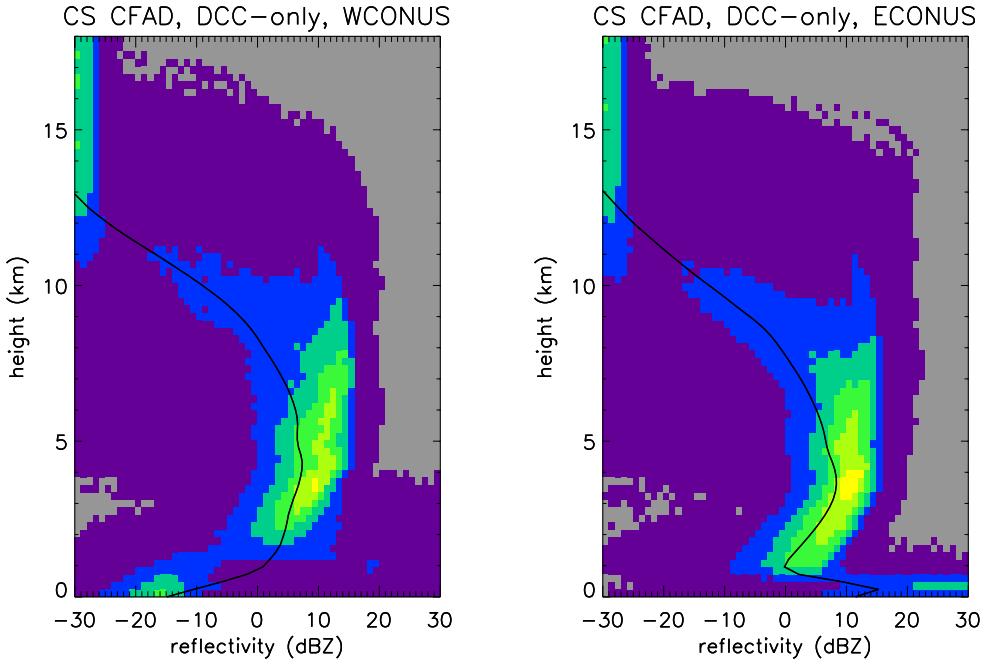

b) NICAM

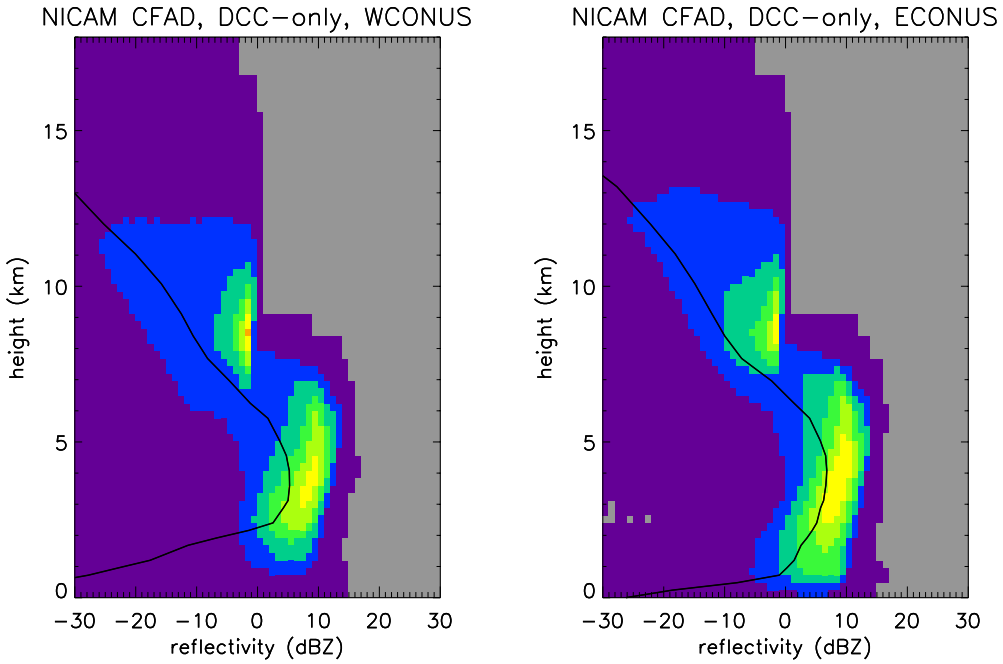

Figure 4.11. DCCAR vertical profiles over WCONUS (left) and ECONUS (right) for a) CloudSat, b) NICAM, c) SPv4, and d) SPv5.

c) SPv4

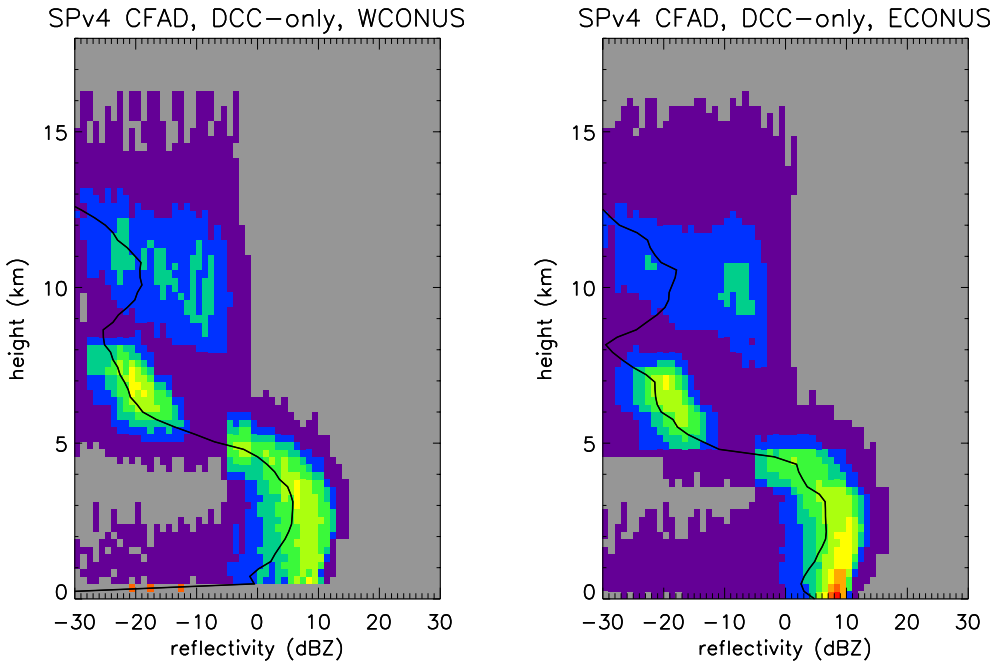

d) SPv5

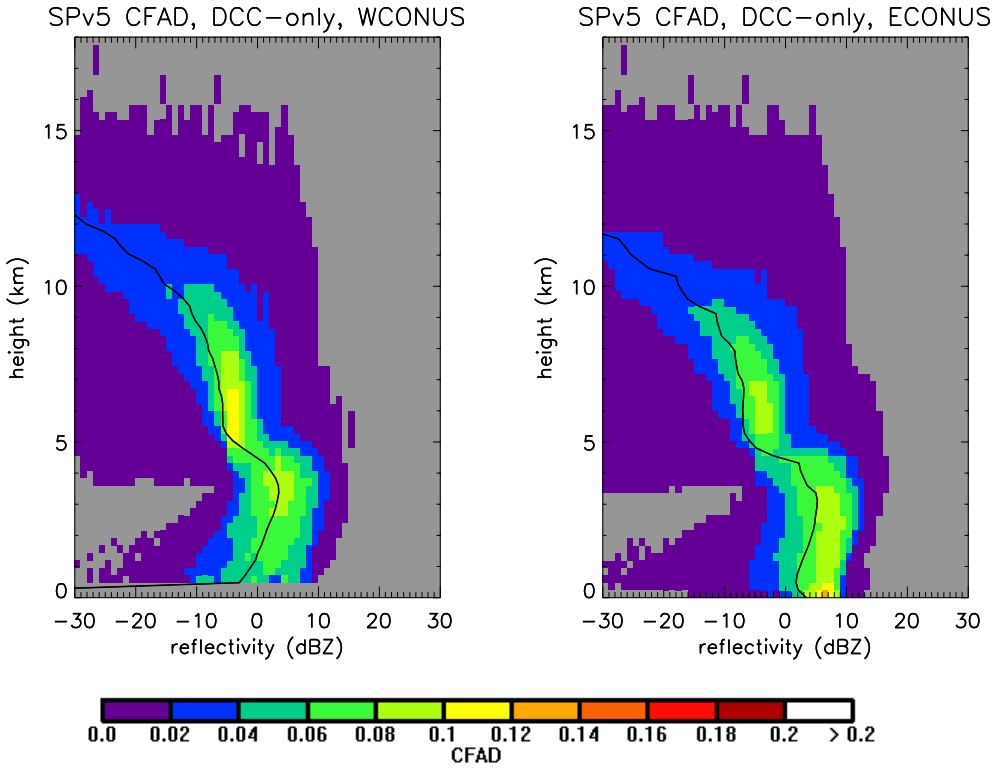

Figure 4.11. (continued)

a) SPv4

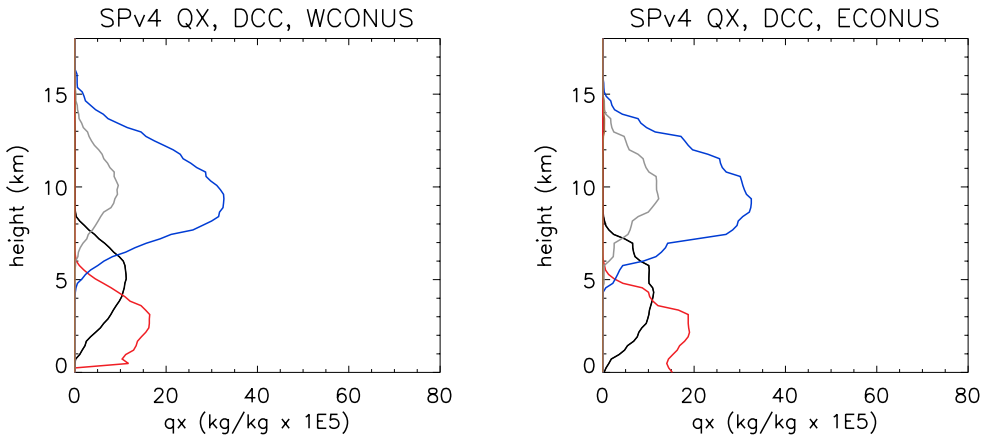

b) SPv5

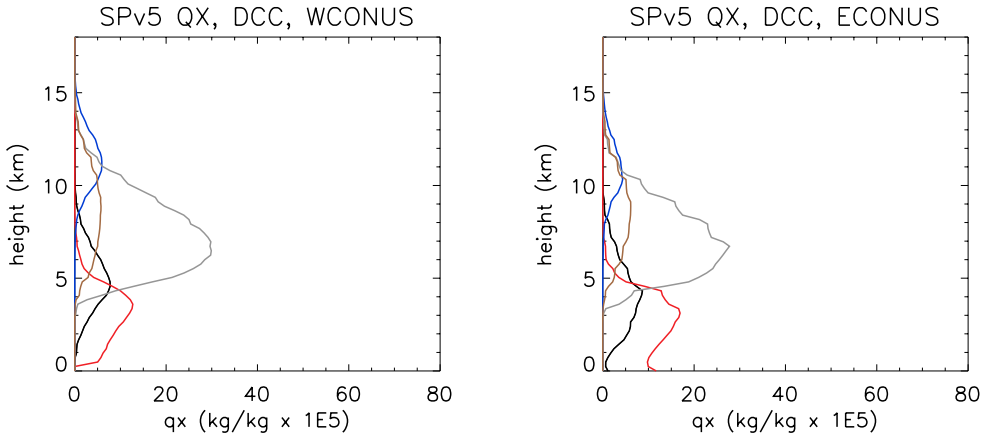

Figure 4.12. Individual hydrometeor profiles within DCCs for a) SPv4, and b) SPv5 over WCONUS (left) and ECONUS (right), on a single graph. Shown are cloud liquid (QC, black), cloud ice (QI, blue), rain (QPC, red), snow (QPS, gray) and graupel (QPG, brown).

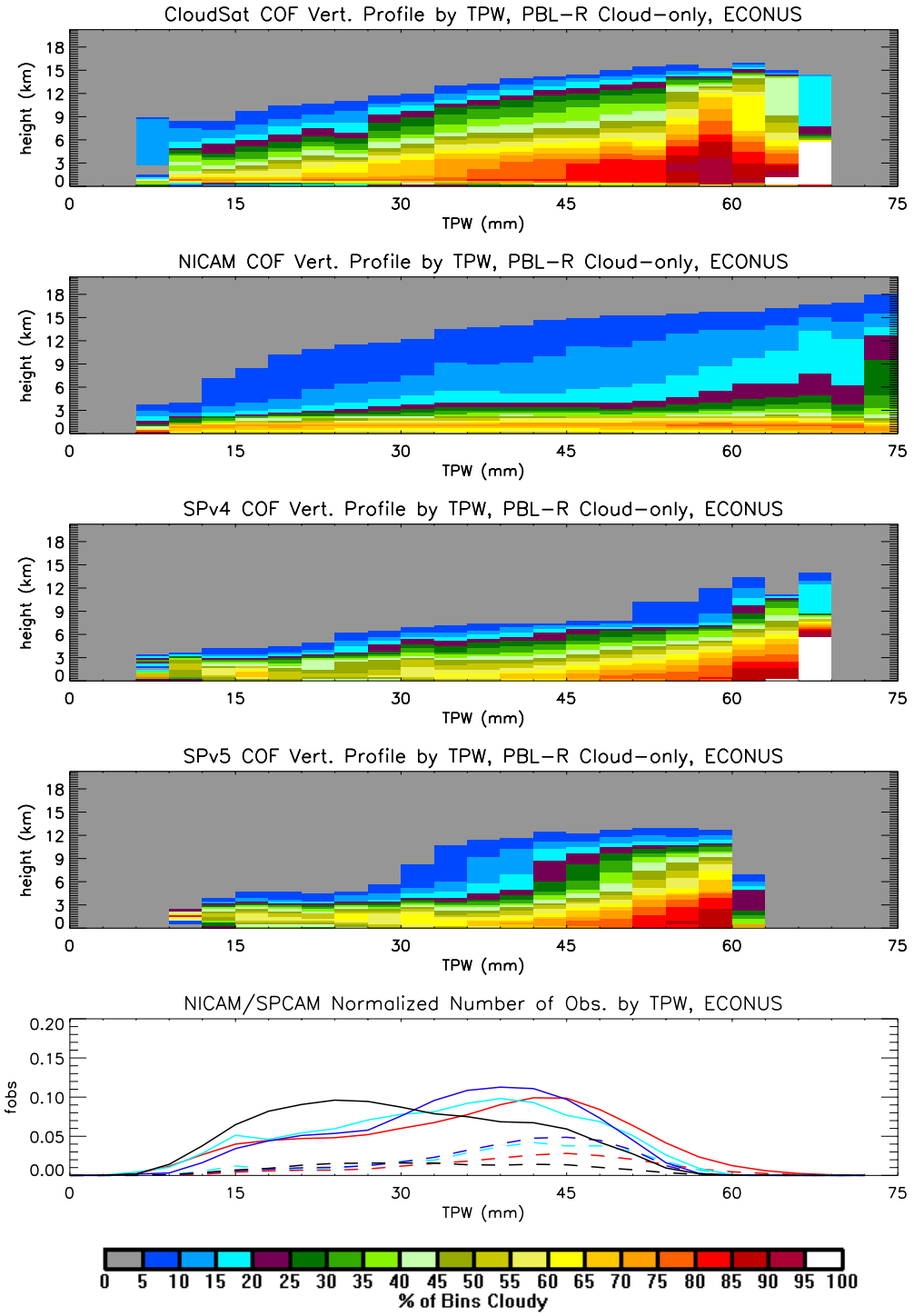

Figure 4.13. The COF vertical profiles for PBLRCs over ECONUS sorted by TPW for top) CloudSat, second) NICAM, third) SPv4, and fourth SPv5. The COF is normalized by the number of clouds observed, so the plots effectively show the altitude at which a cloud occurs when it occurs. The bottom panel shows the sample PDF for all-sky (solid) and PBLR-only (dashed) scenes. The PBLR-only sample PDF is not normalized, so the ratio of the all-sky PDF to the sample PDF is the mean cloudiness for that TPW value.

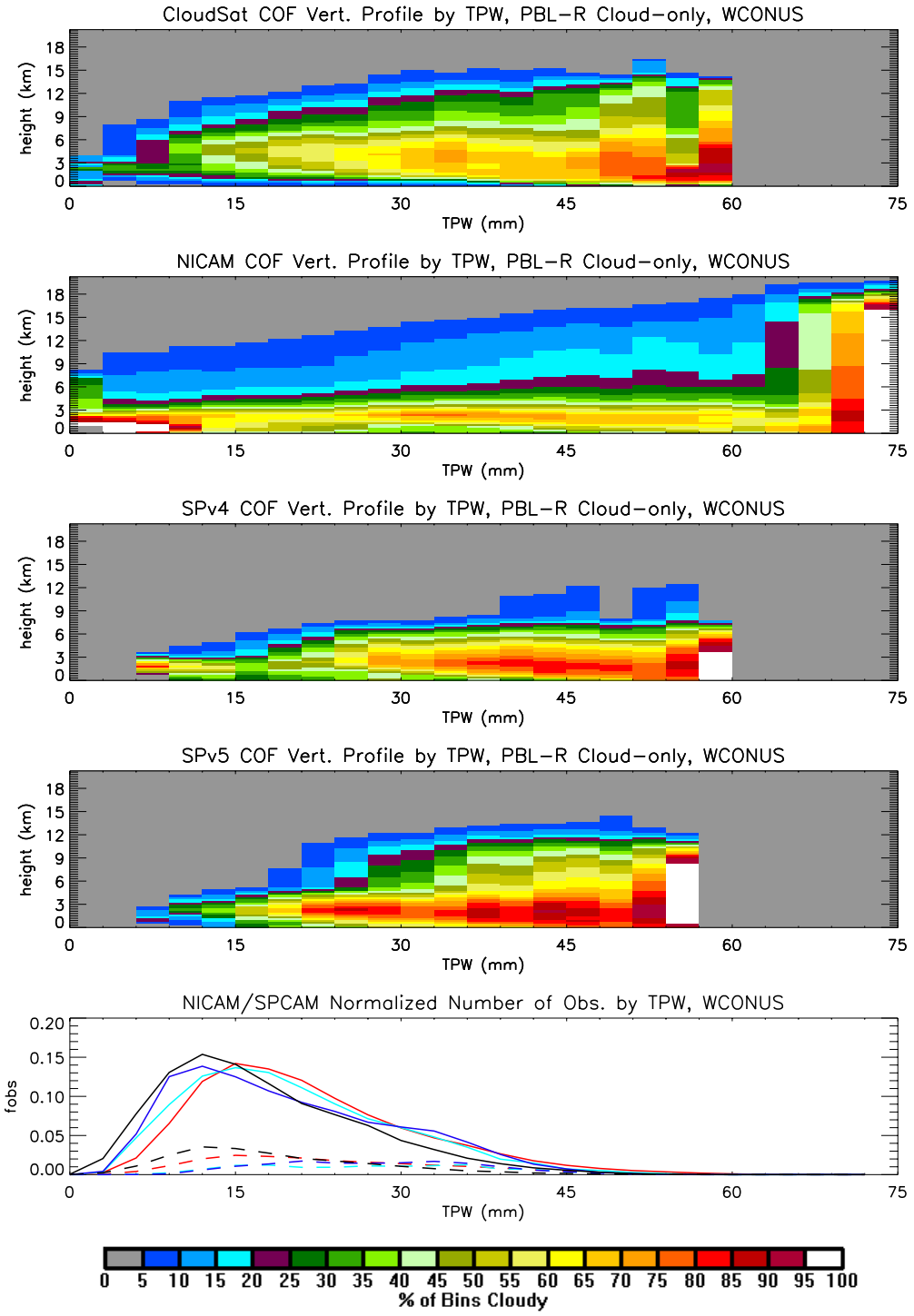

Figure 4.14. Same as Fig. 4.13, but for WCONUS.

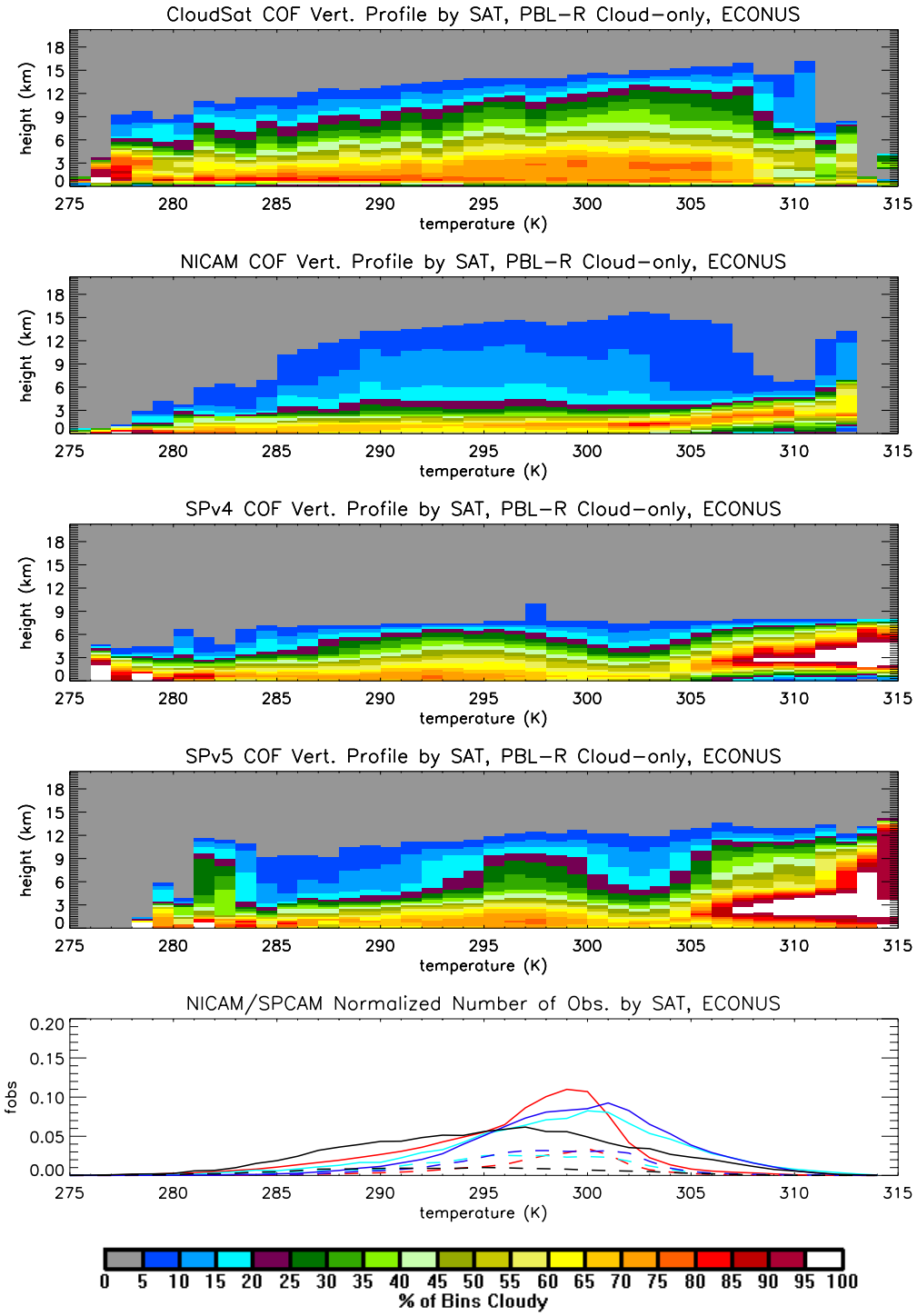

Figure 4.15. Same as Fig. 4.13, but for SAT over ECONUS.

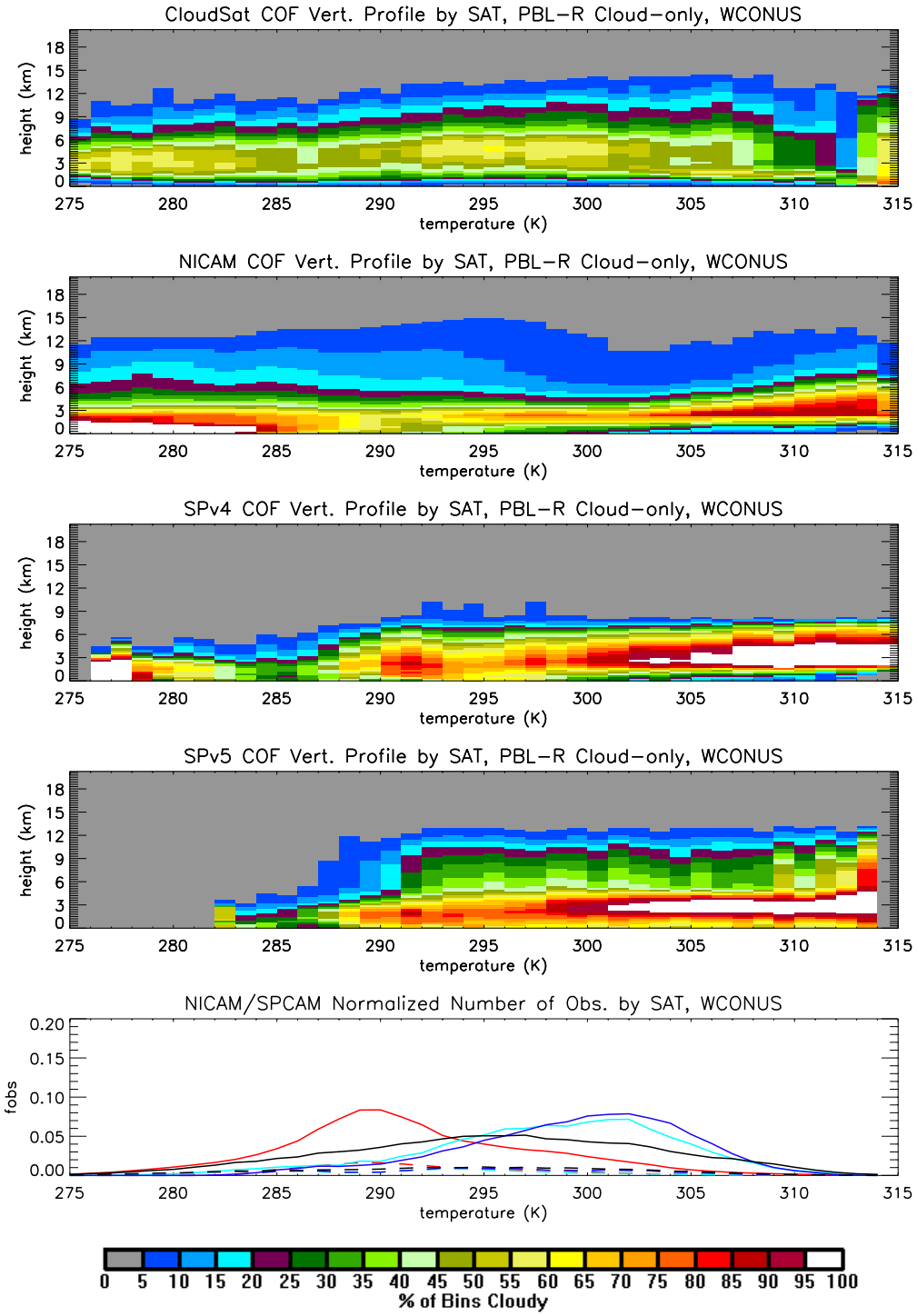

Figure 4.16. Same as Fig. 4.13, but for SAT over WCONUS.

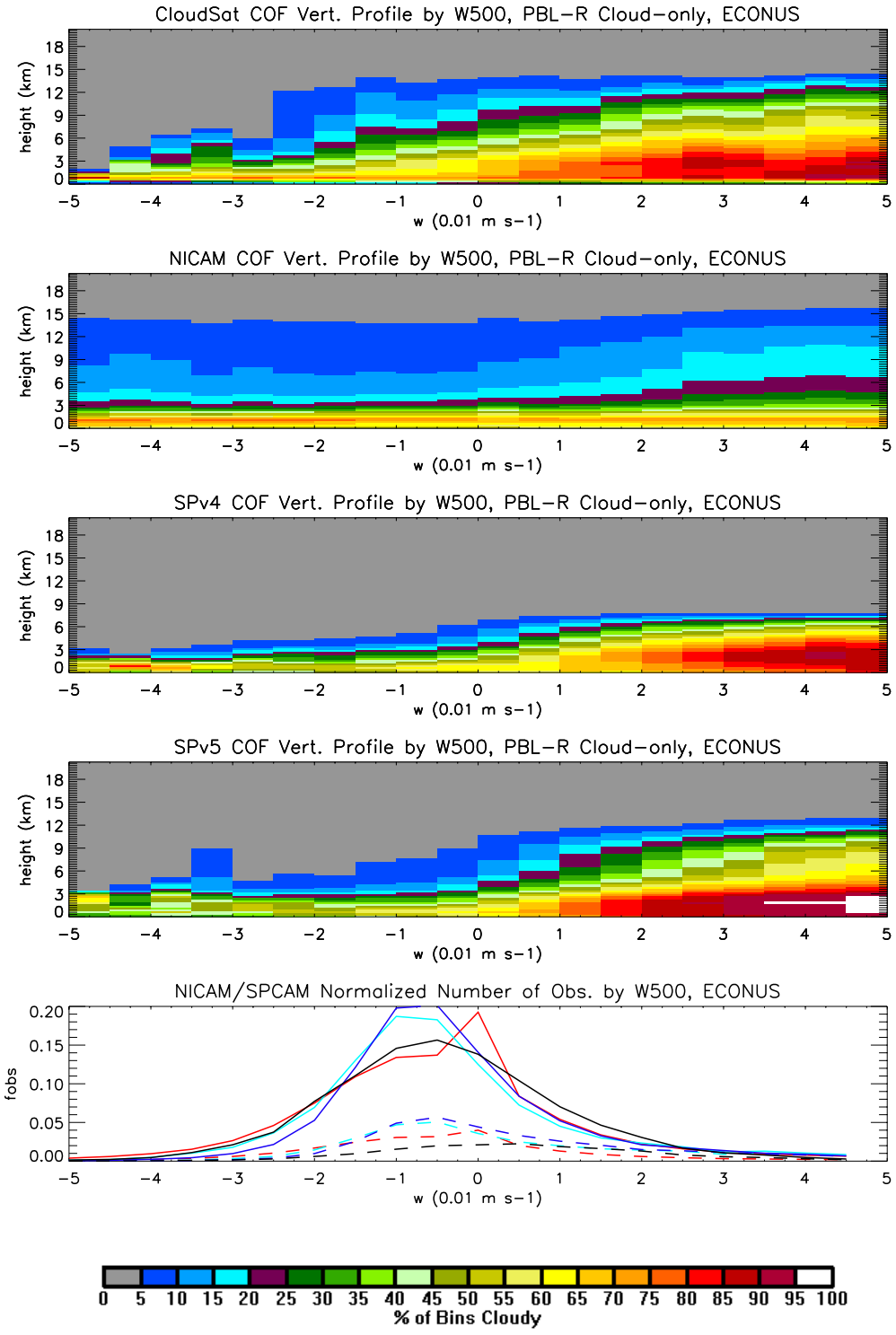

Figure 4.17. Same as Fig. 4.13, but for W500 over ECONUS.

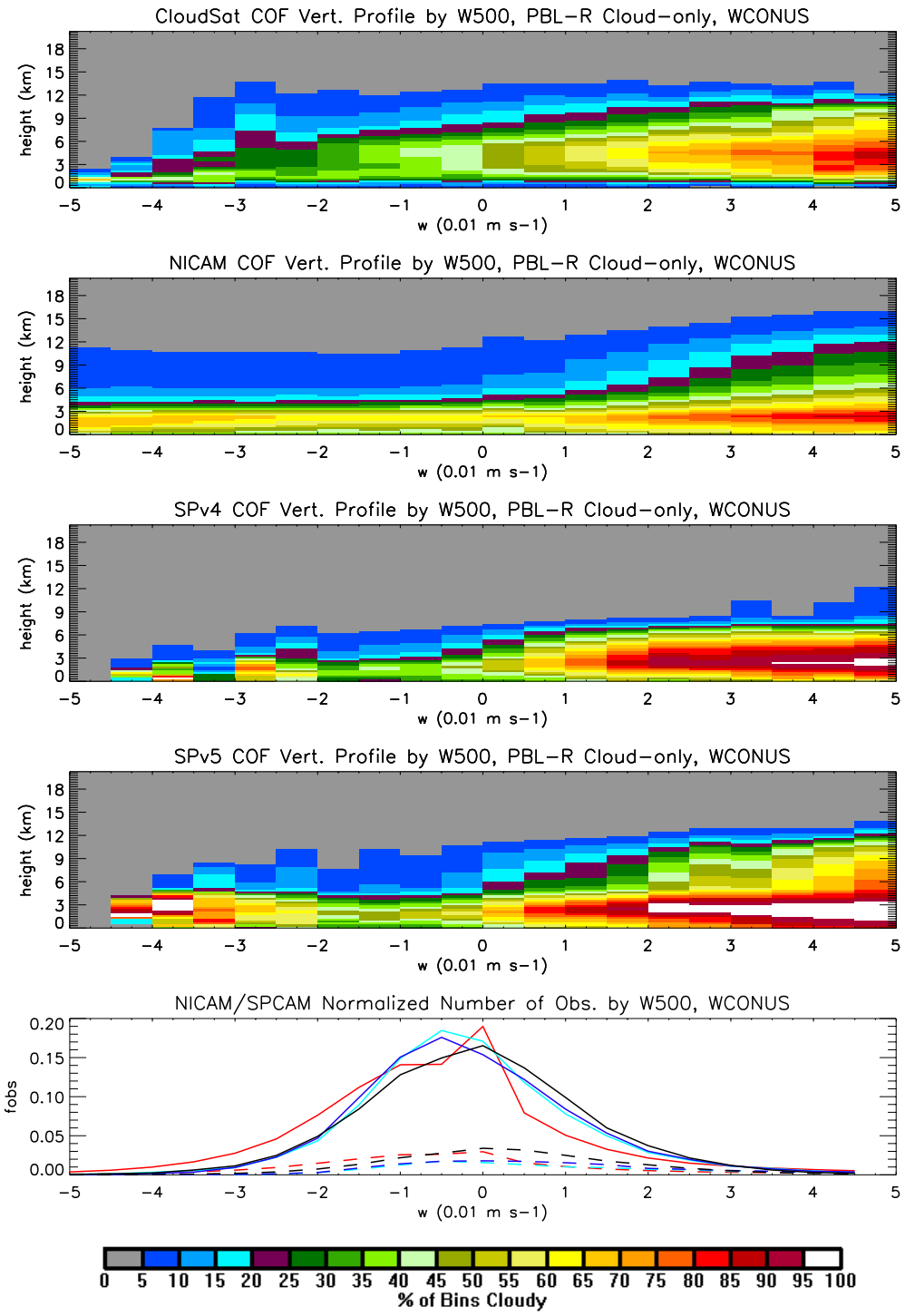

Figure 4.18. Same as Fig. 4.13, but for W500 over WCONUS.

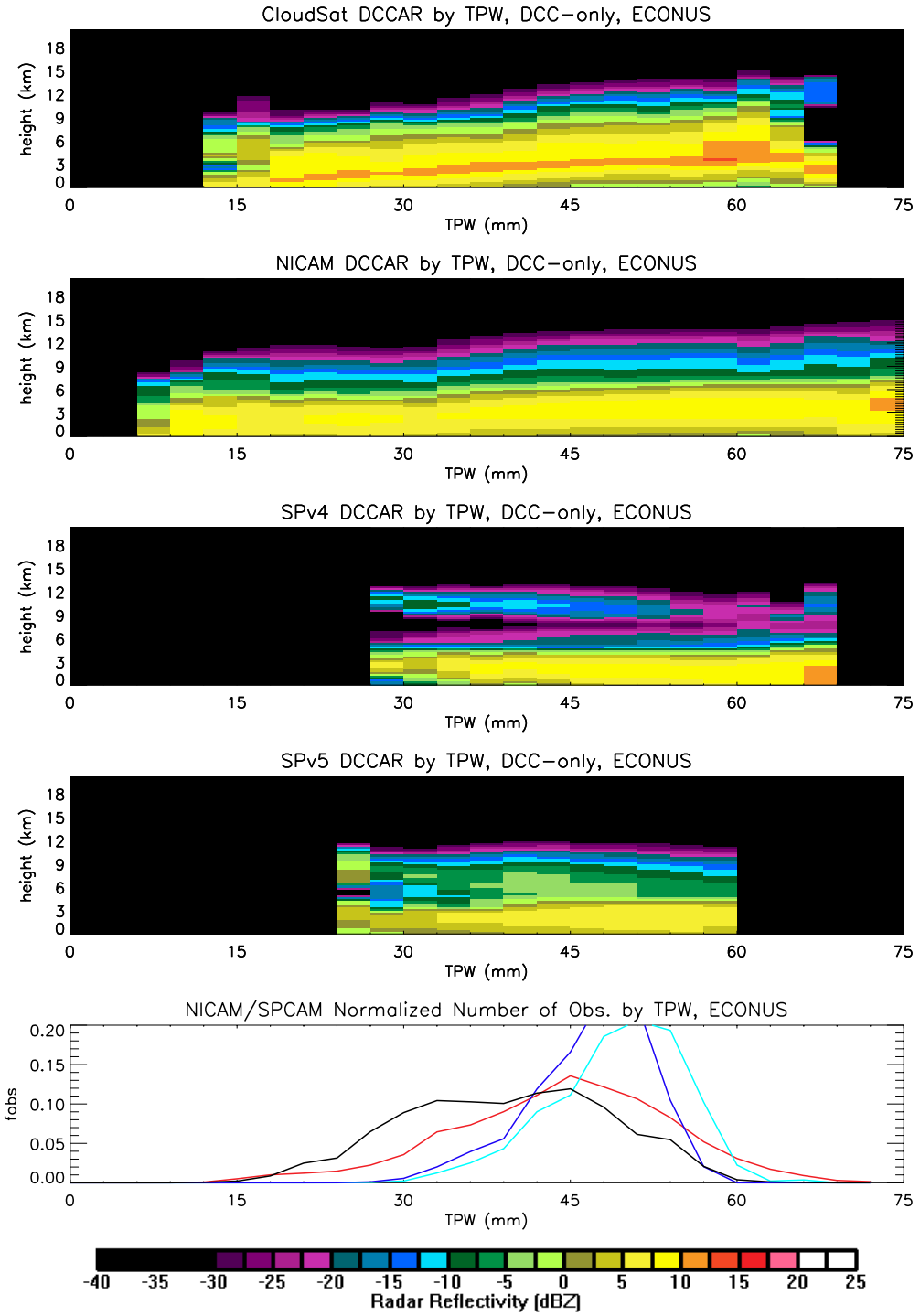

Figure 4.19. The DCCAR vertical profiles for DCCs over ECONUS sorted by TPW for top) CloudSat, second) NICAM, third) SPv4, and fourth) SPv5. The bottom panel shows the sample PDF for DCC-only scenes, normalized by total sample number of DCCs.

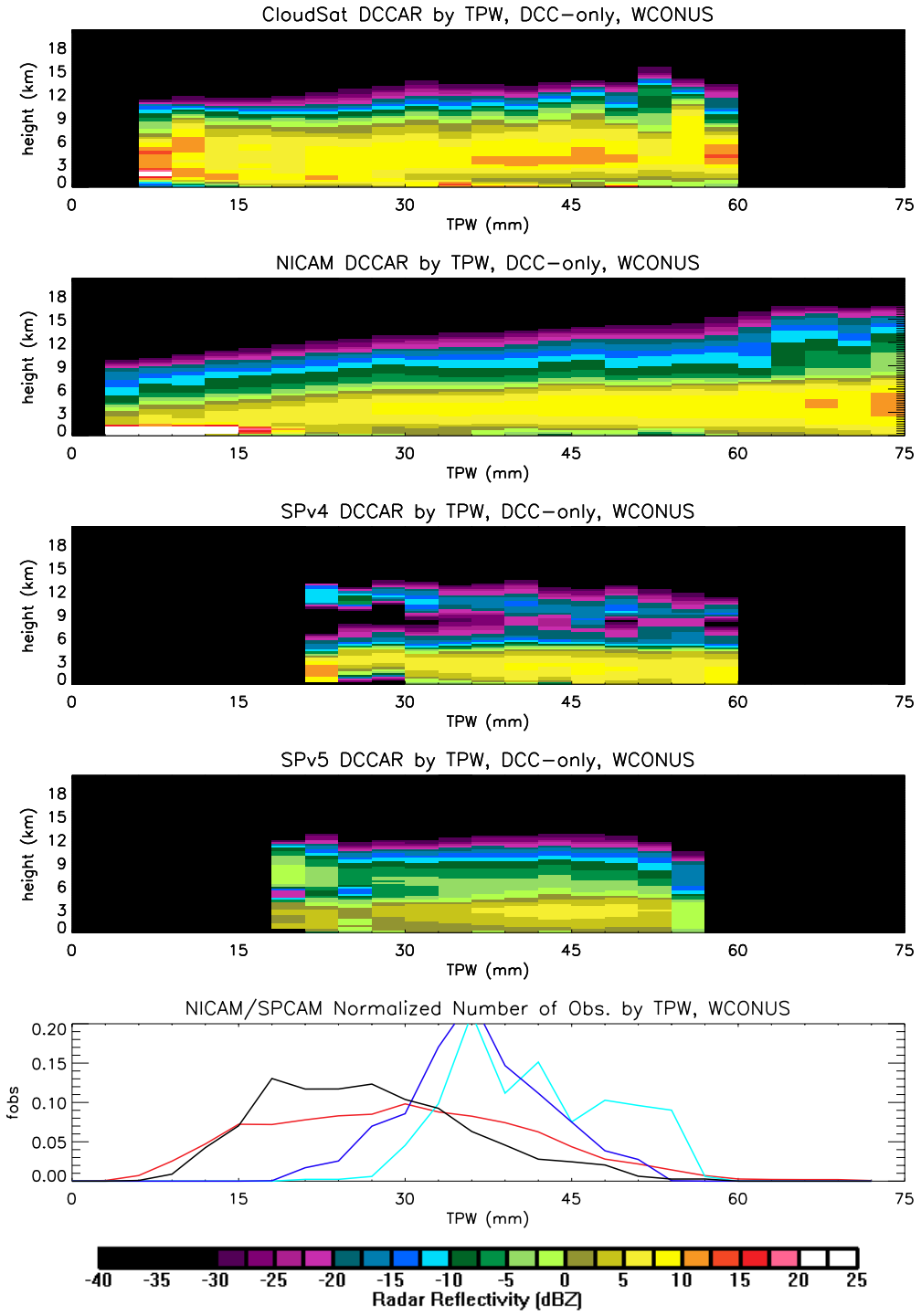

Figure 4.20. Same as Fig. 4.19, but over WCONUS.

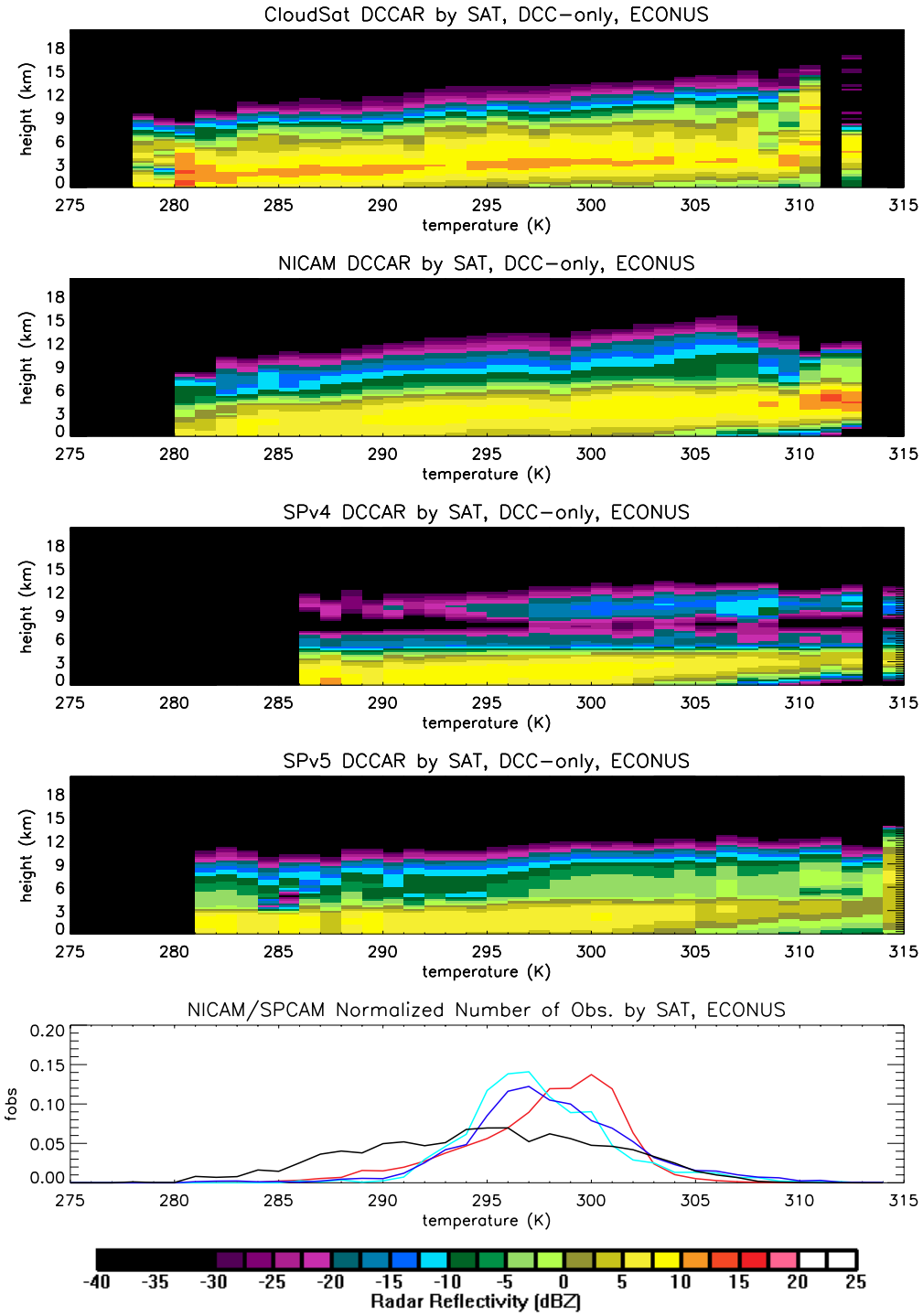

Figure 4.21. Same as Fig. 4.19, but for SAT over ECONUS.

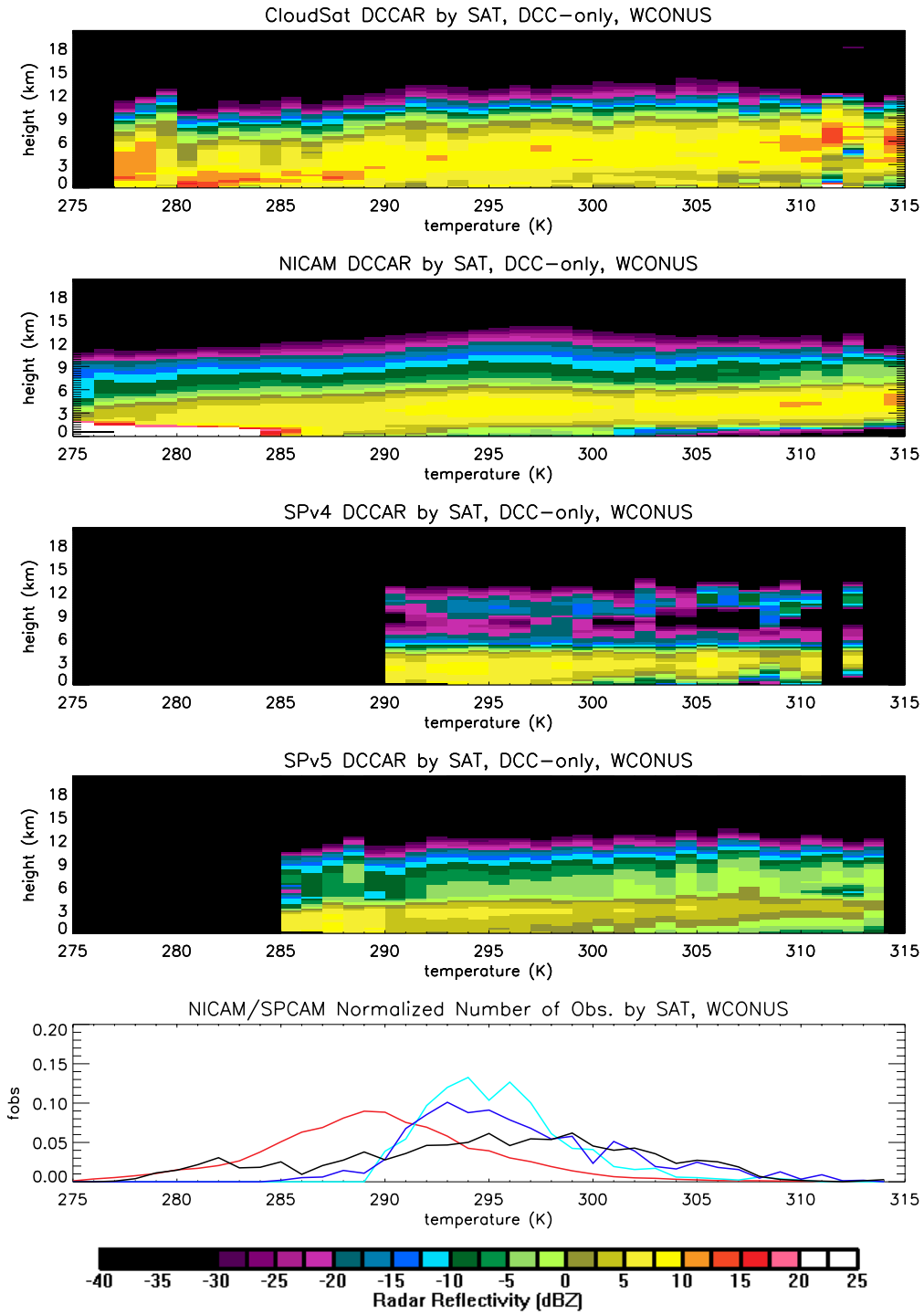

Figure 4.22. Same as Fig. 4.19, but for SAT over WCONUS.

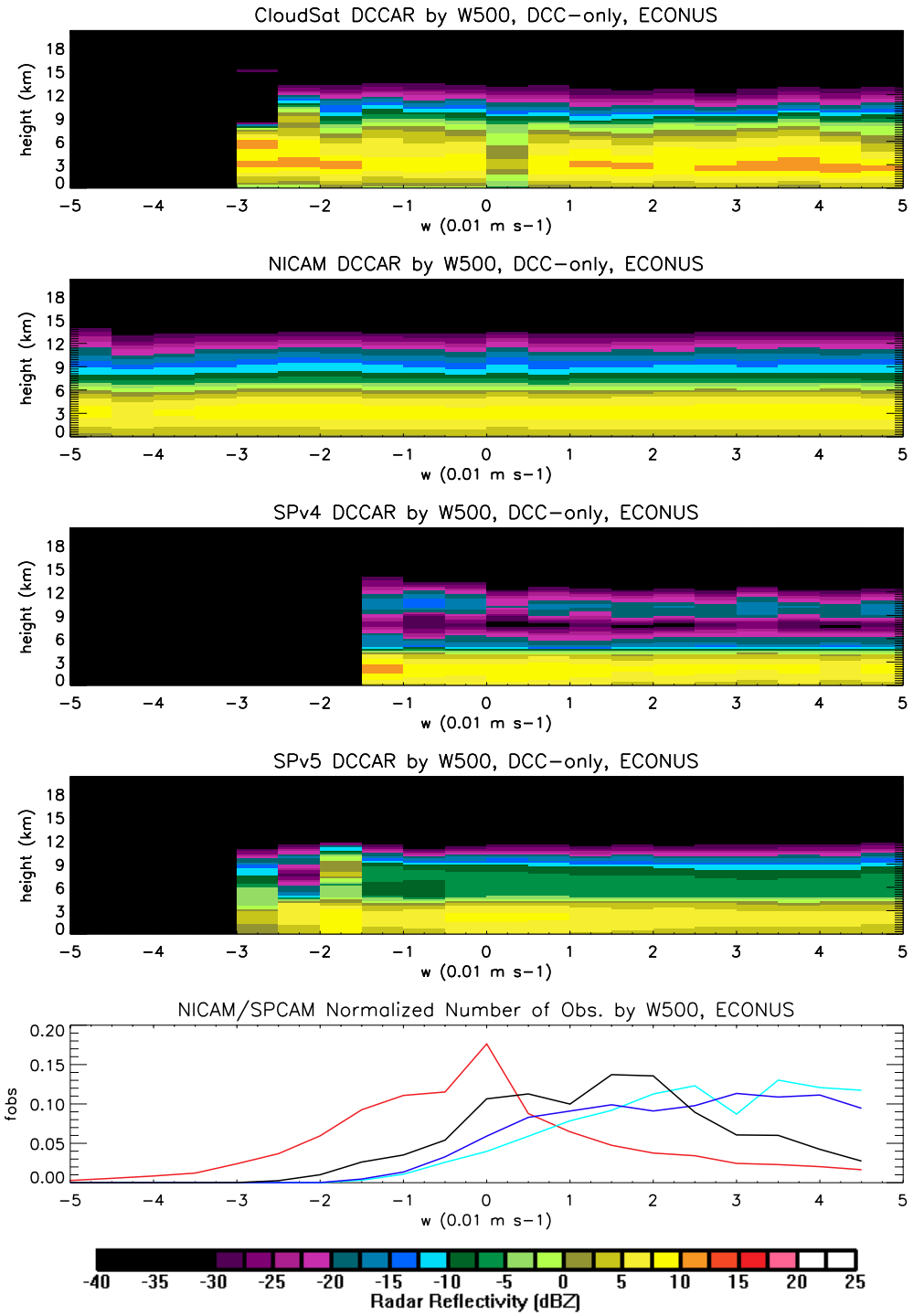

Figure 4.23. Same as Fig. 4.19, but for W500 over ECONUS.

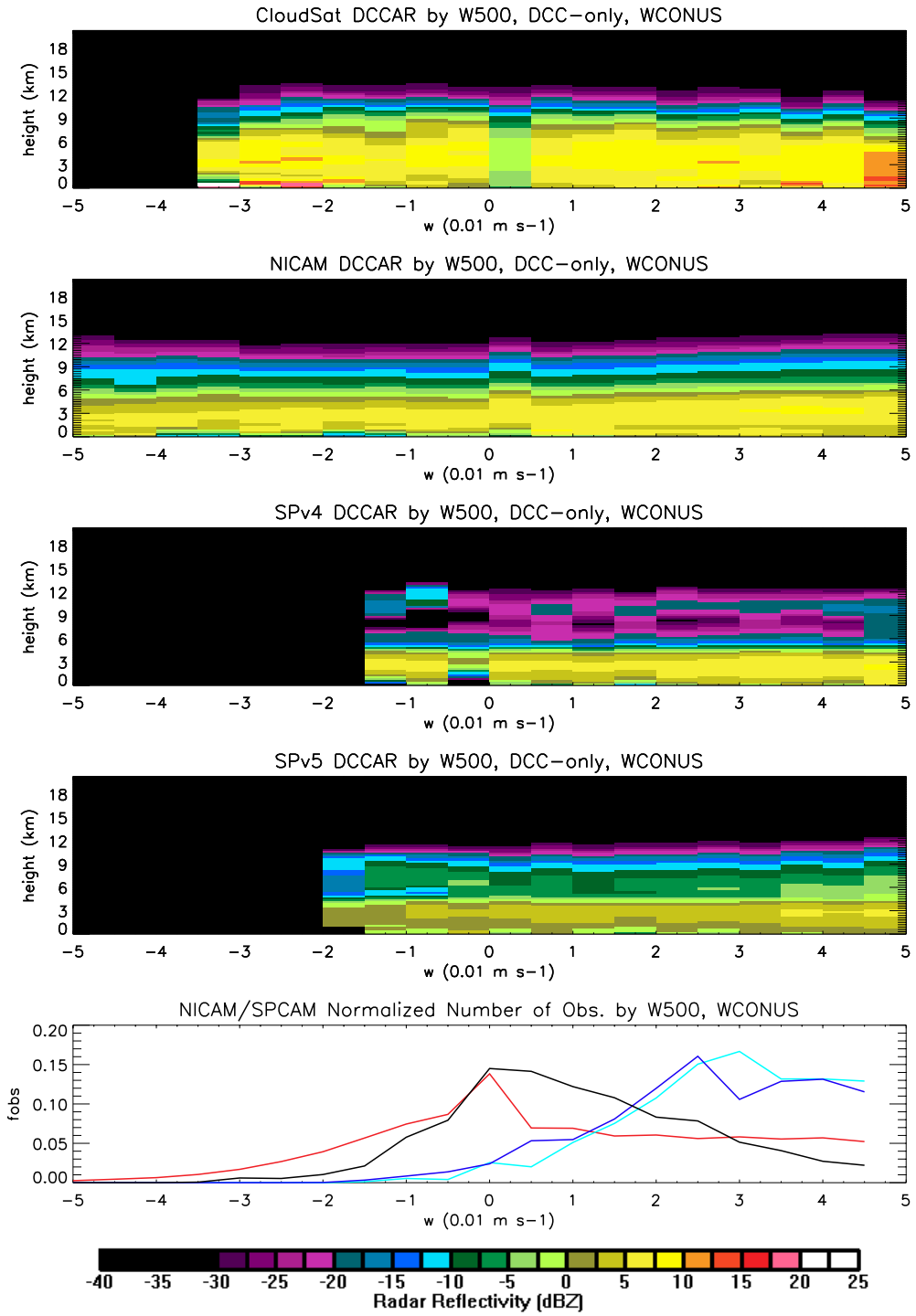

Figure 4.24. Same as Fig. 4.19, but for W500 over WCONUS.

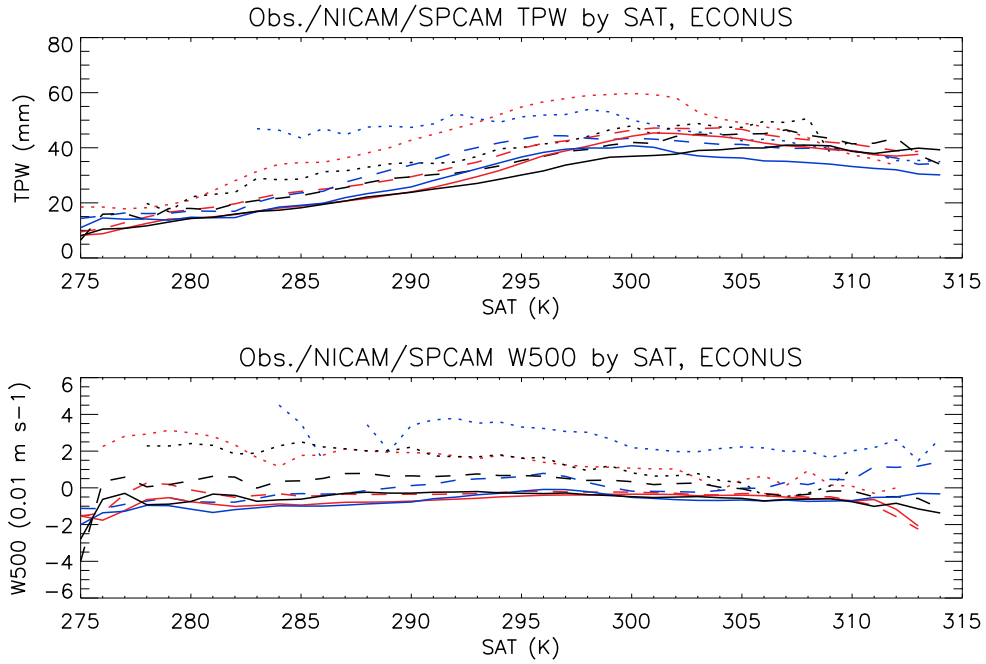

Figure 4.25. Various non-cloud meteorological variables sorted by SAT for ECONUS. The top panel is SAT, and the bottom is W500. Black is the reanalysis, red is NICAM, and blue is SP-CAM. The datasets shown are all-sky (solid), PBLR cloud-only (dashed), and DCC-only (dotted).

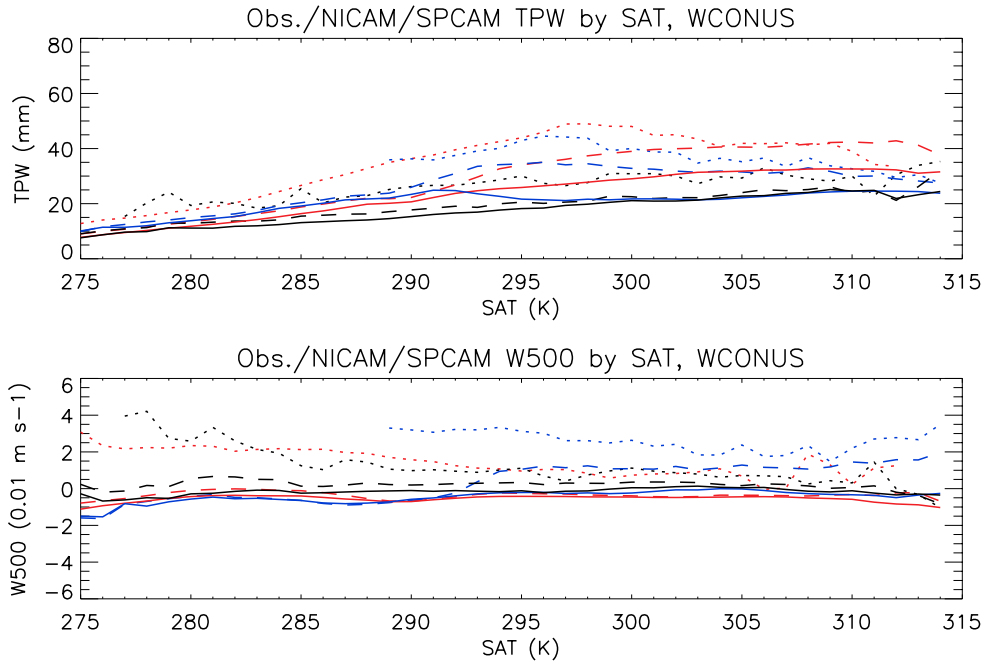

Figure 4.26. As Fig. 4.25, but sorted by SAT for WCONUS.

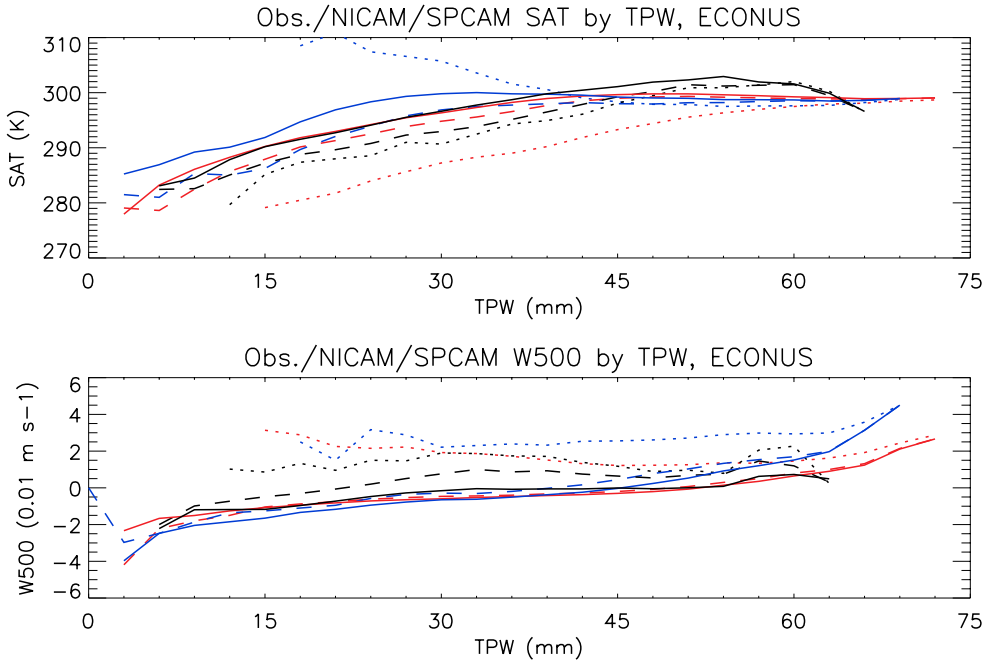

Figure 4.27. As Fig. 4.25, but sorted by TPW for ECONUS.

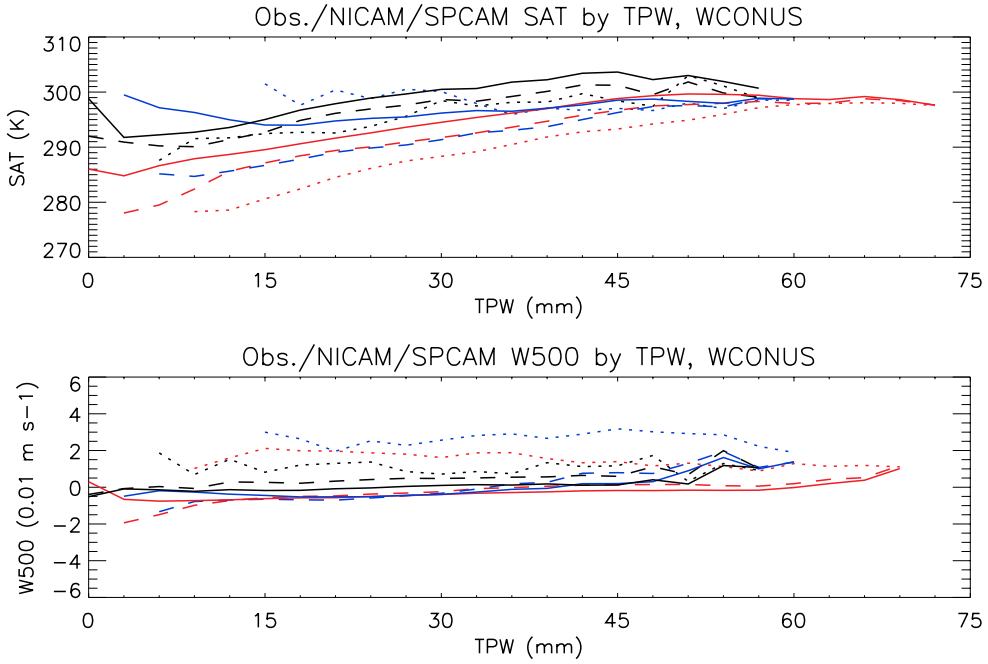

Figure 4.28. As Fig. 4.25, but sorted by TPW for WCONUS.

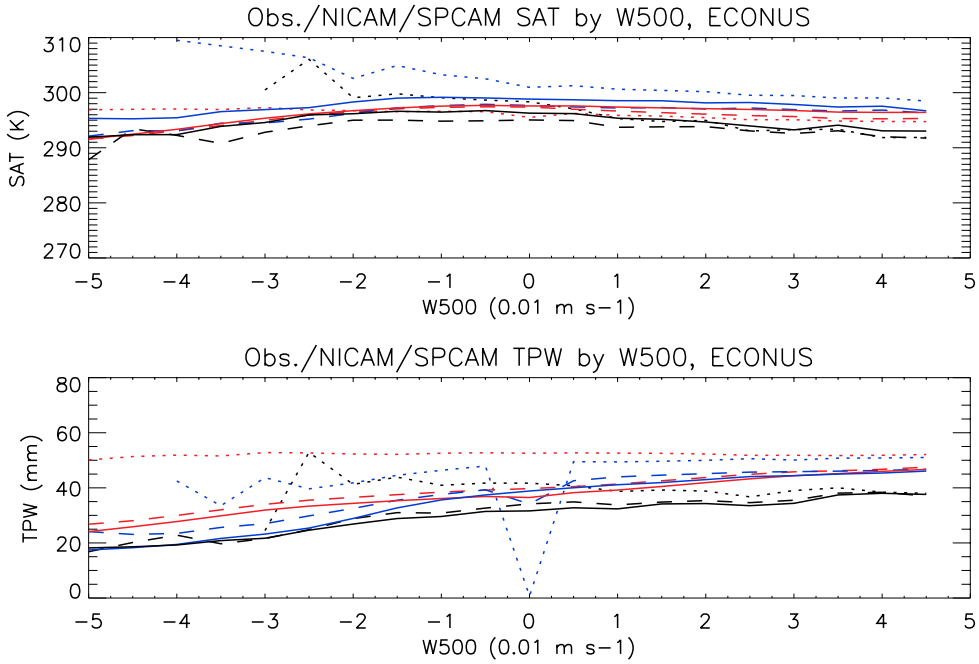

Figure 4.29. As Fig. 4.25, but sorted by W500 for ECONUS.

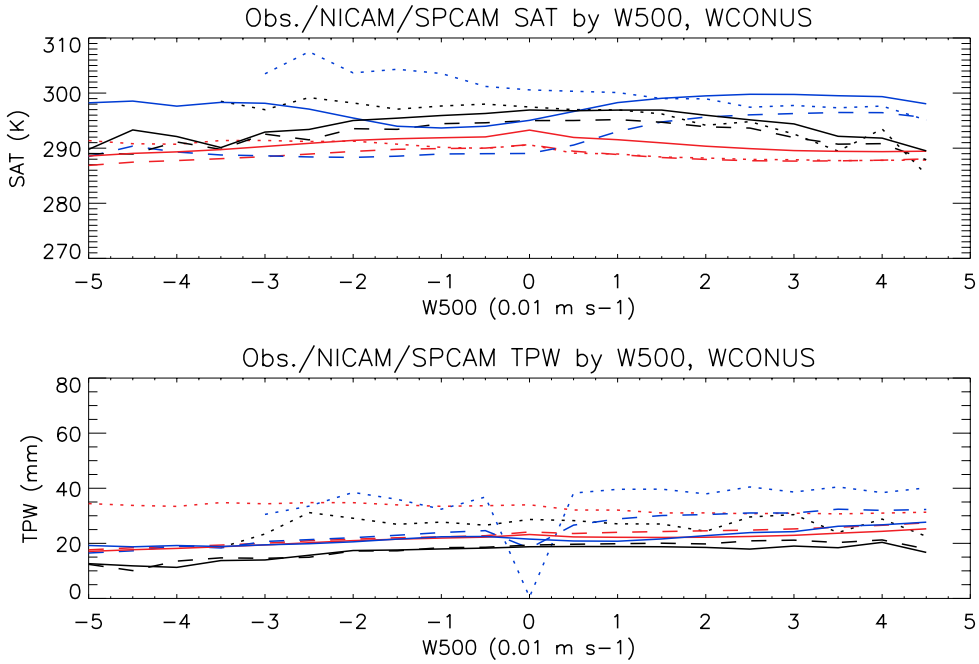

Figure 4.30. As Fig. 4.25, but sorted by W500 for WCONUS.

a. PBLRC-only

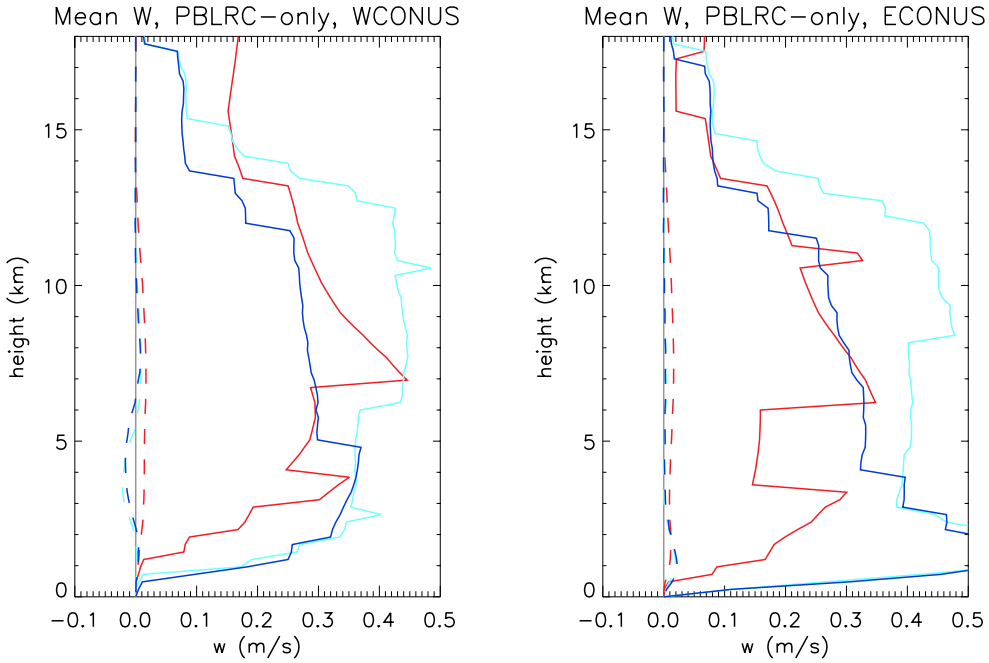

b. DCC-only

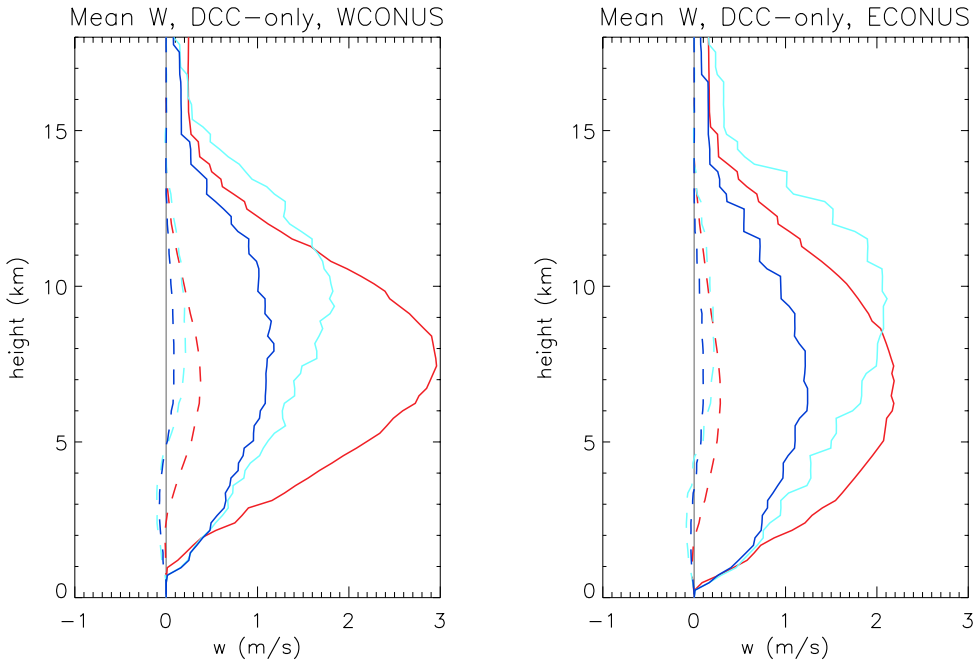

Figure 4.31. Mean vertical velocity vertical profiles over WCONUS (left) and ECONUS (right) for a) PBLR cloud-only, and b) DCC-only. SPv4 is light blue, SPv5 is dark blue. Dashed lines are the mean for all samples, and the solid lines are the mean 95th percentile at each altitude.

a. PBLRC-only

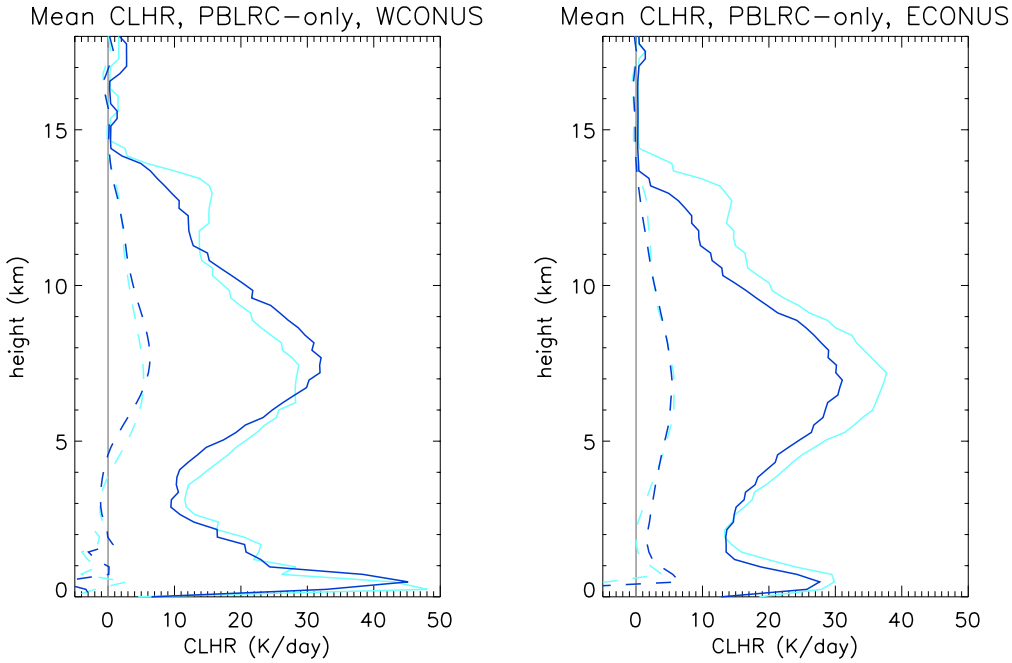

b. DCC-only

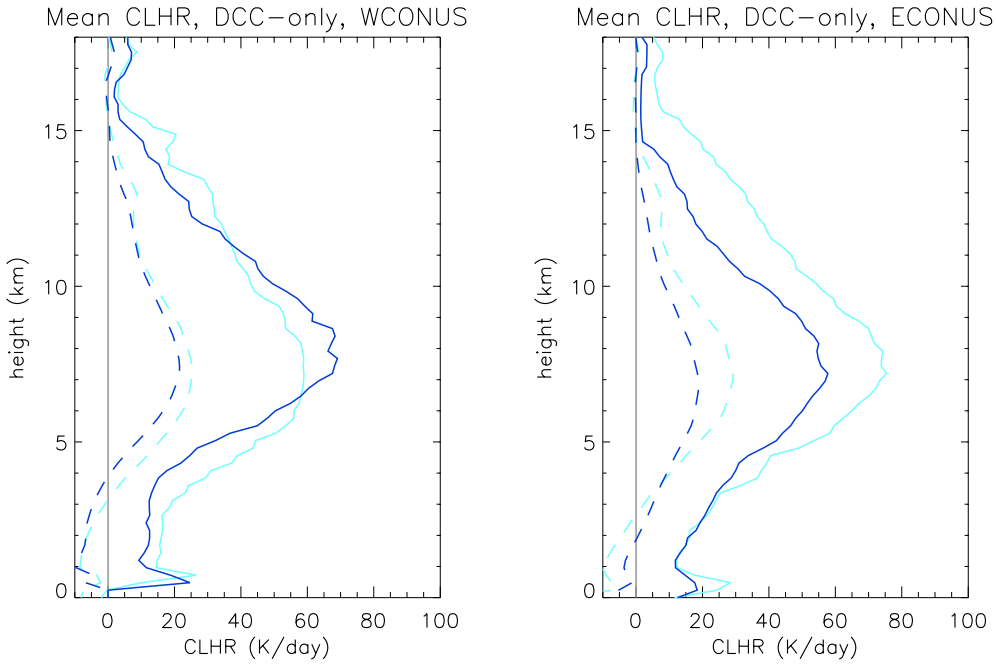

Figure 4.32. Mean non-radiative diabatic heating vertical profiles over WCONUS (left) and ECONUS (right) for a) PBLR cloud-only, and b) DCC-only. SPv4 is light blue, SPv5 is dark blue. Dashed lines are the mean for all samples, and the solid lines are the mean 95th percentile at each altitude.

5. CONCLUSIONS

In this thesis, I have examined the characteristics of convective clouds in two recently developed atmospheric models, NICAM and SP-CAM. One of the main purposes in developing these models was to explore the use of alternatives to cumulus parameterization. Of particular interest for this thesis are the relationships between convective clouds and their environment, and so a conditional sampling technique was applied to help separate errors in convective cloud behavior in a given environment with errors in the simulated convective environment. Using the results of this investigation, it is now possible to answer the questions asked in Chp. 1 with some confidence.

5.1. Main Questions

1. How well do simulated tropical oceanic convective clouds in NICAM resemble those observed by CloudSat?

NICAM has difficulty growing deep clouds as often as they are observed to occur. This appears to be caused by NICAM not developing deep clouds in environments that are observed to be marginal moisture necessary for deep convection. Both NICAM and observations show that cloud top height remains low for low TPW values, and deep clouds frequently develop only above a threshold TPW value. In NICAM this threshold value is about 10 mm higher than observed. Furthermore, environments more humid than average tend to occur more often in the real atmosphere than in NICAM; the observed PDF is skewed from the Gaussian shape towards higher TPW while the NICAM PDF is not. Because humid environments favor deeper clouds in both the real and simulated atmospheres, this causes NICAM to produce fewer deep clouds by

virtue of being drier than the real atmosphere. In addition to moisture, NICAM also has difficulty developing deep clouds in subsidence regions as often as the real atmosphere. Subsidence is more common and stronger in NICAM than observed (according to reanalysis data), leading to a further reduction in NICAM deep cloud frequency.

NICAM simulates DCC vertical reflectivity profile that is roughly similar to CloudSat observations. A major difference between the two is a large reduction in NICAM reflectivity values above the freezing level, at about 8 km. This reduction does not appear to be caused by errors in environmental conditions, as the reduction occurs in all convective environments. The most likely explanation is a lack of graupel in the NICAM microphysics; graupel is more reflective than snow, so missing graupel leads to an overproduction of snow and thus lower reflectivity. But further research using different microphysical schemes is probably necessary to confirm this. NICAM has some difficulty simulating the environment/DCC relationship. Cloud top height in particular appears insensitive to the convective environment, which is clearly not the case with real DCCs. Because of the current interest in how DCC top height will change with global climate change [e.g. Kuang and Hartmann 2007], there is a need to investigate this further.

2. How well do simulated continental convective clouds over the contiguous United States in NICAM and SP-CAM resemble those observed by CloudSat?

As in the tropics, NICAM under-produces deep PBLRCs over CONUS. SP-CAM has the same problem. Both models also produce too many PBLRCs, about double the observed value (though CloudSat may miss very shallow PBLRCs). SP-CAM has a problem producing too much cloud ice in cirrus clouds and taller PBLRCs, with an associated underproduction of snow.

NICAM produces more snow than SP-CAM, though NICAM may produce too much snow because the microphysics lacks graupel, as described previously. The lack of deep clouds does not appear to be caused by the models being too dry to produce them. Both models are more humid than observed across almost all of CONUS. The problem does not seem to occur from an error in reproducing the cloud/TPW relationship. Observations show that unlike in the tropics, over CONUS the mean cloud top height increases steadily as TPW increases. There is no threshold TPW value that separates shallow clouds from deep clouds. The models generally seem to capture this, though the absolute magnitude of COF is too low at all TPW values. The primary exception is SPv5, which produces somewhat realistic COF values for deeper clouds above 45 mm.

Neither model produces the observed SAT/cloud relationship. The observed and simulated relationships are so different that it is hard to draw any conclusions about what the models may be doing correctly or incorrectly. As with the tropics, NICAM under-produces deep clouds in subsidence environments over CONUS. Unlike the tropics, NICAM appears to produce a small number of deep clouds in strong subsidence regions, both over ECONUS and WCONUS. It isn't clear why this occurs. SP-CAM likewise does not produce deep clouds in subsidence regions, and does not produce the observed depth of deep clouds in strong ascent regions, either.

NICAM produces DCCs slightly too infrequently, but SP-CAM produces them far too infrequently, especially over WCONUS. NICAM produces a similar DCC vertical reflectivity over CONUS that is does over the tropics, with the same primary problem of too low reflectivity above the freezing level. The lower cloud is similar to observations, with slightly lower maximum reflectivity. SP-CAM has much more difficulty reproducing the observed reflectivity profile. The lower cloud is reasonable, but the middle cloud has far too low reflectivity. It is so

low that the upper cloud reflectivity data may be unusable because of secondary cloud contamination. SP-CAM DCCs also contain almost no graupel, which partially explains the low reflectivity, but not entirely. The incorrect reflectivity occurs at in all convective environments, so errors in the mean environment are not the cause. In contrast with the tropics, NICAM represents the environment/cloud relationships over CONUS fairly realistically, though there are some discrepancies with the lower cloud sensitivity for SAT and W500. SP-CAM represents the environment/cloud relationship for the lower cloud fairly realistically for TPW and SAT, though W500 is less realistic. The upper cloud is completely unrealistic, to the point that it isn't possible to draw strong conclusions about the environment/cloud relationship.

3. How well do simulated continental convective environments over the contiguous United States in NICAM and SP-CAM resemble observations?

NICAM is too warm over a portion of ECONUS, particularly the Great Lakes region, and too cool over much of WCONUS (particularly the mountains). Some of this coolness in the west may be related to the increased terrain resolution. Both NICAM and NARR, which have high-res. terrain, show a much greater SAT sensitivity to terrain altitude than SP-CAM and N/NR, which have low-res. terrain. NICAM produces too much humidity over much of CONUS, both east and west. SP-CAM produces a summertime mean environment that is too warm and too humid over most of CONUS. The warm bias exists in SP-CAM over most continental regions, and the humid bias exists over much of Earth's surface. The increased humidity in both models could hypothetically lead to an increase in deep PBLRCs and DCCs, as more humid environments tend to favor deeper clouds in nature. But the errors in the TPW/cloud relationships for both models described previously results in decreased vertical cloud growth, not

increased. The magnitude of both positive and negative W500 is too large by over 100% in both NICAM and SP-CAM, and the locations of mean ascent and descent are somewhat different than observed.

SP-CAM underpredicts the diurnal cycle range for SAT and TPW in most locations. SAT reaches a daily maximum about three hours later than observed. The timing of the TPW diurnal cycle is not well represented, though admittedly the cycle magnitude is small compared with the full range of TPW values during JJA. SP-CAM produces too large a cycle in W500 over portions of WCONUS, but it captures the mountain/plains solenoidal circulation realistically.

4. What is the effect of improving the microphysics on convective clouds in SP-CAM?

Convective cloud properties generally improve with the double moment microphysical scheme, especially DCCs. Deep clouds develop more frequently in v5 than v4, though still less frequently than observed. The shallow cumulus cloud vertical frequency profile is not notably improved, but this is expected given the difficulties of a 4 km resolution CRM with shallow cumulus. The problem of overproducing cloud ice in previous SP-CAM versions is mostly if not entirely resolved, which is compensated by an increase in snow and graupel production. Snow appears to fall more like one may expect in v5, as unlike v4 the snow vertical profile is shifted to a lower altitude than cloud ice. V5 produces the same unrealistic, tropics-like minimum TPW threshold that v4 does, which probably is a main cause of the low frequency of deep clouds. Unfortunately, the convective mean environment in v5 is much too humid, at least 10 mm more than observed. This might contribute to the increase in deep cloud frequency from v4, as very humid environments favor very deep clouds. The improvement in microphysics does not resolve

the SAT/PBLR cloud relationship problem. There is no obvious change in the 500 hPa vertical motions, and so this cannot explain the improvement in vertical growth.

The DCC frequency in v5 has greatly increased, and now DCCs occur slightly too frequently. The DCC vertical reflectivity has improved greatly from v4, and now resembles the observed and NICAM profiles. This improvement occurs in all convective environments. V5 shows a similar reduction in 8 km reflectivity as NICAM does, suggesting that there may be more to the problem than simply missing graupel. However, v5 shows a hint of the "double arc" reflectivity structure at 10 km that is observed, meaning that SP-CAM may be simulating some of the variability in the upper cloud structure that occurs in nature (this should be investigated further). The lack of significant graupel seen in v4 has been resolved in v5. DCCs are also much more frequency in v5, and in fact may be a little too frequent. V5 shows that DCCs tend to weaken as TPW increases; that is, the cloud top reflectivity gradient and cloud top height both decrease. While there is some question about how to interpret the observed reflectivity gradient, the observed cloud top height clearly increases with increasing TPW, which is puzzling. This might be a good topic for future research, as it has implications for a warmer, wetter future world. In contrast, the simulated SAT/DCC relationship is very similar to the observed, which is again puzzling given the model's inability to represent the SAT/PBLR cloud relationship. v5 does not reproduce the observed slight reduction in cloud top height in strong ascent environments.

Unfortunately, it appears that SP-CAM v5 has suffered a loss of realism for the mean CONUS summertime environment compared with v4. V4 is already too warm and moist across most of CONUS, and v5 is even moreso. This probably is not the sole reason why the clouds improved, but it is likely a contributing factor to the improvement in PBLR cloud vertical

growth. This topic will be discussed in an appendix to this thesis, so further discussion will be related to there.

5.2. Implications of the conclusions

From these conclusions one can draw three important implications. One involves the model microphysics, the second involves the model clouds, and the third involves the analysis method. First, there are substantial differences in the three microphysical schemes associated with NICAM and SPv4/5, and hence differences in cloud hydrometeor distributions. SPv4 in particular has a major problem with producing cloud ice, but not converting it into snow and graupel. The ice lingers in the upper troposphere, rather than falling into the lower cloud as precipitation. This results in a reflectivity "hole" in SPv4 DCCs. This might also mean that cloud ice lingers in convective anvils, which would correspond to some preliminary results from Masunaga et al. [2008] and Satoh et al. [2010]. NICAM single moment and SP-CAM double moment schemes both appear to behave more realistically, though further investigation with other microphysical schemes would be desirable. Kodama et al. [2012] found that even the newer NICAM microphysical schemes still produces the same problem of overproducing snow that has occurred with older NICAM versions.

Second, researchers should take great care when using satellite simulators to reduce the influence of model microphysical errors as much as possible. With radar, reflectivity is sensitive to the 6^{th} power of hydrometeor diameter, and extinction is sensitive to the 3^{rd} power. Because of this, small errors in the assumed or predicted size distribution can lead to major errors in the reflectivity. For example, comparing the mean N5ETH from observed CONUS convection to simulated convection to compare the strengths of the convective updraft would be problematic

because of the sensitivity of the mean N5ETH to ice phase hydrometeors. To avoid this problem, I used the conditional sampling technique to compare frequency and reflectivity profiles for convective clouds in the same model – with the same microphysics – in different convective environments to identify potential unrealistic behavior in the models. Other techniques should be explored as well, as well as techniques to characterize the errors in convective hydrometeor profiles.

The problem of model hydrometeor distributions affecting CloudSat simulators has been previously investigated. Di Michele et al. [2012] investigated the relative contributions of radar simulator and model microphysics in ECMWF to disagreements between observed and simulated global reflectivity. They found that the total disagreement in reflectivity was significantly larger than the radar simulator's sensitivity to changes in its forward model assumptions. Unfortunately they did not include a complementary comparison of other cloud diagnostics to distinguish between microphysical and macrophysical errors, but at the time that would be difficult because of limited observations of these diagnostics.

Third, both models *may* have difficulty developing convective clouds vertically. Even though both models produce different kinds of ice phase microphysical errors, both models produce a lack of detectable deeper PBLRCs. Even given the limitations of the radar simulation method, there is good reason to accept the possibility that the apparent lack of deeper clouds is related to a true lack of deeper clouds. Petch and Gray [2001] conducted sensitivity tests with a CRM representing the tropical Pacific during TOGA COARE. Among the things they tested was the sensitivity to the total convective mass flux vertical profile to changes in horizontal resolution. They found that the convective mass flux from 0 km to 6 km altitude was particularly sensitive to the resolution change, increasing as grid box size decreased. This indicates that the cumulus

congestus and shallow cumulus are particularly sensitive to horizontal resolution, and even the 4 km resolution of SP-CAM is not sufficiently small to develop these clouds realistically. Unfortunately the other cloud indices do not help clarify the situation, so further investigation is necessary. But it seems that the CLHR, an important variable in cloud/climate interaction, is not reduced significantly above 10 km because of the lack of deep PBLRCs.

Also, in NICAM's case, Kodama et al. [2012] used a combined CloudSat/CALIPSO simulator to investigate tropical clouds. They found that even with the lidar included, NICAM underestimates the formation rate of cumulus congestus clouds. While the lidar simulator may have similar issues with the radar simulator, the lidar should be able to identify even the lowest cloud ice concentrations associated with convection. Perhaps future studies with SP-CAM should include a lidar simulator which would detect a higher convective cloud top even with too much cloud ice and not enough snow.

5.3. Final comments

So do the models get the right answer regarding convection for the right reason? No single study, or even thesis, can completely answer this question. But this thesis provides some information regarding the effect of the convective environment on convective clouds. Both models seem to have difficulty producing deep clouds in marginally humid environments, in which deep clouds frequently occur in nature. The models offset this tendency partially, at least over CONUS, by being unrealistically humid. This doesn't completely remove the lack of deep clouds, but partially masks it. This is of particular concern when models are improved – clouds may improve when the microphysics improve, but not necessarily *because* the microphysics improve. The environment may change, even become more realistic, in a way that makes the

clouds more realistic. This may be the case with SP-CAM developing deep PBLRCs in v5 than v4. Clearly the TPW/PBLR cloud relationship improved, but also the humidity increased beyond realism. Both of these combined lead to improved PBLR cloud vertical growth. The SAT/PBLR cloud relationship is another example for a different reason, where over CONUS the models don't represent the real relationship at all. This means that changes in SAT related to global climate change, all other LSEVs held constant, could potentially result in very different responses in simulated PBLRCs than observed. I think this is a important topic for future study, given the meteorological importance of non-DCC PBLRCs in influencing DCCs.

But this is not the case for every manner in which convective cloud's were examined in this thesis. The major errors in deep convective simulated vertical reflectivity structure do not appear to be caused by errors in the convective environment, nor do errors in the environment mask problems with the environment/DCC relationship. Cleary the DCC vertical structure over CONUS improved in SP-CAM v4 over v4, and it has little to do with changes in the mean convective environment.

So the answer indicated by this thesis, perhaps not surprisingly, is "sometimes". Detecting when a model develops realistic clouds for realistic reasons is challenging, but can be done with some effort. Several techniques have developed for use in standardized model intercomparison projects to help resolve this problem, but there is still room for additional approaches. This thesis applies a conditional sampling technique as a relatively simple and straightforward method to identify errors in simulated cloud behavior that would not be apparent when just looking at regional mean values. As simulated convective processes (hopefully) continue to improve through the use of non-parameterized climate models, the need for such techniques will increase with time. But this thesis only examines two recent such attempts, including an already-outdated

version of NICAM. There are many more opportunities where this technique can be applied to help uncover otherwise latent sources of error. Hopefully the contents of this thesis will help stimulate such investigations.

This project also makes clear the sensitivity of satellite simulators to cloud microphysics when using them to examine clouds. SPv4 produces a large amount of cloud ice, which largely does not convert into snow and graupel. Because cloud ice is difficult to detect for CloudSat, the radar simulator often does not "see" clouds with much more cloud ice than precipitating ice. This is a problem not only for investigating cirrus clouds, but also convective clouds, as they will appear too short in the statistical analysis. Much of the improvement in SPv5 is related to the increased show/graupel within the upper regions of convective clouds. This illustrates why the conditional sampling technique is useful, so that satellite simulators can be used to meaningfully investigate cloud characteristics without the results being muddied with microphysical problems.

In addition, it would be interesting and possibly very useful to run similar investigations using other variables. The three LSEVs where chosen as simple measurements to quantify the convective environment, but there are many more variables from which to choose. Some variables are more closely tied with deep convection, like CAPE, convective inhibition, equivalent potential temperature, and the LNB. Using these variables might make it easier to create a "process-based" investigation than the three variables used here - though it would still be useful to use the latter variables as a "sanity check" of sorts. There are other cloud variables that can be considered as well. Convective vertical velocity and mass flux have only been briefly mentioned here, but of course they are critical to convection and the convective interaction with the environment. A very preliminary analysis of mine suggests that SP-CAM may produce vertical velocities much lower than reality, highlighting the need for further investigation.

Unfortunately, at the moment, there are no reliable observations for these variables beyond field experiments, hence the use of cloudtop vertical reflectivity gradients in this thesis. So studies involving existing data would only be able to compare regional mean vertical velocities, not within individual clouds. But with the launch of EarthCARE [Heliere et al. 2007] in the near future, which will carry a Doppler-capable Cloud Profiling Radar, such studies will be possible.

REFERENCES

Adams, D. K., and A. C. Comrie (1997), The North American Monsoon, *Bull. Amer. Meteor. Soc., 78*, 2197–2213.

Allen, M. R. and W. J. Ingram (2002), Constraints on future changes in climate and the hydrologic cycle, *Nature, 419*, 224-232, doi:10.1038/nature01092

Arakawa, A. (2004), The Cumulus Parameterization Problem: Past, Present, and Future, *J. Climate, 17,* 2493–2525.

Arrhenius, S. (1896), On the influence of carbonic acid in the air upon the temperature of the ground. Philosophical Magazine and Journal of Science Series 5, Volume 41, pages 237-276.

Bacmeister, J. T., and G. L. Stephens (2011), Spatial statistics of likely convective clouds in CloudSat data, *J. Geophys. Res., 116*, D04104, doi:10.1029/2010JD014444.

Balling, R. C., Jr. (1985), Warm season nocturnal precipitation in the Great Plains of the United States, *J. Climate Appl. Meteor., 24*, 1383–1387.

Becker, E. J., and E. H. Berbery (2008), The Diurnal Cycle of Precipitation over the North American Monsoon Region during the NAME 2004 Field Campaign, *J. Climate, 21,* 771–787.

Benedict, J. J., and D. A. Randall (2007), Observed Characteristics of the MJO Relative to Maximum Rainfall, *J. Atmos. Sci., 64,* 2332–2354.

Benedict, J. J., and D. A. Randall (2009), Structure of the Madden–Julian Oscillation in the Superparameterized CAM, *J. Atmos. Sci., 66,* 3277–3296.

Benedict, J. J., and D. A. Randall (2007), Observed Characteristics of the MJO Relative to Maximum Rainfall, *J. Atmos. Sci., 64,* 2332–2354.

Bister, M., and K. A. Emanuel (1997), The Genesis of Hurricane Guillermo: TEXMEX Analyses and a Modeling Study, *Mon. Wea. Rev., 125*, 2662–2682.

Bryan, G. H., J. C. Wyngaard, and J. M. Fritsch (2003), Resolution Requirements for the Simulation of Deep Moist Convection, *Mon. Wea. Rev.*, *131,* 2394–2416.

Brown, R. G., and C. Zhang, 1997: Variability of Midtropospheric Moisture and Its Effect on Cloud-Top Height Distribution during TOGA COARE*. *J. Atmos. Sci.*, 54, 2760–2774.

Bony, S. K.-M. Lau, and Y. C. Sud (1997), Sea Surface Temperature and Large-Scale Circulation Influences on Tropical Greenhouse Effect and Cloud Radiative Forcing, *J. Climate*, *10*, 2055-2077.

Bony , S., J.-L. Dufresne, H. Le Treut, J.-J. Morcrette, and C. Senior (2004), On dynamic and thermodynamic components of cloud changes, *Clim. Dyn.*, *22*, 71-86.

Carbone, R. E., and J. D. Tuttle (2008), Rainfall Occurrence in the U.S. Warm Season: The Diurnal Cycle*, *J. Climate, 21*, 4132–4146.

Carpenter, R. L., K. K. Droegemeier, and A. M. Blyth (1998), Entrainment and Detrainment in Numerically Simulated Cumulus Congestus Clouds. Part III: Parcel Analysis, *J. Atmos. Sci., 55,* 3440–3455. Changnon, S. A., 2001: Thunderstorm Rainfall in the Conterminous United States. *Bull. Amer. Meteor. Soc.*, 82, 1925–1940.

Changnon, D., M. Sandstrom, and C. Schaffer (2003), Relating changes in agricultural practices to increasing dew points in extreme Chicago heat waves, *Climate Res., 24,* 243–254.

Charney, J. G., and A. Eliassen (1964), On the Growth of the Hurricane Depression, *J. Atmos. Sci., 21,* 68–75.

Chou, C., and J. D. Neelin (2004), Mechanisms of Global Warming Impacts on Regional Tropical Precipitation*, *J. Climate*, *17,* 2688–2701.

Chou, C., J. D. Neelin, C.-A. Chen, and J.-Y. Tu (2009), Evaluating the "Rich-Get-Richer" Mechanism in Tropical Precipitation Change under Global Warming, *J. Climate, 22,* 1982–2005.

Corfidi, S. F., J. H. Meritt, and J. M. Fritsch (1996), Predicting the Movement of Mesoscale Convective Complexes, *Wea. Forecasting, 11,* 41–46.

Cotton, W. R., R. L. George, P. J. Wetzel, and R. L. McAnelly (1983), A Long-Lived Mesoscale Convective Complex. Part I: The Mountain–Generated Component, *Mon. Wea. Rev., 111,* 1893–1918.

Dai, A., F. Giorgi, and K. E. Trenberth (1999), Observed and model simulated precipitation diurnal cycle over the contiguous United States, *J. Geophys. Res.,104,* 6377–6402.

Dai, A. (2001), Global Precipitation and Thunderstorm Frequencies. Part II: Diurnal Variations, *J. Climate, 14,* 1112–1128.

Dawson, D. T., M. Xue, J. A. Milbrandt, and M. K. Yau (2010), Comparison of Evaporation and Cold Pool Development between Single-Moment and Multimoment Bulk Microphysics Schemes in Idealized Simulations of Tornadic Thunderstorms, *Mon. Wea. Rev., 138*, 1152–1171.

Deardorff, J. W. (1980), Cloud Top Entrainment Instability, *J. Atmos. Sci., 37,* 131–147.

Del Genio, A. D., Y. Chen, D. Kim, and M.-S. Yao (2012), The MJO Transition from Shallow to Deep Convection in CloudSat/CALIPSO Data and GISS GCM Simulations, *J. Climate, 25*, 3755-3770.

P. A. Dirmeyer, and coauthors (2012), Simulating the diurnal cycle of rainfall in global climate models: resolution versus parameterization, *Climate Dyn., 39*, 399-418, doi: 10.1007/s00382-011-1127-9.

Dessler, A. E. (2013), Observations of Climate Feedbacks over 2000–10 and Comparisons to Climate Models*, *J. Climate*, *26,* 333–342.

Di Michele, S., Ahlgrimm, M., Forbes, R., Kulie, M., Bennartz, R., Janiskova, M. and Bauer, P. (2012), Interpreting an evaluation of the ECMWF global model with CloudSat observations: ambiguities due to radar reflectivity forward operator uncertainties. Q.J.R. Meteorol. Soc., 138: 2047–2065. doi: 10.1002/qj.1936

Emanuel, K. A. (1987), An Air-Sea Interaction Model of Intraseasonal Oscillations in the Tropics, *J. Atmos. Sci., 44,* 2324–2340.

Eyre, J. R., G. A. Kelly, A. P. McNally, E. Andersson, and A. Persson (1993), Assimilation of TOVS radiance information through one-dimensional variational analysis, *Q. J. R. Meteor. Soc.*, *119*, 1427-1463.

Ferreira, R. Nieto, W. H. Schubert, and J. J. Hack (1996), Dynamical Aspects of Twin Tropical Cyclones Associated with the Madden–Julian Oscillation, *J. Atmos. Sci., 53*, 929–945.

Fierro, A. O., J. M. Simpson, M. A. Lemone, J. M. Straka, and B. F. Smull (2009), On how hot towers fuel the Hadley cell: An observational and modeling study of line-organized convection in the equatorial trough from TOGA COARE, *J. Atmos. Sci., 66,* 2730–2746.

Forsythe, J. M., J. B. Dodson, P. T. Partain, S. Q. Kidder, and T. H. Vonder Haar (2012), How Total Precipitable Water Vapor Anomalies Relate to Cloud Vertical Structure, *J. Hydromet.*, *13*, 709-721.

Fu, Q., S. K. Krueger, and K. N. Liou (1995), Interactions of Radiation and Convection in Simulated Tropical Cloud Clusters, *J. Atmos. Sci., 52,* 1310–1328.

Fudeyasu, H., Y. Wang, M. Satoh, T. Nasuno, H. Miura, and W. Yanase (2010), Multiscale Interactions in the Lifecycle of a Tropical Cyclone Simulated in a Global Cloud-System-

Resolving Model Part II: System-Scale and Mesoscale Processes, *Mon. Wea. Rev.*, *138*, 4305-4327.

Fuller, R. D., and D. J. Stensrud (2000), The Relationship between Tropical Easterly Waves and Surges over the Gulf of California during the North American Monsoon, *Mon. Wea. Rev., 128,* 2983–2989.

Gates, W. L. (1992), AMIP: The Atmospheric Model Intercomparison Project, *Bull. Amer. Meteor. Soc., 73,* 1962–1970.

Giorgi, F. (2006), Climate change hot-spots, *Geophys. Res. Lett.*, 33.L08707, doi:10.1029/2006GL025734.

Grabowski, W. W. (1998), Toward cloud resolving modeling of large-scale tropical circulations: A simple cloud microphysics parameterization, *J. Atmos. Sci., 55,* 3283–3298.

Hadley, G. (1735), Concerning the cause of the general trade-winds, *Phil. Trans., 29*, 58–62.

Hartmann, D. L., M. E. Ockert-Bell, and M. L. Michelsen (1992), The Effect of Cloud Type on Earth's Energy Balance: Global Analysis, *J. Climate*, *5,* 1281–1304.

Haynes, J. M., R.T. Marchand, Z. Luo, A. Bodas-Salcedo, and G. L. Stephens (2007), A multi-purpose radar simulation package: QuickBeam, *Bull. Amer. Meteor. Soc.*, *88*, 1723-1727.

Haynes, J. M., T. S. L'Ecuyer, G. L. Stephens, S. D. Miller, C. Mitrescu, N. B. Wood, and S. Tanelli (2009), Rainfall retrieval over the ocean with spaceborne W-band radar, *J. Geophys. Res., 114*, doi:1029/2008JD009973.

Haywood, J., and O. Boucher (2000), Estimates of the direct and indirect radiative forcing due to tropospheric aerosols: A review, *Rev. Geophys.*, *38,* 513–543.

Held, I. M., and B. J. Soden (2000), Water vapor feedback and global warming, *Annu. Rev. Energy Environ.*, *25,* 441–475.

Held, I. M., and B. J. Soden (2006), Robust Responses of the Hydrological Cycle to Global Warming, *J. Climate*, *19,* 5686–5699.

Heliere, A., A. Lefebvre, T. Wehr, J.-L. Bezy, and Y. Durand (2007), The EarthCARE Mission: Mission concept and lidar instrument pre-development, *Geoscience and Remote Sensing Symposium, IEEE,* 4975 – 4978, doi: 10.1109/IGARSS.2007.4423978.

Hendon, H. H., and M. L. Salby (1994), The Life Cycle of the Madden–Julian Oscillation, *J. Atmos. Sci.*, *51,* 2225–2237.

Heymsfield, A. J., and G. M. McFarquhar (1996), High Albedos of Cirrus in the Tropical Pacific Warm Pool: Microphysical Interpretations from CEPEX and from Kwajalein, Marshall Islands, *J. Atmos. Sci., 53,* 2424–2451.

Higgins, R. W., Y. Yao, E. S. Yarosh, J. E. Janowiak, and K. C. Mo (1997), Influence of the Great Plains Low-Level Jet on Summertime Precipitation and Moisture Transport over the Central United States, *J. Climate, 10,* 481–507.

Higgins, W., and D. Gochis (2007), Synthesis of Results from the North American Monsoon Experiment (NAME) Process Study, *J. Climate, 20,* 1601–1607.

Hohenegger, C., and B. Stevens, 2013: Preconditioning Deep Convection with Cumulus Congestus. *J. Atmos. Sci.*, 70, 448–464.

Holloway, C. E., and J. D. Neelin (2009), Moisture Vertical Structure, Column Water Vapor, and Tropical Deep Convection, J. Atmos. Sci., 66, 1665-1683.

Houze, R. A., 1973: A Climatological Study of Vertical Transports by Cumulus-Scale Convection. *J. Atmos. Sci.*, 30, 1112–1123.

Hung, M.-P., J.-L. Lin, W. Wang, D. Kim, T. Shinoda, and S. J. Weaver (2013), MJO and Convectively Coupled Equatorial Waves Simulated by CMIP5 Climate Models, *J. Climate*, *26,* 6185–6214.

Inamdar, A. K. and V. Ramanathan (1994), Physics of Greenhouse Effect and Convection in Warm Oceans, *J. Climate*, *7*, 715-731.

Inoue, T., M. Satoh, H. Miura, and B. Mapes (2008), Characteristics of Cloud Size of Deep Convection Simulated by a Global Cloud Resolving Model over the Western Tropical Pacific, *J. Meteor. Soc. Japan*, *86A*, 1-15.

Inoue, T., M. Satoh, Y. Hagihara, H. Miura, and J. Schmetz (2010), Comparison of high-level clouds represented in a global cloud system-resolving model with CALIPSO/CloudSat and geostationary satellite observations, J. Geophys. Res. 115, doi: 10.1029/2009JD012371.

Jensen, M. P. and A. D. Del Genio (2006), Factors Limiting Convective Cloud-Top Height at the ARM Nauru Island Climate Research Facility, *J. Climate*, *19*, 2105-2117.

Kalnay, E. M. Kanamitsu, R. Kistler, W. Collins, D. Deaven, L. Gandin, M. Iredell, S. Saha, G. White, J. Woollen, Y. Zhu, M. Chelliah, W. Ebisuzaki, W. Higgens, J. Janowiak, K. C. Mo, C. Ropelewski, J. Wang, A. Leetmaa, R. Reynolds, R. Jenne, and D. Josheph (1996), The NCEP/NCAR 40-Year Reanalysis Project, *Bull. Amer. Meteor. Soc., 77*, 437-471.

Kawanishi, T, T. Sezai, Y. Ito, K. Imaoka, T. Takeshima, Y. Ishido, A. Shibata, M. Miura, H. Inahata, and R. W. Spencer (2003), The Advanced Microwave Scanning Radiometer for the Earth Observing System (AMSR-E), NASDA's contribution to the EOS for global energy and water cycle studies, *IEEE Trans. Geosci. Remote Sensing, 41*, 184-194.

Khairoutdinov, M. F., and D. A. Randall (2003), Cloud resolving modeling of the ARM summer 1997 IOP: Model formulation, results, uncertainties, and sensitivities, *J. Atmos. Sci., 60,* 607–625.

Khairoutdinov, M., D. Randall, and C. DeMott (2005), Simulations of the Atmospheric General Circulation Using a Cloud-Resolving Model as a Superparameterization of Physical Processes, *J. Atmos. Sci., 62*, 2136–2154.

Kincer, J. B. (1916), Daytime and nighttime precipitation and their economic significance, *Mon. Wea. Rev., 44,* 628–633.

Kodama, C., A. T. Noda, and M. Satoh (2012), An assessment of the cloud signals simulated by NICAM using ISCCP, CALIPSO, and CloudSat satellite simulators, J. Geophys. Res., 117, D12210, doi:10.1029/2011JD017317.

Kooperman, G. J., M. S. Pritchard, and R. C. J. Somerville (2013), Robustness and sensitivities of central U.S. summer convection in the super-parameterized CAM: Multi-model intercomparison with a new regional EOF index, Geophys. Res. Lett., 40, 3287–3291, doi:10.1002/grl.50597.

Kubar, T. L.,D. E. Waliser, and J.-L. Li (2011), Boundary Layer and Cloud Structure Controls on Tropical Low Cloud Cover Using A-Train Satellite Data and ECMWF Analyses, J. Climate, 24, 194-215.

Lebsock, M. D., T. S. L'Ecuyer, and G. L. Stephens (2011), Detecting the Ratio of Rain and Cloud Water in Low-Latitude Shallow Marine Clouds, *J. Appl. Meteor. Climatol.*, *50*, 419-432.

L'Ecuyer, T. S. and J. H. Jiang (2010), Touring the atmosphere aboard the A-Train, *Phys. Today, 63,* 36-41.

Lee, M.-I., I.-S. Kang, J.-K. Kim, and B. E. Mapes (2001), Influence of cloud-radiation interaction on simulating tropical intraseasonal oscillation with an atmospheric general circulation model, J. Geophys. Res., 106(D13), 14219–14233, doi:10.1029/2001JD900143.

Lin, J-L., and Coauthors (2006), Tropical intraseasonal variability in 14 IPCC AR4 climate models. Part I: Convective signals, *J. Climate*, *19,* 2665–2690.

Lindzen, R. S. and S. Nigam (1987), On the Role of Sea Surface Temperature Gradients in Forcing Low-Level Winds and Convergence in the Tropics, *J. Atmos. Sci.*, *44,* 2418-2436.

Lindzen, R. S., M.-D. Chou, and A. Y. Hou (2001), Does the Earth Have an Adaptive Infrared Iris?, *Bull. Amer. Meteor. Soc., 82,* 417–432.

Liu, S. C., T. M. Donahue, R. J. Cicerone, and W. L. Chameides (1976), Effect of water vapor on the destruction of ozone in the stratosphere perturbed by ClX or NO x pollutants, J. Geophys. Res., 81(18), 3111–3118, doi:10.1029/JC081i018p03111.

Liu, C. and M. W. Moncrieff (2008), Explicitly simulated tropical convection over idealized warm pools, *J. Geophys. Res.*, *113*, doi:10.1029/2008JD010206.

Liu, C., E. J. Zipser, and S. W. Nesbitt (2007), Global Distribution of Tropical Deep Convection: Different Perspective from TRMM Infrared and Radar Data, *J. Climate*, *20*, 489-503.

Louis, J.-F. (1979), A parametric model of vertical eddy fluxes in the atmosphere, *Bound.-Lay. Meteorol., 17,* 187-202.

Lucas, C., E. J. Zipser, and M. A. Lemone (1994), Vertical Velocity in Oceanic Convection off Tropical Australia, *J. Atmos. Sci.*, *51,* 3183–3193.

Lucas, C., E. J. Zipser, and M. A. Lemone (1996), Reply, *J. Atmos. Sci.*, *53,* 1212–1214.

Luo, Z. J., G. Y. Liu, and G. L. Stephens (2008), CloudSat adding new insight into tropical penetrating convection, *Geophys. Res. Lett.*, *35*, doi:1029/2008GL035330.

Luo, Z. J., G. Y. Liu, and G. L. Stephens (2010), Use of A-Train data to estimate convective buoyancy and entrainment rate, *Geophys. Res. Lett.*, *37*, doi:10.1029/2010GL042904

Luo, Y., R. Zhang, W. Qian, Z. Luo, and X. Hu (2011), Intercomparison of Deep Convection over the Tibetan Plateau-Asian Monsoon Region and Subtropical North America in Boreal Summer Using *CloudSat*/CALIPSO Data, *J. Climate*, *25*, 2164-2177.

Madden, R. A., and P. R. Julian (1994), Observations of the 40–50-Day Tropical Oscillation—A Review, *Mon. Wea. Rev.*, *122,* 814–837.

Mahrt, L., (2006), Variation of Surface Air Temperature in Complex Terrain, *J. Appl. Meteor. Climatol.*, *45,* 1481–1493.

Maloney, E. D., and D. L. Hartmann (2001), The Sensitivity of Intrasensonal Variability in the NCAR CCM3 to Changes in Convective Parameterization, *J. Climate, 14*, 2015-2034.

Mantua, N. J., and S. R. Hare (2002), The Pacific Decadal Oscillation, *J. Oceanogr*, *58,* 35–44.

Manabe, S., J. S., and R. F. Strickler (1965), Simulated climatology of a general circulation model with a hydrologic cycle, *Mon. Wea. Rev.*, *93,* 769–798.

Mapes, B. E., and R. A. Houze (1995), Diabatic Divergence Profiles in Western Pacific Mesoscale Convective Systems, *J. Atmos. Sci.*, *52,* 1807–1828.

Masunaga, H., M. Satoh, and H. Miura (2008), A Joint Satellite and Global Cloud-Resolving Model Analysis of a Madden-Julian Oscillation event: Model Diagnosis, *J. Geophys. Res.*,*113*, D17210, doi:10.1029/2008JD009986.

Meehl, G. A., G. J. Boer, C. Covey, M. Latif, and R. J. Stouffer (2000), The Coupled Model Intercomparison Project (CMIP), *Bull. Amer. Meteor. Soc.*, *81,* 313–318.

Mesinger, F., and Coauthors (2006), North American Regional Reanalysis, *Bull. Amer. Meteor. Soc.*, *87,* 343–360.

Michaud, L. (1996), Comments on "Convective available potential energy in the environment of oceanic and continental clouds.", *J. Atmos. Sci, 53*, 1209–1211.

Miura, H., M. Satoh, T. Nasuno, A. T. Noda, and K. Oouchi (2007), A Madden-Julian Oscillation Event Realistically Simulated by a Global Cloud-Resolving Model, *Science*, *318*, 1763-1765.

Miura, H., M. Satoh, and M. Katsunata (2009), Spontaneous onset of a Madden-Julian oscillation event in a cloud-system-resolving simulation, *Geophys. Res. Lett., 36,* doi:10.1029/2009GL039256,

Miyamoto, Y., Y. Kajikawa, R. Yoshida, T. Yamaura, H. Yashiro, and H. Tomita (2013), Deep moist atmospheric convection in a subkilometer global simulation, Geophys. Res. Lett., 40, 4922–4926, doi:10.1002/grl.50944.

Montgomery, M. T., M. E. Nicholls, T. A. Cram, and A. B. Saunders (2006), A Vortical Hot Tower Route to Tropical Cyclogenesis, *J. Atmos. Sci., 63*, 355–386.

Orville, H. D. 1965. A numerical study of the initiation of cumulus clouds over mountainous terrain. J. Atmos. Sci 22:684–689.

Morrison, H., and J. Milbrandt (2011), Comparison of Two-Moment Bulk Microphysics Schemes in Idealized Supercell Thunderstorm Simulations, *Mon. Wea. Rev., 139,* 1103–1130.

Morrison, H., G. Thompson, and V. Tatarskii (2009), Impact of cloud microphysics on the development of trailing stratiform precipitation in a simulated squall line: Comparison of one- and two-moment schemes, *Mon. Wea. Rev.*, *137,* 991–1007.

Partain, P. (2004), Cloudsat ECMWF-AUX Auxiliary Data Process Description and Interface Control Document, http://www.cloudsat.cira.colostate.edu/ICD/ECMWF-AUX/ECMWF-

AUX_PDICD_3.0.pdf, Cooperative Institute for Research in the Atmosphere, Colorado State University, Fort Collins, CO.

Petch, J. C. and Gray, M. E. B. (2001), Sensitivity studies using a cloud-resolving model simulation of the tropical west Pacific, *Q.J.R. Meteorol. Soc., 127*, 2287–2306. doi: 10.1002/qj.49712757705.

Peters, M. E. and C. S. Bretherton (2006), Structure of tropical variability from a vertical mode perspective, *Theor. Comput. Fluid. Dyn.*, doi:10.1007/s00162-006-0034-x

Pritchard, M. S., and R. C. J. Somerville (2009), Assessing the Diurnal Cycle of Precipitation in a Multi-Scale Climate Model, J. Adv. Model. Earth Syst., 1, 12, doi:10.3894/JAMES.2009.1.12.

Pritchard, M. S., M. W. Moncrieff, and R. C. J. Somerville (2011), Orogenic propagating precipitation systems over the United States in a global climate model with embedded explicit convection, J. Atmos. Sci., 68(8), 1821–1840.

Rabin, R. M., D. J. Stensrud, S. Stadler, P. J. Wetzel, and M. Gregory (1990), Observed Effects of Landscape Variability on Convective Clouds, *Bull. Amer. Meteor. Soc., 71*, 272–280.

Rabin, R. M., and D. W. Martin (1996), Satellite observations of shallow cumulus coverage over the central United States: An exploration of land use impact on cloud cover, J. Geophys. Res., 101(D3), 7149–7155, doi:10.1029/95JD02891.

Randall, D. A., Harshvardhan, D. A. Dazlich, and T. G. Corsetti (1989), Interactions among Radiation, Convection, and Large-Scale Dynamics in a General Circulation Model, *J. Atmos. Sci., 46,* 1943–1970.

Randall, D., M. Khairoutdinov, A. Arakawa, and W. Grabowski (2003), Breaking the Cloud Parameterization Deadlock, *Bull. Amer. Meteor. Soc., 84,* 1547–1564.

Randall, D.A., R.A. Wood, S. Bony, R. Colman, T. Fichefet, J. Fyfe, V. Kattsov, A. Pitman, J. Shukla, J. Srinivasan, R.J. Stouffer, A. Sumi and K.E. Taylor (2007), Climate Models and Their Evaluation. In: Climate Change 2007: The Physical Science Basis. Contribution of Working Group I to the Fourth Assessment Report of the Intergovernmental Panel on Climate Change [Solomon, S., D. Qin, M. Manning, Z. Chen, M. Marquis, K.B. Averyt, M.Tignor and H.L. Miller (eds.)], Cambridge University Press, Cambridge, United Kingdom and New York, NY, USA.

Raja, M. K. Rama Varma, S. I. Gutman, J. G. Yoe, L. M. McMillin, and J. Zhao (2008), The Validation of AIRS Retrievals of Integrated Precipitable Water Vapor Using Measurements from a Network of Ground-Based GPS Receivers over the Contiguous United States, *J. Atmos. Oceanic Technol., 25,* 416–428.

Raval, A. and V. Ramanathan (1989), Observational determination of the greenhouse effect, *Nature*, *342,* 758-761.

Riehl, H., and J. S. Malkus (1958), On the heat balance in the equatorial trough zone, *Geophysica, 6,* 503–537.

Riley, G. T., M. G. Landin, and L. F. Bosart (1987), The Diurnal Variability of Precipitation across the Central Rockies and Adjacent Great Plains, *Mon. Wea. Rev.*, *115,* 1161–1172.

Sandstrom, M. A., R. G. Lauritsen, and D. Changnon (2004), A central-U.S. summer extreme dew-point climatology, *Phys. Geogr.*, *25,* 191–207.

Sassen, K., and Z. Wang (2008), Classifying clouds around the globe with the CloudSat radar: 1-year of results, *Geophys. Res. Lett.*, *35*, doi:10.1029/2007GL032591.

Sassen, K., S. Matrosov, and J. Cambell (2007), CloudSat spaceborne 94GHz radar bright bands in the melting layer: An attenuation-driven upside-down lidar analog, *Geophys. Res. Lett.*, *34*, doi:10.1029/2007GL030291.

Satoh, M., and Y. Matsuda (2009), Statistics on High-Cloud Areas and Their Sensitivities to Cloud Microphysics Using Single-Cloud Experiments, *J. Atmos. Sci., 66,* 2659–2677.

Satoh, M., T. Matsuno, H. Tomita, H. Miura, T. Nasuno, and S. Iga (2008), Nonhydrostatic Icosahedral Atmospheric Model (NICAM) for global cloud resolving simulations, *Journal of Computational Physics*, the special issue on Predicting Weather, Climate and Extreme events, *227*, 3486-3514, doi:10.1016/j.jcp.2007.02.006.

Satoh, M., T. Inoue, and H. Miura (2010), Evaluations of cloud properties of global and local cloud system resolving models using CALIPSO and CloudSat simulators, *J. Geophys. Res., 115*, D00H14, doi:10.1029/2009JD012247.

Schneider, T. (2006), The general circulation of the atmosphere, *Annu. Rev. Earth Planet. Sci., 34,* 655–688.

Schlesinger, M. E., and N. Ramankutty (1994), An oscillation in the global climate system of period 65–70 years, *Nature, 367,* 723–726.

Sherwood, S. C., and A. E. Dessler (2000), On the control of stratospheric humidity, *Geophys. Res. Lett., 27,* 2513–2516.

Shindell, D. T. (2001), Climate and ozone response to increased stratosphere water vapor, *J. Geophys. Res. Lett*, *28,* 1551–1554.

Simpson, J., C. Kummerow, W. K. Tao, and R. F. Adler (1996), On the Tropical Rainfall Measuring Mission (TRMM), *Meteor. Atmos. Phys., 60*, 19–36.

Slingo, J. M., and and Coauthors (1996), The intraseasonal oscillation in 15 atmospheric general circulation models: Results from an AMIP diagnostic subproject, *Climate Dyn, 12,* 325–357.

Soden, B. J., and I. M. Held (2006) An Assessment of Climate Feedbacks in Coupled Ocean–Atmosphere Models, *J. Climate*, *19,* 3354–3360.

Song, X., and G. J. Zhang (2011), Microphysics parameterization for convective clouds in a global climate model: Description and single-column model tests, J. Geophys. Res., 116, D02201, doi:10.1029/2010JD014833.

Stensrud, D. J., R. L. Gall, and M. K. Nordquist (1997), Surges over the Gulf of California during the Mexican Monsoon, *Mon. Wea. Rev.*, *125,* 417–437.

Stephens, G. L. (1990), On the Relationship between Water Vapor over the Oceans and Sea Surface Temperature, *J. Climate, 3*, 634-645.

Stephens, G. L., S.-C. Tsay, P. W. Stackhouse, and P. J. Flatau (1990), The Relevance of the Microphysical and Radiative Properties of Cirrus Clouds to Climate and Climatic Feedback, *J. Atmos. Sci.*, *47,* 1742–1754.

Stephens, G. L., D. G. Vane, R. J. Boain, G. G. Mace, K. Sassen, Z. Wang, A. J. Illingworth, E. J. O'Connor, W. B. Rossow, S. L. Durden, S. D. Miller, R. T. Austin, A. Benedetti, C. Mitrescu, and the CloudSat Science Team (2002), THE CLOUDSAT MISSION AND THE A-TRAIN, *Bull. Amer. Meteor. Soc.*, *83*, 1771-1790.

Stephens, G. L., and Coauthors (2002), THE CLOUDSAT MISSION AND THE A-TRAIN, *Bull. Amer. Meteor. Soc.*, *83,* 1771–1790.

Stephens, G. L. (2005), Cloud Feedbacks in the Climate System: A Critical Review, *J. Climate, 18,* 237–273.

Stephens, G. L., D. G. Vane, S. Tanelli, E. Im, S. Durden, M. Rokay, D. Reinke, P. Partain, G. G. Mace, R. Austin, T. L'Ecuyer, J. Haynes, M. Lebsock, K. Suzuki, D. Waliser, D. Wu, J. Kay, A. Gettelman, Z. Wang, and R. Marchand (2008), CloudSat mission: Performance and early science after the first year of operation, *J. Geophys. Res.*, *113,* doi:10.1029/2008JD009982.

Stephens, G. L., T. L'Ecuyer, R. Forbes, A. Gettlemen, J.-C. Golaz, A. Bodas-Salcedo, K. Suzuki, P. Gabriel, and J. Haynes (2010), Dreary state of precipitation in global models, *J. Geophys. Res., 115,* D24211, doi:10.1029/2010JD014532.

Straub, K. H., and G. N. Kiladis (2003), The Observed Structure of Convectively Coupled Kelvin Waves: Comparison with Simple Models of Coupled Wave Instability, *J. Atmos. Sci.*, *60,* 1655-1668.

Su, H., J. H. Jiang, D. G. Vane, and G. L. Stephens (2008), Observed vertical structure of tropical oceanic clouds sorted in large-scale regimes, *Geophys. Res. Lett.*, *35*, doi:10.1029/2008GL035888.

Su, H., J. H. Jiang, J. Teixeira, A. Gettelman, X. Huang, G. Stephens, D. Vane, and V. S. Perun (2011), Comparison of regime-sorted tropical cloud profiles observed by CloudSat with GEOS5 analyses and two general circulation model simulations, *J. Geophys. Res., 116,* doi:10.1029/2010JD014971.

Sun, J., and F. Zhang (2012), Impacts of Mountain–Plains Solenoid on Diurnal Variations of Rainfalls along the Mei-Yu Front over the East China Plains, *Mon. Wea. Rev., 140,* 379–397.

Suzuki, K., T. Nakajima, M. Satoh, H. Tomita, T. Takemura, T. Y. Nakajima, and G. L. Stephens (2008), Global cloud-system-resolving simulation of aerosol effect on warm clouds, *Geophys. Res. Lett.*, *35*, doi:10.1029/2008GL035449.

Swann, H., 1998: Sensitivity to the representation of precipitating ice in CRM simulations of deep convection. *Atmos. Res.*, 48, 415–435.

Thayer-Calder, K. and D. A. Randall (2009), The Role of Convective Moistening in the Madden-Julian Oscillation, *J. Atmos. Sci*., *66*, 3297-3312.

Tomita, H. (2008), New micorphysical schemes with five and six categories by diagnostic generation of cloud ice, *J. Meteor. Soc. Japan, 86A,* 121-142.

Trenberth, K. E., J. T. Fasullo, and J. Kiehl (2009), Earth's Global Energy Budget, *Bull. Amer. Meteor. Soc.*, *90,* 311–323.

Waite, M. L., and B. Khouider (2010), The Deepening of Tropical Convection by Congestus Preconditioning, *J. Atmos. Sci.*, *67,* 2601–2615.

Wang, Z. and K. Sassen (2007), Level 2 Cloud Scenario Classification Product Process Description and Interface Control Document, http://www.cloudsat.cira.colostate.edu/ICD/2B-CLDCLASS/2B-CLDCLASS_PDICD_5.0.pdf, Cooperative Institute for Research in the Atmosphere, Colorado State University, Fort Collins, CO.

Wang, M., S. Ghan, M. Ovchinnikov, X. Liu, R. Easter, E. Kassianov, Y. Qian, and H. Morrison (2011), Aerosol indirect effects in a multi-scale aerosol-climate model PNNL-MMF, Atmos. Chem. Phys., 11, 5431–5455, doi:10.5194/acp-11-5431-2011.

Watson, R. T., M. C. Zinyowera, R. H. Moss, and D. J. Dokken. , Eds. (1998), The Regional Impacts of Climate Change: An Assessment of Vulnerability, Cambridge University Press, 517 pp.

Weisman, M. L., and J. B. Klemp (1982), The Dependence of Numerically Simulated Convective Storms on Vertical Wind Shear and Buoyancy, *Mon. Wea. Rev.*, *110,* 504–520.

Wentz, F. J. and T. Meissner (2000), AMSR Ocean Algorithm Theoretical Basis Document, Version 2, Remote Sensing Systems, Santa Rosa, CA.

Wetzel, P. J., W. R. Cotton, and R. L. McAnelly (1983), A Long-Lived Mesoscale Convective Complex. Part II: Evolution and Structure of the Mature Complex, *Mon. Wea. Rev.*, *111,* 1919–1937.

Weverberg, K. Van, A. M. Vogelmann, W. Lin, E. P. Luke, A. Cialella, P. Minnis, M. Khaiyer, E. R. Boer, and M. P. Jensen (2013), The Role of Cloud Microphysics Parameterization in the Simulation of Mesoscale Convective System Clouds and Precipitation in the Tropical Western Pacific, *J. Atmos. Sci., 70,* 1104-1128.

Wheeler, M. C., and H. H. Hendon (2004), An All-Season Real-Time Multivariate MJO Index: Development of an Index for Monitoring and Prediction, *Mon. Wea. Rev.*, *132,* 1917–1932.

Williams, K. D., and Coauthors (2006), Evaluation of a component of the cloud response to climate change in an intercomparison of climate models, *Climate Dyn.*, *145,* 145–165.

Winker, D. M., M. A. Vaughan, A. Omar, Y. Hu, K. A. Powell, Z. Liu, W. H. Hunt, and S. A. Young (2009), Overview of the CALIPSO Mission and CALIOP Data Processing Algorithms, *J. Atmos. Oceanic Technol.*, *26,* 2310–2323.

Wolyn, P. G., and T. B. Mckee (1994), The Mountain-Plains Circulation East of a 2-km-High North–South Barrier, *Mon. Wea. Rev.*, *122,* 1490–1508.

Zhang, C. (1993), Large-Scale Variability of Atmospheric Deep Convection in Relation to Sea Surface Temperature in the Tropics, *J. Climate, 6,* 1898-1913.

Zhang, G. J. (2003), Roles of tropospheric and boundary layer forcing in the diurnal cycle of convection in the U.S. southern great plains, *Geophys. Res. Lett., 30*, 2281, doi:10.1029/2003GL018554, 24.

Zipser, E. J. (2003), Some views on "hot towers" after 50 years of tropical field programs and two years of TRMM data, *Cloud Systems, Hurricanes, and the Tropical Rainfall Measuring Mission (TRMM)—A Tribute to Dr. Joanne Simpson, Meteor. Monogr., No. 51,* Amer. Meteor. Soc., 49–58.

Zipser, E. J., and K. R. Lutz (1994), The Vertical Profile of Radar Reflectivity of Convective Cells: A Strong Indicator of Storm Intensity and Lightning Probability? *Mon. Wea. Rev., 122*, 1751-1759.

Zipser, E. J., C. Liu, D. J. Cecil, S. W. Nesbitt, and D. P. Yorty, 2006: Where are the most intense thunderstorms on Earth?. Bull. Amer. Meteor. Soc., 87, 1057–1071.

INITIALISMS, ACRONYMS, AND ABBREVIATIONS

CLHR: Cloud latent heating rate

COF: Cloud Occurrence Frequency (# of cloudy samples divided by total number of samples)

CTH: Cloud Top Height

DCC: Deep Convective Cloud

DCCAR: DCC Average Reflectivity

ETH: Echo Top Height

MAXREFL: Maximum Reflectivity

N5ETH: ETH of the -5 dBZ echo region

N5ETHD: the distance between the CTH and the N5ETH

NICAM: Nonhydrostatic Icosahedral Atmospheric Model

PBL: Planetary Boundary Layer

PBLR: rooted in the PBL

PBLRC: cloud rooted in the PBL

SAT: Surface Air Temperature

SP-CAM: super-parameterized Community Atmospheric Model

SPREC: surface precipitation rate (depth per time)

TPW: Total Precipitable Water (depth)

W500: vertical velocity (distance per time) at 500 hPa, averaged over 2° by 2°.